UNIVERSITY OF LEEDS

High resolution studies of early type emission line stars

Hugh Eric Wheelwright

September, 2010

Submitted in accordance with the requirements for the degree of Doctor of Philosophy.

The University of Leeds

School of Physics & Astronomy

Papers Included in this Thesis

Work from the following papers has been included in this thesis:

I "The mass ratio and formation mechanism of Herbig Ae/Be binary systems", Wheelwright H.E., Oudmaijer R.D., Goodwin S.P., 2010a, MNRAS, 401, 1199

II "Probing discs around massive young stellar objects with CO 1st overtone bandhead emission", Wheelwright H.E., Oudmaijer R.D., de Wit W.J., Hoare M.G., Lumsden S.L., Urquhart J.S., 2010b, MNRAS, in-press

Paper I forms the basis of Chapter 2. The primary author (H.E. Wheelwright) was responsible for the data reduction, analysis and interpretation of the data and writing the final publication. The data were obtained by R.D. Oudmaijer and H.E. Wheelwright. S.P. Goodwin compared the results with various modes of star formation and helped write the relevant section of the paper. Both R.D. Oudmaijer and S.P. Goodwin provided useful comments on the manuscript.

Paper II forms the basis of Chapter 6. The primary author (H.E. Wheelwright) was responsible for the data reduction, data analysis and interpretation and writing the final paper. In addition, H.E. Wheelwright constructed the model to aid interpretation of the observations. The data were obtained with proposals written by R.D. Oudmaijer. The observations were obtained in service mode but were prepared by both H.E. Wheelwright and R.D Oudmaijer. The low resolution spectra used to calculate extinction were provided by S.L. Lumsden, and were obtained as part of the RMS survey. M.G. Hoare and S.L. Lumsden provided useful suggestions on calculating the extinction towards MYSOs and W.J. de Wit helped verify the model of CO bandhead emission. All the co-authors provided useful comments on the manuscript.

Abstract

This thesis presents a study of early type, emission line objects on small angular scales.

Spectroastrometry is used to separate the spectra of unresolved Herbig Ae/Be binary systems. The separated spectra allow the mass ratio of the systems to be established. The separation and mass ratio distribution of the systems suggest that they form via disk fragmentation. To test this conclusion, disk and binary position angles are compared to a model in which the circumstellar disk and binary orbits are co-planar. The data are consistent with the coplanar model and thus with the scenario of disk fragmentation.

A search for optical outflows associated with Herbig Ae/Be stars is conducted using integral field unit spectroscopy. No outflows are detected. Therefore, the data cannot constrain the location of the proposed transition from collimated to un-collimated outflows, if such a transition exists. Spectroastrometry is used to probe the origin of the Brackett line emission in the data with sub-milli-arcsecond precision.

To explore the potential of spectroastrometry to detect circumstellar disks, spectroastrometric observations of Be stars are presented. It is shown that spectroastrometric data with an angular precision of 0.1 milli-arcseconds can detect milli-arcsecond sized disks. Comparing the spectroastrometric signatures to models of disks with different kinematics demonstrates that Be star disks rotate in a Keplerian fashion, which constrains their formation mechanism.

Finally, spectroastrometry over CO bandhead emission is employed to search for disks around massive young stellar objects. Fitting the observed overtone profiles with a model of a circumstellar disk allows the spatial distribution of the CO to be predicted. No signatures of disks are detected. This is entirely consistent with the best fitting models of the emission, and thus with the presence of small-scale disks around massive young stellar objects.

This thesis is dedicated to my Grandfather, Ken. Ken has always been a source of inspiration and encouragement for me, and at certain times throughout my PhD his support was especially appreciated. Ken was always inordinately proud of what I did, and seemed to take great pleasure in telling his friends that I was doing a PhD in astronomy. Sadly, he is not here to see the finished article. Therefore, I dedicate this thesis to his memory in thanks for many years of excellent company, amusing anecdotes and constant support.

Contents

List of Figures

List of Tables

List of Abbreviations

ADU	Analogue to Digital Unit
ALMA	Atacama Large Millimeter Array
AMBER	Astronomical Multi-Beam Combiner
AMC	Angular Momentum Conserving
AMR	Adaptive Mesh Refinement
AO	Adaptive Optics
arcsec	Arc-Second
AU	Astronomical Unit
BR	Brackett Series
BSC	Bright Star Catalogue
CCD	Charge-Coupled Device
CO	Carbon-Monoxide
CRIRES	Cryogenic High-Resolution IR Echelle Spectrograph
Dec	Declination
DIT	Detector Integration Time
E-ELT	European Extremely Large Telescope
ESO	European Southern Observatory
EW	East-West
FIR	Far Infrared
FF	Free-Fall
FWHM	Full Width at Half Maximum
GMC	Giant Molecular Cloud
HAEBE	Herbig Ae/Be
HPOL	University of Wisconsin's Halfwave Polarimeter

IDL	Interactive Data Language
IDS	Intermediate Dispersion Spectrograph
IFU	Integral Field Unit
IMF	Initial Mass Function
INES	IUE Newly Extracted Spectra
INT	Isaac Newton Telescope
IPHAS	The INT Photometric Hα Survey
IR	Infrared
IRAF	Image Reduction and Analysis Facility
IRAS	Infrared Astronomical Satellite
IRDC	Infrared Dark Cloud
ISIS	Intermediate Spectrograph and Imaging System
ISM	Interstellar Medium
IUE	International Ultraviolet Explorer
JPL	Jet Propulsion Laboratory
KH	Kelvin-Helmholtz
MAG	Magnitude
MATISSE	the Multi Aperture Mid-Infrared Spectroscopic Experiment
MERLIN	Multi-Element Radio Linked Interferometer Network
MIDI	Mid-Infrared Interferometric instrument
MS	Main Sequence
MSX	Mid-course Space Experiment
MTD	Magnetically Torqued Disk
MYSO	Massive Young Stellar Object
NASA	Nation Aeronautics and Space Administration
NDIT	Number of DITs (exposures)
NIR	Near Infrared
NLTE	Non Local Thermodynamic Equilibrium
NS	North-South

PC	P-Cygni
pc	Parsec
PMS	Pre-main-sequence
PRIMA	Phase Referenced Imaging and Micro-arcsecond Astrometry
RA	Right Ascension
RJ	Rayleigh Jeans
RMS	Red MSX Source
rms	Root-Mean-Squared deviance
SED	Spectral Energy Distribution
SKA	Square Kilometre Array
SNR	Signal to Noise Ratio
TT	T Tauri
UV	Ultraviolet
UVES	Ultraviolet and Visual Echelle Spectrograph
UT	Unit Telescope
VLT	Very Large Telescope
VLTI	Very Large Telescope Interferometer
WHT	William Herschel Telescope
YSO	Young Stellar Object
ZAMS	Zero-Age-Main-Sequence
2MASS	Two Micron All Sky Survey

Acknowledgements

First and foremost I thank my supervisor René Oudmaijer for all his advice and support over the last three years. His guidance, constructive criticism and encouragement have been invaluable. I am extremely grateful for his proof-reading of my proposals, papers and thesis chapters and his continued efforts to teach me that less is sometimes more when it comes to writing. I would also like to thank my secondary supervisor, Stuart Lumsden, and Melvin Hoare for the advice they have given me over the past few years and for making me feel welcome in the group. In addition, I thank all the post-docs I have had the pleasure of meeting during my PhD for making my time at Leeds so pleasant. In particular, I would like to thank Jim Hinton, Sven van Loo, Willem-Jan de Wit, Ben Davies, Cormac Purcell, Izaskun Jimenez-Serra, Ronald Bruijn, Rebecca Gozzini, James Urquhart and Ed Pope for their company and for their advice (which has covered a wide range of topics from thesis chapters to making paella).

In a similar fashion, I extend my warmest thanks to all the fellow students I have met during my PhD. This thesis largely owes its existence to their companionship over the last three years. Special thanks are due to Joe Stead, Ian Ashmore and Jo Skilton for being excellent people to share an office with and for putting up me while I was writing up, Ross Parkin for his friendship (and some painful games of squash) and Jo Skilton for hosting some fantastic parties.

Moving further afield, I wish to thank everyone I have collaborated with in the past three years for finding time to work with me and broadening my horizons. In particular, I would like to thank Jon and Karen Bjorkman for a pleasant and productive stay in Toledo, Ohio. I also extend my gratitude to all the telescope support staff that have helped me during the course of my PhD and astronomers who have given me lifts to and from telescopes when I have been observing.

I extend my sincere gratitude to Jim Hinton for introducing me to climbing and my

climbing buddies Ross, Trish, Dan, Helen, Mark, Lee and Sven for periodically dragging me away from my desk. I would especially like to thank Ross and Trish for countless lifts and their generally excellent company. The fact that I managed to preserve my sanity (or most of it) during the writing up process is due in no small part to these people.

I would like to thank my parents, sisters, brother, extended family and friends, all of whom I have not seen enough of during the past three years, for their support and understanding. In particular, I would like to thank my parents for their assistance, both financially and otherwise, and encouragement. Last, but by no means least, I extend my warmest thanks to my wonderful girlfriend Becky for her support throughout my PhD and her patience during the last few months of writing up.

Chapter 1

Introduction

Stars are the constituent building blocks of galaxies and the primary sources of energy within them. In addition, the chemical evolution of galaxies is driven by stars, and the material which forms the galaxies themselves has already been enriched from the primordial mix of hydrogen and helium by previous generations of stars. On the larger scale, it is thought that the very first generation of stars was responsible for the re-ionisation of the universe, and thus a significant change in the interstellar medium (ISM), a few hundred million years after the big bang (Alvarez et al. 2006; Wyithe & Loeb 2003). Therefore, stars have a cosmological impact beyond their prominent role within the confines of present day galaxies. On a smaller (but no less important) scale, stars are the sites of planet formation, and in our case, the source of energy that ultimately sustains life. Therefore, it is easy to see why stars in general play a prominent role in many areas of astrophysics, astro-chemistry and cosmology.

Massive stars are particularly important in that they have substantially more effect on their surroundings than their low mass counterparts. Massive stars are defined as stars whose initial mass is sufficient to produce a type II supernova following the exhaustion of nuclear fuel in their core (Zinnecker & Yorke 2007). Such stars have masses greater than ~ 8 $M_{\odot}$, are significantly more luminous than solar mass stars ($L_{\star} > 1000$ $L_{\odot}$), and have surface temperatures in excess of 20,000 K (see Figure 1.1). Due to this combination of high temperature and luminosity, massive stars produce copious amounts of ultraviolet (UV) flux, which significantly effects their environment by destroying dust, ionising gas and dispersing molecular clouds (see e.g. Matzner 2002). In addition, massive stars drive strong stellar winds with speeds of ~ 2000 km s^{-1}and mass

loss rates of up to $\sim 10^{-6}$ $M_{\odot}yr^{-1}$ (Herrero et al. 1992), which is approximately 8 orders of magnitude greater than that of the Sun. These strong winds allow massive stars to play a prominent role in shaping their surroundings by dispersing molecular clouds and blowing huge bubbles into the ISM (e.g. McKee et al. 1984; McCray & Kafatos 1987; Strickland & Stevens 1999, also see Figure 1.2). Furthermore, when a massive star exhausts its nuclear fuel, the ensuing supernova explosion can even blow holes in the disk of their host galaxy (Mac Low & McCray 1988). The energy injected into the ISM by massive stars can regulate subsequent star formation; either hampering it by dispersing molecular clouds and photo-ionising accretion disks or by triggering further star formation via wind, H II region and/or supernova driven shocks. Therefore, massive stars can have a significant effect on their surroundings via various physical processes.

Massive stars also play a key role in the chemical evolution of galaxies (Spitoni et al. 2009). During their short time on the main sequence (MS), massive stars produce elements ranging from carbon all the way to iron, unlike lower mass stars. As massive stars loose mass via their strong winds, they enrich the ISM with elements produced as a by product of various fusion reactions (see e.g. Vink 2008). The high mass loss of massive stars ensures the mass they inject into the ISM rivals the mass deposited by the more abundant lower mass stars, despite their rarity (e.g. a massive star can loose up to 90 per cent of its mass, or several 10s of $M_{\odot}$, prior to core collapse, Woosley et al. 1993). Furthermore, the supernova explosion accompanying the demise of a massive star injects more enriched material into the ISM, in addition to producing elements heavier than iron via neutron capture processes (Heger et al. 2005). These heavy elements then form part of a further generation of stars and play a crucial role in planet formation, and in our case, life.

Therefore, the influence of massive stars is felt from galactic to planetary scales. As a result, knowledge of the formation and evolution of massive stars is required to comprehensively understand galaxy evolution, star formation and planet formation.

However, despite their importance, our understanding of massive star formation is less complete than in the case of low mass stars. Massive stars form in significantly less

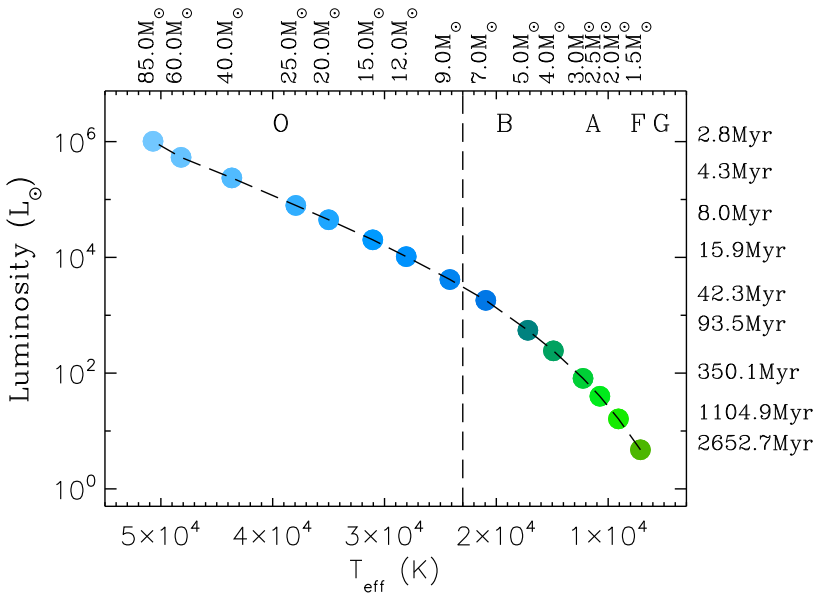

Figure 1.1: *The Hertzsprung-Russel diagram populated with stellar models taken from Schaller et al. (1992). The vertical dashed line marks the boundary between intermediate and massive stars. The zero-age-main sequence is marked by the line connecting the stellar models. For consistency, all models featured standard mass loss rates and overshooting. The masses of the stellar models (while on the ZAMS) are listed at the top of the figure. The main sequence lifetimes of representative models are presented on the right of the figure.*

time than their lower mass counter parts. Indeed, the Kelvin-Helmholtz (KH) timescale, the time taken for a proto-star to convert its gravitational potential to thermal energy and begin nuclear fusion, for a massive star is less than the free-fall (FF) time associated with its constituent material. Therefore, massive stars can attain the luminosity of a massive MS star before their final mass is attained. Given the prodigious luminosity of massive stars, this scenario may result in radiation pressure halting accretion and limiting the final mass attainable by accretion to a few 10s of solar masses (Larson & Starrfield 1971; Kahn 1974; Wolfire & Cassinelli 1987). This has led to alternative formation scenarios being proposed (such as competitive accretion and stellar mergers, e.g. Bonnell et al. 1998; Bally & Zinnecker 2005). Models are difficult to constrain as observing massive star formation is fraught with obstacles, for example: the short

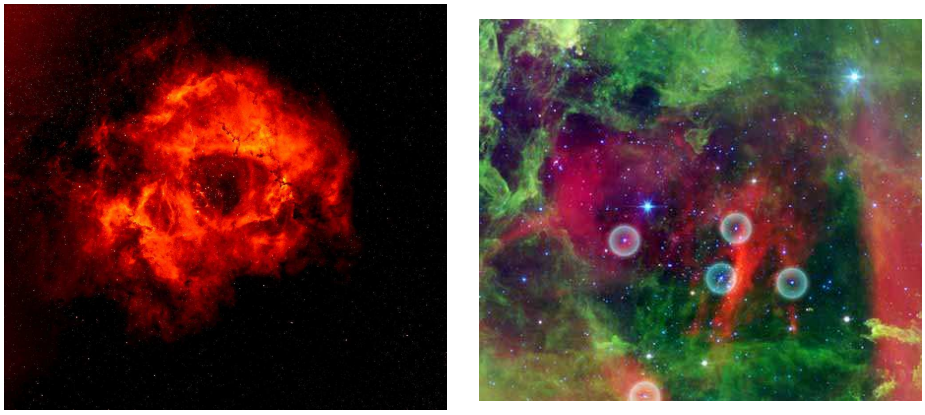

Figure 1.2: *The Rosette nebula. The left panel displays the entire nebula in Hα (taken from the IPHAS survey and prepared by Nick Wright, University College London, on behalf of the IPHAS Collaboration). The right panel presents a zoom in on the centre of the nebular in the three SPITZER bands of 24 μm (red), 8μm (green) and 4.5μm (blue) (Balog et al. 2007, image credit: NASA/JPL-Caltech). The large scale view shows a central cavity where the winds of massive stars have driven the natal gas away. This is also evident in the very centre of the nebula where several massive stars have dispersed layers of dust and gas (shown in green), resulting in a central cavity where only cooler, denser dust (traced in red) remains.*

timescales involved, the rarity of massive stars and their generally large distance from Earth. Consequently, massive star formation is still not fully understood (Zinnecker & Yorke 2007). Massive stars rarely form in isolation (e.g. Maíz-Apellániz et al. 2004), and they begin dispersing their natal molecular cloud long before lower mass stars are fully formed. As a result, this uncertainty over how massive stars form prevents a comprehensive theory of star formation, and hampers our understanding of cluster formation and evolution. Subsequently, massive star formation is a very prominent area of astrophysical research.

In addition, several properties of massive stars on the MS are not fully understood. As an example, Be stars are a class of B type star that display prominent Balmer line emission that originates in a circumstellar disk. Why these stars possess such disks is still unknown. Rapid rotation, magnetic fields and non-radial pulsations have all been

proposed to be capable of producing equatorial disks. However, a consensus on which, if any, of these phenomena plays the dominant role in forming Be star disks has not been reached (see e.g. Owocki 2006). Consequently, Be stars continue to pose 'one of the longest standing challenges in astronomy' (Owocki 2006). Given the importance of rotation and mass loss on massive star evolution, our lack of understanding of these phenomena in the case of Be stars undermines our understanding of massive star evolution. As a result, Be star research is also a very active area of astronomy.

This thesis aims to address unanswered questions relating to the formation and mass loss of massive stars by probing their circumstellar environment on small angular scales. The introduction is structured as follows. To begin with, the general process of star formation is described in §1.1: from the environment in which star formation takes place, to the classical low mass star formation mechanism and the various scenarios invoked to form massive stars. A summary of the observable stages of star formation is then presented, ranging from intermediate mass pre-main-sequence objects (§1.2.1) to the observable stages of massive star formation (§1.2.2). An overview of the enigmatic classical Be stars, MS stars surrounded by circumstellar disks, is presented in §1.3 and the technique of spectroastrometry is then introduced in §1.4. Finally, the thesis is briefly introduced in §1.5

1.1 Star formation

Here a general overview of the theoretical understanding of star formation will be presented, beginning with the classical picture of low mass star formation then moving on to high mass star formation. In subsequent sections, the observational characteristics of young stellar objects of various masses will be summarised. However, to begin with, the environment in which star formation takes place must be introduced and the initial conditions that lead to star formation must be discussed.

1.1.1 The location of star formation – molecular clouds

Stars do not form uniformly throughout the ISM, instead forming in particular locations which satisfy the necessary requirements; namely molecular clouds (e.g. Sargent 1977;

Evans 1999). Molecular clouds are the coolest and most dense components of the ISM, with number densities in excess of $10^2 \mathrm{cm}^{-3}$ and temperatures of approximately 10 K. In addition, molecular clouds are relatively dense and therefore the extinction through them is generally high ($A_V > 1$), which means that the interiors of such clouds are shielded from high energy photons. As a result, the gas is primarily molecular.

The linear extent of molecular clouds ranges from less than a parsec to up to ~ 100 pc (Launhardt et al. 1998; Dame et al. 1986). The largest of such clouds, giant molecular clouds (GMCs) are several tens of parsecs in size, and contain several hundred thousand solar masses of material (Solomon et al. 1985). The smallest clouds are small condensations of molecular material which contain a few tens of solar masses (e.g. Bok globules, Bok & Reilly 1947). Unlike low mass stars, high mass stars form exclusively in the most massive molecular clouds, the GMCs; since massive stars generally reside in clusters and only GMCs can produce stellar clusters (Lada & Lada 2003).

Besides the molecular clouds there is a seemingly additional class of clouds: IR dark clouds (IRDCs), which are dark clouds seen in absorption against the mid infrared (MIR) background. More than 10,000 such IRDCs have been identified from the Mid-course-Space-eXperiment (MSX) data-base Simon et al. (2006a). IRDCs have typical sizes of around 5 pc, peak column densities of approximately $10^{22} \mathrm{cm}^{-2}$, masses of the order of $10^3 \mathrm{M}_\odot$, and volume-averaged H_2 densities of approximately $10^3\,\mathrm{cm}^{-3}$ (Simon et al. 2006b). The similarity of these properties to those of molecular clumps associated with active star formation suggests that IRDCs represent the densest clumps within GMCs where clusters may eventually form, not a different class of clouds. IRDCs often contain condensations of cold massive cores (Rathborne et al. 2006), which have column densities of around $10^{22} \mathrm{cm}^{-2}$ (e.g. Parsons et al. 2009). These cores are thought to be the location of both massive star and cluster formation, and indeed many are associated with 24μm emission – which is indicative of star formation activity (Parsons et al. 2009).

An illustrative example of a cloud complex is presented in Figure 1.3. Typical features to note include the linear scale (several 10s of pc), the elongated morphology and the distinctly clumpy distribution of material. Indeed, observations at high angular resolution generally reveal that all molecular clouds contain substructure and can be

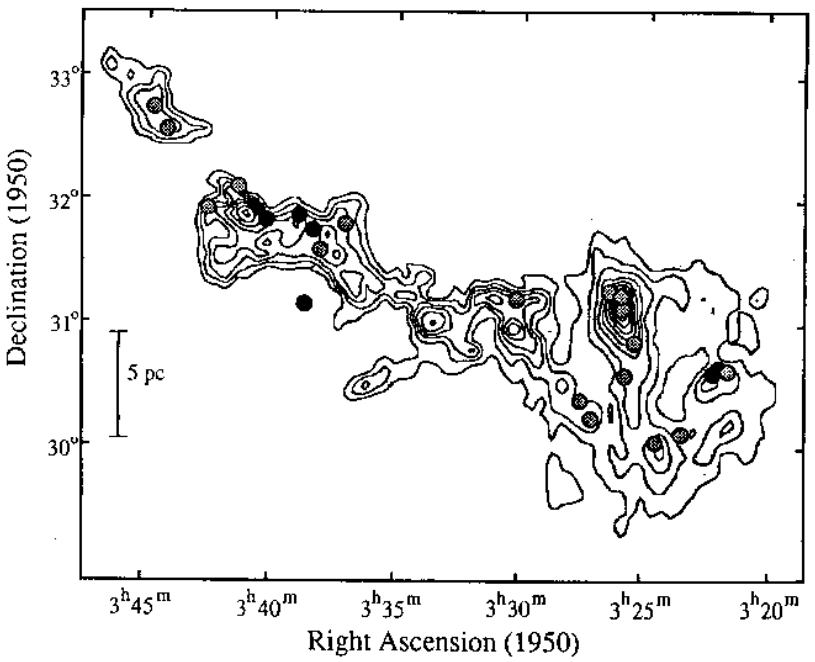

Figure 1.3: *The Perseus molecular cloud complex. The contours mark integrated* ^{13}CO *emission from Bachiller & Cernicharo (1986). The circles mark positions of IRAS sources which are thought to be young stars (taken from Ladd et al. 1993).*

resolved into numerous clumps (Larson 1981; Blitz & Stark 1986; Fuller & Myers 1992; Harju et al. 1991; Hobson 1992). The density of these clumps is approximately ten times that of the average cloud, the mass contained within them ranges from a few to a few thousand solar masses, and their linear extent is typically a parsec (e.g. Williams et al. 1994). Within these clumps are smaller sub-regions of much higher gas density which are referred to as cores. These cloud cores have masses of a few solar masses, densities in excess of $10^4 \mathrm{cm}^{-3}$ and sizes of the order 0.1 parsec (c.f. Williams et al. 2000; Tafalla et al. 2004a). The temperature of these cores is typically 10 K. It is within these cores that stars are formed. This is evident in Figure 1.3 which shows young stellar objects (YSOs) are found in the densest regions of a molecular cloud.

The clumpy structure of molecular clouds is thought to be due to a combination of self gravity and turbulence within the cloud (McKee & Ostriker 2007). Gravitational fragmentation can allow small regions of enhanced density to become gravitationally

unstable and collapse out of the larger background forming regions of high density. However, these initial regions of high density are thought to be due to turbulence driven shocks resulting in compressed regions (Klessen et al. 2000; Padoan & Nordlund 2002). Indeed, it is believed that GMCs themselves fragment out of larger structures on scales determined by turbulence that cascades down from the ISM (McKee & Ostriker 2007). In this picture, molecular clouds are very transient objects, which form from galactic scale turbulent flows (Ballesteros-Paredes et al. 1999; Brunt 2003), form stars in regions of over density caused by the injection of this turbulence into smaller scales, and are dispersed within 10 Myr (Mac Low & Klessen 2004). It should be noted that this picture is not globally accepted. It has been shown that substructure in molecular clouds can be generated via gravitation instabilities – and that the observed turbulence may in fact be due to gravitational collapse (Burkert & Hartmann 2004). However, the scenario of turbulence regulated star formation has gained much support due to its ability to explain star formation in many environments (Krumholz & McKee 2005), in addition to many local characteristics of star formation (Mac Low & Klessen 2004).

1.1.2 Initial conditions

The initial conditions of star formation are represented by the properties of the clouds and cores within which stars form. As stars form in a range of cores, from the low mass, isolated Bok globules to clustered cores in GMCs and infrared dark clouds, there is a corresponding range in conditions prior to star formation. As this thesis primarily focuses on massive stars, attention will be focused on the properties of cores within GMCs, the sites of massive star formation.

Use of the virial theorem unambiguously shows that molecular clouds cannot be supported by thermal pressure alone (Stahler & Palla 2005). However, it is evident from the observed relationship between size and velocity dispersion that molecular clouds are, in general, not gravitationally collapsing but are gravitationally bound and in virial equilibrium (Larson 1981). Therefore, it would appear that there is an additional source of support. Molecular line observations of molecular clouds reveal velocities well in excess of the thermal sound speed (see e.g. Larson 1981). These high velocities exhibit a tight correlation with the size of the host cloud, and are attributed to turbulence. Since the

internal components of a molecular cloud have velocities greater than the thermal sound speeds, their motion may be sufficient to prevent the gravitational collapse of the whole cloud.

However, other phenomena, such as magnetic fields, could also contribute to the support of the cloud. Observational detections of magnetic fields in molecular clouds are difficult, and rely on Zeeman splitting of the 21 cm line of HI or lines of OH near 18 cm and polarisation of background starlight (Crutcher 1999; Bourke et al. 2001). From the few measurements made, it appears the mass to magnetic flux ratio in molecular clouds is approximately twice the critical value, which implies static magnetic fields cannot be the only support against gravity (Crutcher 1999). Nonetheless, there are tentative hints that star formation may be regulated by magnetic fields (Girart et al. 2006; Alves et al. 2008), and the observations do suggest that the magnetic energy of GMCs at least equals their kinetic energy (Crutcher 1999; Novak et al. 2009), implying magnetic fields play an important role in star formation.

Consideration of the importance of magnetic fields in star formation leads to the following problem. Due to magnetic flux freezing, and the contraction required to form a star from the material of a molecular cloud, the ratio of the mass to the magnetically critical mass of the material has to be increased from $\sim$2 to $\sim 10^{5-8}$ (McKee & Ostriker 2007). If this is not the case, the predicted magnetic field of a young star is a million times the observed fields of young stars (Lada & Shu 1990). It has been proposed that ambipolar diffusion allows neutral material to cross the field lines, essentially removing magnetic flux from the material which forms stars (Mestel & Spitzer 1956). However, the associated timescale is approximately equal to the inferred life time of molecular clouds, of the order 10^6 years (Mouschovias 1991). This calls into question the importance of ambipolar diffusion if molecular clouds are short lived entities, as proposed by Hartmann et al. (2001). However, Tassis & Mouschovias (2004) argue that cloud lifetimes are of the order 10^7 years, and as a result, ambipolar diffusion should not be discarded. Consequently, the precise role of ambipolar diffusion in star formation is still debated.

Regardless of the exact timescale of ambipolar diffusion, if the mass of the cloud is sufficient to overcome the magnetic support it will collapse rapidly. This has led to the

bimodal picture of star formation. In this, solar mass stars form in magnetically sub-critical clouds mediated by ambipolar diffusion and massive stars form in magnetically super-critical clouds which collapse under gravity (Shu et al. 1987; Lizano & Shu 1989). Current models of massive star formation implicitly assume that massive stars form in magnetically super-critical regions as they only consider the effects of turbulence (McKee & Tan 2003). Thus, this bimodal picture is generally accepted. However, if the bimodal scenario is correct, the material that forms massive stars must still loose magnetic flux by some phenomena as massive stars are rarely found to have strong magnetic fields (e.g. Silvester et al. 2009).

Attention will now be turned to the smallest, densest regions of molecular clouds, where thermal support is dominant. Given the correlation between cloud size and velocity dispersion, it can be estimated that the velocity dispersion will reduce to the thermal speed at a characteristic size given by 0.1 pc($\frac{\mathrm{T}}{10\ \mathrm{K}}$) (Stahler & Palla 2005). Molecular clouds do indeed contain dense regions approximately 0.1 pc in extent and with temperatures of approximately 10 K (e.g. Myers & Benson 1983; Enoch et al. 2008; Lada et al. 2008), the so-called cores. Once thermal pressure becomes dominant over turbulence, gravitational collapse may form stars. Therefore, it is within these cores that stars form (Beichman et al. 1986; Hatchell et al. 2007). Consequently, the properties of such cores represent the initial conditions of star formation.

The temperature in cores is low, and typically around 5-10 K (e.g. Muench et al. 2007; Friesen et al. 2009; Benson & Myers 1989; Rosolowsky et al. 2008; Caselli et al. 2002a; Crapsi et al. 2007). The associated number density is of the order $10^{3-5}\mathrm{cm}^{-3}$ (Benson & Myers 1989), which results in a typical extinction of A_V=50-100 (Muench et al. 2007). The fractional ionisation in dense cores is also relatively low, $\sim 10^{-8} - 10^{-7}$ (e.g. Caselli et al. 2002b; Maret & Bergin 2007; Miettinen et al. 2009), and is thought to be primarily the result of cosmic rays (ionising photons cannot penetrate the high extinction, Bergin et al. 1999). Due to the low ionisation, magnetic fields are unlikely to add to the thermal support against gravity. Indeed, in a study of six pre-stellar cores, Ward-Thompson et al. (2009) found an offset between the inferred magnetic field and the cores' short axes, in apparent contradiction with the scenario of magnetically

controlled star formation. Nonetheless, magnetic fields with strengths of the order of 100 G have been detected in some molecular cores, and thus magnetic fields should not be discounted (Matthews et al. 2005; Troland & Crutcher 2008).

It is not thought rotation plays an important role in supporting cores as observed velocity gradients are not correlated with core elongation (Goodman et al. 1993). However, the observed rotation of dense molecular cores leads to the following problem (first expressed by Spitzer 1978). The typical specific angular momentum of such cores is of the order of $10^{20-21}\mathrm{cm}^2\mathrm{s}^{-1}$ (Goodman et al. 1993). This is substantially more than the value for the Sun ($\sim 10^{15}\mathrm{cm}^2\mathrm{s}^{-1}$, Lada & Shu 1990). Due to the conservation of angular momentum, the contraction of a core to stellar scales should result in stars being formed with exceedingly high rotation rates. As an example, the contraction of a core with a radius of 0.1 pc to a star with a radius of 1 $\mathrm{R}_{\odot}$ is considered. Conservation of angular momentum would result in the rotation of the core being amplified by a factor of 10^{13}, and thus even a small amount of rotation caused by random thermal motions in the core can result in a rapidly rotating star. This is contrary to observations which indicate young stars are typically slow rotators (Hartmann et al. 1986). Therefore, cores and protostars must shed angular momentum in order to form stars. One mechanism by which cores could achieve this is magnetic braking (Mestel & Spitzer 1956; Mouschovias & Paleologou 1979). In this process, the rotation of a core is reduced by angular momentum being transported outwards via kinks in frozen in field lines. Mouschovias & Paleologou (1979) show that such an effect can reduce the angular momentum of a rotating cloud by several orders of magnitude in less than 10^6 years. However, if the material forming a star decouples from the magnetic field some other mechanism is required to remove angular momentum (Larson 2003). One possibility is disk locking, but this has been shown to be ineffective in slowing the rotation of newly formed stars (Matt & Pudritz 2004). Alternatively, young stars can shed angular momentum by ejecting material. For example, many young stellar objects drive outflows which rotate (see e.g Bacciotti et al. 2002; Woitas et al. 2005), and may thus remove further angular momentum from the star (Matt & Pudritz 2005). Nonetheless, some additional phenomena, such as the creation of a binary system, may be required to remove excess angular momentum (Larson

2003).

Angular momentum transport is also important when considering accretion of mass onto a newly formed protostar. This topic is discussed in more detail in Section 1.1.3.

1.1.3 Low mass star formation

This section presents an overview of the current picture of low (solar) mass star formation and compares this to what is known about massive star formation. Description of the resultant young stellar objects is deferred to Sections 1.2.1 and 1.2.2.

The classical picture of star formation concerns the gravitational collapse of a thermally supported, isothermal sphere of material which represents a molecular cloud (summarised by Shu et al. 1987). Clearly, this is an over simplification as rotation, turbulence and magnetic fields will also add support to molecular clouds. However, the basic picture is useful in highlighting key processes in star formation, and can be refined to incorporate more physics.

To begin with, an isothermal sphere of material will be considered (to represent a molecular core). It is assumed that the sphere is only supported by thermal pressure. Simplistically, it is thought that the sphere will be gravitationally unstable and will begin to collapse if its mass is greater than its characteristic Jeans mass, which is given by the following:

$$M_J = \left(\frac{5k_bT}{G}\right)^{\frac{3}{2}} \left(\frac{3}{4\pi n}\right)^{\frac{1}{2}} \left(\frac{1}{\mu m_H}\right)^2 \tag{1.1}$$

where M_J is the Jeans mass, k_B is the Boltzmann constant, G is the gravitational constant, T is the thermal temperature, n is the number density of the material, μ is the associated mean molecular weight – 2.4 in molecular clouds Stahler & Palla (2005) – and m_H is the mass of a hydrogen atom. If its mass is greater than its Jeans mass, the sphere will begin to collapse, contracting at velocities close to that given by the gravitational free fall time (Shu 1977). The centrally peaked density profile of a singular isothermal sphere results in the collapse occurring inside out. This is because the free-fall time is proportional to the density, so the inner regions collapse more rapidly (Larson 1969). As the inner regions collapse and remove the support of the outer layers, the collapse is propagated outward at the local sound speed (Shu 1977).

Initially, the outermost collapsing material is optically thin to Far Infrared (FIR) radiation from cool dust in the molecular hydrogen. Therefore, the energy released by the material falling into the central gravitational potential is radiated away. This keeps the material at a relatively constant temperature while the density increases. As a result, the Jeans mass decreases, allowing independent collapse of various regions within the collapsing sphere, i.e. the sphere can fragment into multiple independently collapsing regions.

Eventually a point is reached where the increasing density results in the in-falling envelope becoming optically thick to the FIR emission (above $\sim 10^{-13}\,\mathrm{gcm}^{-3}$). The resulting increase in temperature increases the characteristic Jeans mass of the material, eventually halting the collapse and forming a hydrostatic core. However, the outer regions will still be able to cool and remain isothermal, and thus will continue to be in free-fall. The material landing on the central, hydrostatic core results in a shock on the core's surface (Larson 1969), which can contribute to an increase in temperature. The core initially has a low mass (~ 0.05 $\mathrm{M}_{\odot}$ Masunaga et al. 1998), but continues to accrete material. As material continues to fall on the central object, its temperature begins to increase. When the temperature reaches approximately 2000 K, the molecular hydrogen is dissociated. This removes energy from the material, lowering the temperature and thus decreasing the characteristic Jean's mass. This allows a second collapse to begin (Larson 1969). Initially, the in-falling material is optically thin to atomic hydrogen lines, allowing the collapse to proceed in an isothermal fashion, which may result in a secondary stage of fragmentation. Eventually, the increasing density results in the in-falling material becoming optically thick to the atomic hydrogen emission (at $\sim 10^{-2}\,\mathrm{gcm}^{-3}$), resulting in an increase in temperature and pressure. As a result, collapse in the innermost regions is halted and a secondary hydrostatic core is formed, which is the final proto-stellar object. The object is formed with little mass ($\sim 10^{-3}$ $\mathrm{M}_{\odot}$ Masunaga & Inutsuka 2000), but continues to accrete material for a time close to the free-fall time.

The secondary core continues to accrete material from the in-falling atomic hydrogen. As mass is deposited onto its surface its temperature increases. Eventually, the temperature of the object reaches $\sim 10^{6}$ K (Stahler 1988), and initiates a phase of deuterium

burning which lasts for approximately 10^5 years (Mazzitelli & Moretti 1980). Once the deuterium supply is exhausted, the object then contracts on a KH timescale (GM^2/RL) to the ZAMS (Hayashi 1966; Iben 1965; Palla & Stahler 1993). During this evolutionary phase, objects are visible as T Tauri (TT) stars, optically visible pre-main-sequence (PMS) stellar objects which are still accreting.

1.1.3.1 Rotation and magnetic fields

While this simplistic picture is useful to highlight the general processes involved in star formation, it is an over simplification in that it neglects support from magnetic fields, turbulence and rotation. Magnetic fields, turbulence and rotation can add support to the core: slowing or preventing its collapse. The key differences between the classical collapse scenario outlined above and the collapse of a rotating, magnetised core are manifest in the dynamics of the in-falling material. For example, angular momentum due to rotation of the core results in the creation of a disk (Terebey et al. 1984), through which material must accrete. If the rotation is sufficiently slow that the core completes less than one rotation in its free-fall time, the core can be separated into two regions: an inner region which is rotationally dominated and an outer region that is approximately spherical (Terebey et al. 1984). The interface between the two regimes, the centrifugal radius, represents the approximate size of the accretion disk that is formed (Krasnopolsky & Königl 2002), and is approximately 50 AU (for typical parameters of solar mass star formation). The outer region is essentially unaffected by rotation and continues to collapse on the free-fall time scale. However, the mass ultimately has to pass through the disk as the inner regions of the collapsing core are dominated by rotation effects.

Similarly, magnetic fields can have a significant effect on the morphology of a collapsing core (Galli & Shu 1993a). The magnetic field prevents collapse across the field lines and thus results in a flattened structure which is referred to as a pseudo disk (as it is not rotationally supported, Galli & Shu 1993a,b). The typical radius of the pseudo disk is several orders of magnitude larger than the associated centrifugal radius (Galli & Shu 1993b). Therefore, the combined effects of rotation and magnetic fields may result in a small-scale rotationally supported accretion disk which is then fed on a larger scale by a pseudo disk. However, this is very dependent upon the relative importance of the

two phenomena. Hennebelle & Fromang (2008) demonstrate that when the mass to flux ratio is close to its critical value, no centrifugally supported disk is formed. This is because magnetic braking removes significant amounts of angular momentum and the collapse preferentially occurs along the field lines, limiting the amount of angular momentum delivered to the inner regions of the core. Ambipolar diffusion cannot sufficiently decouple the material from the field to facilitate the creation of a disk (Mellon & Li 2009). However, a rotationally supported disk could form once the massive envelope, which acts to support the magnetic braking effect, is dispersed (Mellon & Li 2009). To summarise, rotation and magnetic fields can significantly effect the dynamics and morphology of a collapsing core, particularly on small and intermediate scales (e.g. tens to hundreds of AU). The interplay between the two effects is quite complex and has only recently begun to be parametrised (see e.g. Hennebelle & Ciardi 2009).

1.1.3.2 Disks and outflows

As a result of omitting the effects of rotation and magnetic fields the classical collapse scenario does not feature accretion disks and outflows. However, these phenomena are ubiquitous features of young stars and therefore must play some role in the formation process.

Cores typically have a higher specific angular momentum than stars (see Section 1.1.2). The collapse of a rotating core to stellar dimensions, coupled with the conservation of angular momentum, results in the formation of a rotationally supported disk around the central protostar (e.g. Cassen & Moosman 1981; Terebey et al. 1984; Yorke et al. 1993). Mass from the collapsing envelope will land on the disk and be transported inwards to be accreted onto the central star. As previously discussed, cores must shed angular momentum to form slowly rotating stars (Section 1.1.2, e.g. Prentice & Ter Haar 1971). It is thought that this is achieved through the process of magnetic braking (Mestel & Paris 1979; Mouschovias 1987; Nakano 1989). However, even if this is the case, material in the disk must also loose angular momentum before it is able to accrete onto the central star. This is thought to occur via two agents: angular momentum transport within the disk and outflows which carry mass, and angular momentum, off the disk and the star.

The currently favoured modes of angular momentum transport feature physical instabilities. The most prominent is the magneto-rotational-instability (MRI, Balbus & Hawley 1991). If a magnetic field threads the disk in the radial direction, the differential rotation will result in the magnetic field lines being 'stretched'. The tension on the magnetic field lines acts to increase the rotation rate of the outer annulus and decrease the rotation rate of the inner annulus, thus transferring angular momentum outwards through the disk. As angular momentum is transferred outwards, the inner annulus will move closer to the central star, with the result of increasing its rotation rate, and the reverse will be true for the outer annulus, leading to the instability (Hawley & Balbus 1991). 3D MHD simulations suggest that this effect may provide an important source of viscosity in accretion disks (Hawley et al. 1995). The stretching of the field lines is equivalent to magnifying the field, and thus this instability may occur even when the initial field is very weak (Hawley et al. 1996).

However, there are other instabilities that can transport angular momentum in circumstellar disks. For example, if a disk is sufficiently massive, gravitational instabilities can also transfer angular momentum outward (e.g. Lynden-Bell & Kalnajs 1972). The mechanism is essentially the same as that described above (for the MRI). The only difference is that in this case the tension between two differentially rotating annuli is provided by gravitational attraction due to a concentration of material in the radial direction. The rotational distortion of the initially radial gravitational force between the material in the two annuli can result in a spiral arm, within which, gravitational attraction acts to accelerate the outermost material and decelerate the innermost material – resulting in the outward transport of angular momentum. 3D adaptive mesh refinement (AMR) simulations of massive star formation following the collapse of magnetised Bonner-Ebert spheres (pressure bound, hydrostatic self gravitating spheres) clearly show the development of spiral structure in the resultant disk (see Figure 1.4). It is found that such structure provides efficient removal of angular momentum and thus facilitates accretion of material onto the central star (Banerjee & Pudritz 2007). The gravitational instability can only occur when the disk mass is comparable to the mass of the central star (e.g. see Pringle 1981), although disks more massive than 50 per cent of the sys-

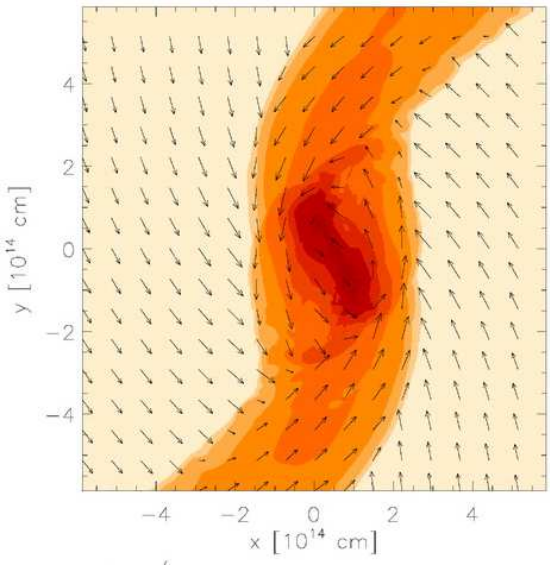

Figure 1.4: *A slice in the disk plane from the (hydrodynamical) simulations of the collapse of Bonner-Ebert spheres by Banerjee & Pudritz (2007). This snapshot is taken* 1.4×10^4 yr *into the collapse. The emergence of spiral structure due to gravitational instability in a massive disk is evident.*

tem mass fragment into multiple components (Kratter et al. 2010). Clearly, the relative importance of the various modes of angular momentum transport are sensitive to the properties of the disk (e.g. mass and magnetic fields). However, the various instabilities are not mutually exclusive and simulations indicate that both play a role in removing angular momentum from disks and allowing accretion onto the central star (Banerjee & Pudritz 2007).

In addition to disks, outflows are ubiquitous features of star formation which the classical collapse scenario does not explain. Furthermore, outflows can remove angular momentum from the inner regions of the disk by ejecting material from the system (e.g. Machida et al. 2007; Ray et al. 2007). Therefore, in order to understand star formation the properties and launching mechanisms of such outflows must also be understood. YSOs have been observed to drive collimated jets several parsecs in length in the optical and radio (Mundt & Fried 1983; Snell et al. 1985; Bally & Devine 1994, see Figure 1.5). In addition, high velocity, bipolar outflows emanating from young stars have been

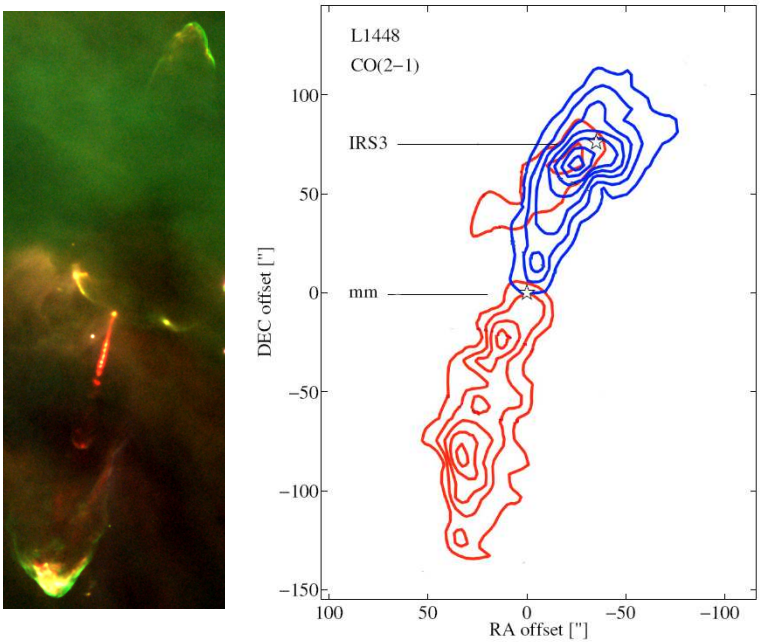

Figure 1.5: *Two examples of outflows from YSOs. In the left panel, a three colour image of the HH 34 jet and bow shock (image credit European Southern Observatory (ESO)). In this image blue represents blue light (429 nm), green represents Hα emission (656 nm) and red represents* SII *emission (673 nm). In the right panel, the CO (2-1) map of L1448 is presented. This is taken from Bjerkeli et al. (2009), although the original data are presented in Bachiller et al. (1995).*

observed in rotational transitions of CO gas (e.g. Snell et al. 1980, see Figure 1.5). In short, it is clear that mass loss is an ubiquitous feature of star formation (Bachiller 1996). What is still not known is exactly how the various outflows are launched and what part they play in removing angular momentum from forming star and disk systems (Ray et al. 2007).

The challenge in developing a unified theory of outflow generation is that outflows of different material (e.g. neutral molecular or ionised atomic material) often exhibit differing properties. Molecular outflows traced by CO are typically poorly collimated with length to width ratios of 2–5 (Bachiller 1996), although relatively collimated molecular outflows have also been observed (collimation factions $\gtrsim 5$, e.g. Bourke et al. 1997;

Tafalla et al. 2004b). In contrast, ionised jets appear highly collimated over distances of up to a pc or more (Mundt et al. 1990; Reipurth et al. 2002; Ray 1987).

Molecular outflows often exhibit a clumpy structure in the high velocity component of the gas (Bachiller et al. 1990, 1991; Qiu & Zhang 2009). Such discrete components indicate that mass is lost in a sporadic fashion (Bachiller et al. 1990, 1991). Optical outflows also exhibit a fragmented, knotty structure (Buehrke et al. 1988; Ray et al. 1996), perhaps indicating that they are connected to the outflows observed in CO emission. The knots in optical outflows are thought to be internal working surfaces, like bow-shocks (Raga & Kofman 1992; Ray et al. 1996; Dougados et al. 2000), and are thought to be related to episodic, FU Ori like accretion events (Reipurth 1989; Zinnecker et al. 1998). This is supported by the observed relationship between accretion rates and outflow activity (Hartigan et al. 1995).

Masson & Chernin (1993) demonstrated that optical jets posses sufficient momentum to drive molecular outflows, and thus suggest that molecular outflows are driven by jets, as opposed to stellar winds as proposed by Snell et al. (1980). Indeed, many observations are consistent with this scenario, in which molecular outflows are generated by molecular material being entrained by bow shock at the head of the optical jets (Bence et al. 1996; Gueth & Guilloteau 1999). However, some molecular outflows are hard to reconcile with the jet driven scenario (Lee et al. 2000, 2002; Santiago-García et al. 2009). Regardless of whether CO outflows are driven by collimated jets or wide angled winds the question remains – how are these original outflows launched?

Jets from YSOs are typically very narrow with opening angles of a few degrees beyond 50 AU (see Agra-Amboage et al. 2009, and references therein). TT stars, which are the source of many observed optical jets, do not possess sufficiently dense envelopes to collimate outflows hydrodynamically to such an extent (Ferreira et al. 2006). Consequently, magneto-hydrodynamic accretion driven wind models are invoked to explain the launching, collimation and the large mass ejection efficiencies exhibited. Several different scenarios are proposed for the origin of the outflow, each of which is characterised by a different location of the jet launching region. The proposed origins of the observed outflows are: the stellar surface (e.g. accretion powered stellar winds, Matt

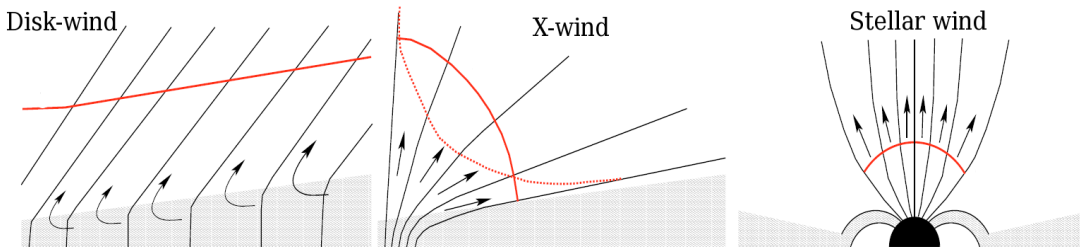

Figure 1.6: *The three primary MHD jet creation scenarios applied to YSOs, taken from Ferreira et al. (2006). From left to right: the disk-wind, the X-wind and a stellar wind. In the disk wind scenario, the disk is permeated with a magnetic field over a range of radii. By contrast, the X-wind model assumes the disk is only threaded by a magnetic field at one point – where the stellar magnetic field penetrates the disk. In the stellar wind scenario, the mass loss is from the stellar surface but is driven by accretion as young T Tauri stars do not rotate rapidly enough to launch such a wind by virtue of their rotational energy alone.*

& Pudritz 2008), the inner region of an accretion disk (an X wind, Shu et al. 1994; Shang et al. 2007), a range of inner disk radii (a disk wind, Pudritz & Norman 1986, see Figure 1.6) or from the stellar magnetosphere (due to reconnection events, Ferreira et al. 2000). Currently, even high angular resolution adaptive optics and near infrared (NIR) spectro-interferometric observations cannot differentiate between the X-wind and disk-wind scenarios (Agra-Amboage et al. 2009; Malbet et al. 2007; Rousselet-Perraut et al. 2010).

Outflows may play a crucial role in star formation as they represent a means by which the inner disk and/or star may loose mass and with it angular momentum. This is of critical importance as the star cannot accrete high angular momentum material without rapidly being spun-up to its break up velocity - preventing further accretion. The removal of angular momentum by outflows has been confirmed with observations of jet rotation (with velocities of the order of 5–30 $\mathrm{km\,s^{-1}}$ Bacciotti et al. 2002; Coffey et al. 2004; Woitas et al. 2005; Coffey et al. 2007; Zapata et al. 2010). It has been found that jets can carry a significant amount (up to $\sim$ 66 per cent) of the estimated transport

rate through the launching region of the disk (Woitas et al. 2005). Furthermore, this has been shown to be true for embedded Class I objects, indicating that outflows are important in regulating angular momentum transport at early evolutionary stages of YSOs (Chrysostomou et al. 2008). Finally, it has been found that outflows may facilitate massive star formation by creating anisotropic radiation fields, and thus reducing the radiation pressure experienced by in-falling material in the in-falling envelope (Yorke & Sonnhalter 2002; Krumholz et al. 2005a, this is discussed in more detail in Section 1.1.4).

To summarise, this section has introduced the basic processes by which a molecular core collapses to form a solar mass star (requiring a compression in density of 20 orders of magnitude). While the classical collapse of an isothermal sphere proves useful in discussing key time-scales and processes relevant to star formation, additional physics, such as rotation and magnetic fields, significantly change the dynamics of the in-falling material. Furthermore, phenomena such as rotation and magnetic fields result in the creation of disks and outflows, both of which provide angular momentum transport, without which the central star would be spun-up and accretion onto the central star would be impeded. To conclude this section, although the precise outflow launching mechanism is still unconstrained, the basic physics of solar mass star formation are thought to be relatively well understood. It is important to note that this sub-section focuses explicitly on solar mass stars, and the processes described may not be applicable to all masses. The following section (1.1.4) will contrast solar mass star formation with high mass star formation and discuss why the above scenario may not apply to massive stars.

1.1.4 High mass star formation

Massive star formation differs from low mass star formation in that the associated timescales are much shorter, massive stars have a greater capacity to affect their formation via feedback processes and massive stars have a different internal structure to low mass stars. How these differences are manifest during the process of massive star formation is still relatively unknown. Consequently, our knowledge of how massive stars form is less complete than in the case of solar mass stars. This section briefly introduces how

massive star formation differs from low mass star formation and discusses the various scenarios proposed to explain the formation of massive stars.

Unlike solar mass star formation, in which the general physical picture is thought to be understood (e.g. Shu et al. 1987; McKee & Ostriker 2007, Section 1.1.3), until recently the formation of massive stars has been subject to considerable theoretical uncertainty. The KH timescale (see equation 1.2), the time taken for a proto-star to convert its potential energy to thermal energy, is of the order 10^{4-5} years for a massive star. This timescale is substantially longer for a solar mass star, e.g. approximately $\sim 10^7$ years (see Figure 1.7). The KH timescale can be compared to the time required to form a star, which can be estimated from the free-fall time associated with its constituent material, with the following equations:

$$t_{KH} = \left(\frac{GM_\star^2}{R_\star L_\star}\right) \tag{1.2}$$

$$t_{\rm FF} = \left(\frac{3\pi}{32{\rm G}\rho}\right)^{\frac{1}{2}} \tag{1.3}$$

where t_{KH} and t_{FF} represent the KH and free-fall timescales, $M_\star$, $R_\star$ and $L_\star$ refer to the final mass, radius and luminosity of the resultant star and ρ is the density of the collapsing core. Using a typical core number density of $10^4{\rm cm}^{-3}$ results in a free-fall time of approximately $4{\times}10^5$ years; substantially longer than the KH time-scale of a massive star, see Figure 1.7. Therefore, a young massive star can attain a high luminosity (i.e. that of a late O, early B type main sequence star) while it is still accreting material, at least according to an extrapolation of the standard low mass star formation scenario of Shu et al. (1987). As a result, it has been thought that the immense luminosity of massive stars could provide sufficient radiation pressure to reverse the in-fall of material (Larson & Starrfield 1971; Kahn 1974; Wolfire & Cassinelli 1987). In addition, massive stars in the act of forming have the potential to ionise their surroundings, which could act to disperse accretion disks and in-falling envelopes, again limiting the final mass obtained. Consequently, alternative modes of massive star formation have been proposed, for example competitive accretion and stellar mergers (Bonnell et al. 1998; Bally & Zinnecker 2005).

This lack of understanding of massive star formation has been compounded by the

difficulty in observing young massive stars. The short KH time-scale of massive stars, in conjunction with their innate rarity, makes it difficult to catch a massive star in the act of forming. Since the formation time of massive stars is very short, massive stars form before their natal material is fully cleared (e.g. Bernasconi & Maeder 1996). Therefore, the process of massive star formation is hidden under many magnitudes of extinction, which makes it difficult to study. Finally, as massive stars are rare, they tend to be further away than nearby sites of low mass star formation. As an example, the nearest solar mass star forming region is the Taurus-Auriga complex at ∼140 pc (e.g. Ungerechts & Thaddeus 1987). The closest region of massive star formation (the Orion Molecular Cloud) is several times further away at ∼450 pc (e.g. Genzel & Stutzki 1989) and a typical distance to a massive young star is of the order of several kpc. This makes massive young stars difficult to study on small scales, which is where key processes, such as accretion, occur. As a result, the process by which the most massive stars form remains elusive.

1.1.4.1 Stellar Mergers

It has been proposed that massive stars cannot be formed via conventional accretion scenarios due to radiation pressure halting infall. To negate this obstacle, Bonnell et al. (1998) proposed that massive stars form via the merger of several, lower mass stars. The mass distribution due to mergers is entirely consistent with a Salpeter IMF (Bonnell & Bate 2002), and the process would explain the preferential location of massive stars in the centres of rich clusters (e.g. Hillenbrand 1997). In addition, this scenario explains how an object many times the local Jeans mass can be formed. Forming a massive star in a monolithic fashion appears difficult as the gas will fragment until the Jeans mass is reached, which is typically less than the mass of a massive star.

Forming massive stars through mergers on a reasonable time scale requires a very high stellar density (e.g. $10^8 \mathrm{pc}^{-3}$ Bonnell & Bate 2002; Davies et al. 2006). Young dense stellar clusters appear to have densities much lower than this, e.g. of the order $10^{3-4} \mathrm{pc}^{-3}$ (Megeath et al. 1996). This discrepancy is reduced slightly by considering binary systems. Perturbed binary systems lower the required stellar density to approximately

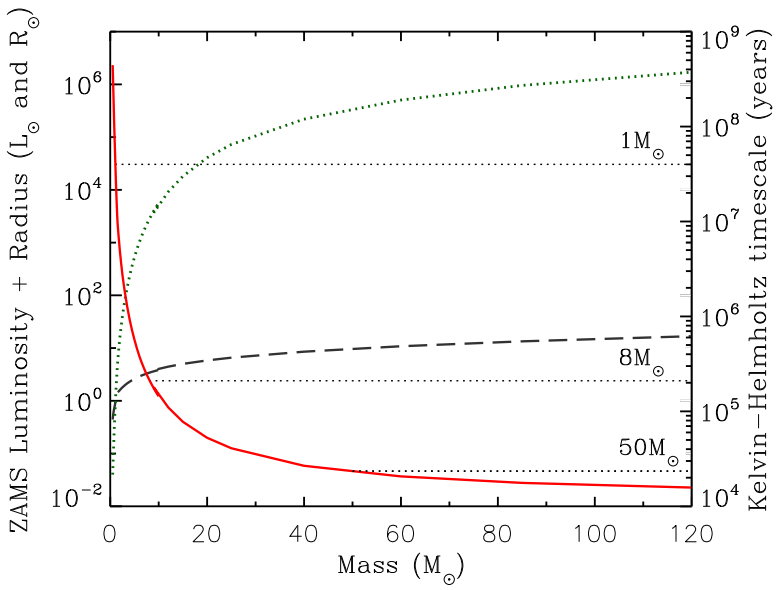

Figure 1.7: *The ZAMS luminosity (dotted), radius (dashed) and KH timescale (solid) as a function of ZAMS mass. At masses over* 12 $M_\odot$ *the data are from the models of rotating stars presented by Meynet & Maeder (2005) and at lower masses from the models of Pietrinferni et al. (2004). KH timescales for* 1 $M_\odot$, 8 $M_\odot$ *and* 50 $M_\odot$ *are indicated with horizontal dotted lines (adapted from Zinnecker & Yorke 2007).*

$10^6 pc^{-3}$ (Bonnell & Bate 2005). This is still several orders of magnitude greater than any observed cluster density (e.g. Trumpler 14 has a stellar density of $7.3 \times 10^3 pc^{-3}$, Ascenso et al. 2007). Therefore, it appears unlikely massive stars form via this mechanism (Hoare & Franco 2007). Recently, Clarke (2008) and Davis et al. (2010) show that the number of stellar collisions in an accreting cluster depends not only upon the number of stars but also upon the accretion rate of the host cluster. These authors estimate that a significant number of collisions do occur in dense cluster cores, although this result is strongly dependent upon the accretion rate onto the core. However, the accretion process invoked by these authors has been questioned (Krumholz et al. 2005b, see the following section). Consequently, it has yet to be shown that collisions between young stars can occur sufficiently frequently to form massive stars.

1.1.4.2 Competitive accretion

At first sight it appears difficult to form a massive star, which is many times the local Jeans mass, in a monolithic fashion. A core with a mass greater than a few solar masses will tend to fragment, making it difficult to form a star of many tens of solar masses. One scenario which circumvents this obstacle to forming massive stars is competitive accretion. In this scenario, a cloud destined to form a cluster fragments to form multiple cores, each of approximately a Jeans mass. The proto-stars formed at the centre of the cores then define the gravitational potential across the newly formed cluster. The cluster potential focuses the reservoir of gas not yet accreted by proto-stars towards the centre of the cluster, where centrally located objects may accrete it via Bondi-Hoyle accretion (Bondi & Hoyle 1944; Bondi 1952). Thus the central objects can grow to many times the local Jeans mass by accumulating material not originally associated with their natal core (Bonnell et al. 1997). As the privileged central objects grow in mass, their gravitational influence increases, allowing them to accrete from an extended area, which in turn results in them becoming more massive (Bonnell et al. 2004). This process leads to the runaway growth of a few central objects, resulting in stars of ~ 30 $M_{\odot}$ (Bonnell et al. 2004).

This scenario is in agreement with the general finding that massive stars are preferentially located in the dense centres of large clusters (e.g. in NGC 3603 3 WR, six O3 and several other O types stars are all located within 0.03 pc^{-3}, Drissen et al. 1995). Furthermore, simulations utilising smoothed-particle-hydrodynamics (SPH) show that this scenario results in an IMF that is consistent with observations (Bonnell et al. 2001; Klessen 2001). However, while Bonnell et al. (2003) find that competitive accretion can result in stars of up to 27 $M_{\odot}$, it is important to note that their calculations did not include radiative feedback. This has led to the physical basis of competitive accretion being questioned (Edgar & Clarke 2004). Furthermore, McKee & Tan (2003) found that competitive accretion does not significantly affect the mass accreted by a forming star in conditions typical of massive star forming regions. Finally, Krumholz et al. (2005b) argue that the simulations of Bonnell et al. (2003) begin with unrealistic initial conditions. Essentially, Krumholz et al. (2005b) argue that the simulations of competitive accretion feature strongly gravitationally bound clouds, whereas star formation is observed to oc-

cur in clouds where the turbulent energy is equal to the gravitational potential. The SPH simulations of Bonnell et al. (2003) did begin with supersonic turbulent motions, but these decay within a crossing time.

It is evident that competitive accretion is by no means an accepted phenomenon. Direct observations of bulk infall of gas onto a forming cluster could confirm the scenario of competitive accretion. As noted by Bonnell & Bate (2006), the typical velocity dispersions in regions of massive star formation are in excess of the infall velocity due to competitive accretion. However, the authors demonstrate that this does not necessarily exclude the competitive accretion scenario when line of sight effects are taken into account. Consequently, while large line-widths do not exclude competitive accretion, they make it difficult to critically evaluate the scenario. Recently, evidence of large-scale gravitational infall in the dense gas surrounding a massive star cluster in the act of forming has emerged (Barnes et al. 2010). This is highly reminiscent of the competitive accretion scenario, but at the current resolution the data are consistent with the monolithic, collapse models/simulations of McKee & Tan (2003) and Banerjee & Pudritz (2007), although the mass infall rate is greater than expected (Barnes et al. 2010). Very high angular resolution observations are required to determine the properties and distribution of the proto-stellar objects at the centre of the infall and assess whether they are compatible with competitive accretion. For example, recent observations indicate that the distribution of core masses is skewed towards much higher values than predicted by competitive accretion (Zhang et al. 2009; Bontemps et al. 2010).

In summary, there is, as yet, no direct evidence of competitive accretion. While it is referred to as the most plausible explanation of the high end IMF (Zinnecker & Yorke 2007), its physical basis has been subject to severe criticism (Edgar & Clarke 2004; Krumholz et al. 2005b; Krumholz & Tan 2007). Consequently, a monolithic mechanism has been proposed as a more accurate representation of massive star formation. This alternative scenario will now be introduced.

1.1.4.3 Disk accretion

As discussed above, it has been proposed that massive stars cannot be formed via conventional accretion scenarios due to radiation pressure halting infall (see e.g. Larson

& Starrfield 1971; Kahn 1974; Wolfire & Cassinelli 1987). However, the initial upper limits on the mass of stars attainable through accretion were derived assuming spherical accretion (see e.g. Wolfire & Cassinelli 1987). Therefore, deviations from spherical accretion have the potential to reduce this constraint and facilitate massive star formation via monolithic accretion (as opposed to competitive accretion). Here, the scenario of massive star formation via disk accretion is discussed and the supporting observations are assessed.

As noted by Nakano (1989), the effects of magnetic fields and rotation will tend to flatten a contracting envelope. Consequently, the idealised spherical collapse of Wolfire & Cassinelli (1987) is not applicable. In a flattened configuration, the stellar radiation can escape the envelope via the lower density polar regions. As a result, the radiation pressure on the in-falling gas is substantially less than in the spherical infall case. Nakano (1989) demonstrate that this allows accretion onto a stellar core of 100 $M_{\odot}$, although this is dependent upon the accretion rate. This was subsequently confirmed by Jijina & Adams (1996), who demonstrate that 100 $M_{\odot}$ stars can, in principle, form from the collapse of a rotating core – whereas this mass is beyond the limit achievable with spherical accretion.

In the first 2D radiation hydrodynamic evaluation of this scenario, Yorke & Sonnhalter (2002) find that the collapse of a slowly rotating molecular clump of 120 $M_{\odot}$ can result in the formation of a 42.9 $M_{\odot}$ star before radiation pressure halts accretion. The simulations feature the creation of a circumstellar accretion disk and a powerful, radiation driven outflow. The combination of the dense disk in the equatorial region and the outflow cavity in the polar directions result in a strongly anisotropic radiation field – which reduces the radiation pressure on gas accreting through the equatorial disk, a phenomena referred to as the 'flashlight' effect. Moving to three dimensions, Krumholz et al. (2009) demonstrate that additional effects not present in the earlier, 2-D simulation, exaggerate this anisotropy and allow further accretion. Specifically, Rayleigh-Taylor instabilities in the in-falling envelope channel gas into filaments that self-shield against radiation, channeling material down to the disk, while allowing radiation to escape through optically thin bubbles (as predicted by Turner et al. 2007).

In addition, gravitational instabilities in the disk (only apparent in the 3-D simulations as the 2-D simulations were axi-symmetric) result in a spiral structure which efficiently transport angular momentum outward, facilitating further accretion, in agreement with Banerjee & Pudritz (2007).

The simulations of Krumholz et al. (2009) were stopped after forming a massive star of 41.5 $M_\odot$, in addition to a 29.2 $M_\odot$ companion. However, at no point in the simulations did the accretion stop due to radiation pressure – indicating that even more massive stars can, in principle, form via disk accretion. Furthermore, the simulations of Krumholz et al. (2009) used the gray approximation (i.e. the opacity is independent of frequency), rather than a multi frequency treatment of the radiation. Yorke & Sonnhalter (2002) demonstrate that using the gray approximation results in less massive stars than the full wavelength dependent treatment. This is because the effect of an anisotropic radiation field is compounded by frequency dependent radiation transfer – or rather the flashlight effect is diminished using the gray approximation. Therefore, the fact that the simulations of Krumholz et al. (2009) produced a star with a mass of ~ 40 $M_\odot$ indicates that even more massive stars may well form via the same process. This has been confirmed by Kuiper et al. (2010) who demonstrate that stars of up to 100 $M_\odot$ can form from disk accretion using 2D, frequency dependent radiative feedback models.

Appraising the properties of accretion disks around massive proto-stars using steady state, alpha disk models Vaidya et al. (2009) find that the mid-plane temperature of such disks can reach high values, e.g. 10^5 K at 0.1 AU. As a result of this high temperature, the disk self sublimates at radii significantly ($3\times$) greater than the sublimation radius due to the stellar radiation alone. This lowers the opacity in the inner region of the disk and facilitates accretion in the face of stellar radiation pressure.

This scenario is supported by a growing, mainly indirect, body of evidence of the presence of circumstellar disks around massive young stellar objects (MYSOs). This is summarised in Section 1.2.2.3. However, there are still no direct detections of a small-scale accretion disk around a MYSO (see Cesaroni et al. 2007, for a discussion on the difficulties in detecting such a disk which is still valid). Nonetheless, detections of dusty

disks around massive young stellar objects (see e.g. Kraus et al. 2010) strongly suggest the presence of small-scale, gaseous accretion disks.

To summarise, disk accretion offers a physically viable formation mechanism for massive stars, negating the obstacle posed by radiation pressure of the luminous accreting star by imposing anisotropy on the radiation field, allowing radiation to escape via tenuous outflow cavities while material accretes unimpeded in a dense equatorial disk. Indirect evidence points to the presence of disks around massive young stellar objects, but there are, as yet, no direct detections of small-scale, gaseous accretion disks around massive young stellar objects.

1.2 Young Stellar Objects

The process of star formation proceeds via several distinct evolutionary stages, for example the initial collapse of a proto-stellar core; the main accretion stage of a proto-star and the final contraction of the resultant YSO to the ZAMS. The various stages involved in solar mass star formation are summarised in Figure 1.8. Proto-stellar objects evolve from class 0 (corresponding to the main core accretion phase and a small proto-stellar mass) to class III (corresponding to a nearly fully formed star with only residual circumstellar material). Class 0 and I objects are heavily embedded and it is difficult to observe the processes by which such objects form. In contrast, the class II objects are readily observable as much of their natal material has been dispersed. Such objects provide a key insight into their formation process as they retain an accretion disk and still drive outflows. Consequently, the work presented in this thesis focuses on young stellar objects similar to class II objects. At intermediate masses, optically visible PMS class II objects are referred to as Herbig Ae/Be stars. These are discussed in more detail in Section 1.2.1.

At high masses, the evolutionary phases of proto-stellar objects are quite different, primarily because of the short timescales associated with massive star formation. A proposed evolutionary scenario is the following (taken from Beuther et al. 2007):
→Massive starless cores (quiescent cores)
→Massive cores harbouring low/intermediate stars (hot cores)

→High mass proto-stellar objects (MYSOs, hyper and ultra compact HII regions)
→Final OB star (compact HII regions and MS stars).
In this scenario, MYSOs are similar to the low mass class II objects as they have assembled most of their mass but may still be accreting material. However, MYSOs differ from low mass class II objects in that MYSOs may have already arrived at the MS. In addition, their formation may well be very different from that of the solar mass T Tauri stars.

This thesis focuses on the young stellar object phase of star formation (class II objects in the case of intermediate mass stars and MYSOs in the case of massive stars). This section describes the properties of YSOs of intermediate and high masses to highlight similarities and key differences in their observational characteristics, fundamental properties and circumstellar environments.

1.2.1 Herbig Ae/Be stars - intermediate mass young stellar objects

1.2.1.1 Definition

Herbig Ae/Be stars are pre-main-sequence stars of intermediate mass ($\sim$2-8 $M_{\odot}$) and are defined as stars of A or B type with lines such as Hα in emission which are located in an obscured region and are associated with nebulosity (Herbig 1960). The stars are higher mass analogs to the well studied T Tauri stars, and as such, are optically visible objects in the process of contracting towards the zero-age-main-sequence (see Figure 1.9). Since the relatively anecdotal definition of Herbig (1960), other, more innate, properties of Herbig Ae/Be (HAe/Be) stars have been discovered. For example, Strom et al. (1972) noted that as a whole, the sample of Herbig Ae/Be (HAe/Be) stars exhibit infrared (IR) excess, photometric and spectral variability and high linear polarisation, in addition to commonly being associated with star forming regions. However, seemingly isolated HAe/Be stars have also been detected, primarily through IR surveys such as *IRAS* (e.g. Oudmaijer et al. 1992). To incorporate these slightly more evolved objects, Malfait et al. (1998) suggest the presence of a broad IR excess should be used as the defining criterion of these stars.

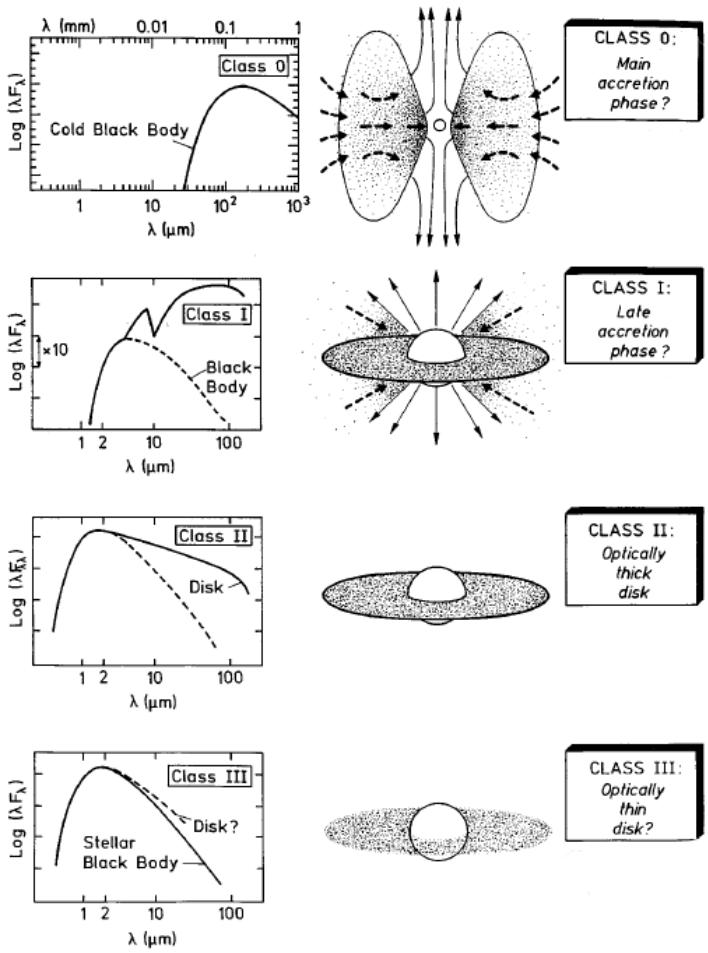

Figure 1.8: *A schematic representation of the evolution of the circumstellar environment and consequently the SED of YSOs, taken from Bachiller (1996).*

Herbig Ae/Be stars are in many ways directly analogous to T Tauri stars (demonstrated by the similarity in spectra, variability, disk properties and outflow characteristics). However, HAe/Be stars are not directly equivalent to a 'scaled up T Tauri star'. Herbig Ae/Be stars experience a shorter PMS lifetime than T Tauri stars as the contraction timescale is a strong function of mass (see Figure 1.7). Furthermore, Herbig Ae/Be stars are thought to have fully radiative exteriors and convective cores (as apposed to the opposite scenario in the case of T Tauri stars, Iben 1965). Due to the lack of surface convection cells, it is not expected that HAe/Be stars will posses magnetic fields. Therefore, the magnetospheric accretion scenario, which successfully explains many properties of

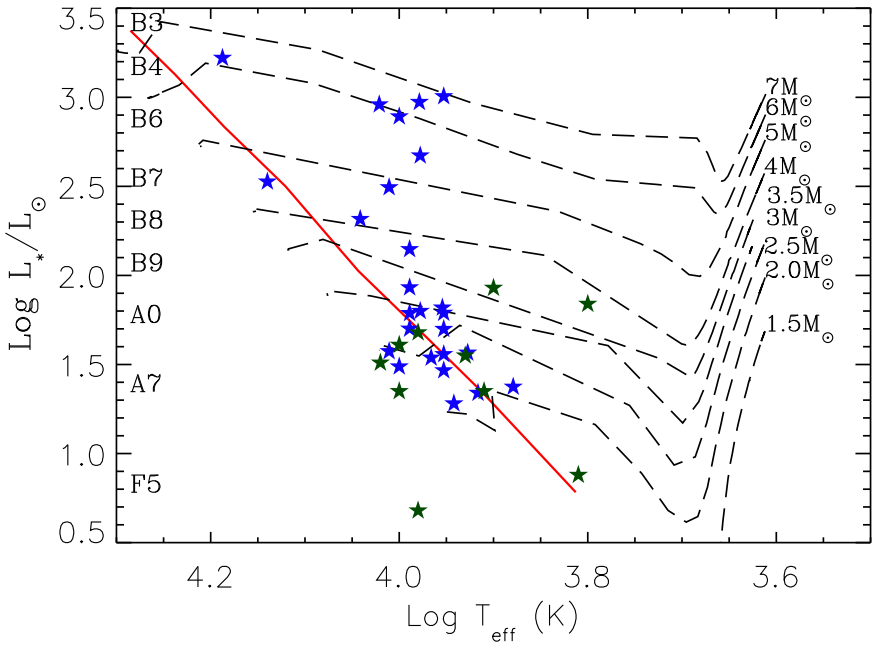

Figure 1.9: *The HR diagram populated with HAe/Be stars. The solid line marks the ZAMS, while dashed lines mark PMS tracks for various masses. The stars mark the positions of HAe/Be stars taken from van den Ancker et al. (1998, green) and Montesinos et al. (2009, blue). The PMS tracks and the position of the ZAMS are taken from Siess et al. (2000).*

T Tauri stars, may not be applicable to HAe/Be stars. While several Herbig stars have now been found to posses magnetic fields, these are thought to be fossil fields (Wade et al. 2007; Alecian et al. 2008, 2009). Even if Herbig Ae stars may be more similar to the T Tauri stars than previously expected (see e.g. the spectro-polarimetric results of Mottram et al. 2007b), it is thought Herbig Be stars form via direct disk accretion as early type stars generally do not posses magnetic fields (e.g. Silvester et al. 2009).

1.2.1.2 Spectroscopic characteristics

Herbig Ae/Be stars are emission line stars, by definition exhibiting emission lines of HI, the strongest of which is the Hα line. Typically, most HAe/Be stars exhibit a double peaked Hα profile (50 per cent), although many also possess a single peaked profile (25

per cent) or a P-Cygni type profile (20 per cent) (Finkenzeller & Mundt 1984). Several of the Hα line profiles are variable on timescales ranging from days to months (Tjin A Djie et al. 1989; Natta et al. 2000; Balona et al. 2002, which is attributed to pulsations and obscuration by orbiting dust clouds respectively). Other HI lines seen in emission towards HAe/Be stars include Brγ and other Br lines, Lyα, and lines from the Pfund and Humphreys series (e.g. Garcia Lopez et al. 2006; Grady et al. 2004; Benedettini et al. 1998; Hamann & Persson 1992, Chapter 4)

The origin of these lines remains uncertain. The observed emission may emanate from a range of environments. The proposed possibilities include: magnetospheric accretion columns and shocks, X-winds, disk-winds, stellar winds, star-accretion disk boundary layers and accretion disks (Muzerolle et al. 2004; Rousselet-Perraut et al. 2010; Catala & Kunasz 1987; Hamann & Persson 1992; Vink et al. 2005a). In a spectro-interferometric mini-survey of Herbig Ae/Be stars, Kraus et al. (2008a) report evidence of a minimum of two distinct Brγ line formation mechanisms. Stars with a P-Cygni Hα line profile were reported to show small Brγ emitting regions, while stars with a double-peaked or single-peaked Hα line profile show a more extended Brγ- emitting region, perhaps tracing a stellar wind or a disk wind. Kraus et al. (2008a) find the spatial distribution of the Brγ emission of most of their targets (4/5) to be larger than that predicted by the scenario of magnetospheric accretion, and thus favour the wind scenario in general. Conversely, Eisner et al. (2010), who also conducted spectro-interferometric observations over the Bγ line, favour magnetospheric accretion shocks in the case of HAe type objects and an extended disk in the case of the HBe objects (although it should be noted that this is based on a small sample). Finally, the models of Muzerolle et al. (2004) and the spectro-polarimetric observations of Vink et al. (2002) and Vink et al. (2005a) also support the magnetospheric accretion scenario, at least in the case of the Ae stars.

Evidence of ongoing accretion is provided by red shifted absorption lines of OI, CI and MgI in the UV, far UV and optical (Grady et al. 1996). The detection of line profiles indicative of accretion of neutral atomic gas has led to the suggestion that some Herbig Ae/Be stars are accreting comets or asteroids, indicating planetesmal formation in their

disks is well underway (Grady et al. 1997). By way of contrast, blue shifted absorption or P-Cygni profiles are often seen in HI recombination lines, indicating HAe/Be stars also drive outflows or winds. Spatially resolved observations of the winds are consistent with a magneto-centrifugally launched outflow – although the data cannot be used to distinguish between the disk-wind and X-wind scenarios (Malbet et al. 2007; Rousselet-Perraut et al. 2010).

1.2.1.3 Infrared excess

One of the defining characteristics of HAe/Be stars is a broad-band IR excess (see e.g. Thé et al. 1994; Malfait et al. 1998). As shown in Figure 1.8, an excess of emission in the IR is indicative of a circumstellar disk. Hillenbrand et al. (1992) fit the SEDs of a sample of 47 objects and discovered the sample was well described by three classes: I, II & III. Group I objects were best described by a stellar photosphere with an additional contribution from an optically thick accretion disk. Group II objects exhibited a composite SED, best fit by a photosphere, disk and dusty envelope[(a)]. Finally, Group III objects display little NIR excess and as such were postulated to represent the intermediate mass analogy of disk-less T Tauri stars. These classes appear similar to the various evolutionary stages outlined for solar mass objects (see Figure 1.8), and thus Hillenbrand et al. (1992) conclude that HAe/Be stars form in a similar fashion to solar mass stars and that many are surrounded by optically thick, accretion disks. This was disputed by various authors (e.g. Hartmann et al. 1993) on the basis of high accretion rates and unphysical assumptions regarding central holes in the disks. Instead, Hartmann et al. (1993) and Miroshnichenko et al. (1997) suggest that the IR excess of HAe/Be stars arises in dusty envelopes and is due to small grains being heated by UV photons from the central star. Furthermore, di Francesco et al. (1994) report that several of the objects classified as belonging to class I by Hillenbrand et al. (1992, i.e. their SED could be modelled using only a stellar photosphere and an accretion disk) were resolved at 100 μm, in direct contradiction of the model of Hillenbrand et al. (1992).

Recent work with spectrally resolved interferometry has confirmed that some HAe/Be stars are surrounded by active accretion disks (Kraus et al. 2008b; Isella et al. 2008).

[(a)] note that in this classification Group II objects are younger than Group I objects

In addition, the pioneering spectro-polarimetry of Vink et al. (2002, 2005a); Mottram et al. (2007b) also indicates that Herbig Ae/Be stars are often surrounded by flattened structures a few stellar radii from the central star, i.e. a disk. In turn, this is consistent with observations of disks in thermal dust emission and CO rotational lines (e.g. Mannings & Sargent 1997; Alonso-Albi et al. 2009). As, a result, it is now widely accepted that HAe/Be stars possess circumstellar disks.

1.2.1.4 Disks and outflows

The first direct probes of the inner disks around HAe/Be stars were provided with long baseline, optical (NIR) interferometry (e.g. with the Infrared Optical Telescope Array, the Palomar Testbed Interferometer and the Keck interferometer). Initial results were not entirely consistent with the accretion disk scenario, instead favouring a spherically symmetric distribution of emission a few AU from the central star (Millan-Gabet et al. 2001). This may be because the observations were detecting the puffed up, inner rim of the disks predicted by Natta et al. (2001), and the curved surface mimicked a spherically symmetric structure (Monnier et al. 2006). In contrast, Eisner et al. (2003, 2004) find that the close circumstellar environment of HAe/Be stars (<5 mas) is well described by models of accretion disks. They find a dichotomy in disk properties, in that flat accretion disks are consistent with the data for the objects with the earliest type, while the observations of later objects are better fit with models incorporating puffed-up rims, perhaps indicating the inner disk of the early type objects are optically thick. This dependence of disk properties on stellar luminosity was confirmed by Monnier (2005), who demonstrate that NIR sizes of most HAe/Be stars (0.2–4 AU) are consistent with a simple disk model which features a central optically thin region surrounded by hot dust emitting at the expected sublimation radii. While they find a close correlation between disk size and object luminosity ($R \propto L^{\frac{1}{2}}$) for Ae and late Be systems, the sizes of the inner cavities of the objects with the earliest spectral types (B0-B3 stars) are undersized compared to predictions of the optically thin inner cavity model. This is thought to be due to optically thick gas within the inner regions of the disk (Vinković & Jurkić 2007). A distinct difference between Ae and Be disks is also apparent at longer wavelengths. The masses of disks around Herbig Ae stars are comparable to that of disks around T

Tauri stars, indicating a similar evolutionary state. However, the disks around Herbig Be stars are generally smaller ($\lesssim$100 c.f. $\gtrsim$100 AU) and less massive ($\sim$0.01 c.f. $\sim$0.05 $M_\odot$), indicating that the early Be stars are photo-ionising their disks and dispersing them from the outside-in (Alonso-Albi et al. 2009, and references therein).

The most recent insights into circumstellar disks around HAe/Be stars have been provided by spectro-interferometry, and in particular by the VLTI instruments: MIDI and AMBER. As an example, Kraus et al. (2008b) present VLTI observations of the Herbig Be star MWC 147 which resolve its IR emission at 2.2 μm and 11 μm and find characteristic sizes of $\sim$ 1 and 9 AU respectively. Simultaneously fitting the SED and observed visibilities with 2D, frequency dependent radiation transfer models, the authors demonstrate that the only scenario that fits both the observed flux and spatial distribution is an active accretion disk with an optically thick inner region, interior to the dust sublimation radius. This constituted the first direct detection of an active accretion disk around an early type star and demonstrated that Herbig Be stars form via disk accretion for the first time. In further work, Kraus et al. (2009) demonstrate the puffed up inner rim of HAe/Be stars predicted by Natta et al. (2001) is most probably curved, confirming earlier conclusions drawn from previous NIR interferometry. In a similar study, Benisty et al. (2010) fit AMBER and MIDI observations of HD 100546 with a 3D Monte-Carlo radiative transfer model to constrain the inner disk geometry. To simultaneously reproduce the observed SED and visibilities, the authors suggest the close circumstellar environment of HD 100546 consists of a tenuous inner disk followed by a gap, which in turn, is surrounded by an optically thick outer disk. The observed $K-$band flux originates from very close to the central star ($\sim$0.3 AU), suggesting that the dust grains emitting the radiation are relatively large (of the order 1 μm). The gap in the disk separating the tenuous inner region from the optically thick outer regions may be the signature of a recently formed giant planet. If this is the case, transitional disks around HAe/Be stars may provide key opportunities to test planet formation mechanisms.

The presence of disks around HAe/Be stars implies that some may still be accreting material. Indeed, some HAe/Be stars exhibit an excess of UV flux over the expected

photospheric level (e.g. Grady et al. 2004). As accretion and ejection are intimately linked, it might be expected that Herbig Ae/Be stars also drive outflows, and indeed several have been found to drive optical outflows (e.g. Corcoran & Ray 1998; Devine et al. 2000; McGroarty et al. 2004; Grady et al. 2004; Sitko et al. 2008). Here, the properties of HAe/Be outflows are briefly discussed and compared to those of T Tauri stars to search for evidence of changes in the process of star formation with mass.

Many Herbig Ae/Be stars are associated with Herbig-Haro (HH) objects (see Mundt & Ray 1994, and references therein). Some HH objects associated with HAe/Be stars objects display an arched or uncollimated morphology, unlike the narrow outflows driven by solar mass T Tauri stars (Poetzel et al. 1992; Corcoran & Ray 1995). However, in several cases the HH outflows driven by HAe/Be stars possess morphologies and dynamical timescales that are similar to those of HH flows from lower mass T Tauri stars (McGroarty et al. 2004). In general, the collimation of the HAe/Be outflows is similar to that of outflows emanating from lower mass stars, suggesting a similar launching mechanism. This is contrary to the expectation that intermediate mass stars will not posses the dynamo generated magnetic field characteristic of solar mass stars. However, if Herbig Ae stars do gain mass via magnetospheric accretion as suggested by Vink et al. (2002) and Muzerolle et al. (2004), it might be expected that they exhibit similar outflow characteristics to T Tauri stars which are known to undergo magnetospheric accretion.

HH outflows are often accompanied by collimated optical jets (e.g. Ray et al. 1990; Corcoran & Ray 1998; Devine et al. 2000), which provide a key probe of the accretion history of the driving source. Such jets extend for ~ 0.1 pc (e.g. Ray et al. 1990) and are typically well collimated (an opening angle $< 10^{\circ}$ Perrin & Graham 2007), resulting in a morphology very similar to that exhibited by jets from T Tauri stars. Jet velocities typically range from $50 - 150$ km s^{-1}, slightly greater than the average T Tauri star jet velocity, although this might be expected as the escape speed from a more massive star will be higher. The observed jets are comprised of distinct knots of emission, indicating sporadic ejection from the central star (Ray et al. 1990; Devine et al. 2000). Detailed studies of jets emanating from HAe/Be stars indicate that their properties (electron density, hydrogen ionisation, electron temperature and mass loss rate) are similar to

those of jets associated with solar mass T Tauri stars (Perrin & Graham 2007; Melnikov et al. 2008). This also indicates a similar launching mechanism.

The similarity exhibited between the jets emanating from the solar mass T Tauri stars and intermediate mass HAe/Be stars indicates the launching mechanism is relatively insensitive to stellar mass. This is at odds with the magneto-centrifugal wind launching models applied to T Tauri stars and the lack of a dynamo generated magnetic field in HAe/Be stars. However, several HAe/Be stars have been shown to posses magnetic fields (Wade et al. 2007), and thus it may be possible for HAe/Be stars to drive magneto-centrifugally launched outflows, although the detected fields are thought to be fossil fields and not to be dynamo generated. Nonetheless, several independent observations of HAe/Be stars indicate the presence of a strong, ordered field (Muzerolle et al. 2004; Deleuil et al. 2005). Hubrig et al. (2009) suggest HAe/Be stars generate a magnetic field via a dynamo effect that decays with age, although this scenario is belied by the lack of a correlation between HAe/Be magnetic field and rotation. More measurements of magnetic fields are required to conclusively test such a scenario as currently there are only a handful of detections (for example, Hubrig et al. (2009) used a sample of only 9 objects).

To summarise, the disk and outflow properties of HAe/Be stars indicate that the process of star formation does not change significantly over the mass range 1–10 $M_{\odot}$. The detection of collimated optical outflows driven by HAe/Be stars suggests that such stars posses ordered magnetic fields, a conclusion initially at odds with their radiative exteriors. However, recent spectro-polarimetric observations have confirmed that several HAe/Be stars do possess strong magnetic fields, although whether these are due to fossil fields or a decaying dynamo effect is still relatively unknown. More observations are required to probe the spatial distribution of such outflows on small scales to attempt to constrain their launching mechanism.

1.2.2 Massive Young Stellar Objects

1.2.2.1 Definition

Massive young stellar objects represent an important phase of massive star formation, one that is more advanced than the hot core phase (as MYSOs are FIR bright, and thus have a higher temperature than hot cores) and prior to the development of a UCHII region (as MYSOs are radio quiet, Urquhart et al. 2008b). Such objects, which are destined to be main-sequence OB stars, are thought to be still accreting material, although they are likely to have already attained a high luminosity. Despite the resultant high surface temperature, MYSOs are not associated with HII regions.

MYSOs represent an advanced stage of star formation, but have yet to attain their final mass and emerge from their natal cocoon as a main-sequence star. MYSOs are distinctly different from solar mass and intermediate mass PMS stars. To begin with, MYSOs are likely to have already attained the luminosity of a MS OB star, due to their short KH contraction time (see Figure 1.7). Therefore, MYSOs are different to PMS stars in this respect, as they have essentially already contracted to the MS. Furthermore, as a result of their rapid formation, MYSOs are still heavily embedded in their natal material. Therefore, the visual extinction to them is very high (of the order 30-50, Porter et al. 1998, c.f. ~ 1 for HAe/Be stars). Consequently, the optical light emitted by MYSOs is completely attenuated by their dusty environment and the stellar photosphere is rendered un-observable. The majority of the energy radiated by MYSOs is reprocessed by their dusty surroundings and re-emitted in the FIR. This makes studying MYSOs much more challenging than studying the optically visible T Tauri and HAe/Be stars.

MYSOs are thought to be undergoing active accretion, gaining mass at a rate greater than 10^{-4} $M_{\odot}yr^{-1}$ (e.g. Zapata et al. 2008). Such a rapid accretion rate has a significant effect on the structure of the forming object. The accreted material deposits entropy in the central star, which in the initial stages of massive star formation is retained in the cool, opaque object. As the temperature of the star rises, the opacity drops and the entropy moves outward, causing the star to expand to a radius of $\gtrsim 100$ $R_{\odot}$ (Hosokawa et al. 2010). Therefore, high accretion rates result in lower temperatures and postpone the onset of nuclear fusion. Consequently, a massive protostar joins the ZAMS and

acquires the temperature to burn hydrogen at a mass of approximately 40 $M_{\odot}$ – a greater mass than expected based purely on an assessment of the KH time-scale (Hosokawa & Omukai 2009). Nonetheless, accretion does not necessarily halt once a massive protostar reaches the ZAMS, and a period of MS accretion is possible (Hosokawa & Omukai 2009; Krumholz et al. 2009).

The initially swollen radii of MYSOs may explain why they have yet to ionise their surroundings; as substantially increased radii result in low surface temperatures and consequently low UV luminosities. As a result, the stars will be unable to ionise their surroundings. However, highly luminous MYSOs are most likely to be in their KH contraction or MS accretion phases (Hosokawa & Omukai 2009). Therefore, other mechanisms may be required to explain the lack of HII regions around MYSOs. Once a HII region begins to form, following the contraction of the central star, it may be quenched if the infall rate is high enough (Walmsley 1995, although this requires the unlikely scenario of spherical infall and high emission measures). Alternatively, a young HII region may be gravitationally confined, if it is small enough to be dominated by the gravitational attraction of the central star (Keto 2003).

1.2.2.2 Observational characteristics

MYSOs are generally characterised as being bright in the FIR (∼several 100s of Jy), invisible in the optical, faint in the NIR (∼15–20 mags) and radio quiet (the only difference between MYSOs and UCHII regions).

Mid Infrared and Far Infrared

In the MIR, MYSOs are generally point sources (Mottram et al. 2007a), although their environments may be resolved on scales of approximately 1000 AU at 24.5 μm (de Wit et al. 2009). de Wit et al. (2009) find that the density distribution of MYSO envelopes at ∼1000 AU is slightly shallower than that probed at larger distances in the sub-mm. This may indicate that the envelopes of MYSOs are rotationally supported, in which case they will be flattened. On smaller scales, approximately 100 AU (probed at 10 μm with MIDI), the dust emission of MYSOs appears to be dominated by warm dust in large envelopes (Linz et al. 2009) and outflow cavity walls (de Wit et al. 2010). Therefore, if MYSOs are surrounded by small-scale optically thick disks they remain

enshrouded in the envelope and have yet to be directly detected in the MIR.

Near Infrared

As a consequence of the high extinction towards them, MYSOs are very red, even in the NIR. For example, MYSOs typically have a $J - K$ colour greater than 4 (the RMS database, see also Bik et al. 2006). MYSOs generally exhibit a relatively rich atomic emission line spectrum in the NIR. In particular, MYSOs have been observed with lines of HI (primarily the Bracket and Pfund series), HeI, FeII and MgII in emission (Bik et al. 2006). In addition, some 27 per cent of MYSOs exhibit CO overtone bandhead emission and a significant fraction ($\sim$50 per cent) exhibit H_2 emission (Clarke 2008). MYSOs do not display any photospheric lines in the NIR spectra (Clarke 2008; Bik et al. 2006), making it difficult to establish their mass. However, their high luminosity ($10^4 - 10^5$ $L_\odot$) indicates that they are young OB stars, which is confirmed in individual cases (for example by the kinematics of the circumstellar environment, see Davies et al. 2010).

The most prominent feature in the NIR spectra of MYSOs is typically Brγ emission. The width of this emission line is generally quite large, of the order a few times 100 $\mathrm{km\,s^{-1}}$, which indicates this line traces gas close to the central star (Bik et al. 2006). The relative strengths of various HI emission lines are generally consistent with the lines originating in an optically thick, stellar wind, although several objects show an additional component to the line flux which may originate in a disk wind (Bunn et al. 1995). The inferred mass loss rates in the stellar winds are of the order of 10^{-6} $M_\odot yr^{-1}$ (Drew et al. 1993), much higher than the corresponding mass loss rates of lower mass PMS objects (which are of the order of 10^{-9} $M_\odot yr^{-1}$; Malbet et al. 2007).

The observed HeI emission of MYSOs is consistent with them being hot, early type stars enshrouded in their natal material as such emission can only be excited via a strong UV field, i.e. that of a hot star (e.g. Hanson et al. 2002). MYSOs which exhibit such emission are generally associated with ultra-compact HII regions (Bik et al. 2006), which are also indicative of stars with high effective temperatures. The FeII emission of MYSOs likely traces a range of environments from shocks (see e.g. Reipurth et al. 1996) to disk surfaces (see e.g. Hamann et al. 1994; Porter et al. 1998). Similarly, the observed

H_2 emission could be excited by shocks or by UV fluorescence in the stellar radiation field (Shull & Beckwith 1982). Finally, the CO emission is suggestive of small-scale circumstellar disks (Carr 1989; Chandler et al. 1995, although winds and shocks have also been proposed as the origin of this emission). This will be discussed in more detail in Section 1.2.2.3

To summarise, MYSOs present a multitude of general properties that suggest they are young, early type stars, still embedded in their natal material. Now the specific properties of disks and outflows associated with MYSOs will be presented to highlight open questions regarding massive star formation.

1.2.2.3 Disks and outflows

The wide HI recombination emission lines exhibited by MYSOs suggest the presence of winds carrying a significant amount of mass (Drew et al. 1993; Bunn et al. 1995). The relative strengths of various Br and Pf lines for several objects are consistent with an expanding stellar wind. However, the line ratios of a few objects indicate an additional, low velocity component (Drew et al. 1993; Bunn et al. 1995). To explain the high mass loss rates and single peaked line profiles, Drew et al. (1998) proposed that such low velocity winds are driven off the surface of a circumstellar disk by the stellar radiation field. As the material is not lifted off the surface of the star, the outflow can be driven at speeds below the escape velocity of the star, allowing outflow at $\sim 100\,\mathrm{km\,s^{-1}}$. This scenario has seemingly been confirmed by Hoare et al. (1994) and Hoare (2006) who report the detection of an elongated concentration of ionised material, perpendicular to observed outflows towards two MYSOs. Such observations are entirely consistent with an equatorial ionized stellar wind, which is provided by the disk wind model proposed by Drew et al. (1998). However, thus far, two-dimensional Monte Carlo simulations of HI line formation in disk winds fail to match observations, predicting double peaked line profiles while the most commonly observed line profile is singly peaked (Sim et al. 2005). This could be the result of the central star being swollen due to high accretion rates (Hosokawa & Omukai 2009), which would reduce the rotation speed in the circumstellar disk and thus lead to a narrower wind line profile. Further models and high resolution observations are required to test this scenario.

Several MYSOs have been observed to drive collimated, clumpy jets several pc in length in the radio continuum . As an example, Marti et al. (1993) present the discovery of a 5.3 pc long collimated jet that terminates in HH objects emanating from a luminous YSO. The morphology of this jet is remarkably similar to that of jets launched by lower mass YSOs, again indicating a similar ejection mechanism. Large proper motions of the condensations in the jet indicate tangential velocities of 600–1400 $\mathrm{km\,s^{-1}}$, significantly greater than the typical velocities of jets associated with low mass YSOs, substantiating that the driving source is indeed a MYSO (Marti et al. 1995). Evidence of MYSOs driving collimated outflows extends to luminosities of 6×10^4 $\mathrm{L_\odot}$, indicating that even the most massive stars pass through a similar evolutionary sequence as their lower mass counterparts (Garay et al. 2007). This is substantiated by the fact that radio jets from luminous young stars obey the relationship between radio luminosity and momentum rate derived for outflows associated with low mass sources (Rodríguez et al. 2008).

To reconcile the various observations of well collimated jets (e.g. Garay et al. 2003), jets with moderate opening angles (e.g. Rodríguez et al. 2005) and wide angled winds (e.g. Shepherd & Kurtz 1999), Beuther & Shepherd (2005) propose an evolutionary sequence in which the outflow characteristics of young massive stars change with time. In this picture, a massive proto-star drives a well collimated outflow while it has the mass of a mid B type star, before it is burning hydrogen in its core. As the star gains mass and becomes hotter, it begins to ionise its surroundings and drive a stellar wind, which can coexist with the outflow. Finally, when the object has attained its final mass and is on the MS, it effectively destroys the collimated outflow by photo-ionising the disk via virtue of copious Lyman continuum emission, leaving only the stellar wind (Beuther & Shepherd 2005). While this scenario is consistent with observations, it has yet to be confirmed via modelling of this evolutionary sequence.

In general, massive stars are not thought to be magnetic as they lack a convective surface and as a result cannot generate a magnetic field via the dynamo effect. Consequently, the magneto-centrifugal launching mechanisms thought to be responsible for the jets of low mass YSOs may not be applicable to MYSOs. However, the similarity in outflow characteristics suggests that the outflow launching mechanism does not depend

on mass. In the simulations of Banerjee & Pudritz (2007), massive young stellar objects drive outflows via the twisting of magnetic field threading their circumstellar disks, the magnetic tower effect (Lynden-Bell 2003). Such a field does not have to be stellar generated but could be a fossil field dragged in by the collapsing material. The field in the simulations ($\sim 1\,\mu$G) is very modest compared to the few observations of magnetic field strengths towards collapsing cores and massive proto-stars ($\sim 10\,$mG, Girart et al. 2009; Vlemmings et al. 2010). Therefore, it is highly likely that MYSO outflows are driven by disk related MHD effects, in a fashion not too dissimilar to solar mass YSOs.

The fact that many massive proto-stellar objects drive molecular outflows and ionised jets indicates that they form via a similar accretion process as their low mass counterparts, and thus indirectly suggests that these objects are surrounded by accretion disks. This is substantiated by other indirect indications of disks (such as NIR silhouettes and polarimetric maps, e.g. Chini et al. 2004; Jiang et al. 2008; Nielbock et al. 2008). In a few isolated cases, direct detections of discs and flattened structures around MYSOs have been made (Shepherd et al. 2001; Beltrán et al. 2005; Patel et al. 2005; Okamoto et al. 2009; Sandell & Wright 2010). However, such studies typically probe emission at long wavelengths, and thus large distances (of order hundreds to thousands of AU) from the central star. Indeed, the rotating structures detected by Beltrán et al. (2005) are too large to be considered circumstellar discs, as they are unstable and may fragment (see the discussion in Cesaroni et al. 2007). Up until very recently, spatially resolved, spectro-interferometric observations have thus far found little evidence of disks on intermediate spatial scales (of the order of 100 AU Linz et al. 2009; de Wit et al. 2010). Therefore, proof that massive stars form via disk accretion has been elusive.

Recently, observations with MIDI have uncovered evidence of a flattened structure (i.e. a disk) surrounding the Kleinmann-Wright object – which is proposed to be the precursor of a Herbig Be star (Follert et al. 2010). However, these MIR observations probe dust at several 100 K, and thus some distance from the central star (see Figure 1.10). To conclusively prove that massive stars form via disk accretion requires the detection of the inner gaseous disk (which is only several AU in size). In the first study of its kind, Kraus et al. (2010) used AMBER observations to reconstruct an image of the circum-

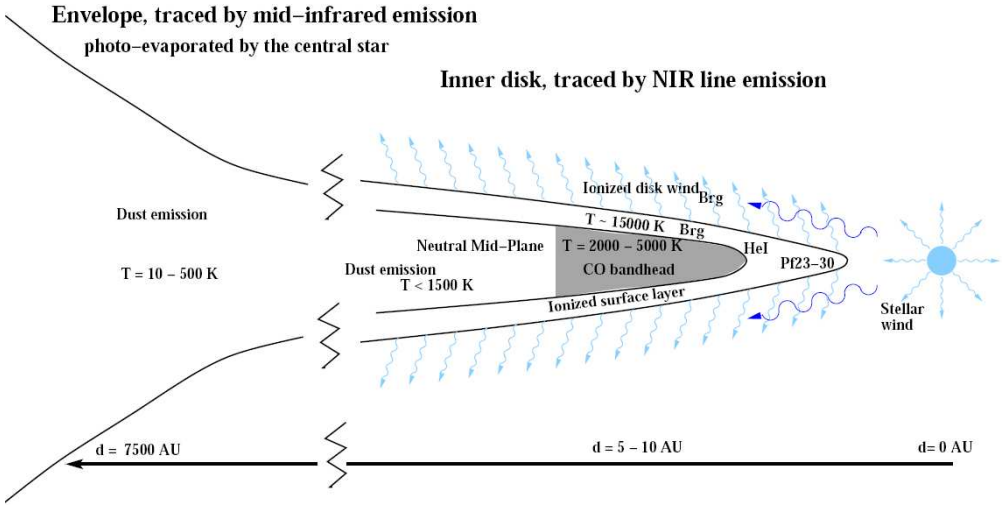

Figure 1.10: *A schematic representation of the circumstellar environment of an accreting MYSO, taken from Bik et al. (2008).*

stellar environment of the MYSO IRAS 13481−6124. The reconstructed image, which traces emission by hot dust, shows an elongated structure with a size of approximately 20 AU, consistent with a moderately inclined disk (see Figure 1.11). Consequently, the presence of disks around MYSOs is beginning to be established, but only in isolated cases. Furthermore, even with the resolution of the VLTI, these observations probe the dusty outer disk. To determine how MYSOs accrete mass and launch outflows requires probing the gaseous inner disk.

A powerful diagnostic of such, small-scale, discs around young stellar objects is provided by CO 1st overtone bandhead emission at 2.3 μm. Such emission requires high densities (n $\gtrsim 10^{10}$cm^{-3}) and high temperatures (T$\sim$ 2500K), indicative of disc material close to the stellar surface (e.g. Carr 1989). In addition, such emission associated with YSOs can be well fit with a model of the bandhead emission originating in a Keplerian disc, a few AU in size (e.g. Carr 1989; Chandler et al. 1995). In particular, Bik & Thi (2004) and Blum et al. (2004) found that the CO bandhead profiles of intermediate and massive YSOs could be fit with emission from discs with small, $\approx$ 0.1 AU, inner radii. However, it has also been suggested that such emission traces shocks, dense winds

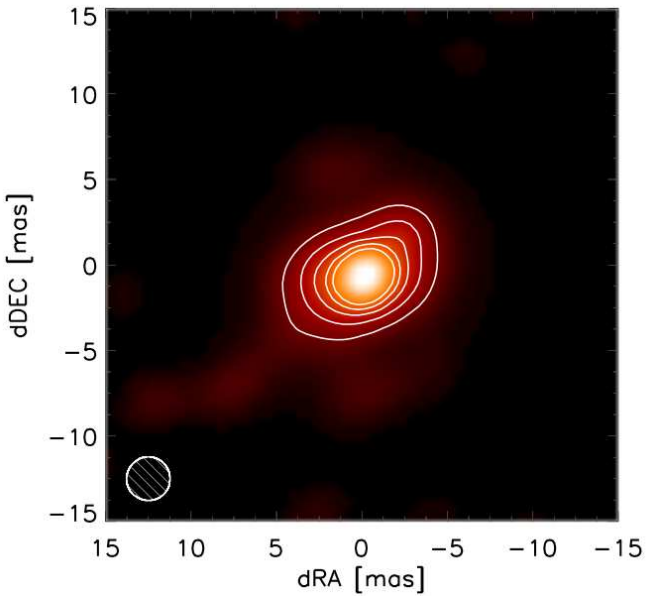

Figure 1.11: *The reconstructed image of the disk around IRAS 13481−6124, taken from Kraus et al. (2010). The resulting resolution is approximately 2.5 mas.*

and large, dense shells rather than small disks (Scoville et al. 1983; Chandler et al. 1995; Grave & Kumar 2007). Consequently, the properties of the inner gaseous disks of MYSOs, if such regions exist, have yet to be unambiguously determined.

1.3 Be stars

Be stars are non-supergiant stars which display HI Balmer lines in emission, or have done so at some point (Collins 1987). This observational definition includes many different classes of Be stars ranging from the PMS Herbig Be stars (Herbig 1960), to the components of interacting binary systems, such as the primaries of Algol type systems (Soderhjelm 1980). Classical Be stars, hereafter Be stars, are unique amongst these types of emission line stars in that they are MS stars and are not expected to display emission lines in their spectra. The Be phenomenon appears throughout the MS lifetimes of B type stars (Zorec et al. 2005; McSwain et al. 2008). Given that a substantial fraction of B type stars exhibit the Be phenomenon (∼17%, Zorec & Briot 1997), Be stars pose a significant challenge to the understanding of intermediate and massive stellar evolution.

The emission lines evident in the spectra of Be stars, notably Hα, often exhibit double peaked profiles, indicative of originating in a rotating medium. Therefore, it has long been thought that they originate in a circumstellar disk (Struve 1931). This was finally confirmed with long baseline optical interferometry (Quirrenbach et al. 1994). Struve (1931) postulated a formation mechanism for such disks, suggesting that Be stars may rotate rapidly enough to shed material at the equator, thus forming a 'nebulous ring' which is responsible for the emission lines. Indeed, Be stars as a group tend to rotate rapidly, with their $v \sin i$[(b)] distribution peaking at around 250 $\mathrm{km\,s^{-1}}$ (Slettebak 1982). However, it is difficult to prove that Be stars are rotating at a sufficient velocity to fling material into orbit without an independent determination of the inclination of their rotation axis. To achieve this, Porter (1996) and Rivinius et al. (2006) used the population of Be shell stars as a proxy for the intrinsic population of Be stars viewed edge on, and found that, on average, Be stars rotate at approximately 70%–80% of their critical velocity $\left(\sqrt{\frac{\mathrm{GM_{star}}}{\mathrm{R_{star}}}}\right)$. Although rapid, such rotation is insufficient to be solely responsible for the creation of a circumstellar disk – for which a rotational velocity within a few sound speeds of the critical velocity is required (Porter & Rivinius 2003).

However, the distribution of Be star rotational velocities presented by Porter (1996) and Rivinius et al. (2006) may not be sufficient to exclude the hypothesis that Be stars are rotating at close to their critical velocity. As a result, Be stars experience gravity darkening, i.e. they become stretched in the equatorial direction which results in a lower surface gravity and thus reduced brightness at the equator (von Zeipel 1924). Townsend et al. (2004) and Frémat et al. (2005) show that neglecting the effects of gravity darkening in $v \sin i$ determinations can result in underestimating the stellar rotation rate. Indeed, the direct determination of the rotational distortion of α Eri and α Arae via spectro-interferometry suggests that Be stars do rotate at close to their critical velocity (Domiciano de Souza et al. 2003; Meilland et al. 2007b). Furthermore, astro-seismology offers a $v \sin i$ independent measure of the rotational velocity of pulsating Be stars and this also suggests that Be stars rotate at close to their critical velocity (Cameron et al. 2008). However, extensive modelling of the Be star population indicates that the Be

[(b)] where i represents the inclination of the rotational axis

phenomenon cannot require critical rotation, and in fact becomes apparent at rotation rates of 70% of the critical velocity (Cranmer 2005; Ekström et al. 2008). Therefore, various mechanisms ranging from non-radial pulsations to wind confinement by magnetic fields have been invoked to explain the presence of circumstellar disks around Be stars (see e.g. Porter & Rivinius 2003). Determining which, if any, of the proposed scenarios is responsible for the creation of such disks is at the forefront of Be research.

Section 1.3.1 summarises what is known about the properties of Be star disks. Various models invoked to match these properties are then described in Section 1.3.1.

1.3.1 Disk properties and models

Disk properties

The sizes of the disks around Be stars can be determined from their IR excess. In general, the NIR excess of Be stars can be fit with a simple model of free-free emission in a disk with a radial density gradient of the form $\rho \propto R^{-\beta}$, with β approximately 2–5 and disk radii greater than 10 $R_\odot$ (Dougherty & Taylor 1992). This density gradient continues into the FIR (Cote & Waters 1987), but steepens in the mm regime, indicating a truncated disk, a change in disk geometry at $\sim 25 - 100\,R_\star$ or additional acceleration at the edge of the disk (Waters et al. 1991). At shorter wavelengths, the extent of Be star envelopes does not appear to depend strongly on wavelength between 8 and 12 μm (Meilland et al. 2009), and is typically less than 10 mas ($\sim$200 $R_\odot$) at these wavelengths.

The properties and kinematics of the disks can also be probed by the line emission emanating from them. For example, the typical sizes of the inferred disks can be estimated from the position of the emission line peaks. Taking the peak location as 100 $\mathrm{km\,s^{-1}}$ and assuming a B0 type star results in an upper limit to the optically thick disk of approximately 40 $R_\star$ (dependent on inclination). In a similar fashion, the equivalent width of the Hα emission can be used to estimate the radius of the disk (e.g. Dachs et al. 1986; Grundstrom & Gies 2006). Finally, if the line emission is resolved it can be used to directly measure the size of the disks. In an attempt to directly probe the spatial structure of such disks, Oudmaijer et al. (2008) employed spectroastrometry over the Paβ line and achieved an angular precision of $\sim$0.3 mas. However, no disks were detected and Oudmaijer et al. (2008) report upper limits of a few stellar radii.

Emission lines can also be used as probes of disk kinematics, which in turn provide an important constraint on their formation mechanism. As an example, Hummel & Vrancken (2000) probed the kinematics of the Hα emitting region of Be stars by fitting the emission line profiles with models of a circumstellar disk. They find that, in at least one case, Keplerian rotation is preferred, provided the line is optically thick. Be stars often exhibit cyclic variability in the ratio of the blue and red peaks of their emission line profiles (e.g. Hanuschik 1996). This can be used to probe the properties in different regions of the disk. Tracing the V/R (the ratio of the blue and red shifted line emission) variations with spectrally dispersed optical interferometry, it has been shown a concentration of emission moves around the central star, exactly as predicted by the scenario of a prograde spiral arm (Vakili et al. 1998; Berio et al. 1999). This is also indirect evidence that the disks rotate in a Keplerian fashion (Okazaki 1991). However, there are few direct confirmations of Keplerian rotation.

Recent insights into the structure and properties of Be stars disks have been delivered by spectrally dispersed, NIR interferometry. In particular, fitting the spatial and kinematic information with radiation transfer models allows the disk kinematics to be unambiguously determined. The first star to be studied this way was α Arae, with the result that the disk appears to be rotating in a Keplerian fashion (Meilland et al. 2007b). In a similar study, it was shown that the disk around κ Dra was not consistent with Keplerian rotation, instead exhibiting a shallower rotation law. Finally, Carciofi et al. (2009) used the sub-mas spatial information offered by this technique to convincingly demonstrate that the V/R variation of ζ Tau is due to a one-armed spiral in the star's circumstellar disk.

The scenarios proposed to explain the creation of the circumstellar disks around Be stars must simultaneously recreate the properties mentioned above. Several models of disk formation have been proposed and will be discussed in the following.

Disk models

To form the disks around Be stars some mechanism must transport material and angular momentum from the central star into the circumstellar environment. Initially, it was thought that this might be achieved via rapid rotation; if a star rotates so rapidly

that its outer layers are rotating at super-Keplerian speeds, material will lift off into orbit, thus forming an equatorial disk. Since it now appears that Be stars do not rotate at their critical velocity several additional mechanisms have been proposed (Cranmer 2005; Rivinius et al. 2006). However, it should be noted that *some* Be stars do appear to rotate at their critical velocity (Domiciano de Souza et al. 2003; Carciofi & Bjorkman 2006)

Essentially, three families of models have been proposed to explain the properties of Be stars: wind compressed disks, magnetic wind compressed disks and viscous disks (see Figure 1.12). The following presents a brief overview of the various models and highlights open questions relating to the disk formation mechanism(s).

Based on two common properties of Be stars, namely rapid rotation and radiatively driven winds, Bjorkman & Cassinelli (1993) proposed that Be star disks may be modelled with a wind compressed disk. In this picture, rapid rotation distorts radial wind streamlines and focuses them towards the equator. If two streamlines from opposite hemispheres intercept in the equatorial region, a shock is produced. The dense post-shock gas is confined to the equatorial region by ram pressure of the winds from both hemispheres, resulting in the formation of a circumstellar disk. However, the model of Bjorkman & Cassinelli (1993) assumes that the line driving force is purely radial. Owocki et al. (1996) demonstrate that non-radial forces, due to asymmetries in the line resonances in the wind and rotational distortion of the stellar surface, effectively inhibit the formation of a wind compressed disk.

The inclusion of a magnetic field reinstates the wind compressed disk model as a physically viable possibility. Cassinelli et al. (2002) propose a magnetically torqued disk model in which a stellar, dipole magnetic field channels material from the wind in both hemispheres into the equatorial region. Colliding flows result in shocks and a density enhancement in the equatorial plane, which forms a circumstellar disk. An obvious criticism of this model is that early type stars do not posses convective cells, and thus are thought to be incapable of generating a magnetic field via the dynamo effect. However, several early type stars have been found to posses strong ordered fields of the order of 1000 G (Donati et al. 2002; Neiner et al. 2003; Donati et al. 2006a,b;

Petit et al. 2008; Grunhut et al. 2009). Nonetheless, such fields are not commonplace (with upper limits of ∼100 G, Schnerr et al. 2008), calling into question whether this scenario can explain the presence of disks around all Be stars.

Furthermore, the physical basis of this model has been questioned. In 2D MHD simulations of a rotating star with a dipole magnetic field aligned along the rotation axis, Ud-Doula et al. (2006) investigate whether this scenario can result in a steady state disk. They find that no stable configuration is reached. While material is channeled into the equatorial region, material in the inner disk falls back onto the central star and the remaining disk is subject to episodic breakouts due to field reconnection events. In further work, Ud-Doula et al. (2008) demonstrate that the only way to generate a circumstellar disk in this scenario is to increase the magnetic confinement, confining the material against the centrifugal force due to rotation and forcing the accumulated material in the equatorial region to rotate as a solid body. However, Brown et al. (2004) question the results of Ud-Doula & Owocki (2002) and Owocki & Ud-Doula (2003), claiming their MHD code is poorly suited to dealing with large magnetic fields (several 100s of Gauss). Therefore, there is considerable uncertainty over whether this model is applicable to Be stars.

The final disk model, the viscous disk model, differs from the previous two in that it does not explain the creation of the disk. Instead, it simply describes a type of disk that is consistent with observations. Viscous disks are essentially accretion disks in reverse; material and angular momentum are injected into the inner regions of the disk (by an unspecified mechanism) and are gradually diffused outward via turbulent viscosity (Lee et al. 1991; Porter 1999; Okazaki 2001). Such disks recreate many of the observed properties of Be star disks. For example, their density distribution and V/R variability (Jones et al. 2008; Carciofi et al. 2009) are both well fit with viscous disk models. However, this model still requires a mechanism to provide the necessary material and angular momentum to create the disk. Brown et al. (2008) argue that the magnetically torqued wind compressed disk model could result in a slowly outflowing disk in Keplerian rotation, a key feature of the viscous disk model, provided some source of viscosity is present in the distributed material. Alternatively, Cranmer (2009) suggests that non-

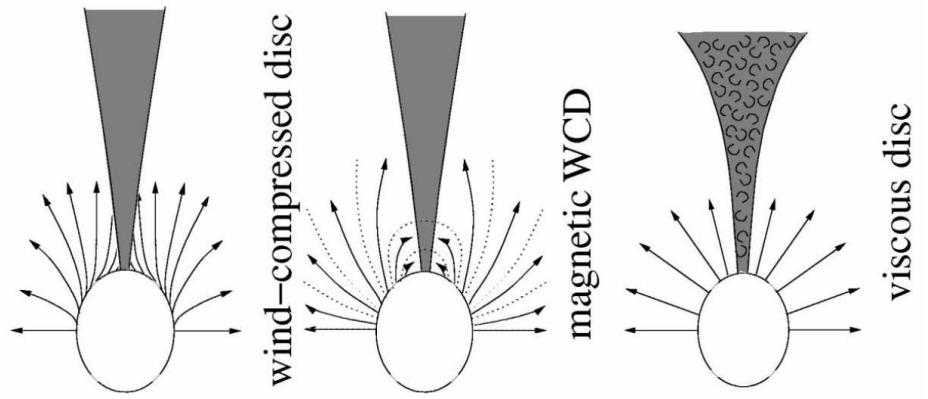

Figure 1.12: *The wind streamlines and disks of the three Be disk models: wind compressed disks, magnetic wind compressed disks and viscous disks, taken from Porter & Rivinius (2003).*

radial stellar pulsations inject enough angular momentum into the upper atmosphere to spin up a Keplerian disk.

To summarise, the formation mechanism of Be star disks is essentially unknown. While the viscous disk model is consistent with many of the properties of such disks, it does not provide any insight into the creation of the disk as the model simply describes a type of disk and not how the material of the disk is assembled. Non-radial pulsations and magnetic fields offer ways to inject material and angular momentum into the equatorial region of Be stars but currently observations cannot differentiate between the two possibilities. More stringent constraints on the properties and kinematics of Be star disks are required, as the current sample of disks with direct measurements of both their size and kinematics is only 4 objects.

1.4 Spectroastrometry

Spectroastrometry is a relatively simple technique which delivers spatial information on scales well below the Rayleigh resolution limit of a telescope. Indeed, the technique can achieve an angular precious of less than a mas and thus can probe scales inaccessible with other techniques (apart from optical interferometry). As a result, spectroastrometry is

becoming one of the foremost techniques used to study unresolved structures such as binary systems, circumstellar disks and outflows from young stars. Consequently, the work in this thesis makes extensive use of this technique. This section briefly describes the basic principle of spectroastrometry and how it is applied.

Spectroastrometry involves measuring the centroidal position of a conventional long-slit spectrum as a function of wavelength. Asymmetries in the source of the emission at a particular wavelength, such as a binary system with one component dominating the flux over an emission line, are revealed by the centroid moving away from its continuum position.

The technique of probing an unresolved, asymmetric flux distribution by measuring the centroid as a function of wavelength has been used in astronomy for some time. Indeed, the general concept pre-dates the term spectroastrometry. For example, the technique of differential speckle interferometry (which involves determining the photo-centre of several narrow band speckle images and searching for changes with wavelength) was used by Petrov & Lagarde (1992) to probe an unresolved binary system. In a fashion more similar to spectroastrometry, Hirth et al. (1994) used continuum subtracted long-slit spectra to study outflows from T Tauri stars. These authors produced position-velocity diagrams of emission lines and then used Gaussian fitting to achieve a positional accuracy of $\sim$0.1 arcsec. This is essentially spectroastrometry. However, the technique was not widely acknowledged until Bailey (1998b) demonstrated that it can be used to detect binary systems with separations of only 100 mas. In particular, Bailey (1998b) demonstrated that the technique delivers information on small angular scales using only a standard spectrograph and CCD detector. The technique described by Bailey (1998b) differs from previous incarnations of the same principle in that it does not require any prior processing such as continuum subtraction and can be conducted by directly fitting standard long-slit spectra with one dimensional Gaussian profiles in the spatial direction. This is shown schematically in Figure 1.13.

To provide an example of a spectroastrometric signature, an unresolved binary system is considered. Over an arbitrary wavelength range, one of the components is a

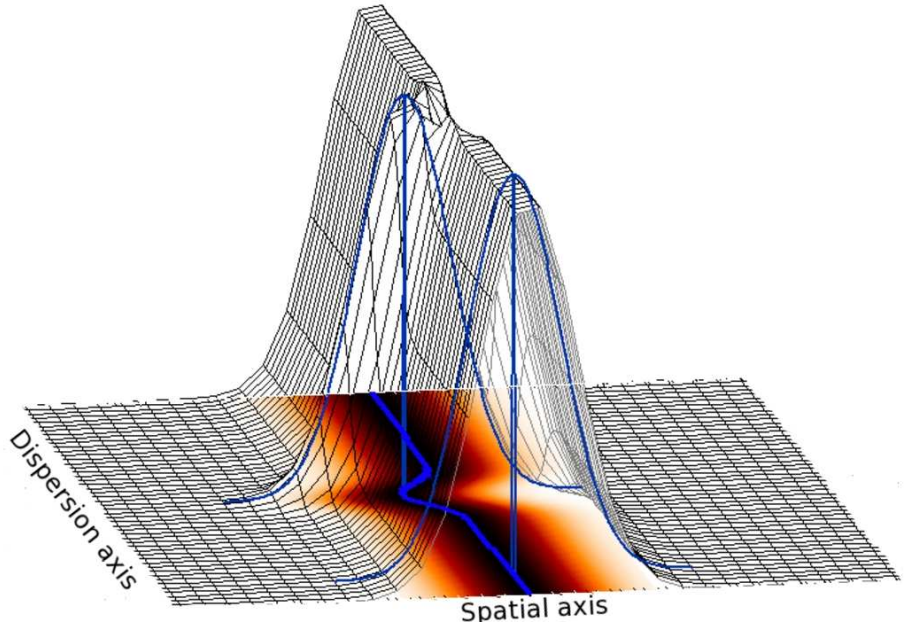

Figure 1.13: *A schematic representation of conducting spectroastrometry by fitting the spatial profile of a spectrum (the grid surface) with a Gaussian function (blue lines). An exaggerated centroid shift has been added to visualise a spectroastrometric signature; i.e. a change in centroid with wavelength.*

continuum source while the other exhibits an additional emission line. To conduct spectroastrometric observations, a long-slit spectrum of the system is obtained. Note that it is supposed that the slit is parallel to the orientation of the two components so that the spatial axis of the resultant spectrum is aligned with the system. If the reverse was true, i.e. the spatial axis of the slit and the binary system were perpendicular, no signature would be detected. Therefore, it is important to obtain data at multiple position angles. The observation is depicted schematically in Figure 1.14. The system is unresolved and the photo-centre of the resultant (single) spectrum is between the positions of the two components. For example, if the two stars are equally bright the photo-centre will be equally distance from both, i.e. midway between their positions. In the continuum the flux ratio of the two stars does not change so the photo-centre is also constant across the continuum (see the left panel of Figure 1.14). Over the emission line however, the flux ratio changes as the star with the emission line accounts for a higher fraction of the total flux than it does in the continuum. As a result, the location of the photo-centre

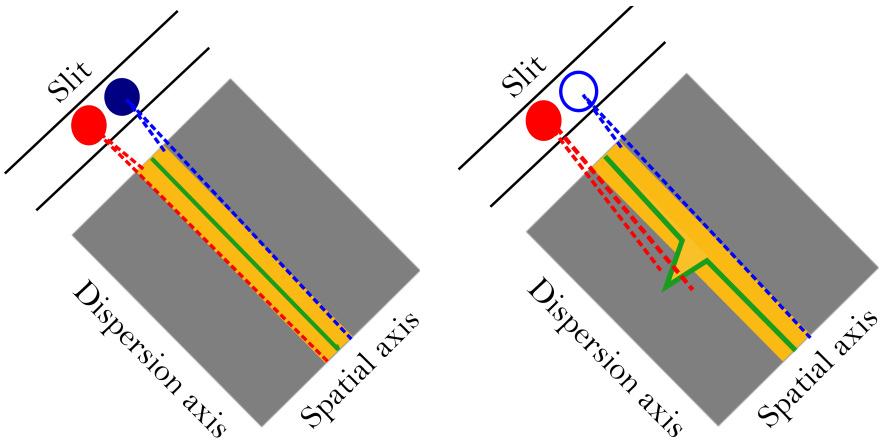

Figure 1.14: *A schematic representation of the spectroastrometric signature of a binary system. In the left panel, only the continuum emission of the system is considered. In the right panel, the star on the left exhibits an additional emission line.*

shifts towards the position of the emission line star (see the right panel of Figure 1.14). Consequently, if the centroid of a spectrum can be traced accurately enough, unresolved binary systems can be detected via a shift in the photo-centre over spectral lines.

The power of spectroastrometry is due to the fact that the centroid can be traced very accurately. The error in the centroid of the spectrum is essentially governed by Poisson statistics, and thus the positional accuracy scales as FWHM/SNR^{-1} (Takami et al. 2003). Consequently, for bright sources, e.g. SNR $\sim$250, a positional accuracy of the order of a mas is possible. As a result, this technique can probe scales that are not conventionally resolved.

Since spectroastrometry is used extensively in this these the possible applications of this technique are not discussed here. Instead, this section has described the fundamental concept of the technique and highlighted its potential to probe small scales. Further details about the observational procedure and the interpretation of spectroastrometric signatures are deferred to subsequent chapters.

1.5 An introduction to this thesis

This chapter has presented an overview of the current understanding of solar mass star formation and discussed why less is known about massive star formation. In addition, intermediate and massive young stellar objects were introduced, and insights into the process of star formation gained from the study of such objects were presented. This chapter has also presented an overview of the properties of Be stars and the disks surrounding them. Currently, it is not known why Be stars loose mass and form circumstellar disks. Given the importance of mass loss in the evolution of massive stars, Be stars represent a significant gap in our understanding of stellar evolution.

The work presented in this thesis aims to address these questions regarding massive star formation and evolution via high resolution observations of the circumstellar environments of young stellar objects and Be stars.

Chapter 2 presents a spectroastrometric study of HAe/Be stars in an attempt to determine the properties of unresolved binary systems such as their mass ratio and thus constrain their formation mechanism. Another key property of such systems is the relative orientation of circumstellar disks and the binary orbit. Chapter 3 attempts to determine whether the circumstellar disks in HAe/Be binary systems are coplanar with the binary orbit by comparing binary position angles, circumstellar disk angles and a model of such systems.

It is thought that there is a change in the accretion mechanism from magnetospheric accretion to direct disk accretion over the HAe/Be mass range. To investigate whether this is manifest by a difference in outflow characteristics, Chapter 4 presents NIR integral field unit observations of a sample of Herbig Be stars. Chapter 5 demonstrates the capabilities of spectroastrometry in observing disks on mas scales and applies this to Be stars in an attempt to determine the kinematics of a sample of disks, in order to constrain their formation mechanism.

In Chapter 6, spectroastrometry is applied to the CO 1^{st} overtone bandhead emission of a sample of MYSOs to search for evidence of small scale disks. Properties of disks are inferred from fitting the observed emission profiles with a model of a circumstellar disk and these are compared to the spectroastrometric data to determine whether

massive young stellar objects possess dense circumstellar disks. Finally, conclusions and possibilities for future work are presented in Chapter 7.

Chapter 2

The mass ratio and formation mechanisms of Herbig Ae/Be star binary systems

2.1 Introduction

Our understanding of the formation and early evolution of massive stars is less complete than in the case of low mass stars. As observations of massive young stars are challenging, the full extent of the differences and similarities between low and high mass star formation are still unknown. Between the two extremes of mass lie the Herbig Ae/Be stars (Herbig 1960). These stars represent the most massive of objects to experience an optically visible PMS evolutionary phase. Therefore, HAe/Be stars offer a unique opportunity to study the early evolution of stars more massive than the Sun. In the largest study of it kind, Baines et al. (2006) utilised spectroastrometry to study a sample of HAe/Be stars with milli-arcsecond (mas) precision. It was found that the majority, 68 ± 11 per cent, of HAe/Be stars reside in relatively wide (probably a few-hundred AU, see Section 2.5.3) binary systems.

Little is known about the properties of such binary systems. Since these systems are still relatively young (1–10×10^6 yrs), the properties of the binary components and configurations of such systems will contain an imprint of the binary formation mechanism. Therefore, the properties of HAe/Be binary systems may lead to an insight into the star formation mechanism at intermediate masses. The seminal study to date is that

by Bouvier & Corporon (2001), who used Adaptive Optics assisted observations to construct Spectral Energy Distributions (SEDs) for each component in a number of HAe/Be binary systems. The drawback of SED fitting is that PMS stars, as young stars, are inevitably associated with dusty, obscured environments. Therefore, the brightness ratio of a binary determined by SED fitting can occasionally be ambiguous. However, very few HAe/Be binary systems have been studied with spatially resolved spectroscopy, and thus far such studies have been conducted with seeing limited resolution (e.g. Carmona et al. 2007; Hubrig et al. 2007).

The position angles of HAe/Be binary systems seem to be preferentially aligned with their spectropolarimetrically detected circumprimary disks (Baines et al. 2006). This already places constraints on the formation modes of these stars, in that it seems the systems formed via fragmentation of a molecular core or disk. This has already been suggested for lower mass binaries (Wolf et al. 2001; Kroupa & Burkert 2001), but little is known about the formation mechanisms of more massive stars. This chapter continues the work of Baines et al. (2006) with dedicated observations to study both components of binary systems. The objective is to determine the properties of these binary systems and thus place stronger, more quantitative, constraints on the formation of intermediate mass stars. In this chapter this is done by determining the mass ratio of these binary systems. In turn, this is done using a spectroastrometric technique to disentangle the constituent spectra of unresolved binary systems, allowing the spectral type, and hence mass, of each component to be determined. Spectroastrometry itself is a relatively simple technique that extracts the spatial information present in conventional longslit spectra. Crucially, spectroastrometry can probe changes in flux distributions with a typical precision of a mas (Bailey 1998a), allowing binaries with separations as small as 100 mas to be studied.

This chapter is structured as follows: Section 2.2 presents the sample selection, observation method and data reduction procedures. In Section 2.3 spectroastrometric signatures observed are discussed. Section 2.4 presents the method of splitting unresolved binary spectra and in Section 2.4.1 the results of separating binary spectra into their constituent spectra are reviewed. The results are discussed in Section 2.5. Finally,

the chapter is concluded in Section 2.6 by summarising the salient points raised.

2.2 Observations and data reduction

2.2.1 Observations

The data presented in this chapter consist of long-slit spectra in the B band (4200 − 5000Å) and/or the R band (6200 − 7000Å) of 45 HAe/Be stars, and 2 emission line objects which are possible HAe/Be stars. The objects were chosen from the catalogs of Thé et al. (1994), Vieira et al. (2003) & Hernández et al. (2004), and were selected to be reasonably bright ($V \leq$ 12-13). Some objects previously observed by Baines et al. (2006) were observed to provide a consistency check on the spectroastrometric signatures. Given the relatively small population of HAe/Be stars (∼100), the objects observed constitute a representative sample of HAe/Be stars, albeit brightness limited.

The data were obtained using the 4.2m William Herschel Telescope (WHT) and the 2.5m Isaac Newton Telescope (INT). At the WHT, data were obtained on the 6th & 7th of October 2006, using the Intermediate Dispersion Spectrograph and Imaging System (ISIS) spectrograph. Spectra of 20 objects were taken simultaneously in the B and R bands using the dichroic slide of ISIS. In most cases a slit 5 arcsec wide was used to ensure all the light from a given binary system entered the slit, even in poor seeing. This allows individual binary components to be studied, unlike the data of Baines et al. (2006), which were obtained with a slit of 1 arcsec. The R1200B and R1200R gratings were used and the resulting spectral resolving power was found to be ~ 3500, corresponding to $85\,\mathrm{km\,s^{-1}}$. The angular pixel size was 0.20 and 0.22 arcsec in the B band and R band respectively, which means that the spatial profile of the longslit spectra was well sampled (since the average FWHM was 1.9 arcsec). At the INT, data were obtained using the 235mm camera and the Intermediate Dispersion Spectrograph (IDS). Observing was conducted from the 27th of December 2008 to the 3rd of January 2009. Adverse weather conditions prevented observing for the better part of three nights. None the less, the spectra of 32 objects were obtained. As at the WHT, the slit width was generally 5 arcsec. The R1200R and R1200B gratings were used and the resulting spectral resolution was found to be ~ 3800, or $80\,\mathrm{km\,s^{-1}}$. The angular size of the pixels

was 0.4 arcsec, which fully sampled the average spatial profile of the spectra (1.8 arcsec).

Multiple spectra were taken at four position angles (PA) on the sky. The PAs selected always comprised of two perpendicular sets of two anti-parallel angles, e.g. 0°, 90°, 180° and 270°. Dispersion calibration arcs were made using CuNe and CuAr lamps. Table 2.1 presents a summary of the observations.

Table 2.1: *Log of the observations, column 1 lists the objects observed, column 2 denotes the spectral type of the objects, column 3 lists the V band magnitudes of the sample, and column 4 designates which telescope the object in question was observed with. Columns 5 and 6 list the average seeing conditions, columns 7 and 8 list the total exposure times and column 9 denotes the slit width used. Column 10 lists the total Signal to Noise Ratios, and finally, column 11 presents the date(s) each object was observed. Information on the objects is taken from SIMBAD (simbad.u-strasbg.fr) unless otherwise stated.*

Object	Spec type	V	Telescope	FWHM[a] ($''$)	FWHM[b] ($''$)	t_{blue} (s)	t_{red} (s)	Slit ($''$)	SNR	Date
VX Cas	A0e	11.3	WHT	1.3	1.2	4800	4800	5.0	600_B,570_R	07/10/06
VX Cas	A0e	11.3	INT	1.1	1.7	2800	3600	$2.5_B, 5.0_R$	370_B,370_R	28+31/12/08
V594 Cas	Be	10.6	INT	1.3	–	3200	–	5.0	610	01/01/09
V1185 Tau	A1	10.7	INT	1.7	–	3200	–	5.0	430	03/01/09
IP Per	A3	10.3	INT	1.2	1.4	2000	2400	$2.5_B, 5.0_R$	110_B,320_R	28+31/12/08
AB Aur	A0Vpe	7.1	WHT	1.9	1.9	330	320	5.0	110_B,650_R	06/10/06
MWC 480	A3pshe	7.7	WHT	2.0	2.1	960	640	5.0	1100_B,800_R	06/10/06
UX Ori	A3e	9.6	WHT	2.4	2.4	3600	3600	5.0	1200_B,940_R	06/10/06
V1012 Ori	Be[c]	12.1	INT	2.1	–	4800	–	5.0	150	02/01/09
V1366 Ori	A0e	9.8	INT	1.3	–	2400	–	3.0	570	31/12/08
V346 Ori	A5III	10.1	INT	1.5	–	3600	–	5.0	200	01/01/09
HD 35929	A5	8.1	WHT	1.9	1.7	2060	1470	5.0	40_B,900_R	07/10/06
V380 Ori	A0	10.7	INT	1.5	1.6	3600	2940	$3.0_B, 5.0_R$	100_B,200_R	28+31/12/08
MWC 758	A3e	8.3	WHT	1.4	1.3	1080	960	5.0	50_B,660_R	07/10/06
HK Ori	A4pev	11.9	INT	2.4	–	4800	–	5.0	200	02/01/09
HD 244604	A3	9.4	WHT	1.7	1.6	3180	3660	5.0	100_B,720_R	07/10/06

Continued on next page

Table 2.1 – continued from previous page

Object	Spec type	V	Telescope	FWHM[a] ($''$)	FWHM[b] ($''$)	t_{blue} (s)	t_{red} (s)	Slit ($''$)	SNR	Date
V1271 Ori	A5	10.0	INT	1.6	–	2460	–	5.0	410	01/01/09
T Ori	A3	9.5	INT	1.9	–	3200	–	5.0	300	03/01/09
V586 Ori	A2V	9.8	INT	3.3	–	2940	–	5.0	650	02/01/09
HD 37357	A0e	8.8	INT	1.4	1.4	2060	1470	$3.0_B, 5.0_R$	200_B,350_R	28+31/12/08
V1788 Ori	B9Ve	9.9	INT	1.7	–	1350	–	5.0	450	01/01/09
HD 245906	B9IV	10.7	INT	1.8	–	2800	–	5.0	100	03/01/09
RR Tau	A2II-IIIe	10.9	INT	1.7	–	2800	–	5.0	250	03/01/09
V350 Ori	A0e	10.4(B)	INT	1.9	–	4800	–	5.0	130	03/01/09
MWC 120	A0	7.9	WHT	2.1	1.9	480	480	5.0	1500_B,690_R	06/10/06
MWC 120	A0	7.9	INT	1.4	1.6	2460	1250	$3.0_B, 5.0_R$	1200_B,560_R	28+31/12/08
MWC 790	Be	12.0	INT	3.1	–	4050	–	5.0	200	02/01/09
MWC 137	Be	11.2	INT	–	2.1	–	4560	5.0	200	28/12/08
HD 45677	Bpshe	8.0	WHT	2.0	1.9	360	240	5.0	900_B,550_R	06/10/06
LkHα 215	B7.5e	10.6	INT	1.5	2.3	3600	3600	$5.0_B, 4.0_R$	300_B,360_R	27+31/12/08
MWC 147	B6pe	8.8	WHT	1.8	1.5	3000	1700	5.0	1200_B,500_R	07/10/06
MWC 147	B6pe	8.8	INT	1.3	–	2400	–	5.0	620	01/01/09
R Mon	B0	10.4	INT	4.2	2.5	3600	3600	5.0	100_B,240_R	28/12/08,02/01/09
V590 Mon	B8pe	12.9	INT	1.5	–	2670	–	5.0	200	01/01/09
V742 Mon	B2Ve	6.9	INT	1.4	2.8	1740	2535	5.0	400_B,800_R	30+31/12/08
OY Gem	Bp[e]	11.1	INT	1.8	–	2880	–	5. 0	100	03/01/09
GU CMa	B2Vne	6.6	WHT	2.5	2.4	360	360	5.0	1500_B,900_R	06/10/06

Continued on next page

Table 2.1 – continued from previous page

Object	Spec type	V	Telescope	FWHM[a] ($''$)	FWHM[b] ($''$)	t_{blue} (s)	t_{red} (s)	Slit ($''$)	SNR	Date
GU CMa	B2Vne	6.6	INT	1.8	–	720	–	5.0	1400	03/01/09
MWC 166	B0IVe	7.0	WHT	2.5	2.3	210	120	5.0	1200_B,800_R	06/10/06
HD 76868	B5	8.0	INT	1.5	2.4	4830	2100	5.0	100_B,100_R	30/12/08,01/01/09
HD 81357	B8	8.4	INT	1.7	–	4800	–	5.0	100	03/01/09
MWC 297	Be	12.3	WHT	1.4	1.2	4100	3120	5.0	100_B,500_R	07/10/06
HD 179218	B9e	7.2	WHT	2.6	2.4	2100	1200	1.0/1.5	2300_B,940_R	06/10/06
HD 190073	A2IVpe	7.8	WHT	1.5	1.2	540	360	5.0	600_B,800_R	07/10/06
BD +40 4124	B2	10.7	WHT	2.1	1.9	600	660	4.0	500_B,370_R	07/10/06
MWC 361	B2Ve	7.4	WHT	1.7	1.7	1350	960	2.5/4.0	1400_B,1400_R	06/10/06
SV Cep	Ae	10.1(B)	INT	1.6	–	3000	–	5.0	600	02/01/09
MWC 655	B1IVnep	9.2	INT	1.7	–	2400	–	5.0	400	03/01/09
Il Cep	B2IV/Ve	9.3	WHT	1.4	1.2	3500	3000	5.0	800_B,500_R	07/10/06
BHJ 71	B4e	10.9	WHT	1.8	1.8	1200	1080	4.0	500_B,340_R	06/10/06
BHJ 71	B4e	10.9	INT	1.7	–	4200	–	5.0	500	01/01/09
MWC 1080	B0	11.6	WHT	2.0	2.0	3300	4170	5.0	200_B,500_R	06/10/06

[a] Average seeing in the $B-$band; approximated by the average of the individual median FWHM.

[b] Average seeing in the $R-$band; approximated by the average of the individual median FWHM.

[c] Thé et al. (1994)

2.2.2 Data reduction

Data reduction was conducted using the Image Reduction and Analysis Facility (IRAF)[(a)] and routines written in Interactive Data Language (IDL). Initial data reduction consisted of bias subtraction and flat field division. The total intensity spectra were then extracted from the corrected data in a standard fashion. Wavelength calibration was conducted using the arc spectra. The resultant wavelength calibration solution typically had a precision of < 0.1Å.

Spectroastrometry was performed by fitting Gaussian functions to the spatial profile of the long-slit spectra at each dispersion pixel. This resulted in a positional spectrum, the centroid of the Gaussian as a function of wavelength, and a Full Width at Half Maximum (FWHM) spectrum, the FWHM as a function of wavelength. Spot checks were used to ensure that a Gaussian was an accurate representation of the data. The continuum position exhibited a general trend across the CCD chip: of the order of 10 pixels in the case of the ISIS data and 2 pixels in the IDS data. This was removed by fitting a polynomial function (of 4^{th} or 5^{th} order) to the continuum regions of the spectrum.

All intensity, positional and FWHM spectra at a given PA were combined to make an average spectrum for each PA. A correction for slight changes in the dispersion across PAs was determined by cross-correlating average intensity spectra obtained at different PAs. The correction was then applied to the average intensity, positional and FWHM spectra. The average positional spectra for anti-parallel PAs were then combined to form the average, perpendicular, position spectra, for example: $(0^\circ - 180^\circ)/2$ and $(90^\circ - 270^\circ)/2$. This procedure eliminates instrumental artifacts as real signatures rotate by 180° when viewed at the anti-parallel PA, while artifacts remain at a constant orientation. In addition, all positional spectra were visually inspected for artifacts not fully removed by this procedure. As with the positional spectra, the FWHM spectra at anti-parallel PAs were also combined to make two averaged, perpendicular spectra.

[(a)] IRAF is distributed by the National Optical Astronomy Observatories, which are operated by the Association of Universities for Research in Astronomy, Inc., under cooperative agreement with the National Science Foundation (see e.g. Tody 1993).

While FWHM features do not rotate across different PAs, the features observed at anti-parallel PAs were used to exclude artifacts via a visual comparison. All conditions being constant, a real FWHM signature should not change from one PA to the opposite angle at +180°.

2.2.3 Artifacts

Several spectroastrometric signatures present in the data were found to be artifacts. Here an artifact is defined as a spectroastrometric signature which does not rotate by 180° when viewed at two anti-parallel position angles. Artifacts in spectroastrometric data can arise from a number of sources. Instrumental effects include: the misalignment of the dispersion axis with the CCD rows, a change in focus along the slit, curvature of the spectrum and any departure of the CCD array from a regular grid (Bailey 1998b). As discussed in Section 2.2.2, such artifacts are readily identified and negated. The observation of unresolved lines can also result in false signatures (Bailey 1998b). Here, the data were obtained with a resolution sufficient to resolve most spectral lines. However, the narrow absorption troughs in many of the double-peaked H I emission profiles may cause some of the artifacts as these features are often barely resolved.

In addition, Brannigan et al. (2006) report an artifact that is a consequence of image distortion, regardless of whether the spectral lines are well resolved. If a wide slit is used, there is a chance the object observed is not located at the centre of the slit. This can be exaggerated if the point-spread-function is unstable (for example due to unstable adaptive optics). If there is an offset between the image centre and the centre of the slit, the slit is not uniformly illuminated. This results in a varying angle of incidence of light onto the grating. In turn, this results in a slightly blue or red shifted image. Since the shift in wavelength is dependent upon the position of the source in the slit, this causes a wavelength dependent change in position and thus an artificial spectroastrometric signature. As these data were obtained with a wide slit of 5 arcsec this effect is likely to be origin of many of the artifacts observed.

The empirical finding is that it is crucial to obtain multiple spectra, comprising of anti-parallel sets of data. Such data will identify artifacts regardless of their cause, and can also be used to remove systematic effects.

2.3 Spectroastrometric signatures

2.3.1 Binary spectroastrometric signatures over H I lines

An unresolved binary system, in which each component has a unique spectrum, displays a clear signature in the behaviour of the spectral photocentre. As the spatial profile is the sum of the two stars convolved with the seeing, the peak is not located at the position of either star, but somewhere between the components. The exact location of the photo-centre depends on the intensity ratio and the separation of the two components. Over spectral lines the binary flux ratio changes from its continuum value, which results in the peak position shifting towards the dominant component. Therefore, unresolved binary systems are revealed by a displacement in the positional spectrum over spectral lines. In addition, an unresolved binary system is also revealed by a change in the FWHM over lines in the spectrum. Again, this is because the spatial profile of an unresolved binary system is dependent upon the binary flux ratio, which changes from its continuum value across certain lines. As the error in the centre of the Gaussian profile is governed by photon statistics, changes of mas scales can be traced. This allows binary systems with separations as small as ~ 0.1 arcsec and differences in brightness up to 5 magnitudes to be studied (Baines et al. 2006).

To illustrate the detection of a binary system the observations of GU CMa are presented in some detail. GU CMa is known to be a Herbig Be binary system with a separation of ~ 0.65 arcsec, a PA of $\sim 195°$, a brightness difference between components of 0.7-1.0 magnitudes in the optical band and a primary with a spectral type of B1 (Fu et al. 1997; Fabricius & Makarov 2000; Bouvier & Corporon 2001).

GU CMa presents a very clear binary signature in the spectroastrometric observations (Figures 2.1 & 2.2). Across the H I lines the photo-centre of the spectrum clearly shifts towards the North-East. This demonstrates that the primary, the component brightest in the continuum, dominates the emission spectrum. It also indicates that the secondary, the component least bright in the continuum, has the larger absorption profile of Hγ. As the photo-centre shifts to the North-East the FWHM of the spectrum is seen to decrease. This also indicates that the primary dominates the spectrum at these

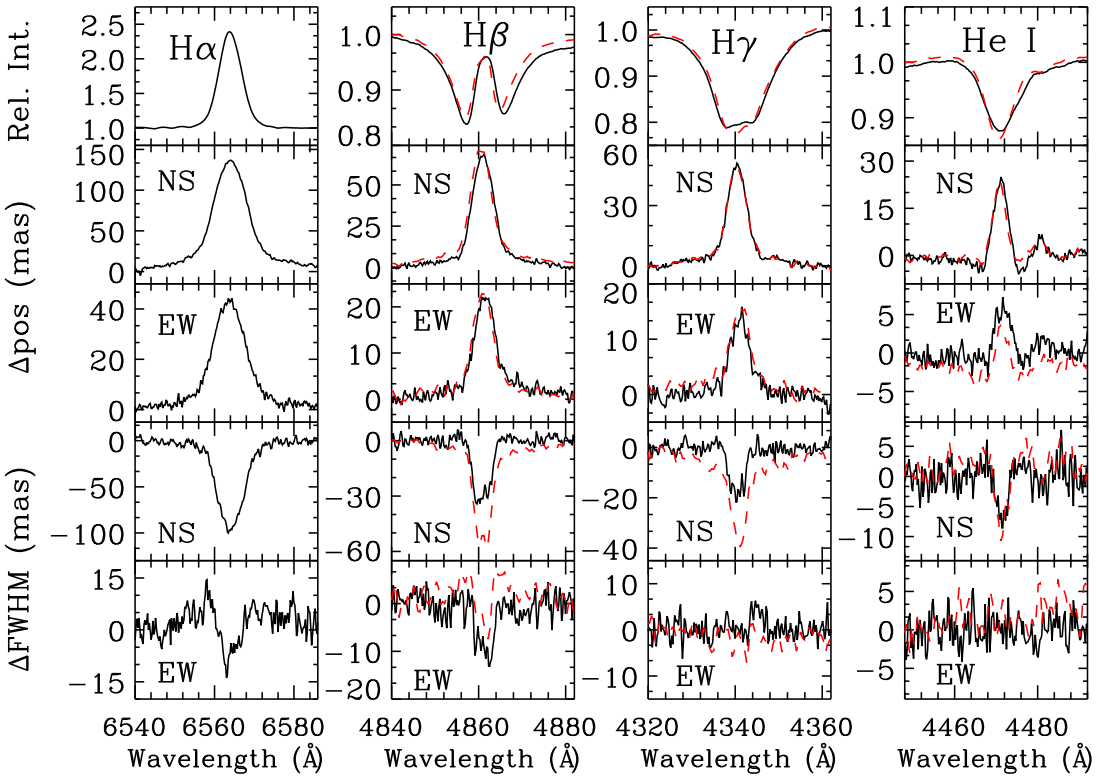

Figure 2.1: *The spectroastrometric signatures of GU CMa. Presented from left to right: the Hα, Hβ, Hγ and He*I *λ*4471 *spectral profiles and associated spectroastrometric signatures. In the spectroastrometric signatures North and East are positive. Data obtained at the WHT is represented by the solid lines, while the data obtained at the INT is represented by the dashed lines.*

particular wavelengths. The photo-centre is also observed to shift to the North-East across the He I lines. This again indicates that it is the primary that dominates the binary flux over this line.

All the spectroastrometric excursions across the H I lines produce a PA consistent to within $\sim 1^{\circ}$. The agreement between the spectroastrometric displacements across different lines is an important consistency check. In addition, the close agreement between the data gathered at different telescopes provides compelling evidence that the signatures observed are real and not contaminated by instrumental affects. The difference in the

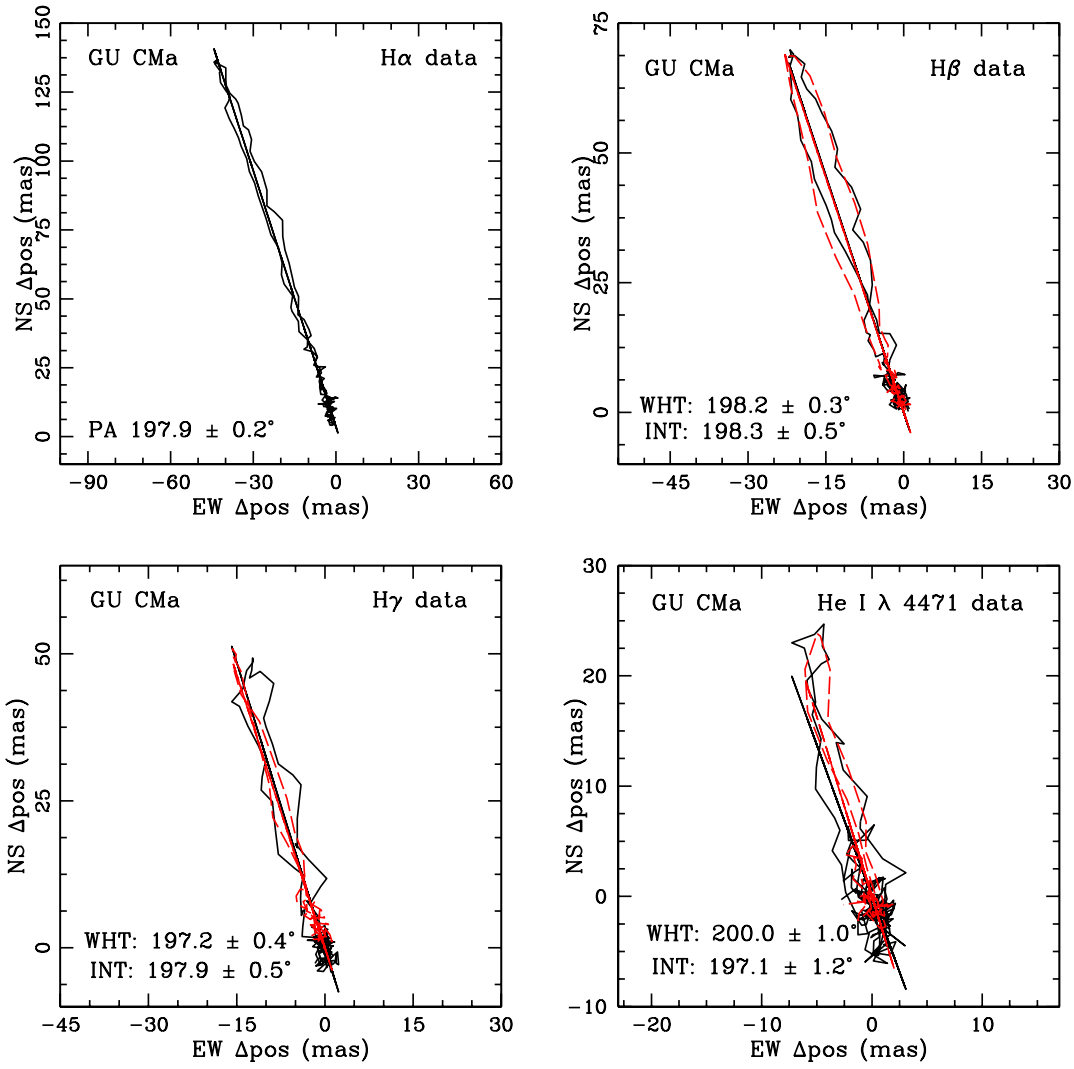

Figure 2.2: *The spectroastrometric signatures of GU CMa. Here the XY-plots of the Hα, Hβ, Hγ, and by way of contrast, the* He I *λ 4471 spectroastrometric displacements are presented. In the XY-plots North is up and East is to the left. As before, ISIS data is represented by the solid lines, while IDS data is represented by the dashed lines. As can be seen the two datasets agree within the errors.*

FWHM changes can be explained by the difference in the seeing between observations. Finally, that these observations concur with the results of Baines et al. (2006), further proves that these signatures are real and no instrumental effect. As demonstrated by the spectroastrometric signature associated with the He I line such features do not solely occur across lines with an emission component. This is important to note as it means the spectra splitting method does not require emission lines to separate spectra.

In the case of some stars, significant FWHM changes are observed which are not accompanied by a change in the spectral photo-centre. Baines et al. (2006) regard such a signature as a possible binary detection. This is substantiated as Baines et al. (2006) demonstrate that the spectroastrometric signature of a binary system with a separation of greater than half the slit width exhibits larger FWHM than positional features. However, in the data presented here, this scenario is unlikely. As a wide slit was used, a binary with a separation of half the slit width would be resolved, even in seeing conditions of 2 arcsec. As a resolved system does not exhibit a spectroastrometric signature, there may be an alternative explanation to the FWHM features not accompanied by positional features. It is noted that such features are not instrumental as some stars exhibit no change in FWHM over spectral lines. In many cases the large FWHM features occur over absorption features in the emission profiles. This suggests that these features may trace an extended structure which scatters the line profile, rather than being an intrinsic source. If the scattering media were close to being symmetrically distributed around the central star it could generate a large FWHM increase while not resulting in a positional signature. Such sources of flux could be a disk/stellar wind (Azevedo et al. 2007), the halos reported by Leinert et al. (2001) and Monnier et al. (2006), or nebulosity. This topic will be returned to in Section 2.5.1.

The observational results naturally fall into three categories: clear binary signatures, possible binary/other signatures and null detections. A summary of the detections in the results is presented in Table 2.2. It is important to note that it is not only binaries that are detected by spectroastrometry, optical outflows and disks can also result in a spectroastrometric feature (Bailey 1998a; Takami et al. 2001). However, there are no disk signatures, and only a few detections of outflows, in the data presented here.

There are 29 stars in the sample that are referred to in the literature as being part of a binary system. However, AB Aur and HD 244604 are excluded from this list as the binary nature of these objects is open to question; section 2.5.1 explains why this is the case. Twenty of the twenty-seven previously known binary systems are detected. As six of the seven undetected systems have separations greater than 2 arcsec and/or brightness differences as great as 8 magnitudes, all but one, UX Ori, of the binary systems that are able to be detected via spectroastrometry are detected. Given that the majority of known binary systems are detected, objects which are not known to be part of a binary system but exhibit similar spectroastrometric signatures to the known binary systems are classified as new binary detections. Eight new binary systems are detected. The raw binary fraction of the sample is 0.60. Including the non detections of known binary systems the binary fraction of the sample is 0.74. While these figures are high for a limited separation range, they are consistent with previous work (Pirzkal et al. 1997; Baines et al. 2006).

As expected, binaries with separations greater than ~ 2.0 arcsec and differences in brightness greater than 5 magnitudes, e.g. HD 179218 and MWC 297, are not detected. The wide companions are not detected in the longslit spectra as distinct sources. VX Cas, T Ori, LkHα 215 and Il Cep are all known to be binary systems and all display a binary signature in their spectroastrometric signatures. Therefore, these stars are classified above as detections of known binary systems. However, these systems are wide binaries with separations greater than 5 arcsec. These companions are clearly resolvable, and thus the spectroastrometric signatures observed can not be due to the previously reported companion. Therefore, it is suggested these signatures are due to previously unknown companions to VX Cas, T Ori, LkHα 215 and Il Cep.

Table 2.2: *Previously known binary systems and new detections. Column 1 list the objects in question, columns 2 and 3 list the separation and PA of the known binaries, taken from the literature. Column 4 contains difference in brightness between the two binary components. The amalgamation of data is not complete, if more than one value of binary parameter is available in the literature, only one is presented for the sake of clarity.*

Object	Separation (mas)	PA (°)	Δflux (magnitudes)
Known binaries detected:			
VX Cas	5340[A]	165.3[A]	*K*:4.8[A]
V380 Ori	125 ± 25[B]	224.0 ± 2.0[B]	*K*:1.42[B]
HK Ori	347.7 ± 2.5[B]	41.8 ± 0.7[B]	*V*: 0.87[B]
T Ori	7700 ± 200[C] and spectroscopic[D]	72.6[C]	*K*:> 4.5[C]
V586 Ori	990[A]	30.3[A]	*K*:2.8[A]
HD 37357	186[E]	49.0[E]	*K*:1.7[A]
V1788 Ori	520[A]	352.9[A]	*K*:3.5[A]
HD 245906	130[A]	77.1[A]	*K*:1.5[A]
V350 Ori	290[A]	206.8[A]	*K*:3.2[A]
HD 45677		150 ± 17[F]	
LkHα 215	8500[A]	226.6[A]	*K*:4.8[A]
MWC 147	150[A]	55.6[A]	*K*:3.8[A]
R Mon	670[G]	290.7[G]	*K*:4.9[A]
GU CMa	654[H]	194.5[H]	V:0.95 ± 0.02[H]
MWC 166	654[H]	297.8[H]	*V*:1.41[H]
BD +40 4124	720[A]	175.1[A]	*K*:5.4[A]
MWC 361	2250 ± 240[I]	164.0 ± 1.0[I]	*K*:4.9[I]

Continued on next page

Table 2.2 – continued from previous page

Object	Separation (mas)	PA (°)	Δflux (magnitudes)
SV Cep[J]			
Il Cep	6960[I]	147.0[I]	K:0.0[I]
MWC 1080	760 ± 2[C]	267.0 ± 1.0[C]	K:3.25 ± 0.08[4]
Known binaries not detected:			
UX Ori	22(min)[K]	257.4 ± 18.4[K]	
MWC 758	2280[A]	311.3[A]	K:8.3[A]
V1271 Ori	8380[A]	294.7[A]	K6.7[A]
V590 Mon	5007[A]	97.1[A]	K6.6[A]
MWC 297	3930 ± 200[L]	313 ± 2[L]	H:8.5 ± 0.25[L]
HD 179218	2540[A]	140.5[A]	K:6.6[A]
BHJ 71	6170[A]	29.2[A]	K8.3[A]
New spectroastrometric detections:			
V1366 Ori, HD 35929, RR Tau, MWC 120, V742 Mon, OY Gem, HD 76868 and HD 81357			

References: A) Thomas et al. (2007); B) Smith et al. (2005); C) Leinert et al. (1997); D) Shevchenko & Vitrichenko (1994); E) Hartkopf et al. (1996); F) Baines et al. (2006); G) Weigelt et al. (2002); H) Fabricius & Makarov (2000); I) Pirzkal et al. (1997); J) Rodgers et al. priv. com. (2008); K) Bertout et al. (1999); L) Vink et al. (2005b).

Spectral variability is a common behaviour of HAe/Be stars (Rodgers et al. 2002; Mora et al. 2004). In the case of the few objects observed twice, some line profile variations are seen. However, the spectroastrometric signatures of objects observed twice are generally consistent, e.g. the example of GU CMa (Figures 2.1 & 2.2). In addition, in the case of objects common to this sample and that of Baines et al. (2006), the spectroastrometric signatures presented here are consistent with the previous results. Therefore, it is concluded that spectral variability, on timescales of years, does not effect the spectroastrometric signatures observed. No line profile variability on timescales of minutes is observed.

To summarise, spectroastrometry is a powerful tool with which to study binary systems, as GU CMa demonstrates. Not only does it allow the clear detection of a 0.6 arcsec binary in seeing as large as 2.5 arcsec, it also traces the PA of the system with a precision of 1° or less. Spectroastrometry detects all but one of the known binary systems with separations less than ~ 2 arcsec and differences in brightness of less than 5 magnitudes. In addition, the PAs of these systems are all traced with a precision of the order of 1°, and are generally consistent with literature values to within $\sim 5°$. Most importantly, the spectroastrometric displacements contain information as to which component of the binary system dominates the flux over certain spectral features. This information can be used to separate the constituent spectra.

2.4 Splitting binary spectra

As spectroastrometric signatures trace changes in flux distributions they can be used to disentangle the spectrum of an unresolved binary spectrum into its constituent spectra.

The spectroastrometric signature of an unresolved binary system is directly proportional to the system separation and continuum flux ratio. Therefore, if these properties of a binary system are known, the intensity and positional spectra observed can be used to disentangle the individual fluxes of the two components. The first approach was pioneered by Bailey (1998b), and later used by Garcia et al. (1999) and Takami et al. (2003). Bailey (1998b) presented two equations which can be used in conjunction with spectroastrometric positional offsets and conventional intensity spectra to separate the

spectrum of an unresolved binary system into its constituent spectra. These equations are:

$$I_{\rm prim}(\lambda) = I_\lambda \times \left(\frac{P(\lambda) - P_{\rm sec}}{P_{\rm prim} + P_{\rm sec}} \right) \tag{2.1}$$

and

$$I_{\rm sec} = I(\lambda) \times \left(\frac{P_{\rm prim} - P(\lambda)}{P_{\rm prim} + P_{\rm sec}} \right), \tag{2.2}$$

where $I(\lambda)$ represents the unresolved intensity spectrum, $I_{\rm prim}$ and $I_{\rm sec}$ are the intensity spectra of the two components of an unresolved binary system, $P(\lambda)$ represents the positional spectrum and $P_{\rm prim}$ and $P_{\rm sec}$ are the positions of the two components on the spatial axis of the detector. The two equations contain two unknowns, the relative positions of the two binary components ($P_{\rm prim}$ and $P_{\rm sec}$), and therefore cannot be used without additional information.

Bailey (1998b) used this technique to separate the constituent spectra of the 0.6 arcsec binary Mira. In this case the binary separation was known, and thus the unknowns were reduced to one ($P_{\rm prim}$) as $P_{\rm sec} = P_{\rm prim} + d$, where d is the binary separation. This unknown was determined by Bailey (1998b) by systematically varying $P_{\rm prim}$ until the two component spectra appeared well separated; for example when the strong TiO absorption bands were only seen in the M type primary spectrum. However, this approach does not necessarily result in a complete separation of the two constituent spectra due to the subjective element in determining the best value of $P_{\rm prim}$. As an example, the spectrum of the M type primary of the Mira binary system presented by Bailey (1998b) has a similar Hα profile to the secondary, indicating that the component spectra have not been completely separated.

This difficulty can, in principle, be avoided if the equations above are expressed in terms of binary system properties that can be measured independently. This was done by Takami et al. (2003) who expressed the spectroastrometric positional spectrum of a binary system in terms of its separation (d) and the brightness ratio of the two binary components as follows:

$$P(\lambda) = P_{\rm prim} + \frac{I_{\rm sec}(\lambda)}{I(\lambda)} d, \tag{2.3}$$

where $P_{\rm prim}$ is the offset of the primary position from the photocentre. Consequently,

$$P'(\lambda) = P_{\rm prim} - P(\lambda), \tag{2.4}$$

where P' represents observed spectroastrometric positional spectrum and $P(\lambda)$ is the photocentre position in the continuum. The observed positional offsets are therefore given by:

$$P'(\lambda) = \left(\frac{I_{\rm sec}(\lambda)}{I(\lambda)} - \frac{I_{\rm cont(sec)}}{I_{\rm cont}} \right) d, \tag{2.5}$$

where $I_{\rm sec}(\lambda)$ and $I_{\rm sec(cont)}$ represent the flux from the secondary component at each wavelength and in the continuum respectively and $I(\lambda)$ is the total flux emanating from the binary system as a function of wavelength (the observed spectrum). Finally, inserting the binary flux ratio in the continuum (f_c) simplifies this equation to:

$$I_{\rm sec}(\lambda) = \left(\frac{f_c}{1+f_c} + \frac{P'(\lambda)}{d} \right) I(\lambda), \tag{2.6}$$

which allows the flux of the primary component to be obtained via:

$$I_{\rm prim}(\lambda) = I(\lambda) - I_{\rm sec}(\lambda). \tag{2.7}$$

Takami et al. (2003) used the above equations in an attempt to separate the constituent spectra of six unresolved binary systems which exhibit prominent Hα emission. For four of these systems the determined Hα line profiles of the primary and secondary components are remarkably similar. The separations of these systems are comparable to the slit width, and thus it is likely some flux from the system has been lost. Consequently, the total flux quantity in the above equations will be incorrect as they do not account for slit losses. Therefore, the similarity of the Hα profiles presented by Takami et al. (2003) may be an indication that in this case the spectra splitting was incomplete. However, regardless of whether the spectra presented by Takami et al. (2003) were completely separated or not, the method used by these authors is dependent upon *a priori* knowledge of the binary separation and continuum flux ratio. Therefore, this approach is limited in that it is only applicable to relatively well studied systems.

In contrast, Porter et al. (2004) present a spectra splitting method that does not require any prior knowledge to separate binary spectra. This is made possible by the use of an additional spectroastrometric observable, the FWHM spectrum. To utilise this extra data, Porter et al. (2004) present a series of simulations, in which the dependence of spectroastrometric observables on the flux ratio and separation of a binary system

were characterised. Using relationships established by the models of Porter et al. (2004), and the three spectroastrometric observables (the centroid, total flux and width), the individual fluxes of the binary components can be recovered. The exact methodology is as follows.

Initially, a model binary system is considered with a range of separations. For each separation the continuum flux ratio is estimated using the observed width of the spectral profile in the continuum ($\sigma_{\rm cont}$) in the following:

$$\frac{\sigma_{\rm cont} - \sigma_{\rm S}}{\sigma_{\rm S}} = A \left(\frac{d}{\sigma_{\rm S}} \right)^{B} \left[1 - \left| 1 - \min \left(\frac{f_{2,\rm cont}}{f_{1,\rm cont}} \text{or} \frac{f_{1,\rm cont}}{f_{2,\rm cont}} \right) \right|^{C} \right], \tag{2.8}$$

where $\sigma_{\rm S}$ is the intrinsic seeing width, $\sigma_{\rm cont}$ is the observed width of the spatial profile in the continuum. A, B and C are constants determined by Porter et al. (2004) who fit the above equation to synthetic spectroastrometric observations of model binary systems. As evident in equation 2.8, to estimate the continuum flux ratio accurately it is crucial to know the seeing at the time of the observations. This can be estimated from the spatial profile in the continuum, but this is only an upper limit as the spatial profile of an unresolved binary may be slightly larger than the spatial profile of a single star. Therefore, the seeing is estimated from the width of the spatial profiles of stars which do not exhibit a binary signature. Once the continuum flux ratio for a given separation is calculated, the binary flux ratio as a function of wavelength (r_λ) is calculated using the observed position spectrum, $\Delta{\rm pos}(\lambda)$, and the following:

$$r_\lambda = \frac{A}{1 - A}, \tag{2.9}$$

where A is given by:

$$A = \frac{\Delta{\rm pos}(\lambda)}{d} + \frac{r_c}{r_c + 1}, \tag{2.10}$$

and this is determined from equation 2.5. The component spectra are then easily calculated using:

$$f_{1,\lambda} = \frac{f_{\rm tot,\lambda}}{1 + r_\lambda} \tag{2.11}$$

$$f_{2,\lambda} = f_{\rm tot,\lambda} - f_{1,\lambda} \tag{2.12}$$

Finally, the resultant spectra are used to predict the expected FWHM signature of the binary in question using equation 2.8. This is compared to the observed FWHM signature to determine the best fitting binary separation. Once the best fitting separation

is determined, the component spectra are obtained by repeating this process with the best fitting separation. The approach was first applied to dedicated spectroastrometric data by Wheelwright et al. (2009, not included in this thesis). These authors used this technique to study the unresolved binary β Cep and show that the secondary appears to be a Be star, thus resolving the long standing mystery of the source of the system's Hα emission. Here the method of Porter et al. (2004) is applied to the current data in the red region, as the Hα line is often associated with the largest features. Then the determined properties of the binary system are used with the method of Bailey (1998b) to separate the binary spectra in the blue region

2.4.1 Separated binary spectra

To separate unresolved binary spectra into the constituent spectra it is required that prominent spectroastrometric signatures are observed across photospheric lines in the B region. Also, separating the component spectra is only attempted when the spectroastrometric signatures trace a linear excursion in the XY plane, as opposed to a loop. If a spectroastrometric signature is solely due to a binary system, the signature will trace a linear excursion in the XY plane, as demonstrated by the example of GU CMa (Fig. 2.2). Therefore, this criterion should exclude contaminated binary signatures and signatures not due to binary systems, issues discussed in Sections 2.5.1 and 2.5.2. As a result of these criteria it was not possible to separate the constituent spectra of all the binary systems detected.

Consequently, the unresolved binary spectra of 9 systems are split into the constituent spectra (the binary properties used/established are presented in Table 2.3). Spectral types for each spectra were determined by comparing the spectra to that of Morgan-Keenan standard stars and comparing ratios of key diagnostic lines. The results of assessing the spectral type of each component are presented in Table 2.4. The system mass ratios are determined by assessing the mass of each component from its spectral type, using the data of Harmanec (1988). In some cases the spectral types of each component of a binary system had already been estimated, e.g. GU CMa and MWC 166 (see Bouvier & Corporon 2001). The spectral types determined using the spectroastrometrically split spectra are in good agreement with previous results. This provides an

Table 2.3: *A summary of the binary properties used/established when separating the unresolved spectra. Column 1 presents the binary systems for which the constituent spectra were separated, column 2 lists the binary separations used or established and column 3 presents the binary separations in the literature. Column 4 presents the binary PAs determined from the data discussed here, and column 5 lists the binary PAs from the literature. Finally, column 6 contains the difference in brightness between the two components that was used. References for the literature values are presented in Table 2.2.*

Binary	d	$d_{\rm lit}$	PA	$PA_{\rm lit}$	ΔB
	$''$	$''$	(°)	(°)	(magnitudes)
HK Ori	0.36	0.35	46.9 ± 3.1	41.8	1.0
T Ori	0.84	–	107.2 ± 2.5	–	2.5
V586 Ori	1.00	0.99	216.8 ± 3.3	30.3	3.5
HD 37357	0.14	0.19	61.5 ± 4.1	49.0	1.75
V1788 Ori	0.69	0.52	131.3 ± 6.6	352.9	3.5
HD 245906	0.13	0.13	81.9 ± 3.1	77.1	2.5
GU CMa	0.65	0.65	197.9 ± 0.2	194.5	1.1
MWC 166	0.52	0.65	298.3 ± 0.7	297.8	1.2
Il Cep	0.44	–	54.3 ± 2.0	–	3.5

important check on the validity of the spectroastrometric procedure. In addition, the spectral types determined for the primary components generally agree with previous classifications of the composite spectra, which also provides a consistency check.

The separated spectra are presented in Fig. 2.3. From examination of the spectra (Fig. 2.3 and spectra split in the R band) it is clear that in some cases only the primary component is responsible for the emission lines seen in the composite spectrum. This is in agreement with the finding of Bouvier & Corporon (2001), who report that in many HAe/Be binary systems only the primary exhibits a significant NIR excess, i.e possess circumstellar material.

Table 2.4: *The results of separating binary spectra into the two constituent spectra. Column 1 lists the objects in question and column 2 denotes the spectral type of the primary. Column 3 lists the spectral type of the secondary. The spectral types of these objects taken from the literature are listed in column 4. The resulting mass ratio is presented in column 5. Finally, the predicted mass ratio of the system, if the secondary were drawn at random from the IMF (see text for explanation), is listed in column 6.*

Binary	$Type_1$	$Type_2$	Spec $Type_{lit}$	q_{ob}	q_{pred}
HK Ori	A0	K3	G1Ve[A],A4pev[B]	0.33	0.07
T Ori	A2	A2	A3IVev[A],A0[C]	1.00	0.07
V586 Ori	A2	F5	A2V[D]	0.65	0.07
HD 37357	A2	A4	A0Ve[E]	0.94	0.07
V1788 Ori	A2	F5	B9Ve[E]	0.65	0.07
HD 245906	A1	G5	B8e[F]	0.52	0.07
GU CMa	B1	B2	B2vne[G]	0.78	0.02
MWC 166	B0	B0	B0IVe[H]	1.00	0.01
Il Cep	B3	B4	B2pe[H]	0.84	0.03

References: A) Mora et al. (2001), B) Bidelman (1954), C) Hernández et al. (2004), D) Smith (1972), E) Thé et al. (1994), F) Herbig & Bell (1988), G) Guetter (1968), H) Hiltner (1956).

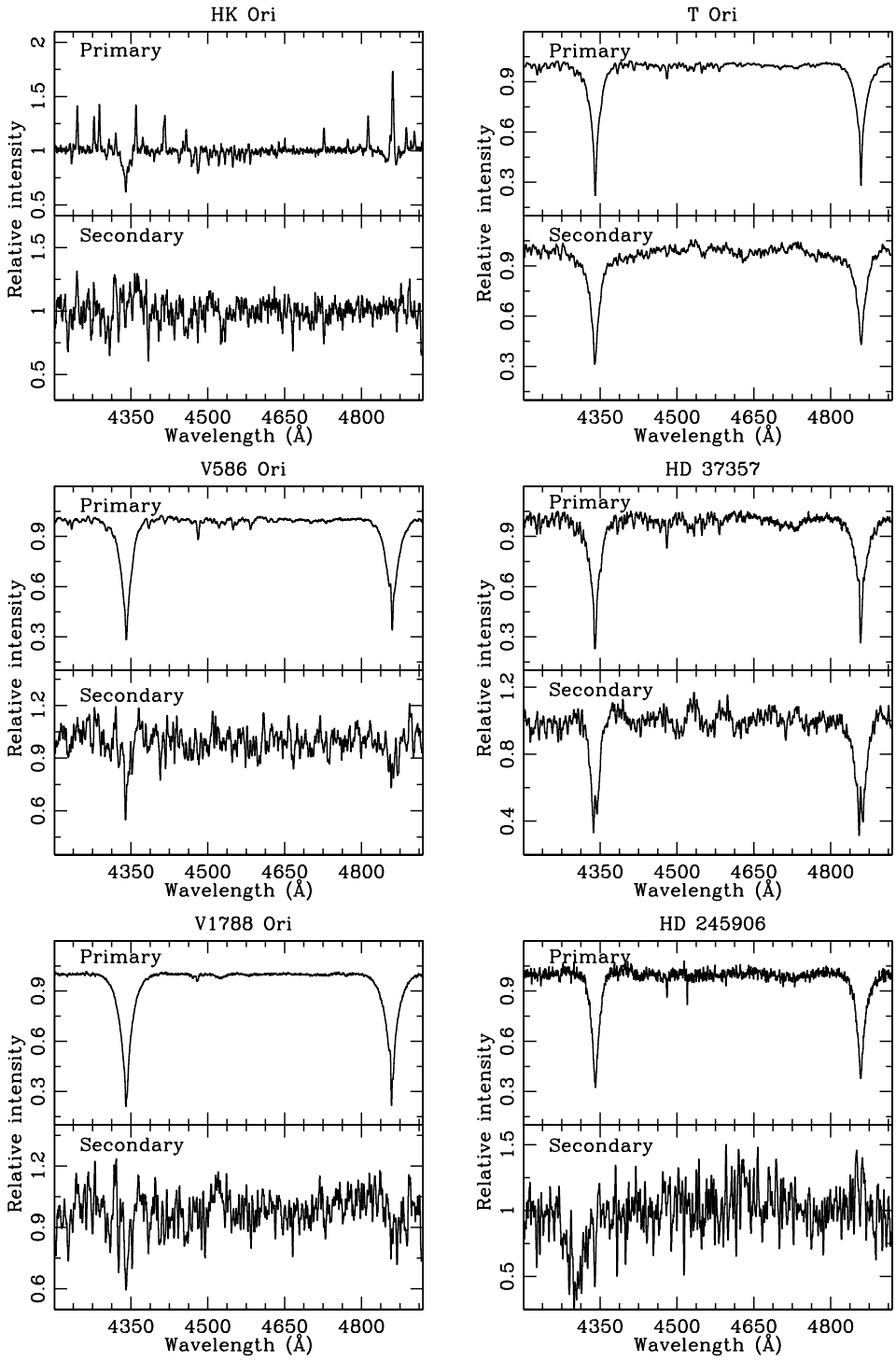

Figure 2.3: *The separated spectra in the B band. From top to bottom and left to right: HK Ori, T Ori, V586 Ori, HD 37357, V1788 Ori and HD 245906.*

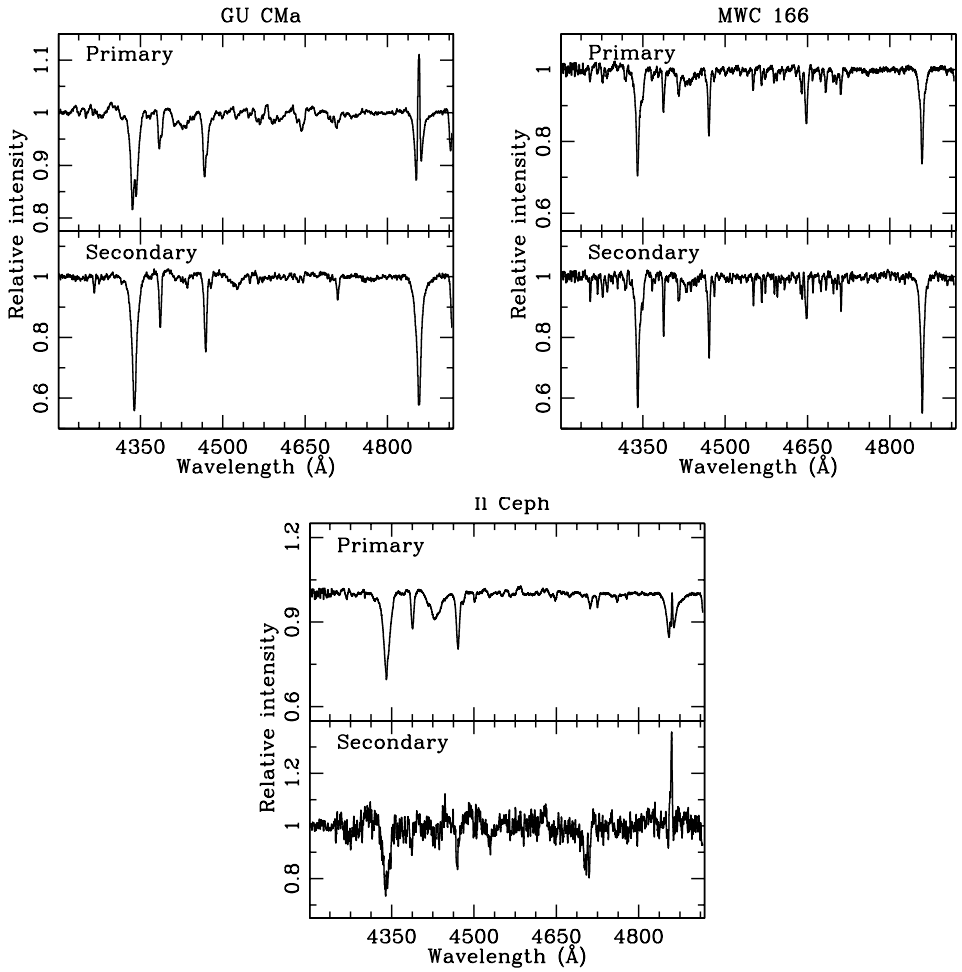

Figure 2.3 continued. Here the separated spectra of the GU CMa, MWC 166 and Il Ceph binary systems are presented.

2.4.2 Binary mass ratios

The binary mass ratio distribution observed is compared with that predicted assuming the secondary mass is drawn at random from the Initial Mass Function (IMF). For the determined mass of each primary a companion mass is randomly drawn from the IMF given by Kroupa (2001). To estimate the most probable companion mass this is done 10,000 times and the resultant average mass is then used to calculated the predicted mass ratio. Table 2.4 compares the observed and the predicted mass ratio. The predicted mass ratio distribution peaks at a relatively low values, and no systems are predicted to have a mass ratio greater than 0.1. In contrast, the observed mass ratio distribution is noticeably skewed towards higher values, see Fig. 2.4.

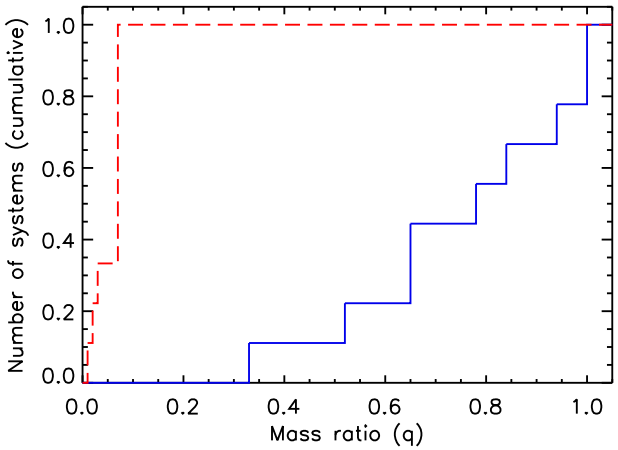

Figure 2.4: *The cumulative distribution of the observed binary mass ratio (solid line) and the mass ratio distribution predicted by random sampling of the IMF, from Kroupa (2001) (long dashed line).*

The difference between the two distributions is assessed using the one sample Kolmogorov Smirnov (KS) Test. According to the KS test the scenario that the secondary mass is randomly selected from the IMF may be rejected with more than 99.9999 per cent confidence. Thus it appears the mass ratio distribution of the binary systems is almost certainly not determined by random sampling from the IMF. Clearly, this finding only retains its statistical significance if all mass ratios are detected equally well. The sensitivity of spectroastrometry is limited by the relative brightness of binary components. If the primary component of a binary system is more than 5 magnitudes brighter than the secondary the system will probably not be detected by spectroastrometry. As a result the lowest detectable mass ratio is ~ 0.3, greater than the location of the peak of the mass ratio distribution predicted. Therefore, it is possible that a large number of low mass ratio systems are undetected, which would introduce a bias to the mass ratio observed, skewing the distribution to high values.

To quantify the effect this may have, the case in which this bias has the largest effect possible is considered. It is assumed every star that is a non detection *is* a binary system which is not detected due to a large difference in brightness between the two components. Then each fictional system is assigned a mass ratio determined by the IMF, which is

generally 0.1 and below the detection limits, and added to the sample. Using the KS test it is found that the hypothesis that the new 'observed' mass ratio originates from randomly sampling the secondary mass from the IMF may still be rejected with 99.55 per cent confidence. In this case the observed mass ratio distribution appears incompatible with the secondary mass being selected at random from the IMF at almost a 3σ level. Therefore, the result appears robust, despite the detection limit.

2.5 Discussion

2.5.1 On the large FWHM features unaccompanied by positional features

Many stars in the sample, such as AB Aur, present spectroastrometric signatures in which the FWHM features are much more prominent than any positional excursions. Baines et al. (2006) suggest that these features are due to wide binary systems, where wide refers to a separation greater than half the slit width. In the case of AB Aur, the data presented here exhibit a similar spectroastrometric signature over Hα to Baines et al. (2006). However, a 'wide' binary would be resolved in the data, as the data were obtained using a wide a slit ($\sim$5 arcsec). The longslit spectra were visually checked for evidence of a resolved companion and none was found. Therefore, as a resolved system does not create a spectroastrometric signature, there must be another, as yet unconsidered, source of the spectroastrometric signature. It is plausible that light from nebulosity could have distorted the spectroastrometric signatures. Extended emission is noticeable in many longslit spectra. However, it was found that masking the nebulosity had no effect on the spectroastrometric signature observed.

As an alternate explanation, the suggestion of Monnier et al. (2006) that some spectroastrometric features could be caused by the presence of dusty halos around HAe/Be stars is considered. Monnier et al. (2006) found that many HAe/Be stars, including AB Aur, are surround by extended features of up to 0.5 arcsec. These features contribute up to 20 per cent of the NIR flux detected. Such halos are not well studied, but could constitute light scattered from the remnant natal envelopes of such stars, dust entrained in a wind or localised thermal emission a few AU from the central star (Monnier et al.

2006). Such extended emission would be unresolved in a longslit spectrum, and could lead to an increase in the FWHM while not changing the photo-centre position. However, this requires that the line profile of the scattered light is different from the original emission source profile. As discussed by Monnier et al. (2006) this is certainly plausible. A non-uniform distribution of Hα flux and line of sight dependent absorption would both result in the observer and the scattering media seeing slightly different line profiles.

Here this scenario (i.e. whether an unresolved, extended halo could result in a spectroastrometric signature, similar to that observed over the Hα line in the case of AB Aur and other stars) is explored using a simple model. The model treats a single star as a point source and surrounds the star with a halo which contributes 20 per cent of the total flux. Here the halo is offset from the central star position by 0.0750 arcsec. The flux emanating from the halo has a uniform distribution in space. A P-Cygni type profile is assigned to the star and a similar line profile, minus the blue-shifted absorption component and with a slightly different line to continuum ratio, assigned to the halo flux. The total flux distribution is mapped onto an array representing a CCD chip. The array is then convolved with a Gaussian in the spatial direction to represent the effects of seeing. Finally, the output spectrum is extracted in a standard fashion and spectroastrometry is conducted on the artificial observation. The results of this exercise are presented in Figure 2.5.

There exists a qualitative similarity between the model and observed signatures (Fig. 2.5). The model did not completely recreate the extent of the FWHM feature observed in the case of AB Aur. However, given the unknowns involved, e.g. the amount of light scattered and the extent of the halo, this does not exclude this scenario. Therefore, it is concluded that it is likely that FWHM features accompanied by small or nonexistent positional signatures are due, at least in part to unresolved, extended, halos. Alternatively, a wind could also result in a similar positional spectroastrometric signature, see Azevedo et al. (2007). This has important implications on splitting the binary spectra, which are discussed in Section 2.5.2. It is noted that some known binary systems exhibited larger FWHM features than positional features, and as such, this is not a unique diagnostic.

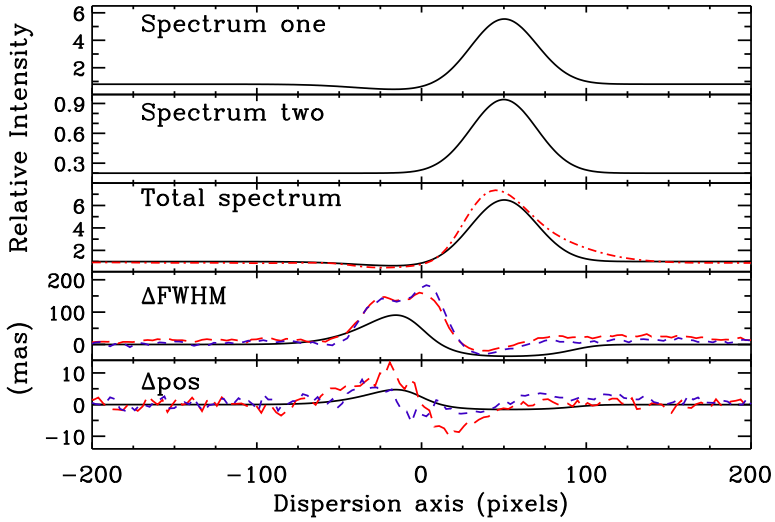

Figure 2.5: *The input spectra, the resultant spectrum and the spectroastrometric signature of the model comprising a star surrounded by a halo. The halo is modelled as a uniform ring from* 0.45 *arcsec to* 0.60 *arcsec, centred on a point* 0.075 *arcsec offset from the star. The seeing used was* 1 *arcsec and the halo contributes 20 per cent of the total flux. The long dashed lines are the spectroastrometric signature of AB Aur over the Hα line, in the North-South direction and the short dashed lines are the spectroastrometric signature of AB Aur in the East-West direction. The dot-dashed line is the averaged spectrum of AB Aur in the Hα region.*

2.5.2 An evaluation of the method of Porter et al. (2004)

Implicit in both methods of splitting spectra is the assumption that the system in question comprises of two point sources. In Section 2.5.1 it is demonstrated that dusty halos, which surround some HAe/Be stars (Leinert et al. 2001; Monnier et al. 2006), can give rise to spectroastrometric signatures. It may be expected that if the spectroastrometric signature of a binary system is contaminated by the signature of a halo, the spectra splitting method of Porter et al. (2004) will not be able to correctly separate the constituent spectra. In many situations the method of Porter et al. (2004) failed to fit the observed FWHM spectrum of a known binary system, even when the separation considered was increased to many times the binary separation. Here the possibility that

this could be due to contamination of the binary spectroastrometric signature by an additional, unresolved source of flux is explored.

A model of a binary system is constructed with a separation of 0.3 arcsec. The binary system has a difference in brightness of 3.5 magnitudes and is surrounded by a halo that extends from 0.4 arcsec to 0.6 arcsec from the central star. An artificial longslit spectra is generated and spectroastrometry is applied to the synthetic data to generate the observables necessary to separate the constituent spectra. Finally, the method of Porter et al. (2004) is used to attempt to split the unresolved binary spectrum into its constituent spectra.

The results of first modelling the aforementioned binary system without an extended halo component, and the results of including an extended halo component, are displayed in Fig. 2.6. When no halo component is added the two spectra are clearly separated, demonstrating the power of this approach. The method of Porter et al. (2004) fits the observed FWHM spectrum, and as a consequence splits the binary spectra correctly. In contrast, when the halo component is added to the binary model, the method of Porter et al. (2004) can no longer correctly separate the constituent spectra. The method of Porter et al. (2004) no longer fits the observed FWHM signature, as shown, and consequently fails to separate the two binary spectra correctly. This is only to be expected as: a) the positional and FWHM features observed are no longer due to two point sources and b) the method attempts to apportion the observed flux, which is due to three sources, to only two sources.

This would also be the case if the spectroastrometric signature observed were due to a triple system. The degree to which a third component would compromise the spectra splitting procedure would depend on the relative brightness of the system components. For example, the least bright component would have to be brighter than 1 per cent of the combined flux emanating from the two brightest components to contaminate the spectroastrometric signature. A triple system might be expected to exhibit distinctly different spectroastrometric signatures over different lines. The norm for this sample is for the spectroastrometric signatures over different lines to be consistent, as demonstrated by the example of GU CMa (Fig. 2.2). Therefore, if triple systems are present

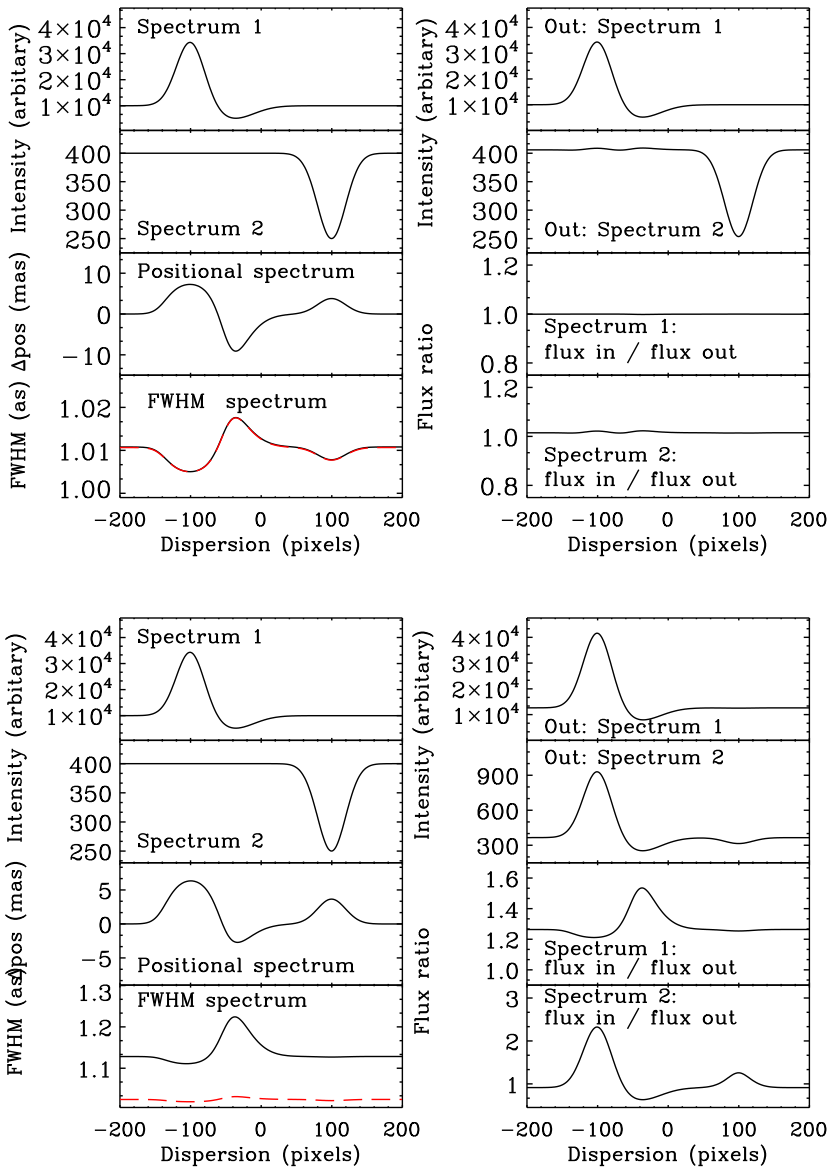

Figure 2.6: *The results of splitting the spectra of the model of a binary system (top two panels) and the model of the same binary system plus an unresolved halo which contributes 20 per cent of the system flux (lower two panels). In the panels presenting the observed σ distribution the solid line is the observed quantity while the dashed line is the best fit σ distribution predicted by the method of Porter et al. (2004).*

in the sample, it would appear that the tertiary components are not bright enough to significantly affect the spectroastrometric signatures observed.

In summary, the method of Porter et al. (2004) is compromised if an additional source of flux (such as an extended wind or halo of dusty material) is present. This might be expected from basic principles, but has not been discussed previously. It is suggested that this is the reason that, more times than not, the method of Porter et al. (2004) clearly does not fit the observed FWHM features and, as a consequence, fails to separate the spectra of many unresolved binary systems. If this is the case for the systems where the spectra splitting procedure is applied, the returned spectra will not be correctly separated. However, separated spectra are only presented for systems whose spectroastrometric signature appears solely due to a binary system, with none of the complications mentioned above (see Section 2.4.1 for the condition used to exclude contaminated signatures).

2.5.3 On the separation of HAe/Be binary systems

The previously detected systems in the sample have physical separations between ~ 40 and 1200 AU. Unfortunately, this cannot be easily translated into a separation distribution as the stars are at very different distances (between 143 and 2000 pc), and also due to the various selection effects in different detection methods. Of the newly discovered binaries the angular separation to which spectroastrometry is sensitive is in the range 0.1 – 2.0 arcsec. However, the different distances to each star change the physical separation to which this corresponds. For the nearest system at 143 pc, the separation range is 14 – 285 AU. For a system at the average distance of a star at 600 pc it is ∼60 – 1000 AU. For the most distant system at 2000 pc, it is 200 – 4000 AU.

None of the previously detected binaries are closer than 30 AU, which is the peak of the field G-dwarf distribution. Half of all G-dwarf binary systems have separations less than 30 AU (Duquennoy & Mayor 1991). Of the newly discovered binaries, only one *could* be closer than 30 AU (V1366 Cas at 164 pc), and two other systems could have separations as small as 30 – 40 AU. Therefore, at least 60 per cent of HAe/Be stars have a companion between about 30 – 4000 AU, and probably in the range 60 – 1000 AU. This is significantly greater than the fraction of G-dwarfs at the same

separations (around 40 per cent between 30 – 4000 AU, and 25 per cent between 60 – 1000 AU). This overabundance of binaries is not dissimilar to, but apparently larger than, the overabundance of binary systems found in young T Tauri stars (see Duchêne et al. (2007) and references therein).

Thus, unless there is an almost complete lack of companions < 30 AU, it is difficult to imagine that the binary fraction of HAe/Be stars is much less than 100 per cent. If HAe/Be stars exhibit a similar abundance of companions < 30 AU to G-dwarfs this would suggest that many HAe/Be stars are triple or higher-order systems. Indeed this chapter presents the detection of four additional components in previously detected binary systems, meaning that these systems are at least triple systems.

It is worth noting that many of these systems are relatively soft, with separations greater than a few hundred AU. As a result, these systems are susceptible to destruction in dense clusters (see Parker et al. (2009) and references therein). This suggests that many of these HAe/Be stars have not spent a significant time in a very dense environments, e.g. densities of $> 10^4$ $M_\odot$ pc^{-3}, which are not unusual in star forming regions of young clusters. Indeed, Testi et al. (1999) found that no Herbig Ae stars are associated with clustered environments, and that while Herbig Be stars are sometimes situated in a small cluster, the associated stellar densities are approximately $10^2 - 10^3 pc^{-3}$.

2.5.4 MWC 758

Recent high resolution observations of MWC 758 in the dust continuum indicate that the star is surrounded by a disk which is cleared of dust within the inner 70 AU (Andrea Isella, 2010, priv. comm.). This clearing of the inner disk might be due to the presence of giant planets, or to the presence of an undetected stellar companion orbiting between 30 and 60 AU (or 0.15 and 0.3 arcsec assuming the Hipparcos distance of $\sim$200 pc). To differentiate between these two possibilities, the limits on the mass of an undetected companion imposed by the spectroastrometric data are explored. This is done by comparing the spectroastrometric signatures of model binary systems to the spectroastrometric observations of MWC 758. To generate synthetic signatures for model binary systems with a range of separations and flux ratios it is assumed that the primary is responsible for the Hα flux and that the secondary component has a flat continuum.

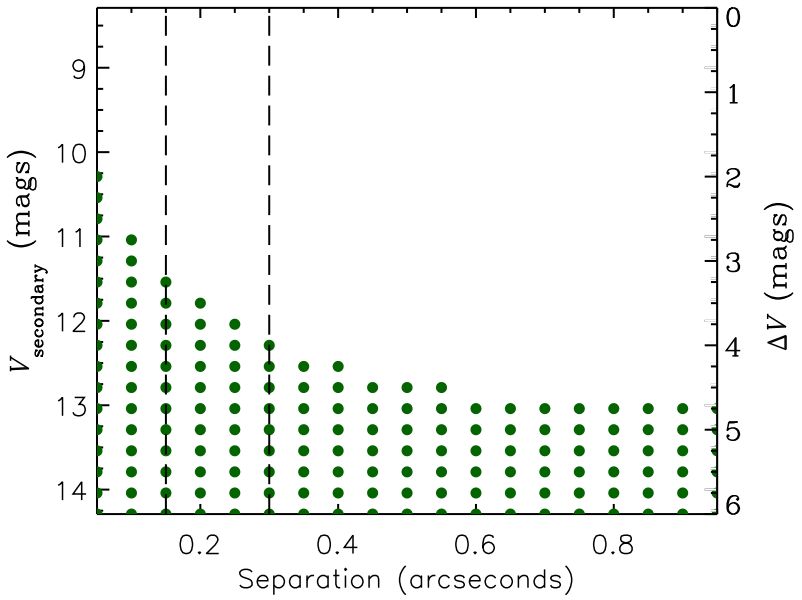

Figure 2.7: *Potential stellar companions to MWC 758 that are not excluded by the current data, assuming that the Hα flux emanates from the primary component and observed with 1.5 arcsec seeing.*

Limits on the $V-$band magnitude of the potential companion are presented in Figure 2.7. In the separation range 0.15–0.3 arcsec a binary companion more than 3.5–4 magnitudes fainter than the primary ($V-$band: 8.29) cannot be excluded with the current data. Using ZAMS models this translates to secondary companions with masses less than $\sim$0.9 $M_{\odot}$ being consistent with the data. Therefore, the spectroastrometric data cannot unambiguously differentiate between the two scenarios proposed to explain the observed disk clearing. Further, higher precision observations are required to improve the limits on the possible mass of the potential companion. This exercise highlights that the spectroastrometric non-detections generally do not exclude the presence of K and M type companions, and therefore the true binary fraction of the sample may be substantially higher than the figure presented here.

2.5.5 The mass ratio and formation mechanisms of HAe/Be binary systems

It appears that the mass ratio of Herbig Ae/Be binary systems is skewed towards relatively high values, and is inconsistent with random sampling from the IMF. However, as the spectra splitting technique did not work in every case, the sample size is too small to attempt to determine the underlying distribution of mass ratios. Instead, the possible implications this finding has on the formation mechanisms of intermediate mass stars are discussed.

Baines et al. (2006) found that the circumstellar discs of the components of Herbig Ae/Be systems are preferentially aligned with the binary position angle. This already suggests that the secondary formed by disc fragmentation (e.g. see Goodwin et al. 2007). As noted by Kouwenhoven et al. (2009), disc fragmentation would be expected to produce stars of roughly similar mass (within a factor of a few). Disc fragmentation should occur during the earliest phases of star formation. During such phases there is an abundance of gas to accrete, and the circumprimary disc is still massive enough to fragment. The secondary in the disc is able to accrete material from the disk more easily than the primary, as the angular momentum of the material is closer to the secondary than the primary (Whitworth et al. 1995; Bate & Bonnell 1997). Therefore, this scenario results in a binary system with a high mass ratio, higher than if random sampling from the IMF determined the mass of the secondary. Indeed, recent models of massive star formation demonstrate that binary systems with high mass ratios (0.7) and large separations ($\sim$ 1000 AU) can be formed from disk fragmentation (Krumholz et al. 2009).

The separations of the binary systems in the sample also suggest disc fragmentation as the mode of binary formation. Whitworth & Stamatellos (2006) show that a massive disc can fragment beyond a critical radius $R_{\rm frag}$ which depends on the mass of the primary $M_\star$ as follows:

$$R_{\rm frag} > 150 \left(\frac{M_\star}{\rm M_\odot} \right)^{1/3} \quad \rm AU$$

For a Herbig Ae/Be star $M_\star \sim 10 M_\odot$, and so $R_{\rm frag} > 300$ AU, which is a typical separation of the systems in our sample.

Therefore, the properties of the Herbig Ae/Be binary systems observed indicate that these systems formed via disk fragmentation. Given that the sample includes stars as massive as $\sim 15 M_{\odot}$, this is consistent with the core collapse and subsequent monolithic accretion scenario of massive star formation (see e.g. Krumholz et al. 2009).

If the high mass ratio of HAe/BE star binary systems is indeed a consequence of their formation mechanism, older binary systems with main-sequence B and A type components should also exhibit a high mass ratio. No spectroastrometric study of main-sequence binary systems is available for direct comparison. However, several results obtained using adaptive optics are consistent with this hypothesis. For example, it has been found that B and A type binary systems in Sco OB2 have a mass ratio inconsistent with random pairing of component masses and exhibit an excess of high mass ratios (Shatsky & Tokovinin 2002; Kouwenhoven et al. 2005). In addition, Söderhjelm (2007) finds an excess of high mass ratio systems amongst Hipparcos visual binaries of intermediate mass. Therefore, the properties of main-sequence binary systems with B and A type components are in general agreement with the findings of this chapter.

The Herbig Ae/Be stars in this sample are not located in dense clusters (Testi et al. 1999). In addition, the wide separations of the binary systems and their young ages suggest that they formed in isolation. Firstly, binaries this wide are relatively soft and could not have spent a significant amount of time in a dense cluster, see Parker et al. (2009). Secondly, no binary this wide could have survived ejection from a cluster. Together, this suggests that a fairly large core ($> 10 M_{\odot}$) formed in relative isolation and produced a massive binary system, rather than a small cluster. That these HAe/Be stars formed in a massive, isolated core shows that competitive accretion, e.g. Bonnell et al. (1998), is not required to form stars of up to at least $10 M_{\odot}$, as presumably no larger reservoir of gas existed beyond the single core.

This cannot be infrequent as several Herbig Ae/Be systems are found which fit this pattern. However, the sample that was used is not complete, the population of HAe/Be is heterogeneous to begin with and the selection criteria may well impose certain selection effects on membership of the HAe/Be class. Biases and incompleteness are impossible to fully quantify, but it can be stated that a not insignificant fraction of A/B stars can

form in isolation from a massive core. This is in qualitative agreement with de Wit et al. (2005), who report that perhaps even O type stars may form in isolation. In addition, Parker & Goodwin (2007) also find that a few per cent of massive stars might form in relative isolation.

2.6 Conclusions

This chapter presents spectroastrometric observations of a relatively large sample of HAe/Be stars. Here the salient findings of this work are presented:

- The data support a high binary fraction, 74 ± 6 percent, consistent with previous studies.
- Using spectroastrometry to separate the unresolved binary spectra the spectral types for the components of 9 systems are determined.
- The mass ratios of these systems, determined from the constituent spectral types, appear inconsistent with a secondary mass randomly selected from the IMF.
- Although the sample is small, this result constrains the mode of binary formation in that the mass ratios and separations of the binary systems observed suggest that the secondary forms via disk fragmentation.
- Since the observational definition of Herbig Ae/Be stars includes objects as massive as $\sim 15 M_{\odot}$ this result also suggests massive binary systems form via disk fragmentation. This is in agreement with recent simulations of massive star formation via disk accretion which feature binary formation via disk fragmentation. Therefore, this result indirectly suggests that massive stars do indeed form via disk accretion.
- The properties of the binary systems observed indicate that these systems have not spent a significant amount of time in dense, clustered environments. Therefore, these systems demonstrate that relatively isolated star formation can produce stars as massive as $\sim 10 - 15 M_{\odot}$.

Chapter 3

On the relative orientation of HAe/Be binary systems and circumstellar disks

3.1 Introduction

This chapter aims to decisively test the conclusion of the previous chapter, namely that HAe/Be star binary systems form via disk fragmentation. A key prediction of binary formation via disk fragmentation is that the binary orbit will be co-planar with the circumstellar disks around the binary components. Therefore, the relative orientations of orbital planes and circumstellar disks in HAe/Be systems binary systems may allow a critical test of the previous chapter's conclusion.

Consequently, the goal of the chapter is to compare the orientations of HAe/Be binary systems and circumstellar disks around the individual components. This was done by Baines et al. (2006) with a sample of six objects, with the result that random orientations could be rejected at the 98.2 per cent level, analogous to a 2.4σ effect. Therefore, it already appears an intrinsic alignment is preferred, consistent with the disk fragmentation scenario. However, there remains a non-negligible possibility that this result is purely due to chance. This is especially so since Baines et al. (2006) only considered binary position angles, which are not equivalent to the binary orbital planes (unless all 6 systems were viewed edge on). Thus, it has yet to be demonstrated that orbital planes and circumstellar disks of HAe/Be binary systems are aligned or

otherwise. Achieving this requires a larger sample and a model to include the effects of inclination. This chapter addresses both requirements.

Due to their small angular size and low contrast with the central star, observing disks around HAe/Be stars is challenging. As a result, very few disks have been directly imaged (although it is possible, see e.g Fukagawa et al. 2006). However, the position angles of such disks *can* be determined via spectropolarimetry (see e.g. Oudmaijer & Drew 1999; Vink et al. 2002, 2005a; Mottram et al. 2007b).

If a star is surrounded by a hot disk, free electrons in the disk can polarise the light of the central star. Emission line photons emanating from the disk do not pass through the polarising medium, unlike the continuum light. As a result emission lines can be depolarised with respect to the continuum. Therefore, a depolarisation signature over an emission line can be used to infer the presence of small-scale, otherwise undetected disks (Clarke & McLean 1974; Poeckert 1975; Poeckert & Marlborough 1976). The scattering medium that produces a spectropolarimetric signature must lie close to the central star, as the polarisation is due to electron scattering (Coyne & Kruszewski 1969). Therefore, spectro-polarimetric signatures are ideally suited to tracing disk-like structures very close to the central star. The behaviour of such a signal in QU space, where Q and U are the two Stokes linear polarisation vectors separated by 45°, allows the intrinsic polarisation angle to be determined. This is independent of uncertainties in the interstellar polarisation (e.g. Jensen et al. 2004). Furthermore, the polarisation angle is directly related to the orientation of the scattering medium (as illustrated by Quirrenbach et al. 1994, 1997). Therefore, spectropolarimetry offers one of the few opportunities to determine the position angles of small, unresolved, circumstellar disks. The benefit of this technique is that it is essentially distance independent and can be used to observe a large sample. A large sample is crucial to test whether or not circumstellar disk and binary position angles are related. Therefore, in this chapter spectropolarimetry is used to determine the position angles of circumstellar disks around binary HAe/Be stars. The disk position angles are then compared to binary position angles and a model in which circumstellar disks and binary orbital planes are co-planar.

However, before this is done, the hypothesis that all spectropolarimetric signatures of

HAe/Be stars are due to disks must be re-assessed. Recently, it has been proposed that the polarisation signatures of HAe/Be stars are not due to disks (Harrington & Kuhn 2007, 2009b,a), and thus cannot be used to determine disks position angles. Therefore, the first objective of this chapter is to assess whether or not spectropolarimetry can be used to determine the presence and orientation of small-scale disks.

This chapter is structured as follows: in section 3.2 an attempt is made to critically assess the origin of the spectropolarimetric signatures of HAe/Be stars, and in particular ascertain whether or not these signatures trace small-scale circumstellar disks. Then, a simple model is presented to determine the expected relationship between binary and disk position angle if the binary orbit and circumstellar disks lie in the same plane (Section 3.4). Spectropolarimetric observations of a sample of HAe/Be stars over the Hα line are then presented in Section 3.3. The data and model predictions are compared in Section 3.5 and the results are discussed in Section 3.6. Finally, this chapter is summarised in Section 3.7.

3.2 Testing whether or not spectropolarimetry traces small scale circumstellar disks

Following the success of using spectropolarimetry to the constrain the environments of classical Be stars, it was applied to study intermediate mass PMS stars (HAe/Be stars). In an effort to determine whether Herbig Be stars were surrounded by circumstellar disks, Oudmaijer & Drew (1999) used spectro-polarimetry to observe a sample of Herbig Be stars across the Hα line. The finding that approximately half the sample exhibited spectropolarimetric signatures was the first direct evidence that such stars posses circumstellar disks, a finding now confirmed with long baseline optical interferometry (e.g. Kraus et al. 2008b).

The work of Oudmaijer & Drew (1999) was extended by Vink et al. (2002, 2005a) and Mottram et al. (2007b), who demonstrated that Herbig Ae and Herbig Be stars exhibit different spectropolarimetric signatures. Assuming that the polarising medium is a circumstellar disk leads to the conclusion that this change in behaviour may trace the

transition from magnetospheric to disk accretion. However, Harrington & Kuhn (2007) report variable spectropolarimetric signatures in the absorption components of HAe/Be Hα emission profiles. Such signatures are inconsistent with the classical scattering and depolarisation scenario of McLean & Clarke (1979, which was extended by Vink *et al.* 2002 to incorporate intrinsic polarisation of photons from accretion shocks). Instead, Harrington & Kuhn (2007) suggest that an anisotropic radiation field results in optical pumping, and thus polarisation effects associated with absorption in a wind or envelope. Clearly, if this is the case for the majority of HAe/Be stars, spectropolarimetry cannot be used to trace the orientation of small-scale disks. Harrington & Kuhn (2009a) report that approximately two-thirds of HAe/Be stars exhibit spectropolarimetric features that are associated with absorption components of emission lines which are inconsistent with the disk scattering scenario. This would then suggest that spectropolarimetry cannot be used to trace circumstellar disks in the case of HAe/Be stars. Nonetheless, Vink et al. (2005a) found a correlation between spectropolarimetric angles and the position angle of directly imaged disks. However, this was not statistically significant due to a small sample. Therefore, there is a need for a clear assessment of the disk scattering scenario, and whether it applies to HAe/Be stars or not.

3.2.1 The control sample

Here spectropolarimetric observations of HAe/Be stars are compared to independent determinations of the orientation of disks around the stars in question in a bid to determine whether there is a correlation between spectropolarimetric and disk position angle. This was done by Vink et al. (2005a), but they were only able to do this for three objects, and thus their result was not conclusive. Additional spectropolarimetric observations, in conjunction with subsequently published imaging and radio, mm and optical interferometry almost triple the available sample.

Table 3.1 presents the sample of HAe/Be stars which have the required combination of spectropolarimetric observations over Hα and independent observations of their circumstellar disks. This table presents polarisation angles calculated from linear spectropolarimetric signatures over HI emission lines, disk position angles taken from the

literature, the width of the spectropolarimetric signature used to calculate the polarisation angle and the behaviour of the spectropolarimetric signature in the Stokes QU plane (e.g. linear excursions or loops). In addition, the table also states whether the spectropolarimetric signatures used to calculate the polarisation angle were consistent with the scenario of depolarisation or not (as opposed to intrinsic polarisation). These points are discussed in more detail shortly.

Table 3.1: *HAe/Be stars (Col. 1) for which spectropolarimetric observations* and *a direct measurement of the disk position angle are available. The spectral types (Col. 2) are taken from SIMBAD, unless stated otherwise. Cols 4, 5 & 6 present the various spectropolarimetric observations in the literature (all in °). Particularly uncertain angles are presented in brackets. Col. 7 designates whether an observed spectropolarimetric signature is consistent with a depolarisation signature (see Vink et al. 2002). Cols 8 and 9 list the fractional width of the polarisation signature and its QU morphology.*

Object	Type	Disk PA (°)	Pol PA (1) Vink et al. (2005a)	Pol PA (2) Mottram et al. (2007b)	Pol PA (3) Patel et al. (2006)	Depol	$\frac{\Delta\lambda(\mathrm{pol})}{\Delta\lambda(\mathrm{I})}$	*QU*
HD 200775	B2	$6.9\pm1.5^{\mathrm{A}}$	(90)	3 ± 2		yes	1.13	Exc
MWC 147	B6	80^{B}		168 ± 4		no	0.50	Exc
HD 45677	$\mathrm{B2^C}$	$77\pm13^{\mathrm{D}}$	(~ 70)		164 ± 3	poss	$\sim$1.0	Exc?
BD +40 4124	B3	$110^{+3\,\mathrm{E}}_{-4}$	83	36 ± 3		yes	0.75	Exc
MWC 1080	B0	$55^{+12\,\mathrm{E}}_{-45}$		165 ± 4		yes	1.11	Smear
CQ Tau	$\mathrm{A8^Z}$	$120\pm10^{\mathrm{F}}$	20			no	0.17	Loop
MWC 480	A3	$150^{+16\,\mathrm{E}}_{-13}$	55			no	0.67	Loop
AB Aur	A0	$79^{+2\,\mathrm{G}}_{-3}$	160			no	1.00	Loop+Exc

A: Okamoto et al. (2009), B: Kraus et al. (2008b), C: Cidale et al. (2001), D Monnier et al. (2006), E: Eisner et al. (2004), F: Doucet et al. (2006)

G: Mannings & Sargent (1997), Z: Herbig & Bell (1988).

The multiple spectropolarimetric datasets presented in Table 3.1 contain several contradictions, namely: HD 200775, BD +40 4124 and HD 45677. Before the sample is utilised to investigate the origin of the spectropolarimetric signatures, the datasets must be reconciled. In the case of HD 45677, the difference between the values reported by Vink et al. (2005a) and Patel et al. (2006) may well be explained by large uncertainties in the data of Vink et al. (2005a), as they only present an approximate value. The difference between the values of Vink et al. (2005a) and Mottram et al. (2007b) for the polarisation angle of BD +40 4124 may be explained by systematic uncertainties in the data of Vink et al. (2005a, priv. comm. J. Vink, 2009).

In the case of HD 200775, the data of Vink et al. (2005a) and Mottram et al. (2007b) are consistent when viewed in the QU plane. The 90° difference between the two values is analogous to a 180° rotation in space; the vector used to calculate the angle is essentially correct, but it has the wrong direction. This is illustrated in Figure 3.1, which demonstrates that changing the direction of a vector in QU space changes the resultant angle by 90°. Therefore, the direction (in QU space) of the vector used to calculate the spectropolarimetric angle is of key importance. If the signature is due to depolarisation, the polarisation vector should be measured from the line to the continuum, whereas for intrinsic polarisation the reverse is true. It is evident that Mottram et al. (2007b) measured the polarisation vector from the continuum to the line, which is not appropriate in the case of HD 200775 as its signature is consistent with depolarisation. Reversing the direction of the vector in QU space rotates the polarisation angle by 90°, thus removing the discrepancy between the data of Vink et al. (2005a) and Mottram et al. (2007b).

While the prominent discrepancies between the multiple datasets are now resolved, doing so has highlighted that different authors may inadvertently calculate spectropolarimetric position angles using the wrong QU vector. To ensure consistency in the data-set it is imperative that all the position angles are calculated in the same way. To check that is the case, the QU data associated with the angles presented in Table 3.1 were used to determine approximate position angles. If these differed by more than 90° with the values presented in Table 3.1, the literature values were rotated by 90°. Besides

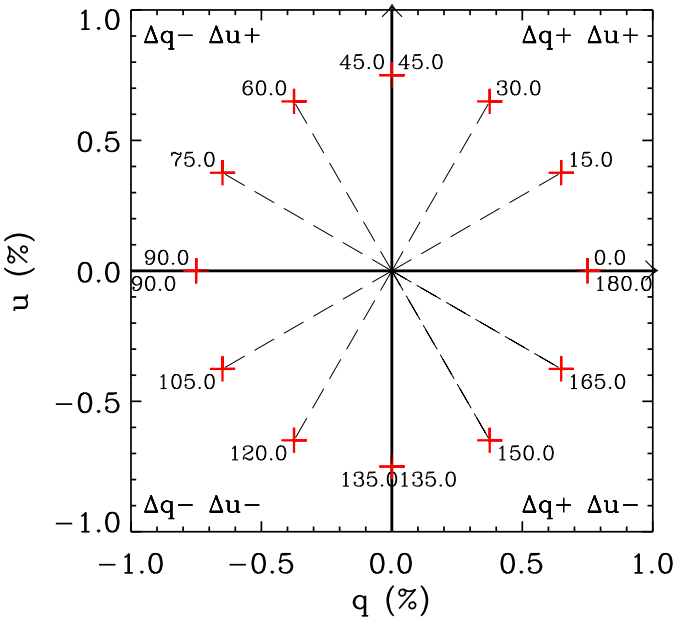

Figure 3.1: *The axes of the QU diagram. Note that the axes of the plots q and u represent the normalised Stokes parameters Q/I and U/I. Polarisation angles are calculated using* $\theta = \frac{1}{2}\text{atan}(\frac{u}{q})$. *However, this contains a degeneracy, for example:* $\frac{1}{2}\text{atan}(\frac{0.5}{0.5})$ *is the same as* $\frac{1}{2}\text{atan}(\frac{-0.5}{-0.5})$, *i.e.* 22.5°. *The signs of the arguments,* ΔQ *and* ΔU *are used to break this degeneracy, as shown in the diagram. Thus it can be show in the first example* 22.5° *is the correct result, while in the second example the angle is really* $22.5 + 90 = 112.5°$. *Therefore, the direction in which* ΔQ *and* ΔU *are measured determines the resulting position angle. Here, the QU vector is calculated from the origin to the red crosses. Reversing the vector (i.e. from the crosses to the origin) would flip the position angle by* 90°.

Table 3.2: *The same as Table 3.1 but with changes in polarisation angle taken into account to resolve discrepancies between multiple datasets. Where multiple observations were available the value with the smallest uncertainty was selected.*

Object	Type	Disk PA (°)	Pol PA (°)	Depol	$\frac{\Delta\lambda(\mathrm{pol})}{\Delta\lambda(\mathrm{I})}$	*QU*
HD 200775	B2	$6.9\pm1.5^{\mathrm{A}}$	$93 \pm 2^{\mathrm{B}}$	yes	1.13	Exc
MWC 147	B6	80^{C}	$168 \pm 4^{\mathrm{B}}$	no	0.50	Exc
HD 45677	$\mathrm{B2}^{\mathrm{D}}$	$77\pm13^{\mathrm{E}}$	$164 \pm 3^{\mathrm{F}}$	poss	∼1.0	Exc?
BD +40 4124	B3	$110^{+3\,\mathrm{G}}_{-4}$	$36 \pm 3^{\mathrm{B}}$	yes	0.75	Exc
MWC 1080	B0	$55^{+12\,\mathrm{G}}_{-45}$	$75 \pm 4^{\mathrm{B}}$	yes	1.11	Smear
CQ Tau	$\mathrm{A8}^{\mathrm{Z}}$	$120\pm10^{\mathrm{H}}$	20^{I}	no	0.17	Loop
MWC 480	A3	$150^{+16\,\mathrm{G}}_{-13}$	55^{I}	no	0.67	Loop
AB Aur	A0	$79^{+2\,\mathrm{J}}_{-3}$	160^{I}	no	1.00	Loop+Exc

A: Okamoto et al. (2009), B: Mottram et al. (2007b), C: Kraus et al. (2008b), D: Cidale et al. (2001), E Monnier et al. (2006), F: Patel et al. (2006), G: Eisner et al. (2004), H: Doucet et al. (2006), I: Vink et al. (2005a), I: Mannings & Sargent (1997), Z: Herbig & Bell (1988).

HD 200775 the polarisation angle of MWC 1080 reported by Mottram et al. (2007b) also has to be rotated by 90°. The final sample is presented in Table 3.2.

3.2.2 Statistical tests

Using the sample presented in Table 3.2 the following hypotheses are evaluated.

1) The intrinsic polarisation angle is parallel to the position angle of the circumstellar disk.

2) The intrinsic polarisation angle is perpendicular to the disk position angle.

3) The intrinsic polarisation angle and the disk angle are randomly orientated.

To compare the data to the three scenarios uncertainties in the measurements must be considered. At most the error in the difference between the polarisation and disk position angles will be ∼ 20° (due to an uncertainty in disk PA of ∼15° and an uncertainty

in polarisation angle of $\sim 5^{\circ}$). To allow for this the following procedure is employed. An equally sized sample is constructed with a difference between disk and polarisation angle given by the hypothesis in question. Then, a random error, with a maximum size of 20° is added to each value. 1000 such samples are made, and the resulting distributions in the difference between the two angles are averaged. The data are then compared to this averaged distribution using the Kolmogorov-Smirnov (KS) test. Adding uncertainty does not affect the random distribution as the noise averages out, whereas it smooths the two preferentially aligned distributions, which are otherwise step functions.

Figure 3.2 presents a comparison of the data presented in Table 3.2 and the 3 hypotheses described above. Hypothesis 1 can be summarily rejected with a confidence of approximately five sigma. Hypothesis 3 can be discounted at a significant level (3 sigma). This leaves hypothesis 2, which cannot be rejected at greater than a one sigma level, and is thus consistent with the data. This would seem to indicate that the spectropolarimetric data presented in Table 3.2 is entirely consistent with the polarisation being due to the conventional disk scattering scenario; unless the optical pumping is directly related to the position angle of the disk. Since Harrington & Kuhn (2009a) claim half the sample have polarisation signatures associated with the absorption component of the emission line profile, this may well be the case.

Since a randomly orientation of disk and spectropolarimetric angles can be discarded, it would appear that spectropolarimetry can indeed be used to trace the position angles of small-scale disks. However, it is important to note that the sample size is relatively small. Therefore, if any of the spectropolarimetric signatures in the sample are not related to disks, a chance alignment between the imaged disks and observed polarisation angles in these cases could significantly bias the statistics. To investigate this possibility, certain selection criteria are imposed on the sample, in an attempt to remove contaminant signatures and assess the resultant change in statistics.

Examination of Table 3.1 reveals that the spectropolarimetric signatures in the sample essentially have no defining characteristic. The spectral types of the objects range from B0 to A8. Therefore, if the scenario of Vink et al. (2002) and Mottram et al. (2007b) is correct, the spectropolarimetric signatures in the sample are due to both

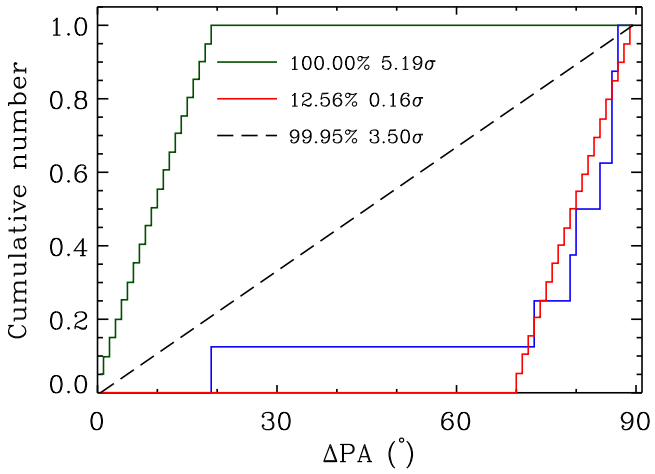

Figure 3.2: *A comparison of the cumulative distributions in disk and polarisation position angle of the sample presented in Table 3.2 (blue) and based on the three hypotheses: 1) the polarisation angle is parallel to the disk angle (green), 2) the polarisation angle is perpendicular to the disk angle (red) and 3) the position angles of disks and spectropolarimetric signatures are randomly orientated (dashed black).*

depolarisation and intrinsic polarisation. The *QU* morphologies of the data used range from linear excursions to loops, consistent with the view that the signatures are due to both depolarisation and intrinsic polarisation (Vink et al. 2002). The one feature that the data have in common is the relative width of the spectropolarimetric signature compared to the line profile $\left(\frac{\Delta\lambda(\mathrm{pol})}{\Delta\lambda(\mathrm{I})}\right)$. All but one of the signatures in the sample has a fractional width greater than 0.5. In general, depolarisation signatures have a width comparable to the emission line profile. Intrinsic polarisation of photons originating interior to a compact disk can result in a signature that is narrower than the emission line profile as the polarised photons may be emitted with a restricted range of velocities. However, since the polarisation signature is related to the emission component of the line, it might be naively expected that the polarisation signature is of a comparable width to the emission line. On the other hand, Harrington & Kuhn (2009a) present several very narrow features, only associated with absorption features. These are clearly difficult to explain using the disk scattering scenario. Therefore, it is suggested that, to the first order, the relative width of a spectropolarimetric signature may be used to as-

sess whether it is consistent with the disk scattering scenario. In general, the signatures presented in Table 3.1 are of a comparable width to the emission lines, which suggests that these signatures are due to scattering in a circumstellar disk and therefore, that these signatures should be aligned with the position angles of the disks, which appears to be the case.

One object in the sample, CQ Tau, has a narrow spectropolarimetric signature ($\frac{\Delta\lambda(\mathrm{pol})}{\Delta\lambda(\mathrm{I})}$=0.17). Furthermore, the polarisation signature is not associated with the emission components of this objects line profile, which is difficult to reconcile with the scenario of disk scattering. Therefore, this signature may be due to the optical pumping scenario proposed by Kuhn et al. (2007). Due to the possibility that the signature of this object is not due to scattering in a disk, and may trace the angle of the circumstellar disk by chance, the object is discarded from the sample in case it biases the statistics. Figure 3.3 presents the comparison of the resultant sample and the 3 hypotheses. The conclusions are unchanged. Hypothesis 1 can still be rejected with a high confidence (nearly five sigma), and hypothesis 3 can be discounted at a significant level (over three sigma level). As before, only hypothesis 2 cannot be rejected at greater than a one sigma level, and is thus consistent with the data. Therefore, the correlation between disk and spectropolarimetric angle is demonstrated to be robust over the range of spectropolarimetric signature widths in the sample.

However, the relative width does not necessarily identify signatures that are inconsistent with the disk polarisation scenario. For example, while the signatures of AB Aur and MWC 480 are relatively wide ($\frac{\Delta\lambda(\mathrm{pol})}{\Delta\lambda(\mathrm{I})}$ of 0.67 & 1.00), Harrington & Kuhn (2007) point out that the polarisation signature of these objects occurs in the P-Cygni absorption component of the line profile. A polarisation signature associated with absorption in outflowing gas is contrary to the scenario in which the polarisation signatures are due to scattering in a circumstellar disk. Therefore, it is possible the alignment of these signatures with the imaged disks is due to chance, biasing the statistics. To remove this possibility these two objects are discarded from the sample. The new sample is then compared to the three hypotheses described previously (see Figure 3.4). Due to the reduction in the sample size the statistics change slightly. However, hypothesis 1 can still

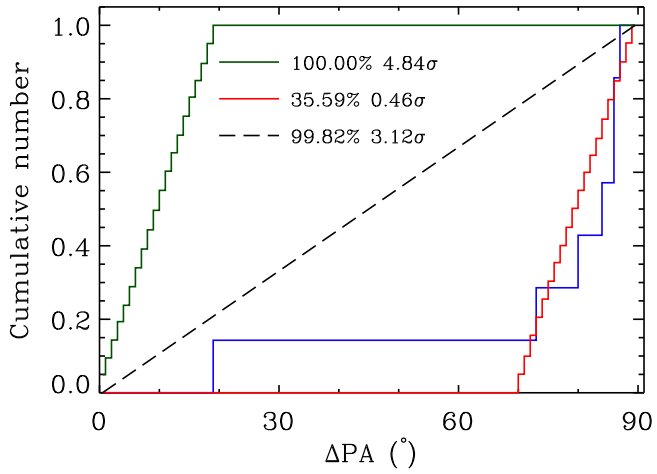

Figure 3.3: *The same as Figure 3.2, but now neglecting the CQ Tau data.*

be rejected with a high degree of confidence (99.99 per cent or greater than four sigma certainty). Hypothesis 2 is still consistent with the data and cannot be discarded with a confidence greater than one sigma. Hypothesis 3 still provides a relatively poor fit to the data, although it cannot quite be rejected with a significant confidence (only 99.3 per cent or 2.7 sigma). Nonetheless, discarding the AB Aur and MWC 480 does little to qualitatively change the statistics. Therefore, it appears that the early conclusion is relatively robust and unlikely to be due to chance alignment of disk and polarisation angles (at a minimum of 99.3 per cent confidence).

3.2.3 Disk optical depth

It is noted there is only one object in the sample with an offset between disk and polarisation angle that is not consistent with the hypothesis that these two angles should be orthogonal. In fact, this offset (that of MWC 1080) is essentially consistent with the two angles being aligned (within the assumed error of 20°). In a similar fashion, Vink et al. (2005a) report that the majority of the T Tauri stars they observed with previously determined disk position angles also exhibit an alignment between polarimetric and disk position angles. The hypothesis advanced by Vink et al. (2005a) is that while the spectropolarimetric signatures of all YSOs are due small-scale circumstellar disks, the

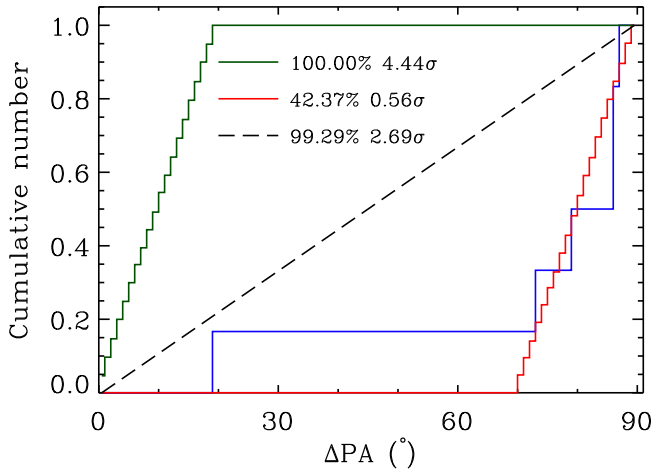

Figure 3.4: *The same as Figures 3.2 and 3.3, but using the further reduced sample (i.e. without MWC 480 and AB Aur).*

position angle of the resulting polarisation vector is dependent upon the properties of the inner disk. If the inner disk is optically thin the polarisation vector is perpendicular to the disk position angle. Conversely, if the inner disk is optically thick, the polarisation vector is parallel to the disk position angle. The optically thin scenario provides a better fit to the data presented in Table 3.1 than the optically thick scenario. However, a more appropriate hypothesis to compare to the data may be that polarisation angles are directly related to the position angles of disks, but that the relationship between the two angles is dependent upon whether the disks are optically thick or thin. The difficulty in assessing this hypothesis is determining whether a disk is optically thick or optically thin.

To reiterate, the difference between the disk and spectropolarimetric angle is either 0 or 90° depending upon the optical depth of the inner disk. Consequently, it can be expected that the offset from 45° to the difference between disk and spectropolarimetric angle (henceforth $\Delta\Psi$) is always 45°. Here this hypothesis is tested using the sample presented in Table 3.2. The disk and spectropolarimetric angles in Table 3.2 are used to calculate $\Delta\Psi$. This is then compared to the hypothesis that $\Delta\Psi$ is 45° by calculating the average of 1000 equally sized samples in which the $\Delta\Psi$ is 45° with an additional

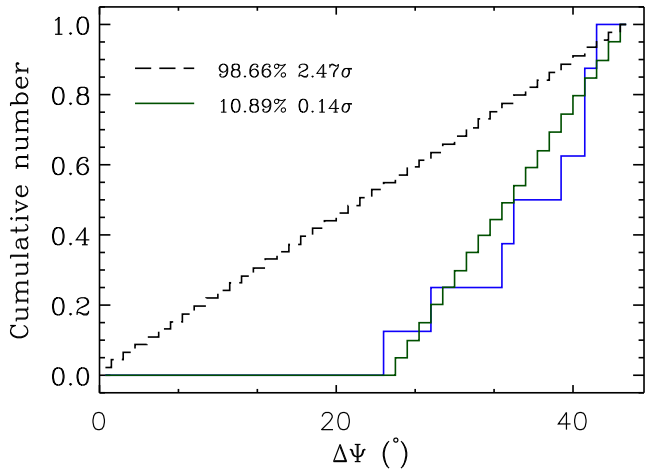

Figure 3.5: *The distribution in difference in spectropolarimetrically predicted disk position angle and observed disk position angle for the sample presented in Table 3.2 (blue) compared to a distribution where the two angles are the same and disks may be either optically thick or thin (green) and a random distribution of angle differences (black dashed).*

random error contribution (see Figure 3.5).

Clearly the data are entirely consistent with the new hypothesis. However, the scenario of random alignment cannot be discarded at with more than 95 per cent confidence. This is because the change in the x axis (0–90° to 0–45°) reduces the difference between the two scenarios. As a result, allowing for optical depth effect in this fashion makes it more difficult to exclude a random orientation of disk and polarimetric angles. Therefore, allowing for different optical depths does not improve the statistics. Since the initial hypothesis of optically thin disks was shown to be consistent with the data it will be assumed that all disks are optically thin. However, it is noted that this is not necessarily true for all disks, and if the sample includes optically thick disks any intrinsic agreement between the model and the data will be decreased.

3.2.4 Interim summary

Searching the literature for HAe/Be stars with complimentary spectropolarimetric observations over Hα and independent determinations of the orientations of disks around them resulted in a sample of eight objects. These objects are used to assess the relationship between polarisation and disk angle. The full sample unambiguously favours the scenario in which the spectropolarimetric angles are orientated perpendicularly to the disk position angle, indicating that the polarisation originates in small-scale, circumstellar disks. This is shown to be relatively robust by discarding several of the objects in the sample as their spectropolarimetric signatures may not be due to disks. Allowing for contaminant objects, random alignment between disk and polarisation angles is consistent with the data at a low confidence level. However, this scenario can be rejected with a minimum confidence level of 99.3 per cent. Therefore, it would appear the spectropolarimetric signatures in the sample do trace circumstellar disks.

It is noted that all but one of the current sample have polarisation and disk angles that are within 10–20° of perpendicular, while for one object the two angles are within 20° of being aligned. It is suggested that this object may have an optically thick disk which would result in a spectropolarimetric signature aligned along the disk position angle. It is noted that regardless of the disk optical thickness the offset between the difference between disk and spectropolarimetric angle and the angle 45° is always 45°. This hypothesis is shown to be entirely consistent with the data, although its use in differentiating between various scenarios is hampered by a compression of the data in the x-direction, which acts to reduce the difference between various distributions.

Admittedly, the statistics are limited by the small sample. However, in all but one case a random alignment between polarisation and disk position angle can be discarded with more than 99 per cent confidence. Even when using the smallest sample, the scenario in which the polarisation angles are preferentially aligned perpendicularly to disks is notably preferred over a random orientation of the two angles. Therefore, it appears that the polarisation signatures of HAe/Be stars are intrinsically linked to their circumstellar disks. Consequently, these signatures can be used to determine the position angle of unresolved disks around such stars.

3.3 Observations

The aim of this chapter is to compare HAe/Be disk and binary position angles. Observations of binary systems are relatively straightforward, and as a result outweigh spectropolarimetric and other observations capable of determining disk orientation (see e.g. Leinert et al. 1997; Bouvier & Corporon 2001; Baines et al. 2006; Thomas et al. 2007, Chapter 2). The most promising technique to deliver a sample of disk position angles is spectropolarimetry – as several objects can be observed in one night of observing. However, only a handful of HAe/Be stars have been observed with spectropolarimetry (e.g.$\sim$20; Vink et al. 2005a). To increase the potential sample, additional spectropolarimetric observations were conducted and are presented here.

Specifically, the data presented in this chapter consist of linear spectropolarimetric observations of HAe/Be stars conducted in the R band, centred on Hα. In the following, the observing procedure and data reduction steps are described before the results are added to the sample drawn from the literature and used to assess the relative orientation of HAe/Be binary orbits and circumstellar disks (Section 3.5).

3.3.1 Sample selection

The sample was predominately chosen from the catalogue of Thé et al. (1994), with the criteria that targets were reasonably bright ($V \leq$ 12-13), as spectropolarimetry requires high signal to noise ratio (SNR) data. Most of the targets were binary Herbig Ae/Be stars that had not been observed with spectropolarimetry previously (and these were primarily drawn from Baines et al. 2006; Thomas et al. 2007, see also Chapter 2). Several objects with existing spectropolarimetric data were observed to provide a consistency check on the data.

3.3.2 Observations

The linear spectropolarimetric data were obtained using the William Herschel Telescope (WHT) from 08-11-2008 to 10-11-2008. Clouds were present for the majority of the three nights, preventing observation for much, but not all, of the time. The seeing was typically fair ($\sim$1$''$), although on occasions it became relatively poor (2–2.5$''$). The observations

were conducted with the ISIS spectrograph, equipped with polarising optics comprising of a calcite block and a rotating half-wave plate. The R1200R grating was used and the central wavelength was set to 6560 Å. This resulted in a spectral range of approximately 1000 Å. Several slit widths were used, ranging from 1 to 5 arcsec, and the minimum spectral resolution was found to be ∼4250, or 70 $\mathrm{km\,s^{-1}}$.

The calcite block separated the incident light into two perpendicular rays: the ordinary (O) and the extraordinary (E) rays. Each observation comprised of both the O and the E ray spectrum of the science target, and a corresponding set of sky spectra. The polarisation at position angles (PA) of 0°, 22.5°, 45° & 67.5° was measured by rotating the half-wave plate. Multiple polarisation standard stars were observed to characterise the instrumental polarisation and calibrate the polarisation angle. A log of the observations is presented in Table 3.3.

Table 3.3: *The log of observations.*

Object	RA (J2000)	Dec (J2000)	Spec. Type	V (mags)	Exp. Time (minutes)	Slit ($''$)	Seeing ($''$)	Date
Science targets								
HD 179218	19 11 11.3	+15 47 15.6	A0IVe	7.2	60.0	1.5	1.2	08-11-2008
HD 203024[†]	21 16 3.0	+68 54 52.1	A	8.9	80.0	1.8	1.1	08-11-2008
Il Cep	22 53 15.6	+62 08 45.0	B2IV-Vne	9.3	86.7	1.5	1.3	08-11-2008
MWC 758	05 30 27.5	+25 19 57.1	A5IVe	8.3	60.0	1.5	1.0	08-11-2008
HK Ori	05 31 28.1	+12 09 10.2	A4pev	11.7	133.3	1.5	1.5	08-11-2008
GU CMa	07 01 49.5	−11 18 3.3	B2Vne	6.6	15.3	1.5	1.3	08-11-2008
HBC 310	21 52 34.1	+47 13 43.6	B9.5Ve	10.2	110.0	1.5	1.0	09-11-2008
MWC 1080	23 17 25.6	+60 50 43.6	B0eq	11.6	96.7	1.5	1.0	09-11-2008
V586 Ori	05 36 59.2	−06 09 16.4	A2V	9.8	146.7	1.5	0.9	09-11-2008
BF Ori	05 37 13.3	−06 35 0.6	A5II-IIIev	10.3	133.3	1.5	0.8	09-11-2008
MWC 147	06 33 5.2	+10 19 20.0	B6pe	8.8	53.4	1.5	0.9	09-11-2008
XY Per	03 49 36.3	+38 58 55.5	A2IIv	9.4	120.0	1.2	0.7	10-11-2008
V350 Ori	05 40 11.8	−09 42 11.1	A1	11.5	120.0	1.5	0.6	10-11-2008
R Mon[‡]	06 39 9.9	+08 44 9.7	B0	10.4	66.7	1.5	2.4	10-11-2008
Standards								
HD 204827	21 28 57.8	+58 44 23.2	O9.5V	8.0	20.0	1.0	0.6	08-11-2008
BD +28 4211	21 51 11.0	+28 51 50.4	Op	10.5	49.3	2.2	0.8	08-11-2008
β Cas	00 09 10.7	+59 08 59.2	F2IV	2.3	2.2	4.0	1.0	08-11-2008
BD +59 389	02 02 42.1	+60 15 26.5	F0Ib	9.1	13.3	1.5	0.9	08-11-2008

Continued on next page

Table 3.3 – continued from previous page

Object	RA (J2000)	Dec (J2000)	Spec. Type	V (mags)	Exp. Time (minutes)	Slit ($''$)	Seeing ($''$)	Date
HD 204827	21 28 57.8	+58 44 23.2	O9.5V	8.0	8.0	3.3	1.9	09-11-2008
β Cas	00 09 10.7	+59 08 59.2	F2IV	2.3	0.4	1.5	0.8	09-11-2008

†: This object has Hα in absorption and is therefore discarded from the sample.

‡: This object exhibits significantly stronger polarisation than the other objects in the sample ($\sim$15 c.f. $\sim$1 per cent).

Therefore, this object is discarded from the sample as this may indicate that the polarisation is not only due to a circumstellar disk.

3.3.3 Data reduction

Data reduction was conducted using the Image Reduction and Analysis Facility (IRAF)[(a)], in conjunction with routines written in Interactive Data Language (IDL). The data reduction process for each observation consisted of trimming, bias subtraction, flat-field division and cosmic-ray removal. Following the above, the target O and E rays, and those of the sky if they were present, were extracted from each frame. Wavelength calibration was performed using CuNe and CuAr arc spectra, which were obtained periodically during the observing run.

Once the O and E rays had been extracted the Stokes parameters for each data set were calculated using a routine written in IDL. The method used is that outlined in the ISIS polarisation manual by Jaap Tinbergen and René Rutten[(b)]. For each set of polarisation data, i.e. data obtained with the half-wave plate at 0° and 45° or 22.5° and 67.5°, the ratio of the O and E rays in each image is calculated. To obtain the degree of polarisation the data obtained at a given PA are averaged, then the following equations are used:

$$R^2 = \frac{I_{\mathrm{O},0^\circ}/I_{\mathrm{E},0^\circ}}{I_{\mathrm{O},45^\circ}/I_{\mathrm{E},45^\circ}} \tag{3.1}$$

$$P_{\mathrm{Q}} = \frac{R-1}{R+1} \tag{3.2}$$

Note that in the above it is assumed the data in question was obtained at 0° and 45°. $P_{\mathrm{Q}} = Q/I$, where I is the total flux input. $I_{\mathrm{O,ang}}$ and $I_{\mathrm{E,ang}}$ are the fluxes of the O and E rays at various half-wave plate position angles.

This procedure is repeated for the other set of polarisation data, i.e. data obtained with half-wave-plate position angles of 22.5° and 67.5°, to calculate P_{U}. To calculate the total polarisation and the polarisation angle the data are combined using the following equations:

$$P = \sqrt{P_{\mathrm{Q}}^2 + P_{\mathrm{U}}^2} \tag{3.3}$$

[(a)] http://iraf.noao.edu/, see Tody (1993)

[(b)] http://www.ing.iac.es/Astronomy/observing/manuals/html_manuals/wht_instr/isispol/isispol.html

$$\theta = \frac{1}{2}\tan^{-1}(\frac{P_{\rm U}}{P_{\rm Q}}) \tag{3.4}$$

where P represents the total polarisation, and θ is the polarisation angle.

The objects observed included several polarisation and zero polarisation standards. These were observed so that the instrumental polarisation and PA could be established. In principle the precision of the data is governed by photon statistics. However, from the standard observations it is evident that the quality of the data is limited by systematic effects. From these data it is found that the typical absolute uncertainty is of the order 0.1 per cent, or greater.

Instrumental and interstellar polarisation are not corrected for, as such corrections are typically subject to significant uncertainties (Jensen et al. 2004). In addition, contaminant polarisation simply adds a wavelength independent vector to the Stokes Q and U parameters. Plotting Q against U, as a function of wavelength, allows the intrinsic angle of polarisation, and hence the polarising media, to be established. This is independent of any assumptions regarding the interstellar polarisation.

Figure 3.6 presents the spectropolarimetric signatures of the stars in the sample and Figure 3.7 presents the associated QU diagrams. The spectropolarimetric signatures of objects previously observed with spectropolarimetry are entirely consistent with published results (e.g. Vink et al. 2002, 2005a; Mottram et al. 2007a), providing an important check on the data reduction process. In general, the data are of slightly inferior quality to previous observations. This is attributed to the poor weather conditions throughout the observing. Consequently, a coarser binning is used than is typical for such data (0.1 c.f. 0.05 per cent). Five objects exhibit a change in both linear polarisation and the polarisation angle over Hα (HD 179218, HK Ori, MWC 1080, V586 Ori & MWC 147). MWC 1080 and MWC 147 were also observed by Mottram et al. (2007b). While the data are broadly consistent with the previous observations, the line effects are not manifest in the QU diagram, perhaps a result of the coarse binning. Less coarse binning does not reveal any signatures as the scatter increases considerably. Therefore, the results of Mottram et al. (2007b) are used over these data. Of the three remaining objects which exhibit line effects, only HK Ori and V586 Ori exhibit an excursion in QU space which

can be used to calculate the intrinsic polarisation angle.

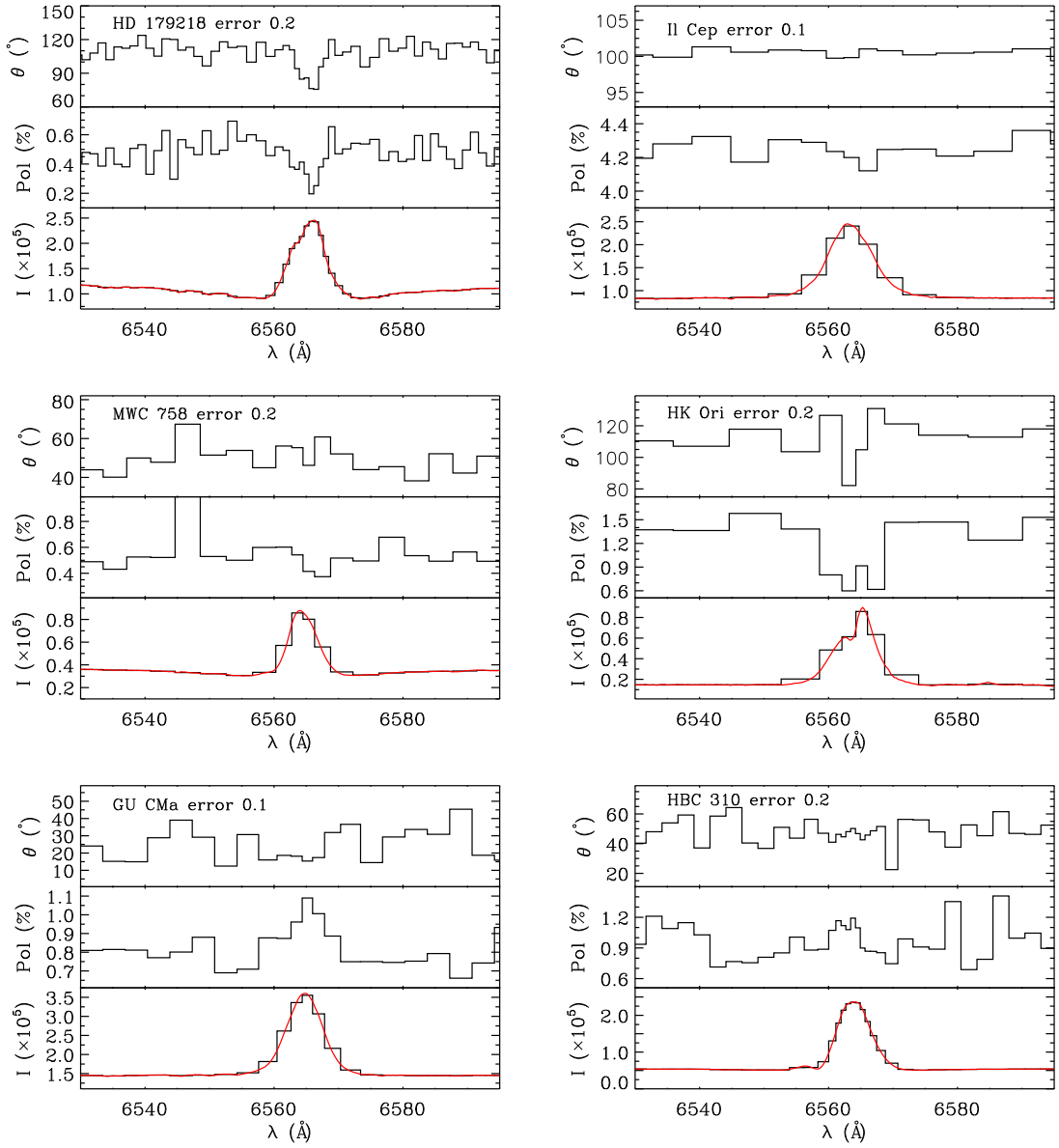

Figure 3.6: *The spectropolarimetric signatures of the sample. For each object the spectropolarimetric PA, the percentage polarisation, and the Stokes intensity spectra are presented centred upon Hα. The data are binned to a constant error, which is stated in the plots. The smooth red line is the un-binned line profile.*

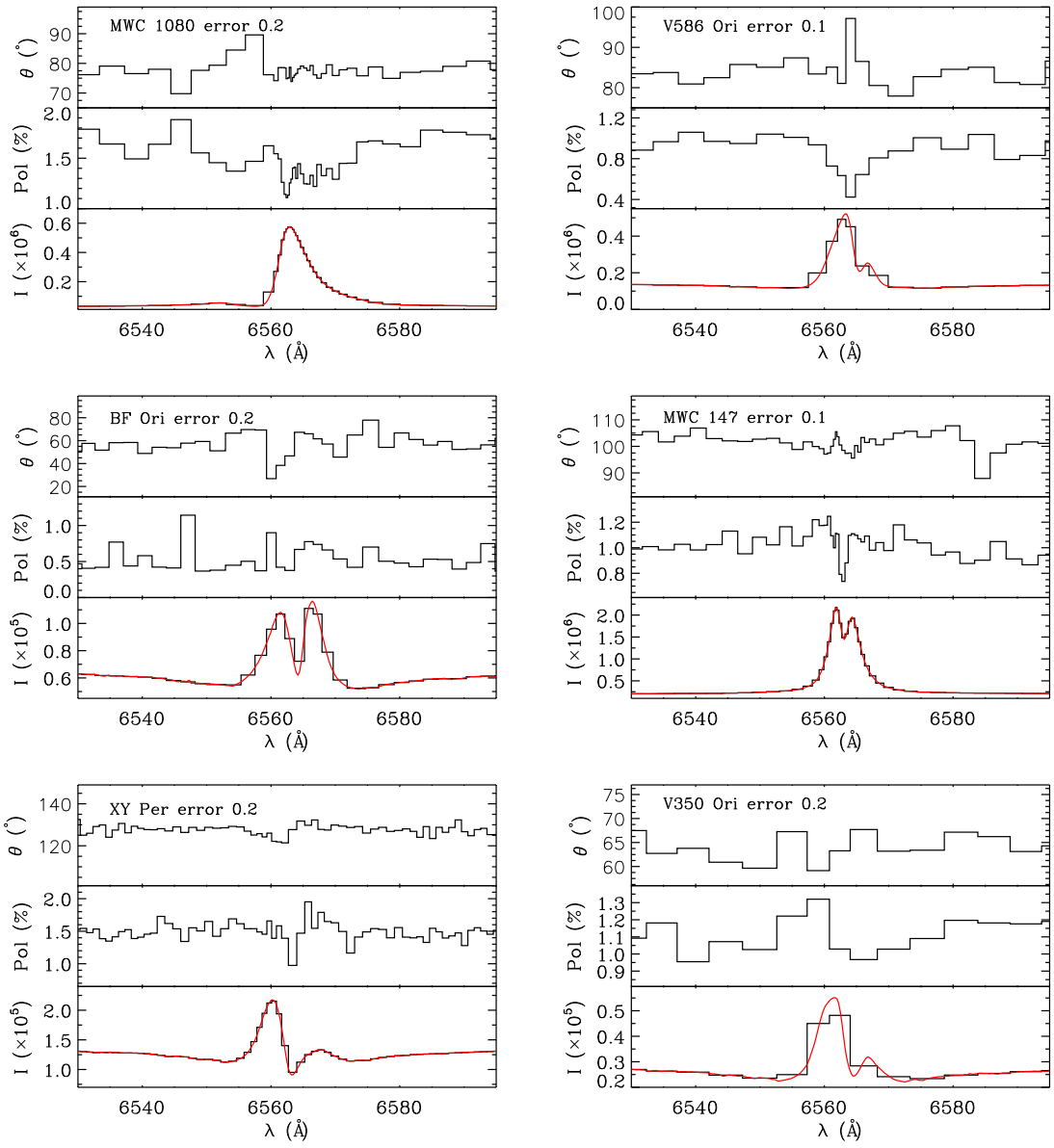

Figure 3.6 continued.

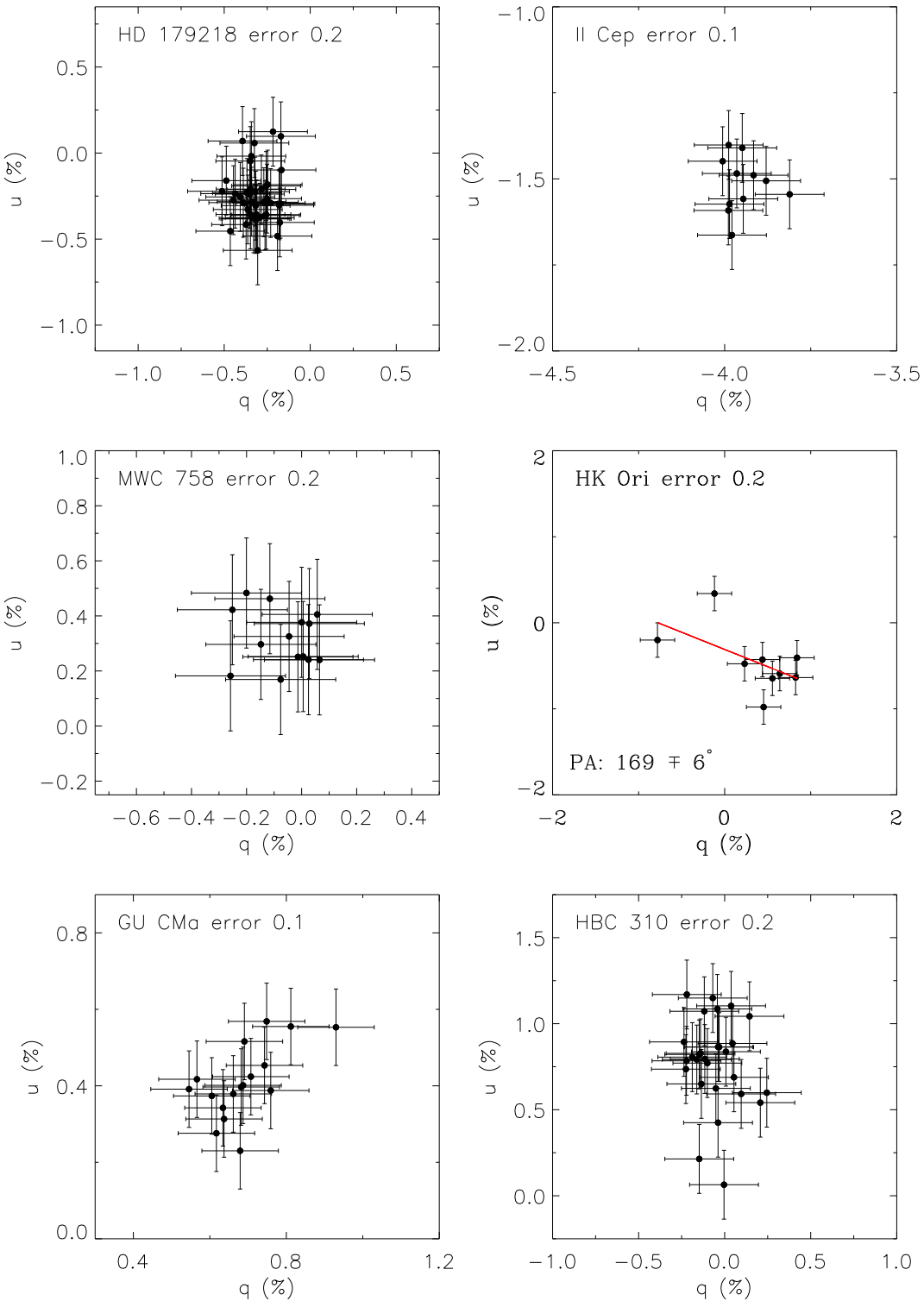

Figure 3.7: *The QU diagrams of the spectropolarimetric signatures in Figure 3.6. The solid red lines mark the linear fit used to determine the polarisation angle.*

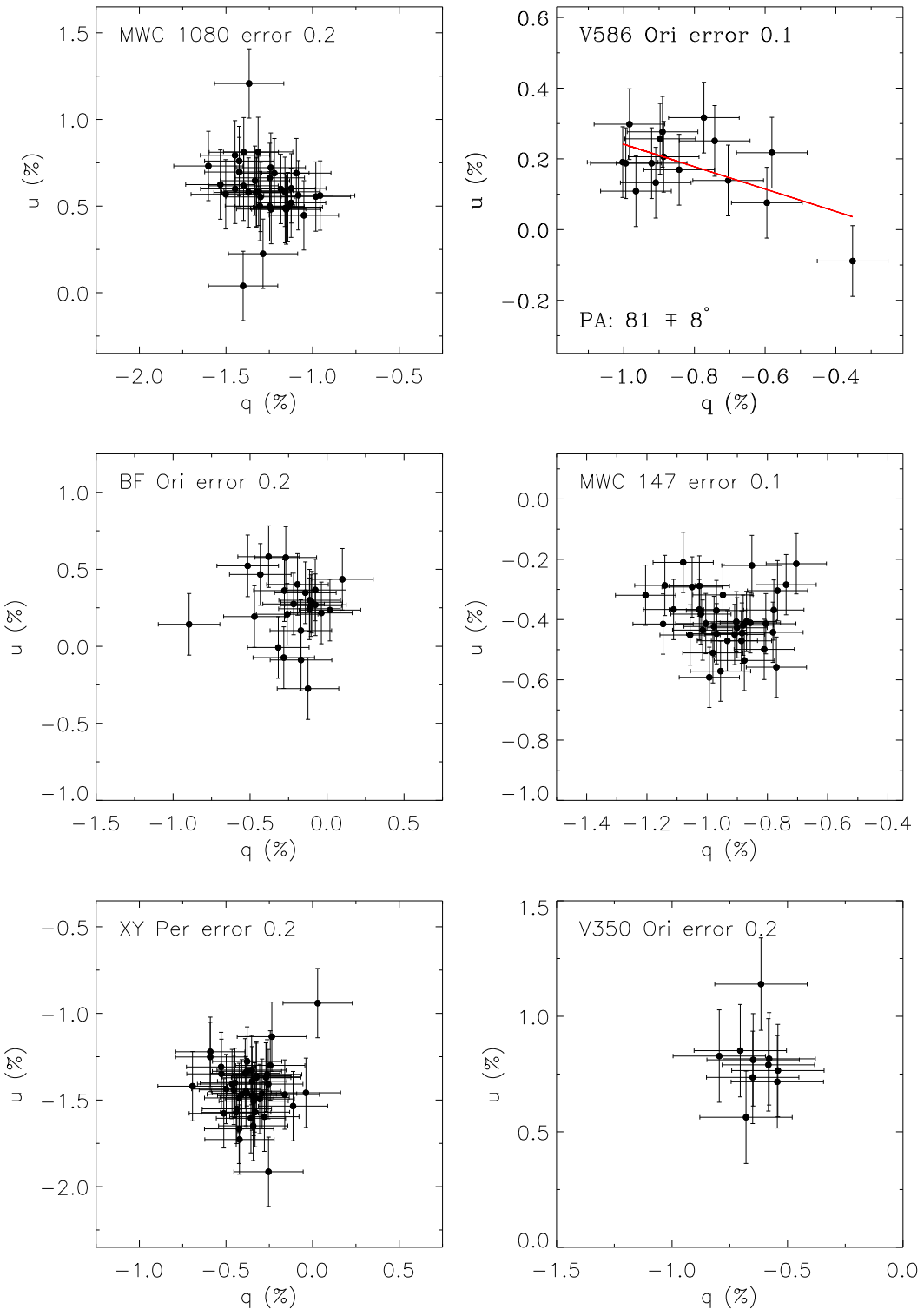

Figure 3.7 continued. Note that the axes of the plots q and u represent the normalised Stokes parameters Q/I and U/I.

3.4 Model

In order to compare disk and binary position angles in a meaningful fashion a model is required to predict the difference in the two angles expected for various scenarios. Baines et al. (2006) simply compare disk and binary position angles. However, unless the systems are edge on, the binary position angles do not necessarily relate to the binary orbit, and thus the results of this approach may be misleading. Here, a simple model is used to predict the distribution in the difference between disk and binary position angle that would be expected if the circumstellar disks and binary orbits lie in the same plane. The model is characterised by a random orbital phase, inclination, semi-major axis and PA of the line about which the system is inclined. The eccentricity of the system can be either random or constant. Admittedly, neither the random or constant eccentricity is truly representative of the eccentricity distribution of PMS binary systems (Goodwin et al. 2007). However, the eccentricity distribution can have a significant effect on the results (see Figure 3.11). Therefore, the input eccentricity distribution is left as a free parameter. The masses of the components were kept constant at 6 & 1 $M_{\odot}$. The component masses have very little effect on the final distribution and are mentioned only for completeness.

Figure 3.8 presents three random systems to indicate various relative orientations of disk and binary position angles. It can be seen that in the case of the face on systems the binary position angle is unrelated to the position angle of the disk. Conversely, for more edge on systems, the binary position angle is likely to be aligned with the disk position angle, but this is not necessarily the case. In the extreme case of an edge on system the disk and binary position angles will be constantly aligned. Many such random systems can be used to determine the average distribution in the difference between the disk and binary position angles ($\Delta\theta$), which in turn can be compared to the data. Figure 3.9 presents the resultant distribution, which has been rotated by 90° to imitate the difference between binary and polarisation angles (due to optically thin scattering). Therefore, an alignment between disk and binary position angles corresponds to an offset of 90°. It can be seen that the distribution tends towards intrinsic alignment

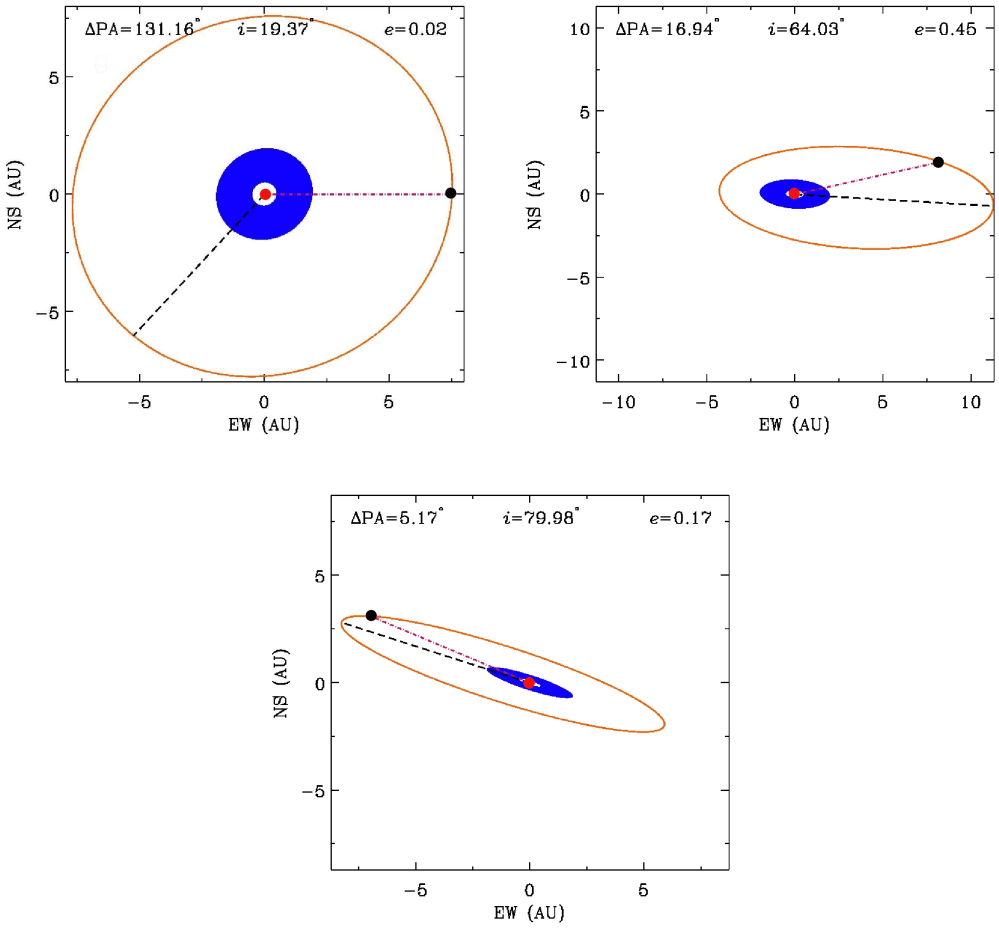

Figure 3.8: *Various random binary systems to illustrate the effect of inclination on the relationship between binary and disk position angle in a co-planar model. Here the binary separations are small, of the order a few AU. However, the random semi-major axis could range from 5 to 1000 AU. The disk radius was kept constant at 2 AU.*

(90°), and appears noticeably different to the distribution expected if the two angles were not related. This can be understood by referring to Figure 3.8. As demonstrated, although there is not a one-to-one correlation between binary and disk position angle, if the two are co-planar they will most likely be aligned in the case of highly inclined systems. However, this is not true for non-coplanar systems. Therefore, if a random inclination distribution is assumed, on average, the two angles are more aligned in the co-planar scenario than in a non-coplanar scenario (in which the two angles are essentially

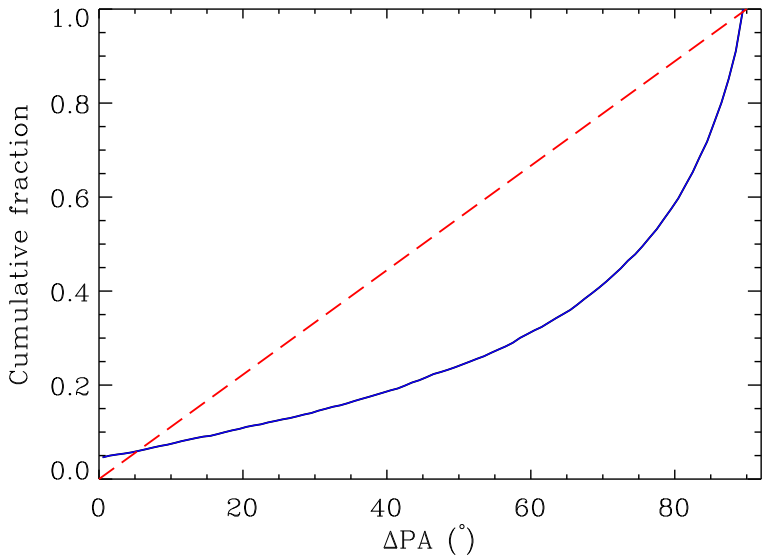

Figure 3.9: *The expected distribution in the difference between spectropolarimetric signatures of disks (orientated perpendicularly to the disks) and binary systems in a co-planar model (blue line). The red line represents the expected distribution due to a random orientation of binary and disk position angles. As can be seen the co-planar model distribution exhibits a marked preference towards intrinsic alignment – a difference of* 90°.

randomly orientated), as shown in Figure 3.9.

3.4.1 Biases

Before the model is compared to the data, various biases that can effect the resultant distribution must be discussed. The primary bias is due to an unquantified selection effect in the spectropolarimetric observations. Intrinsic polarisation angles are derived from line effects in the *QU* plane. If no line effects (changes in the level in polarisation and polarisation angle) are observed, the intrinsic polarisation angle, and thus disk position angle, cannot be determined. However, the absence of a line effect does not necessarily indicate that no disk is present. If a disk is seen face on, the individual polarisation vectors cancel with one another and no line effect is observed. On the other hand, an inclined disk projects an ellipse onto the sky, and thus the individual

polarisation vectors do not cancel, resulting in an observable line effect. Therefore, line effects originate in disks which are inclined to the line of sight. Consequently, the sample of objects which exhibit spectropolarimetric line effects are not drawn from a population of objects with random inclinations – but are instead biased towards some finite inclination. This is a potential source of bias as the parent inclination distribution is essentially unconstrained. To compare the model distribution of the difference in binary and disk position angles a lower inclination limit must be used to select model line effects from inclined systems only.

However, the value of this lower limit can introduce a bias in the resultant distribution as it is not known. Figure 3.10 presents the effect changing the value of this lower limit can have. The higher the limit the more pronounced the trend of the model distribution towards intrinsic alignment (90°) becomes. This is because a face on system exhibits no relationship between binary and disk position angle, as the random phase of the binary system translates to an almost random binary position angle. Conversely, in the case of an edge on system, the binary and disk position angles are always aligned as the binary orbit and disk plane becomes a straight line on the sky. This is what makes the model distribution curve to its peak at $\Delta\theta$ values close to 90. Therefore, choosing a high inclination cut increases the average inclination of the model sample, which in turn emphasises the preferential alignment.

Eccentricity has a similar effect on the final distribution as inclination, which might be expected as there is little difference in the projected orbit of a highly inclined system and a highly eccentric system. This is shown in Figure 3.11, in which the $\Delta\theta$ distributions of systems with a constant eccentricity of 0.1, 0.5 and 0.9 are compared. It can be seen that a higher eccentricity results in a more pronounced trend of the disk and binary position angles to be aligned, as was the case for high inclination distributions. Clearly, the initial eccentricity distribution has a significant effect on the $\Delta\theta$ distribution. In general, the properties of the binary systems such as eccentricity and inclination are not known. Consequently, the model $\Delta\theta$ distribution suffers from biases due to the selected inclination cut-off and underlying eccentricity distribution.

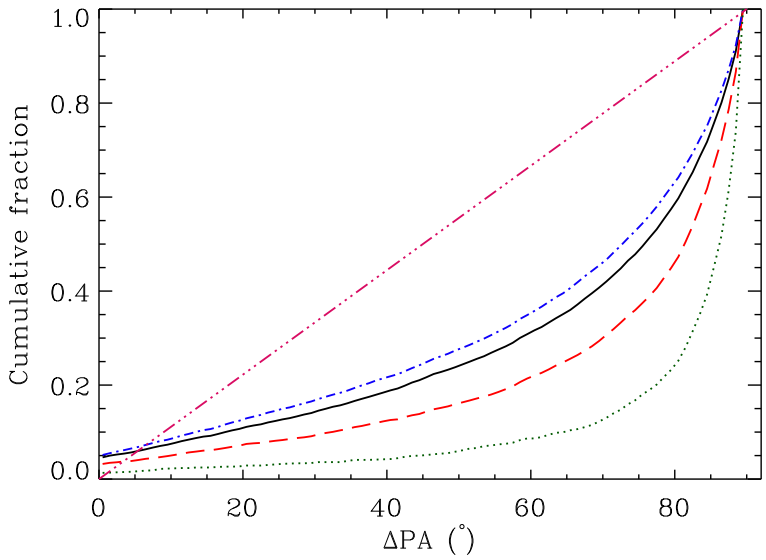

Figure 3.10: *The expected distribution in the difference between spectropolarimetric signatures of disks (orientated perpendicularly to the disks) and binary systems in a co-planar model. Different lines mark rejecting systems with inclinations below some limit. These limits are: blue – 0°, black – 20°, red – 50° and green – 75°. The magenta line represents the expected distribution due to a random orientation of binary and disk position angles.*

3.5 Comparing the data and the model

The primary objective of this chapter is to study the relative orientations of binary systems and circumstellar disks around the individual binary components of HAe/Be binary systems. This is attempted by comparing binary position angles to the intrinsic polarisation angles. To supplement the observed sample, intrinsic polarisation angles (established from spectropolarimetry) are taken from the literature. The binary position angles are primarily taken from the spectroastrometric data presented in Chapter 2, although several are obtained from the literature. The sample of objects for which both spectropolarimetric and binary position angles are available is presented in Table 3.4. The available sample is clearly significantly larger than the sample of 6 presented by Baines et al. (2006). As noted in Section 3.2, the polarisation angles reported in Mottram et al. (2007b) are on occasion 90° at odds with the direction of the polarisation vector.

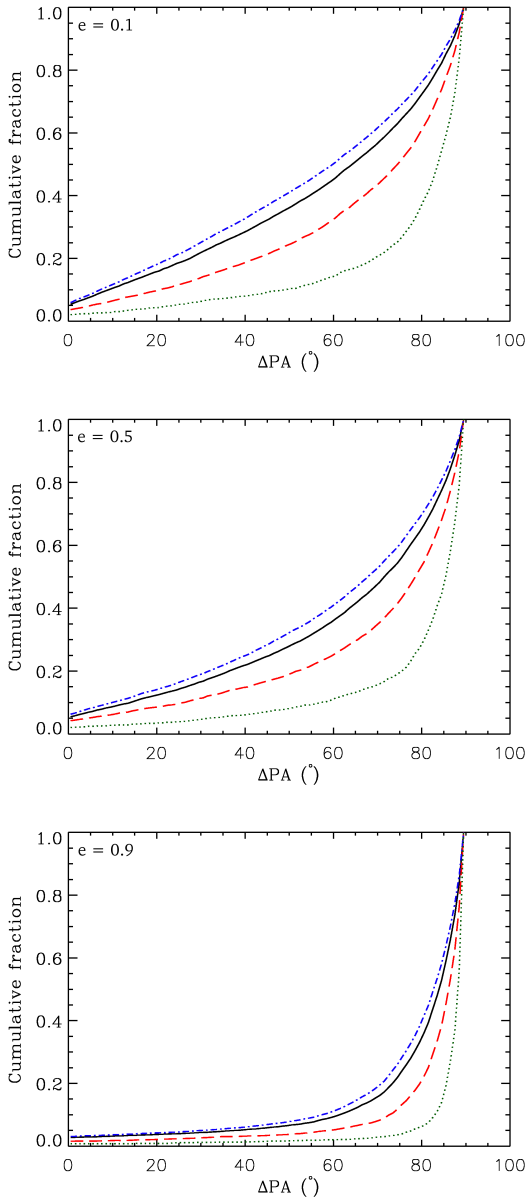

Figure 3.11: *The expected distribution in the difference between spectropolarimetric signatures of disks (orientated perpendicularly to the disks) and binary systems in a co-planar model with different constant eccentricities. The meaning of the lines is the same as in 3.10. From top to bottom the underlying constant eccentricity is 0.1, 0.5 and 0.9.*

It is found that the reported angle of MWC 166 also requires rotating by 90° .

It is noted that the polarisation angles of HD 37357, SV Ceph and XY Per taken from Vink et al. (2005a) are presented as being particularly uncertain. Indeed, in the case of HD 37357 and SV Ceph the data are of such low SNR that the associated spectropolarimetric signatures cannot be used to differentiate between polarisation and depolarisation. Consequently, these angles are uncertain by 90°. Therefore, these objects are discounted as their uncertain polarisation angles may weaken an intrinsic correlation between spectropolarimetric and binary angle. Similarly, HBC 310 is also discarded from the sample as the available data are insufficient to distinguish between intrinsic polarisation and depolarisation, and consequently the polarisation angle is uncertain by 90°.

As noted in Section 3.2, as a first order indication, the relative width of a spectropolarimetric angle may provide a means to separate signatures due to disks and those due to optical pumping. The spectropolarimetric signatures of T Ori and CQ Tau are substantially narrower than the associated emission line profile. As this may indicate that the polarisation is due to line of sight absorption effects and not polarisation in circumstellar disks, these objects are discarded from the sample. Table 3.4 presents the resultant final sample, alongside the objects discarded for the above reasons.

The differences in binary and predicted disk angles, determined from the intrinsic polarisation angles presented in Table 3.4, are compared to the co-planar model described in Section 3.4. In addition, the data are compared to a distribution generated by assuming the disk and binary position angles are randomly orientated. The results are presented in Figure 3.12. The statistics are inconclusive. Both the coplanar model and random distributions are consistent with the data, and a random orientation cannot be discarded with more than approximately 65 per cent confidence. This is essentially due to the small difference between the coplanar model and random distributions. Even if the data matched one of the predictions exactly, the sample of 11 objects is not sufficient to allow a decisive test. Therefore, to conclusively test whether HAe/Be binary systems and circumstellar disks are co-planar, the sample of objects with disk and binary

Table 3.4: *Binary systems for which a measurement of the intrinsic polarisation angle (from linear spectropolarimetry) and the PA of the binary system is available. Column 2 denotes the spectral type of the system primary, taken from SIMBAD unless otherwise stated. Column 3 lists the intrinsic polarisation angle. If effects are observed across multiple lines, the value with the smallest associated uncertainty is used. The final column contains the difference between the binary and polarisation angle, calculated to be in the range* $0° - 90°$.

Object	Type	Pol PA (°)	Depol	$\frac{\Delta\lambda(\mathrm{pol})}{\Delta\lambda(\mathrm{I})}$	QU	Binary PA (°)	$\Delta\theta$ (°)
Selected sample							
HD 200775	B2	$93\pm2^{\mathrm{A}}$	yes	1.13	Exc	164.00^{B}	71.0
MWC 147	B6	$168\pm4^{\mathrm{A}}$	no	0.50	Exc	$81.7 \pm 5.1^{\mathrm{C}}$	86.3
BD +40 4124	B3	$36\pm3^{\mathrm{A}}$	yes	0.75	Exc	175.1^{G}	40.9
MWC 1080	B0	$75\pm4^{\mathrm{A}}$	yes	1.10	Smear	$269.2 \pm 1.5^{\mathrm{C}}$	14.2
MWC 166	B0	$46\pm4^{\mathrm{A}}$	yes	$\sim$1	Exc	$298.3 \pm 0.7^{\mathrm{C}}$	72.3
MWC 120	A2	90^{H}	no	0.65	Loop	$33.7 \pm 1.5^{\mathrm{C}}$	56.3
HD 58647	B9	20^{H}	no	0.67	Loop	$115 \pm 10^{\mathrm{F}}$	85.0
HK Ori	A4	$169\pm6^{\mathrm{K}}$	yes	$\sim$1	Loop?	$46.9 \pm 3.1^{\mathrm{A}}$	57.9
V586 Ori	A2	$81\pm8^{\mathrm{K}}$	yes	$\sim$1	Loop?	$216.8 \pm 3.3^{\mathrm{A}}$	44.2
HD 45677	$\mathrm{B2}^{\mathrm{D}}$	$164\pm3^{\mathrm{E}}$	poss	$\sim$1	Exc?	$150 \pm 17^{\mathrm{F}}$	14.0
MWC 158	B9	135^{H}	no	1.00	Exc	$30 \pm 7^{\mathrm{F}}$	75.0
Discarded sample							
T Ori	A3	20^{H}	no	0.26	Loop	$107.2 \pm 2.5^{\mathrm{C}}$	87.20
CQ Tau	$\mathrm{A8}^{\mathrm{Z}}$	20^{H}	no	0.17	Loop	55.5^{G}	35.5
HD 37357	A0	$(65)^{\mathrm{H}}$	–	–	–	$234.9 \pm 1.0^{\mathrm{C}}$	10.1
SV Ceph	A0	$(100)^{\mathrm{H}}$	–	–	–	311.6^{G}	31.60
XY Per	A2	$(70)^{\mathrm{H}}$	no	0.88	Loop	76^{I}	6.0
HBC 310	B9	110^{H}	–	–	–	309.6^{J}	19.6

A: Mottram et al. (2007b), B: Pirzkal et al. (1997), C: These data (see 2), D: Cidale et al. (2001), E: Patel et al. (2006), F: Baines et al. (2006), G: Rodgers et al. priv. com. (2008), H: Vink et al. (2005a), I: Perryman et al. (1997), J: Thomas et al. (2007), K: These data, see Section 3.3, Z: Herbig & Bell (1988).

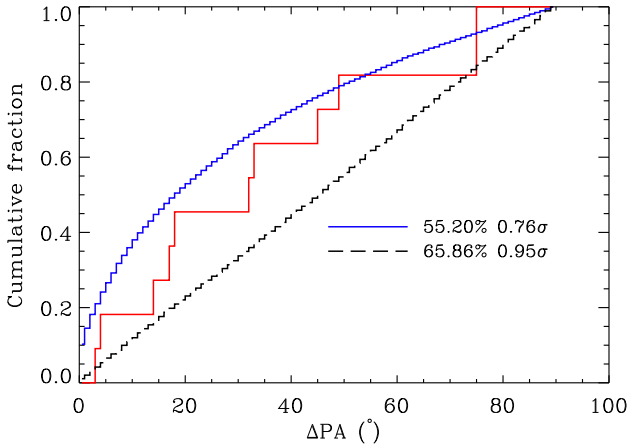

Figure 3.12: *The difference in disk and binary position angles presented in Table 3.4 (red) compared to the co-planar model described in Section 3.4 (blue) (with an inclination cut of 30°, and a constant eccentricity of 0.1) and a distribution generated by assuming the two angles are randomly aligned (black). The confidence in discarding each scenario is presented in the plot. Note that ΔPA refers to the difference between disk and binary position angle, i.e. the 90° offset of the polarisation signature has been taken into account.*

position angles must be enlarged. To this end, the sample is supplemented by adding disk position angles determined from direct imaging and multi-baseline interferometry. The additional sample is presented in Table 3.5.

The resultant sample, of 20 objects, more than three times that of Baines et al. (2006), is again compared to the two scenarios described above. The results are presented in Figure 3.13. As before, the co-planar model provides a better fit to the data than the random scenario. However, the random hypothesis cannot be rejected with more than 2 sigma certainty, making this result inconclusive.

It is shown that the data are inconsistent with the coplanar model and a constant eccentricity of 0.9 (see Figure 3.14), indicating that if disk and binaries are co-planar the orbits of the system are not highly eccentric. Conversely, the data are well fit by the co-planar model with a constant eccentricity of 0.1. However, this results in a distribution

Table 3.5: *HAe/Be stars for which independent measurements of binary and circumstellar disk position angles are available in the literature.*

Object	Binary PA (°)	Disk PA (°)	Δ PA (°)
MWC 758	311.3[A]	128.0[B]	3.3
V892 Tau	23.0[A]	53.0[C]	30.0
CQ Tau	55.5[A]	120±10[D]	64.5
R Mon	287±1[E]	∼80.0[F]	27.0
MWC 297	313±2[G]	165±15[H]	32.0
HR 5999	∼111.0±0.5[I]	∼25[J]	86.00
HD 101412	226.3[A]	38±5[K]	8.3
HD 179218	140.5[A]	23±3[K]	62.5
PDS 144	28.7±0.3[L]	∼30[L]	1.30

A: Rodgers et al. priv. comm. (2008), B: Eisner et al. (2004), C: Monnier et al. (2008), E: Weigelt et al. (2002), F: Fuente et al. (2006), G: Vink et al. (2005b), H: Manoj et al. (2007), I: Stecklum et al. (1995), J: Preibisch et al. (2006), K Fedele et al. (2008), L: Perrin et al. (2006)

closer to the random distribution than a higher eccentricity. Consequently, even if the data followed the model distribution exactly, differentiating between the two scenarios at a 3σ level would require a sample of approximately 50 objects. Therefore, the current sample of 20 objects is still insufficient to decisively evaluate whether HAe/Be star binary orbits and circumstellar disks are intrinsically aligned or not.

3.6 Discussion

The data are best fit with the results of the co-planar model when using a relatively low eccentricity (e.g. < 0.5). Here this is compared to what is know about the eccentricity of young binary systems.

As HAe/Be stars are typically situated at distances of several hundred pc, the typical angular separations of $1''$ corresponds to ∼1000 AU. In turn, this corresponds to periods of several thousand years. Close companions with short periods (∼ 100 years) have separations of several ∼100 AU or typically $<1''$, and are generally unresolved. Therefore, these orbits are difficult to determine. From optical interferometric observations, Monnier et al. (2006) and Monnier et al. (2008) constrained the orbits of two

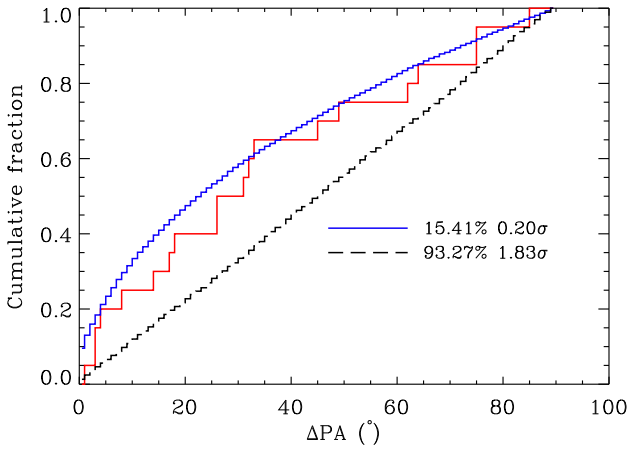

Figure 3.13: *The same as Figure 3.12, but for the difference in binary and disk position angle presented in Tables 3.4 and 3.5. The model output was generated using an inclination cut-off of 10° and a constant eccentricity of 0.1. The inclination cut-off was relaxed as the sample includes imaging data, which is less sensitive to inclination than spectropolarimetry.*

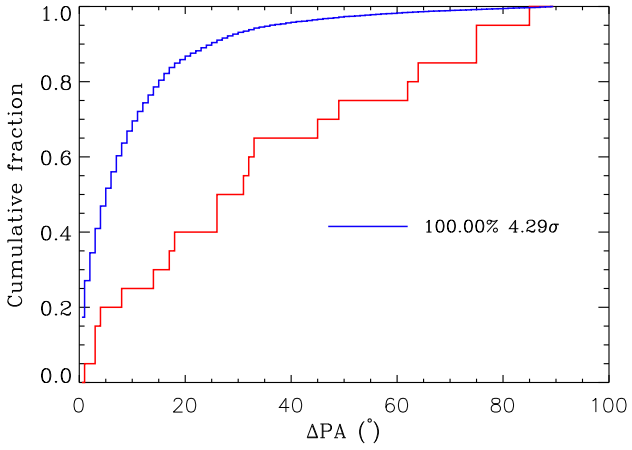

Figure 3.14: *The same as Figure 3.13, but the model output was generated using an inclination cut-off of 10° and a constant eccentricity of 0.9.*

HAe/Be binary systems: MWC 361 and HD 45677. Both the calculated eccentricities are relatively low: 0.3±0.06 and 0.12 ±0.05 respectively, in general agreement with the previous result.

It should be noted that these companions are typically closer (a few AU) to the primary than the separations of the binaries presented in this chapter. Therefore, the eccentricities of the sample presented here may be substantially larger, as small orbits tend to low eccentricities due to tidal effects. However, since the eccentricities of binaries with larger separations are completely unknown this is pure conjecture. Kroupa (1995) present a model eccentricity distribution that peaks at ~ 0.8. However, this is presumably dependent upon the star formation mechanism assumed. If the companions in question did indeed form via disk fragmentation it might be expected that their orbits will be only slightly eccentric due to the drag of disk material. For example, in a simulation showing massive binary formation via disk fragmentation Krumholz et al. (2009) report the creation of a binary system with a separation of ∼1000 AU and an upper limit to the eccentricity of 0.25 – which is consistent with the data presented here. Therefore, there is no evidence for highly eccentric HAe/Be binary systems, and as a result the data are consistent with the coplanar model.

Increasing the sample to a sufficient size to definitively assess whether HAe/Be binary orbits are coplanar with circumstellar disks is likely to be challenging. The entire sample of HAe/Be stars contains of the order of 100 objects. Approximately half of all HAe/Be stars do not exhibit a spectropolarimetric line effect. Furthermore, the selection criteria discussed in Section 3.2 result in a fraction of observed line effects being discarded. Finally, spectropolarimetry is a 'photon-hungry' technique and requires bright objects ($V < 12$). Therefore the entire sample of HAe/Be stars is unlikely to be observed with spectropolarimetry. Consequently, the sample of disk position angles is unlikely to be increased to the required size using this technique alone.

Spatially resolved interferometry provides a complimentary approach to probe the orientations of circumstellar disks around HAe/Be stars. However, to probe small-scale disks generally requires the resolution of optical/NIR interferometers. Constraining the morphology of small-scale disks in detail requires substantial sampling of the u, v

plane, and as a result only several disks have been probed in detail with long baseline interferometers such as the Very Large Telescope Interferometer (VLTI) (see e.g. Kraus et al. 2008b; Benisty et al. 2010). However, in principle, the orientation of circumstellar disks can be determined with limited u, v coverage and only several baselines, provided simple models are used. Therefore, this technique has the potential to determine the orientations of disks of a substantial number of HAe/Be stars in the future and perhaps enlarge the sample to the required size.

3.7 Conclusion

This chapter presents a comparison between HAe/Be binary and circumstellar disk position angles in an attempt to assess whether the binary orbits of HAe/Be stars lie in the same place as their circumstellar disks: a key prediction of binary formation by disk fragmentation. The disk position angles are predominately derived from linear spectropolarimetric observations over Hα, but are also taken from imaging and interferometric observations in the literature. The salient conclusions are summarised below.

It appears that the linear spectropolarimetric signatures of HAe/Be stars can be used to trace the orientation of their circumstellar disks. This is an important finding as it has been suggested that the spectropolarimetric signatures of Herbig Ae/Be stars are not related to circumstellar disks. This finding is significant at the approximately the 3 sigma level. Various selection criteria to eliminate contaminant objects from the sample are discussed and shown to have a minimal effect on this conclusion.

It is found that if the spectropolarimetric signatures of HAe/Be stars do trace small scale disks, the majority of the disks must be optically thin in the inner region. This finding is consistent with the occurrence of puffed up inner rims in the disks of many HAe/Be stars.

The data are most consistent with the scenario in which binary orbital planes and circumstellar disks lie in the same plane (although the small sample size limits the significance of this to ~ 95 per cent).

It is shown that the difference between binary and disk position angle is quite similar in the case of random orientations and the co-planar model with a low eccentricity. As a result a large sample ($\sim$50) is required to conclusively evaluate whether HAe/Be star disks lie in the same plane as their binary orbit.

To conclude this chapter, while it is not possible to decisively prove that HAe/Be binary orbits and circumstellar disks are co-planar, the data are shown to be consistent with this scenario, and thus with the scenario of binary formation via disk fragmentation proposed in the previous chapter. Dedicated spectropolarimetric and interferometric observations are required to increase the sample in order to definitively probe the relative orientations of HAe/Be binary orbits and circumstellar disks.

Chapter 4

NIR IFU observations of HAe/Be stars

4.1 Introduction

As shown in the previous chapters, it appears that intermediate and massive stars form via disk accretion, despite previous theoretical objections to this scenario. However, it is still not clear how the accretion mechanisms of intermediate and massive stars differ. Pre-main-sequence models show that it is across this mass range that the exterior of stars switches from being convective to being radiative (e.g. see Iben 1965). Since convective cells generate stellar magnetic fields, it appears that intermediate and high mass stars are unlikely to possess dynamo generated magnetic fields. Given that the solar mass T Tauri stars form via magnetospheric accretion (e.g. Bouvier et al. 2007, and references therein), it has been suggested that intermediate and massive stars must form through direct disk accretion. Recent observations of Herbig Ae (HAe) stars have revealed a distinct similarity to T Tauri stars. In contrast, spectropolarimetry indicates that early type Herbig Be (HBe) stars do not experience magnetospheric accretion (Vink et al. 2005a; Mottram et al. 2007a), and therefore may gain mass via disk accretion. However, this has yet to be confirmed. Locating the transition between the accretion mechanisms and characterizing accretion at high masses is necessary to understand the processes involved in star formation in general, and to determine the difference between low and high mass star formation in particular.

The central accretion mechanism acts on sub AU scales, and generally cannot be

resolved, which makes this transition in star formation mechanisms difficult to observe. However, accretion may be traced indirectly, for example by outflows. T Tauri star outflows are thought to be collimated by magnetic processes (see e.g. Shang et al. 2007; Pudritz et al. 2007). As stars more massive than a few solar masses are not thought to be magnetic, a reduction in outflow collimation might be expected; the change tracing the diminishing influence of stellar magnetic fields in star formation, and thus the transition between magnetospheric and disk accretion.

Mundt & Ray (1994) suggest there is little difference in collimation between outflows associated with low and intermediate mass stars. This has been confirmed regarding HAe stars (see e.g Melnikov et al. 2008). The task is now to test whether or not this conclusion is valid for higher mass objects (e.g. HBe stars). Poetzel et al. (1992) found seemingly uncollimated Herbig-Haro objects around a Herbig Be star (MWC 1080). This is consistent with the simplistic scenario in which such stars evolve via disk accretion, and thus do not produce collimated outflows. However, some MYSOs drive collimated jets a few pc in length (Davis et al. 2004), which is at odds with this scenario. Studies like that of Poetzel et al. (1992) had to contend with seeing limited resolution, and thus small scale collimated outflows would have been unresolved. In addition, previous studies have employed relatively wide filters (FWHM of $\sim$50 Å). High spectral and spatial resolution observations, limited to two objects, display clear evidence of collimated outflows emanating from HBe stars (see Garcia et al. 1999; Movsessian et al. 2002). Therefore, a high resolution investigation of a larger sample is needed to fully address the occurrence of jet-like outflows associated with HBe stars and whether there is a difference between HAe and HBe star outflows. This forms the main objective of this chapter.

In addition, HI emission lines may also be used to search for changes in the accretion mechanism of Herbig Ae/Be stars. These emission lines may originate in a variety of phenomena; such as bipolar outflows, accretion flows, accretion disks and winds (see Malbet et al. 2007; Kraus et al. 2008a, and references therein). If there is a change in accretion mechanisms across the HAe/Be mass range, this may well be manifest by a change in the source of these emission lines. Spatially resolved observations of HI

emission of a sample of five HAe/Be stars do reveal changes in the spatial distribution of the emission with spectral type (Kraus et al. 2008a). In the case of the later type objects, the data of Kraus et al. (2008a) indicate the emission originates interior to the continuum. In the case of the earliest object observed, the line emission originates from an area larger than the continuum. Although these results are essentially consistent with the change in accretion mechanisms suggested by spectropolarimetry, Kraus et al. (2008a) suggest the difference in the size of the emitting region traces the dependence of the dust sublimation radius on stellar temperature.

On the other hand, recent spectro-interferometric observations of the Brγ emission of young stellar objects with the Keck Interferometer suggest that the change in the spatial distribution of the Brγ emission traces the transition from magnetospheric accretion in late type objects to direct disk accretion in the case of early B type objects (Eisner et al. 2010). However, in this study only one early Herbig Be star was observed. Therefore, the behaviour of the HI line emission of HAe/Be stars with spectral type is still debated. To make progress, high resolution observations of a much larger sample of Herbig Be stars are required.

The second objective of this chapter is to explore the potential of spectroastrometry to address this requirement. Both objectives are achieved via observations of a sample of HBe stars using integral field unit (IFU) spectroscopy in the near infrared. The spatial and spectral resolution of the observations constitute a significant improvement in sensitivity to outflow features compared to previous studies, allowing the uncertainty in the outflow characteristics of HBe stars to be addressed. Furthermore, the technique of spectroastrometry enables the origin of HI emission lines observed to be probed with an angular precision of approximately 0.5 mas (0.25 AU at 500 pc).

This chapter is structured as follows. Section 4.2 presents the observations and data reduction procedures used. The results are presented in Section 4.3. The implications of the results are discussed in Section 4.4 and the chapter is concluded in Section 4.5.

4.2 Observation and data reduction

4.2.1 Sample selection

The sample observed consists of HBe stars which are not known to drive optical outflows. The objects were drawn from the catalogues of Thé et al. (1994) and Vieira et al. (2003) and were selected based on their $H-$band magnitude, their distance from Earth and evidence of youth (such as the presence of forbidden emission lines in their optical spectra and an association with nebulosity). A summary of the sample and observations is presented in Table 4.1.

Table 4.1: *A summary of the sample and observations.*

Object	Alternative names	RA (J2000)	Dec (J2000)	Spec Type	H (mags)	d (pc)	Time* (mins)	Seeing arcsec	Date
PDS 37		10 10 00.33	−57 02 07.40	B2†	8.36	720†	2.0	0.6	02/06/2009
HD 101412	PDS 57	11 39 44.46	−60 10 27.74	B9.5V‡	8.22	410†	1.6	0.8	22/06/, 23/06/2009
PDS 353		12 22 23.28	−63 17 16.70	B5†	8.65	1200†	4.0	1.0	23/06/, 11/07/2009
PDS 364		13 20 03.58	−62 23 54.10	B2⋆	10.64	2600†	6.0	0.7	27/06/2009
HBC 596		15 03 23.81	−63 22 58.90	B?	8.75	175†	2.6	0.7	17/08/, 25/08/, 26/08/2009
HD 323771	PDS 96	17 34 04.63	−39 23 41.30	B5V†	8.53	1300†	3.6	0.6	20/06/, 26/06/, 11/07/2009
LkHα 118	HBC 281	18 05 49.72	−24 15 20.50	B5Vpe	8.25	?	3.6	0.4	30/07/, 15/08/2009
PDS 543		18 48 00.40	+02 54 13.00	B1	7.90	414†	0.4	0.5	23/08/2009
MWC 610	HD 174571, PDS 545	18 50 47.18	+08 42 10.09	B3Vpe	7.23	560†	2.0	0.6	20/06/, 30/07/2009

Notes:

The $H-$band magnitudes are from 2MASS.

$*$: Ideally the objects would have been observed for longer but the programme was not completed at the end of the observing semester.

⋆: Reed (2003).

†: Vieira et al. (2003).

‡: from SIMBAD (http://simbad.u-strasbg.fr/simbad/).

§: Perryman et al. (1997).

Table 4.2: *A summary of the standard stars.*

Object	RA (J2000)	Dec (J2000)	Associated science target	Type	H (mags)	d (pc)	Time (mins)	Seeing arcsec	Date
HD 92155	10 37 16.11	−53 51 18.94	PDS 37	B3V	6.80	508[§]	0.6	0.6	02/06/2009
HD 105613	12 09 38.78	−58 20 58.76	HD 101412	A3V	7.03	108[§]	0.6	0.9	23/06/2009
HD 112123	12 55 02.57	−62 33 31.91	PDS 353	A0/A1V	7.52	179[§]	1.4	1.1	23/06/2009
HD 119020	13 42 17.35	−58 37 10.72	PDS 364	A6V	7.37	182[§]	1.4	0.6	27/06/2009
HD 138153	15 33 27.04	−61 16 24.25	HBC 596	A2V	6.24	159[§]	0.4	0.6	17/08/, 26/08/2009
HD 164776	18 04 37.693	−40 38 15.26	HD 323771	B5V	7.34	315[§]	1.6	0.6	26/06/, 11/07/2009
HD 171254	18 34 41.11	−22 32 47.94	LkHα 118	A1V	7.91	448[§]	2.8	0.5	15/08/2009
HD 161677	17 46 41.04	+05 46 27.39	PDS 543	B8	7.04	267[§]	1.0	0.6	23/08/2009
HD 176304	18 59 17.342	+10 08 27.62	MWC 610	B2V	6.15	1190[§]	0.2	0.5	20/06/, 30/07/2009

4.2.2 Observations

The data presented in this chapter consist of $H-$band integral field unit observations conducted with SINFONI, the integral field unit on UT4 (Yepun) of the VLT (see Eisenhauer et al. 2003; Bonnet et al. 2004). The observations were performed in service mode in period 83 between 02/06/2009 and 26/08/2009. The 0.125 arcsec pixel size was selected to provide the largest possible field of view (8×8 arcsec). The typical seeing during the observations was ∼0.7 arcsec, and thus the spatial profile of the flux was generally well sampled (although not in all cases, this is discussed in more detail in Section 4.3.3). The observations were conducted using the $H-$band grating which results in a spectral resolution of 3000, or ∼100 $\mathrm{km\,s^{-1}}$. As the science targets are relatively bright (e.g. H <8), the individual exposure times were generally 10–20 seconds. A standard AB–BA–AB[(a)] sequence was used to obtain equally deep exposures of the sky to correct for the sky background. The offset to the sky region was generally 10–20 arcsec, and the sky regions were chosen by inspection of 2MASS images to avoid contamination. Telluric standard stars were observed following the science targets and at a similar air-mass. These stars had spectral types of B and A and were typically brighter than the science targets (H ∼7). Consequently, the individual exposure times for these observations were generally of the order of 5–10 seconds. The total exposure times and the seeing conditions during the observations are summarised in Tables 4.1 and 4.2.

4.2.3 Data reduction

The initial data reduction step consisted of cleaning defective lines caused by data processing at the detector level. The four pixels at the edge of the detector are used to estimate the bias level, which is automatically subtracted from the data before it is saved. If one of the non-illuminated edge pixels is struck by a cosmic ray or is simply defective, the bias level can be over-estimated. This can result in a negative line in the data when it is subtracted. Such lines were identified and corrected for with the median value of the 'good' non-illuminated pixels. This was done using a routine written in IDL

[(a)] where A and B denote the positions of the target and sky positions respectively

provided with the SINFONI pipeline manual.

Subsequent data reduction was performed with the SINFONI pipeline via GASGANO. The first step in this process consisted of bad pixel correction. To do this, a map of the bad pixels was generated. Pixels which behaved in a non-linear fashion were identified using the 24 linearity frames provided by ESO as part of the calibration package. Then defective hot pixels were identified using dark frames, which were also provided by ESO as part of the calibration package. Subsequently, the non-linear pixel and hot pixel maps were combined with flat field frames to create a master flat frame and a map of all the bad and non-linear pixels. The data were then corrected for the bad pixels and divided by the master flat field.

Raw SINFONI data consist of the readout from the Hawaii 2RG detector (2048×2048 pixels). The field of view of the instrument is sliced into 32 slices and each one of the 32 'slitlets' is imaged onto 64 pixels of the detector. This results in 32 spectra of the imaged region on the sky, each 64 pixels wide in the spatial domain. Following the flat fielding and correction for bad pixels, data reduction consists of stacking the slitlets to create a 3D data-cube – or a stack of reconstructed images ordered in the dispersion direction. Initially, geometrical distortion was corrected for using a set of 80 distortion frames (frames obtained placing the optical fiber in different locations). This allowed the distance between each slitlet to be determined. It is important to note that the slitlet positions are calculated independently of the science data. Therefore, if there is a slight error in the position of a certain slitlet this should be constant across various observations, and will not be related to the flux from the science target. Consequently, positional offsets cannot be induced by changes in flux levels, e.g. due to emission lines. Therefore, spectroastrometry should not be contaminated by errors in the slitlet positions, and if it is – any artifacts induced will be systematic and easily identifiable. The data were wavelength calibrated using Xe and Ar lamp spectra. Finally, sky subtraction was performed using the sky exposures and the data were co-added to create the final 3D data-cube.

The spectral resolution of the final data-cubes is approximately 100 $\mathrm{km\,s^{-1}}$. Typically, the HI emission lines of Herbig Ae/Be stars span several hundreds of $\mathrm{km\,s^{-1}}$.

Therefore, these data should be sufficient to resolve the emission lines of the sample. The data-cubes are oversampled in the dispersion direction by a factor of approximately 5. The wavelength range is approximately 1.5–1.75 μm.

Final data reduction and analysis was conducted using IDL. The object spectra were extracted using a window determined by the width of the spatial profile (generally several pixels) and background subtraction based on the average value of pixels at the edge of the data cube. Telluric absorption lines were removed using the spectra of the standard stars, which were early A or late B type stars. The HI absorption lines in the spectra of the standard stars were removed using model atmospheres calculated using ATLAS9 and SPECTRUM (see Sbordone et al. 2004; Gray & Corbally 1994). Finally, spectroastrometry was conducted by fitting a Gaussian profile to the flux distribution of the 3D data cubes in the vertical and horizontal directions at each dispersion pixel.

To assess the sensitivity of the data, the counts in the data-cubes were converted into flux densities. Initially, the 2MASS magnitudes of the standard stars were used to determine photometric zero points. These were then used to check the magnitude of the science targets were consistent with their 2MASS magnitude. It is found that the calculated magnitudes are generally within 0.2 magnitudes of the 2MASS values. The calculated magnitudes of two objects deviate by approximately one magnitude from their 2MASS values. This could be due to changing atmospheric conditions between the science and standard observations. However, since the data are generally consistent with the 2MASS magnitudes, the published magnitudes are adopted from hereon. The objects' $H-$band magnitudes are then used to convert the data counts in the appropriate wavelength range (1.5365–1.7875 μm) to flux densities.

4.3 Results

4.3.1 An overview of the data and analysis

To search for outflows emanating from the Herbig Be stars in the sample, an emission line which explicitly traces shocked regions is required. One such line in the wavelength range observed is the [FeII] line at 1.644 μm (Reipurth & Bally 2001). This line has been shown to trace collimated outflows emanating from pre-main-sequence stars (see

e.g. Perrin & Graham 2007) and traces higher velocity shocks than another commonly used shock tracer in the NIR, H_2 emission. Therefore, this line is an ideal tracer of 'optical' outflows from young stellar objects. Images of the target objects are created in this line to search the environments of the sample for evidence of outflow activity. In principle, the HI emission of the sample could also originate in outflows (see e.g. Davies et al. 2010). However, it is generally thought that the line emission of Herbig Ae/Be stars originates in winds and/or accretion disks (see e.g. Kraus et al. 2008a). To probe these structures, observations with an angular resolution of milli-arcseconds or less are required. To this end, this chapter explores the possibility of probing the source of such line emission on mas scales via spectroastrometry of the IFU data.

To begin with, attention is focused on the extracted spectra of the target objects, which are presented in Figure 4.1. As can be seen, the majority of the sample exhibit prominent HI Brackett series emission. The ratios of the individual lines are generally consistent with predicted values assuming case B applies[(b)] (see Storey & Hummer 1995). This is consistent with the lines originating in a region of relatively low density, for example a disk wind (see e.g Bik et al. 2008). The most common line profile consists of a single peak (although several also exhibit double peaked profiles). In general the Brackett lines exhibit a similar line profile to the Hα emission of the objects, indicating that the HI recombination lines share a common origin. Two objects, HD 101412 and PDS 543, do not exhibit any emission lines and are subsequently discarded from the sample. Noticeably, none of the spectra exhibit prominent [FeII] emission indicative of outflow activity. However, this could be because the spectra were extracted from a region centred on the target object. The spectra of PDS 37 and PDS 353 may exhibit weak [FeII] emission, but this is difficult to assess as the line lies in the wing of the Br 12 line.

As a preliminary search for extended emission, images are created from the observations of the sample in the integrated light from 1.5 to 1.75 μm. These are compared to the extrapolated continuum flux over this wavelength range to search for extended emission, see Figure 4.2. Most of the stars appear to be point sources, with the exception of

[(b)] i.e. that the optical depth in all the HI Lyman lines is significant

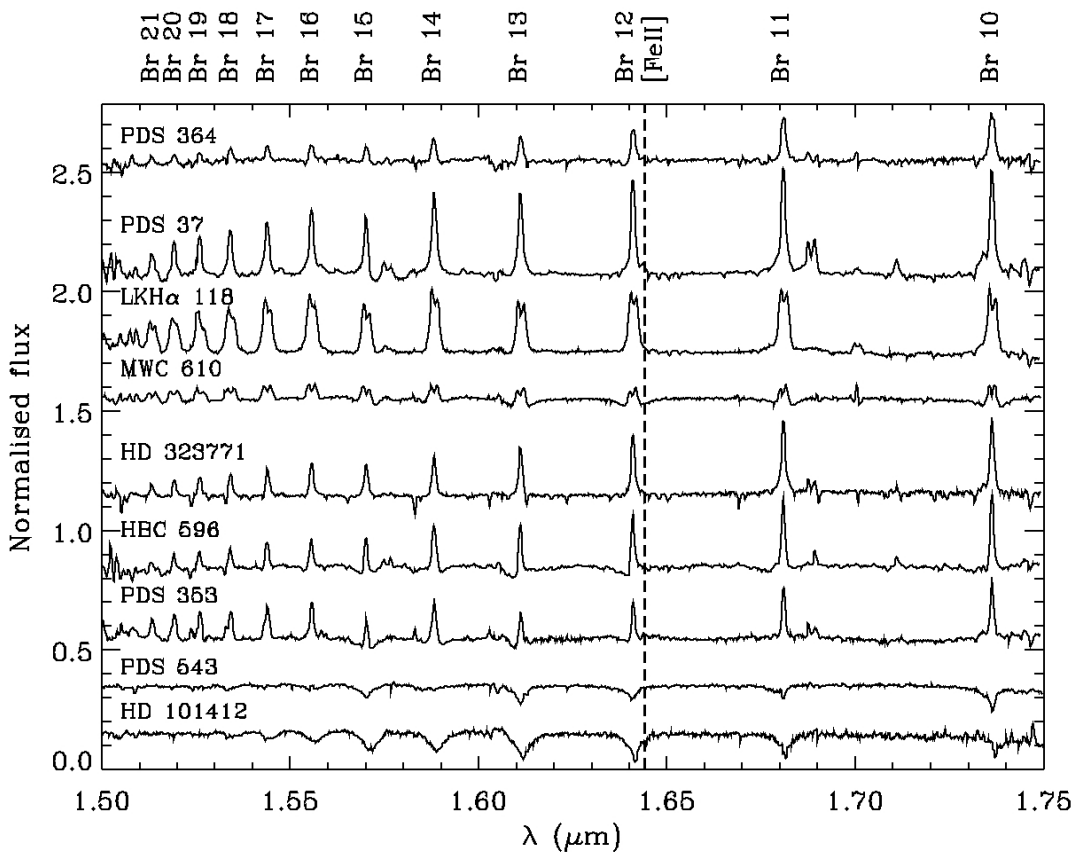

Figure 4.1: *The spectra of the sample.*

several binary systems, e.g. PDS 353. The image of PDS 37 appears to exhibit extended nebulosity around the central star. The extended emission is closely coincident with the continuum emission, which indicates that this region is scattered star light rather than intrinsic emission. Therefore, these images contain no evidence for extended emission which could be associated with outflow activity.

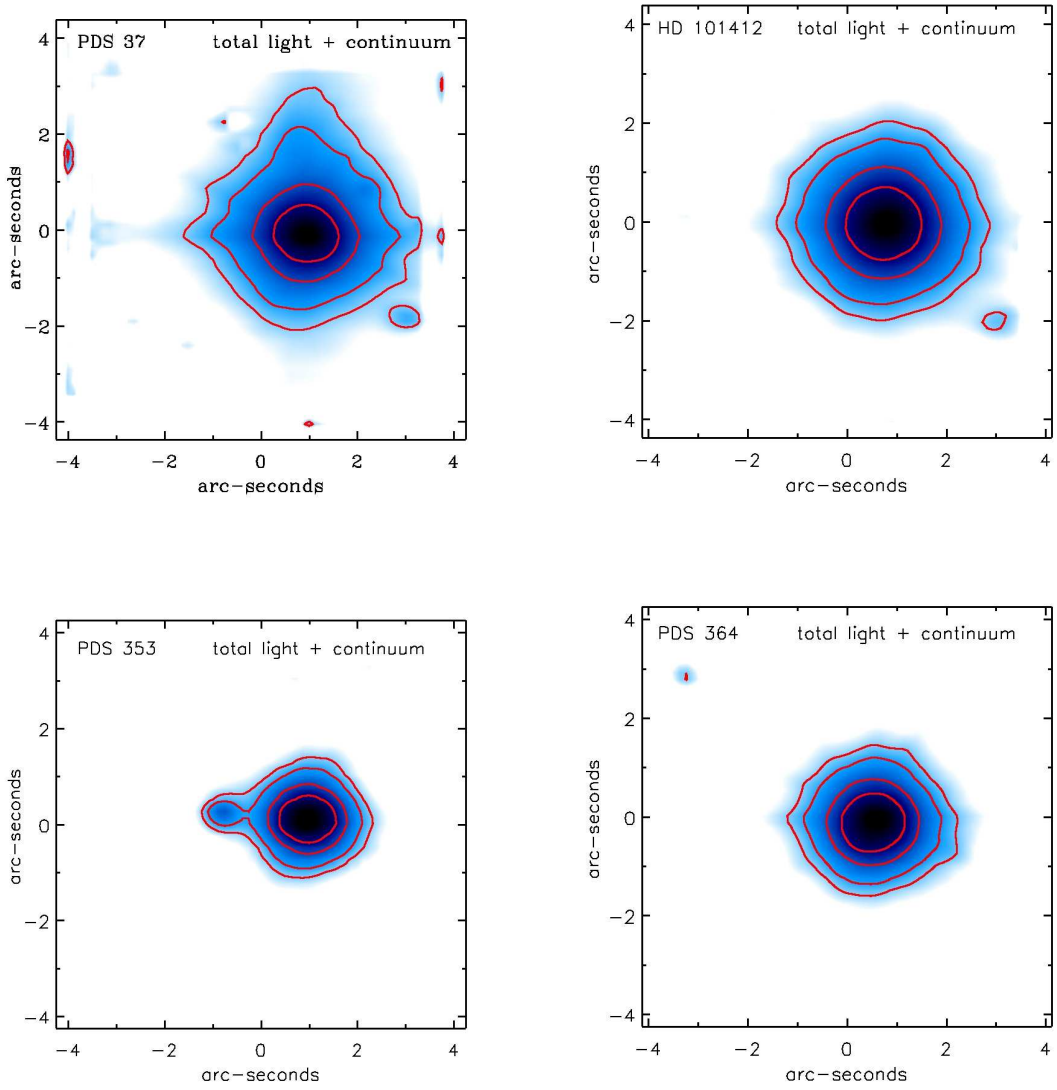

Figure 4.2: *Integrated light (1.5–1.75 μm) and continuum images of the sample. The image brightness is scaled logarithmically with a maximum of 95 per cent and a minimum of 15 per cent of the maximum image brightness. The contours mark the extrapolated continuum emission over the wavelength range and are spaced at* $\log_{10}(\mathrm{cont}_{\mathrm{max}})/1.5$, $\log_{10}(\mathrm{cont}_{\mathrm{max}})/2$, $\log_{10}(\mathrm{cont}_{\mathrm{max}})/3$ *and* $\log_{10}(\mathrm{cont}_{\mathrm{max}})/4$.

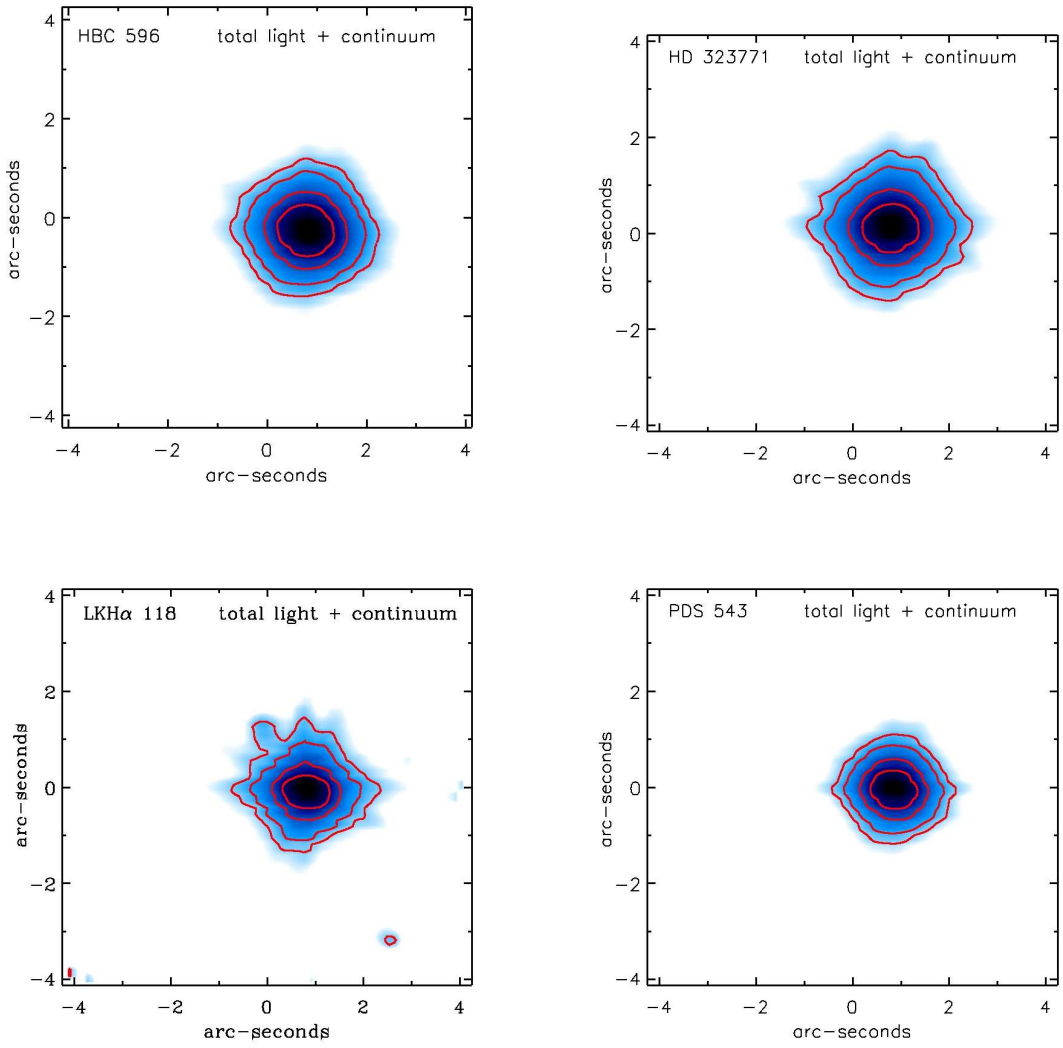

Figure 4.2 continued.

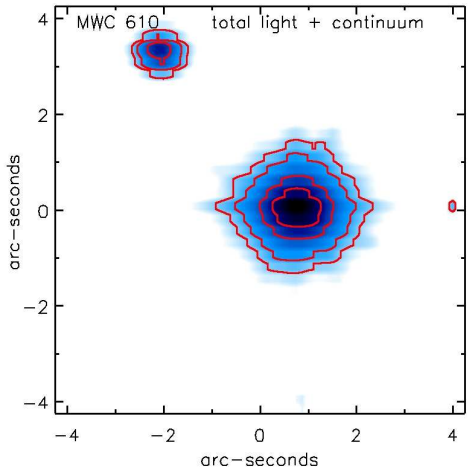

Figure 4.2 continued.

4.3.2 Extended [FeII] emission

The integrated images presented in Figure 4.2 do not exhibit any evidence of extended emission indicative of outflow activity. However, in principle, such emission could be present but undetected due to a low contrast with the central star. To continue the search for outflows, images of the stars in the sample were made in the [FeII] line at 1.644 μm and several of the Br lines observed in emission. To do this, 3D data cubes were extracted from the total data cubes using a region of the cube centered on the line in question with a width of 0.002 μm or $\sim$350 km s^{-1}, which were then collapsed in the wavelength direction. Continuum emission was subtracted using a low order polynomial fit to the data cube over the continuum adjacent to the 1.644 μm window. This procedure revealed extended [FeII] emission in the vicinity of one object, PDS 37 (see Figure 4.3). No extended Br line emission was detected around any of the objects.

4.3.2.1 PDS 37

The extended [FeII] emission associated with PDS 37 is presented in Figure 4.3. This emission does not point directly back to the star, and is instead offset by approximately 45° from the line between PDS 37 and the base of the emission. It appears that there is some emission surrounding the central star. However, this follows the extension of

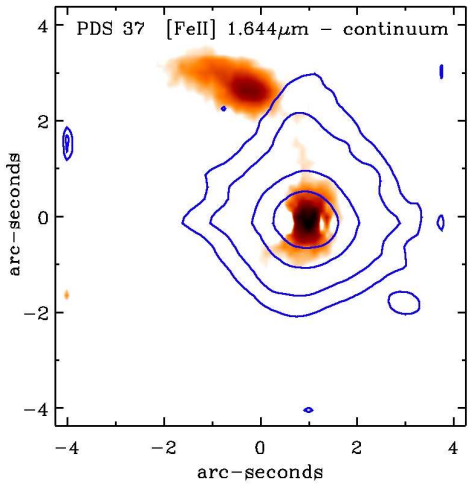

Figure 4.3: *The [FeII] 1.644 μm− continuum image of the PDS 37. The image brightness is scaled logarithmically with a maximum of 95 per cent and a minimum of 15 per cent the maximum image brightness. The contours mark the extrapolated continuum emission over the [FeII] wavelength range and are spaced at* $\log_{10}(\mathrm{cont_{max}})/1.5$, $\log_{10}(\mathrm{cont_{max}})/2$, $\log_{10}(\mathrm{cont_{max}})/3$ *and* $\log_{10}(\mathrm{cont_{max}})/4$.

the continuum emission and thus may be continuum emission that was not completely removed by fitting the continuum with a low order polynomial function.

Since the [FeII] emission is not obviously connected to PDS 37, it may trace an unrelated Herbig-Haro object or the jet of a companion of PDS 37. If the emission does trace the jet of a companion the companion must be in an early evolutionary phase and thus dim in the NIR (as a counterpart to the [FeII] emission was not seen in the adjacent continuum – see Figure 4.2). Constraining the source of the emission requires probing the physical conditions in the emitting region. Here, the [FeII] forbidden emission lines can be used to determine the electron density in the region of extended emission.

Spectra were extracted from several regions in the extended [FeII] emission and at the position of PDS 37 (see Figure 4.4). The resultant spectra are presented in Figure 4.5. As can be seen, little or no [FeII] emission is evident at the position of PDS 37, while only [FeII] emission is observed in the extended region of emission. Subsequent

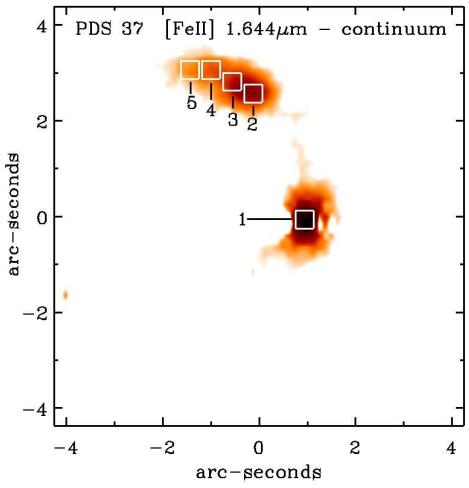

Figure 4.4: *The regions used to extract spectra in the case of PDS 37.*

observations with higher spectral resolution ($\sim 60\mathrm{km\,s^{-1}}$) using XSHOOTER confirm that no [FeII] emission at 1.644 μm is present in the stellar spectra (Oudmaijer, 2010, priv. comm.). Using the model of Nisini et al. (2002) the ratio of the emission lines at 1.644 and 1.600 μm were used to determine the electron density of the emitting material (see Figure 4.6). The determined densities are of the order of 5,000–10,000 $\mathrm{cm^{-3}}$ and are similar to those of previously studied jets (see e.g. Perrin & Graham 2007). Furthermore, assuming that the driving source lies in the high density region at the base of the extended emission, the electron densities decrease with increasing distance from the apparent source of the shocked emission. This is in agreement with previous studies of bipolar jets (Perrin & Graham 2007; Podio et al. 2006). Therefore, these data are consistent with the scenario that the extended emission in the environment of PDS 37 traces the jet of a source that is not yet visible in the continuum. The absence of a South-Western counterpart to the 'lobe' of the jet could be due to obscuration of the opposing lobe by a massive circumstellar disk. This is in keeping with the proposed early evolutionary status of the source object.

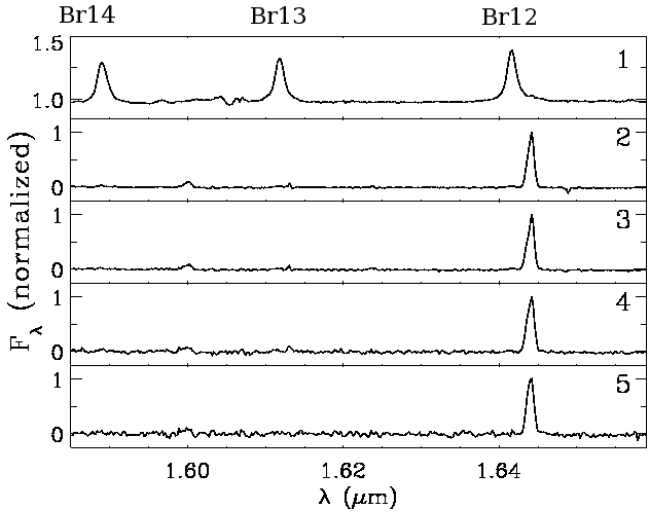

Figure 4.5: *The spectra extracted from the regions indicated in Figure 4.4. Note that the region of [Fe*II*] emission does not exhibit any of the Br lines, indicating that it is not scattered light.*

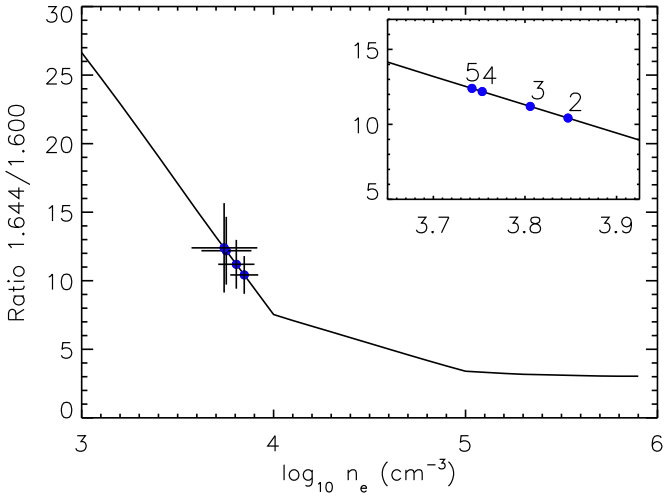

Figure 4.6: *The ratio of the Fe*II *lines at 1.644 and 1.600 μ*m *line emission in the spectra presented in Figure 4.5. The solid line marks the predicted ratio as a function of electron density for a temperature of 4000 K (which is no different from the line corresponding to 15,000 K within the observational errors), which is taken from Nisini et al. (2005).*

Table 4.3: *The uncertainty in the flux of the continuum subtracted [FeII] images.*

Object	rms_1	rms_2
	$Wm^{-2}\mu m^{-1}\,arcsec^2 \times 10^{-17}$	$Jy\,arcsec^2 \times 10^{-5}$
PDS 37	7	6
HD 101412	6	5
PDS 353	7	6
PDS 364	2	2
HBC 596	5	5
HD 323771	5	5
LKHα 118	9	8
PDS 543	14	13
MWC 610	34	31

Based on the images presented in Figure 4.2, it would appear that Herbig Be stars do not drive collimated, optical outflows. However, this is only true if the data are of sufficient quality to detect such outflows. The detection of one area of extended emission close to PDS 37 suggests that this is the case. To put this statement on a firmer footing requires assessing the uncertainties in the images presented in Figure 4.3. The one sigma uncertainty in the flux of the images presented in Figure 4.3 is typically 0.0001 Jy/arcsec^2 (see Table 4.3). This is comparable to the data of Perrin & Graham (2007), who detect a collimated outflow emanating from the Herbig Ae stars LKHα 233. This suggests that if outflows similar (both in terms of physical properties and distance) to that emanating from LkHα 233 were present in the sample they would have been detected (at least in the integrated image – the data of Perrin & Graham (2007) is deeper allowing the observed jet to be imaged at different velocities). Therefore, these data confirm that Herbig Be stars do not drive small scale collimated outflows. However, uncollimated Herbig-Haro objects as reported by Poetzel et al. (1992) are not detected either. Consequently, these data are not necessarily consistent with the scenario in which massive Herbig Be stars drive poorly collimated optical outflows either.

4.3.3 The HI lines

No extended HI emission was detected in the reconstructed images. Therefore, this section explores the potential of spectroastrometry to probe the origin of this unresolved emission. This technique has been used in the past to probe the source of the emission lines of T Tauri stars on AU scales (see e.g. Whelan et al. 2004; Podio et al. 2006). More recently, Davies et al. (2010) used spectroastrometry and K-band IFU data to detect an unresolved bipolar outflow from the MYSO W33A. However, applications of this technique to HAe/Be stars have mainly concentrated on detecting binary systems (see Garcia et al. 1999; Baines et al. 2006, and Chapter 2). In this chapter, spectroastrometry is used to probe the source of the emission lines of the sample with an angular precision of ~ 0.5 mas (0.25 AU at 500 pc). In this respect, binary signatures are essentially contaminant features as they will mask the smaller signatures due to sources of line emission such as disks. However, by observing in the NIR the seeing is significantly smaller than in the previous observations in the optical (and can be further reduced with the use of AO). Consequently, many intermediate separation systems can be spatially resolved, allowing spectroastrometry to probe the circumstellar environment of the star in question.

Spectroastrometry of the emission lines was conducted by tracing the photocentre of the emission in the North–South (NS) and East–West (EW) directions at each dispersion coordinate of the data-cubes. In turn, this was done by fitting the spatial distribution of flux with a Gaussian function in both the x and y directions. As a result of the small pixels (0.125 arcsec in the x direction) and the narrow spatial profiles (down to $\sim$0.4 arcsec), the resulting positional accuracy is typically $\sim$0.5 mas. However, it should be noted that the pixels are not square but are rectangular. The pixel sizes are 0.125$\times$0.250 arcsec. Therefore, the positional accuracy in the y direction is typically less than in the x direction.

The sample exhibits a range of signatures ranging from no positional excursions to centroid offsets of up to 10 mas. Two objects (PDS 353 and PDS 364) exhibit positional offsets indicative of binary systems. Since such signatures are conceptually easy to understand, these two signatures are presented in detail with the aim of assessing the

quality of the data.

4.3.3.1 Binary signatures

Both PDS 353 and PDS 364 exhibit positional offsets over the Br emission lines of ∼10 mas toward one side of the continuum position (see Figure 4.7). Since these positional offsets only occur in one direction they indicate the presence of previously unknown binary companions of PDS 353 and PDS 364 (see Chapter 2 for a discussion of the spectroastrometric signature of binary systems). The PDS 353 system is almost resolved (see Figure 4.2), providing confirmation that the spectroastrometric signature traces a real change in the flux distribution. However, there is no indication that PDS 364 is a binary system in the reconstructed images. It is noted that the binary signatures are generally consistent over the various Br emission lines in the data, providing compelling evidence that these features are real and not due to a systematic effect.

It is also noted that since the spectroastrometric observations of these objects are dominated by binary signatures, it would be challenging to use these data to probe the origin of their emission lines. Therefore, these objects are henceforth discarded from the spectroastrometric sample. Nonetheless, these signatures demonstrate that spectroastrometry of IFU data can probe the source of emission lines with sub-milliarcsecond positional accuracy via excursions only several milli-arcseconds in size.

4.3.3.2 Artifacts

The majority of the remaining objects exhibit positional offsets of a few mas in the NS direction. In general, these signatures consist of excursions to opposite sides of the continuum position over the blue and red sides of emission lines (see Figure 4.8). In general, the appearance of these signatures is consistent across different emission lines. However, when viewed in the x, y plane, the signatures do not trace a consistent position angle (see Figure 4.9), suggesting that they are not real. Furthermore, the fact that these signatures predominately occur in the NS direction also casts doubt upon their nature.

This NS direction corresponds to the axis with the largest pixels (0.25 arcsec). In principle, under-sampling could result in artificial signatures as the data presented in

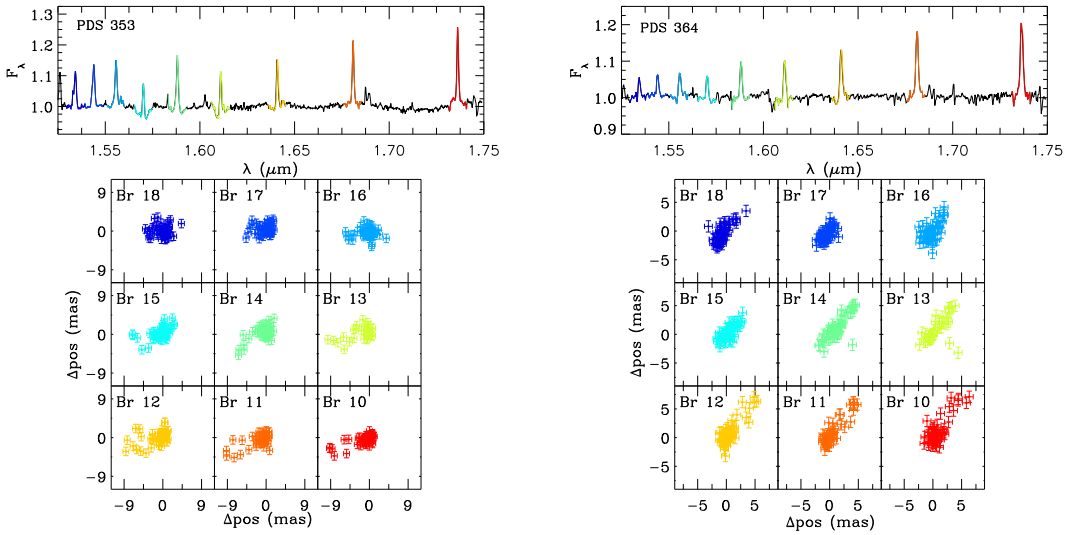

Figure 4.7: *The spectroastrometric signatures of PDS 353 and PDS 364 in the xy plane.*

the figures above consist of the weighted average of co-added individual data cubes corresponding to multiple observations. If the spatial profile during one observation is insufficiently sampled, the continuum position could appear to shift. When combined with a slight offset in wavelength, this could result in a signature similar to those discussed here.

To investigate this possibility, spectroastrometry was conducted on individual observations. The data were obtained using an ABBAAB nodding sequence alternating between the target object and a pre-defined sky region. Each A or B observation produces one data file, which are normally combined to create the final data-cube. Here spectroastrometry is conducted upon each individual file. In Figure 4.10 the individual spectroastrometric signatures of PDS 37 (an object with potential artifacts in the y direction) and PDS 364 (an object with a consistent binary signature) are compared. It can be seen that in both cases the spectroastrometric signatures in the x direction are consistent. In contrast, the spectroastrometric signatures of PDS 37 over the line in question (Br 17) in the y direction are not consistent. One of the observations contains an excursion of $\sim$2 mas (the short dashed line) while another data-set contains no signature (the dotted line). Since the seeing was relatively constant during the individual

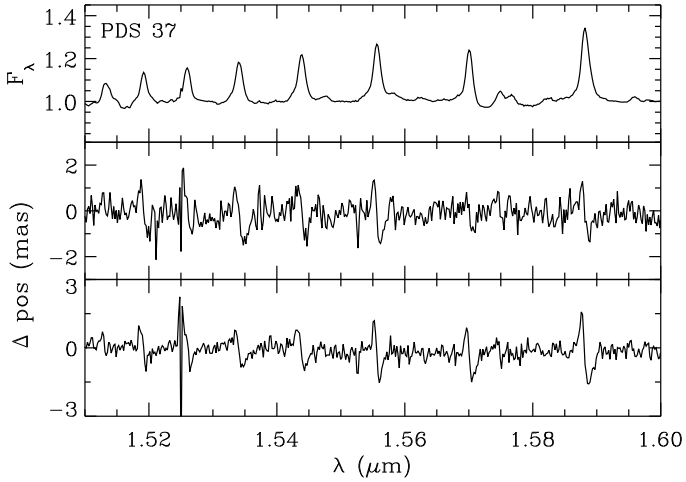

Figure 4.8: *The spectroastrometric signatures of PDS 37. The middle panel presents the spectroastrometric signature in the EW direction and the lower panel presents the spectroastrometric signature in the NS direction. The top panel presents the average, normalised spectrum.*

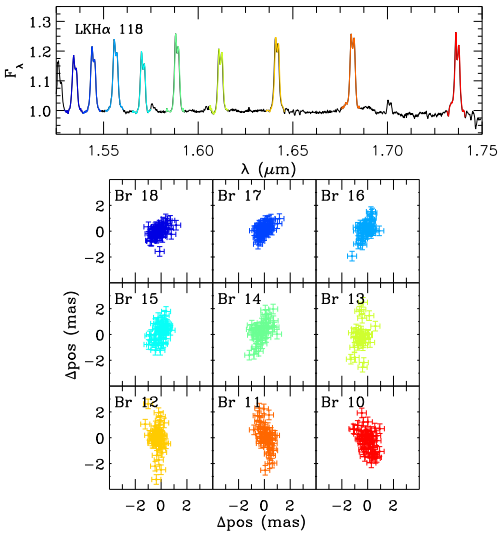

Figure 4.9: *The spectroastrometric signatures of LKHα 118.*

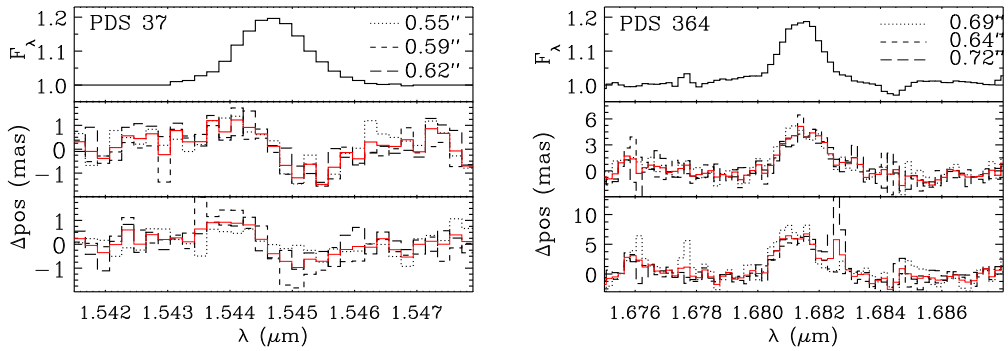

Figure 4.10: *The spectroastrometric signatures over the Br 17 emission of PDS 37 and the Br 11 emission of PDS 364. The top panel displays the average emission line profile. The lower panels display the spectroastrometric signatures of the individual observations which comprise the total data-set for each object. The middle panel presents spectroastrometric data in the x direction and the lower panel contains the spectroastrometric data in the y direction.*

observations, this inconsistency is difficult to explain. Therefore, these signatures may be artifacts and should be treated with caution. It is noted that this inconsistency is only evident over certain lines, which explains why the signatures in the x, y plane over different Br lines are not consistent.

Since the spectroastrometric signatures in the y direction are present in the individual observations, the signatures seen in the final data cannot be induced by co-adding the individual data. However, the individual data files are already the result of several internal co-adds as the number of exposures per integration (NDIT) was generally ∼10. The artifacts could have been introduced at this stage. It is noted that in many cases of objects with questionable spectroastrometric signatures in the y direction, the seeing profile was insufficiently sampled (i.e. <2 pixels across the FWHM). This is demonstrated in Figure 4.11. In seeing of ∼0.5 arcsec, the seeing profile is under-sampled in the y direction. This could lead to artificial shifts in the centroid between two exposures. When combined with an offset in wavelength this could introduce an artifact in the final data. It is noted the prominent spectroastrometric signatures of PDS 353 and PDS 364 (the two binary detections) are consistent across multiple observations and different

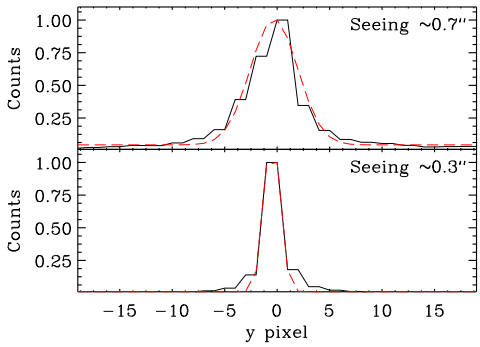

Figure 4.11: *Comparisons of the spatial profile of PDS 364 and LKHα 188 in the y direction – where the pixels are largest.*

seeing conditions, suggesting that they are real. The seeing during the observations of PDS 353 and PDS 364 was relatively large (1.0 and 0.7 arcsec), which substantiates that the NS artifacts are due to under-sampling the seeing. Therefore, it is surmised from hereon that this is the case. It is noted that this is readily verifiable by conducting observations with a smaller pixel size (e.g. 0.1 or 0.025 arcsec) or by utilising a drizzle technique (see e.g. Fruchter & Hook 2002).

4.3.3.3 The spectroastrometric signature of PDS 37

To negate the problem caused by insufficient sampling of the spatial profile, all the spectroastrometric signatures in the NS direction are discarded. In the EW direction the pixels are 0.125 arcsec wide, allowing even the smallest spatial profile to be sufficiently sampled. Besides the objects with binary signatures (PDS 353 and PDS 364) only PDS 37 exhibits spectroastrometric signatures in this direction. Examples of these signatures are shown in more detail in Figure 4.12.

The positional offsets over the Brackett emission lines extend in one direction over positive velocities and in the opposite direction over negative velocities. Such a signatures are consistent with the line emission originating in a rotating disk or a bipolar outflow. In both scenarios, the blue and red-shifted emission is located on opposite sides of the continuum position resulting in an 's' shaped signature, similar to those presented in Figure 4.12. In principle, the signatures of disks and outflows can be differentiated

via the behaviour of the positional excursions. In a disk, the outer regions rotate less rapidly than the inner regions. Since the outer regions contribute most to the spectroastrometric signature, the largest positional offset due to a disk occurs at low velocities. Conversely, outflows are generally accelerating. Therefore, in the spectroastrometric signature of an outflow, the highest velocities are associated with the largest positional excursions. The spectroastrometric signatures of PDS 37 appear most consistent with the signature of a rotating disk. However, the limited resolution ($100\,\mathrm{km\,s^{-1}}$) is not sufficient to make an unambiguous differentiation between the two scenarios.

It is noted that the largest positional excursions occur at velocities of $\sim 100\,\mathrm{km\,s^{-1}}$. In a Keplerian disk around a 10 $M_{\odot}$ star (an approximation for an early type B star) such a velocity corresponds to a radius of approximately 1 AU or 1.4 milli-arcseconds at a distance of 720 pc. Spectroastrometry traces centroid offsets which are dependent on the flux ratio between the line in question and the adjacent continuum. Consequently, spectroastrometry does not return the true distance between the source of an emission line and the continuum (see Chapter 5). Therefore, the radius of 1 AU determined by assuming the signature is due to a disk is inconsistent with the 1 mas photo-centre excursions observed. Consequently, it is suggested that the spectroastrometric signatures presented in Figure 4.12 cannot be due to a disk and thus most likely trace an unresolved, bipolar outflow. It should be noted, the positional signatures are very similar to the artifacts discussed previously. However, in this case the spatial profile of the observations is well sampled (i.e. the FWHM spans ∼5 pixels). Therefore, there is no reason to discount these signatures. Nonetheless, observations with greater spectral resolution are required to probe the kinematics of the signature and thus confirm the detection of a small-scale bipolar outflow.

4.4 Discussion

This chapter presents near infrared integral field unit observations of a sample of Herbig Be stars in order to search for evidence of outflows traced by shock excited emission lines. In addition, spectroastrometry is used to probe the HI line emission of the sample

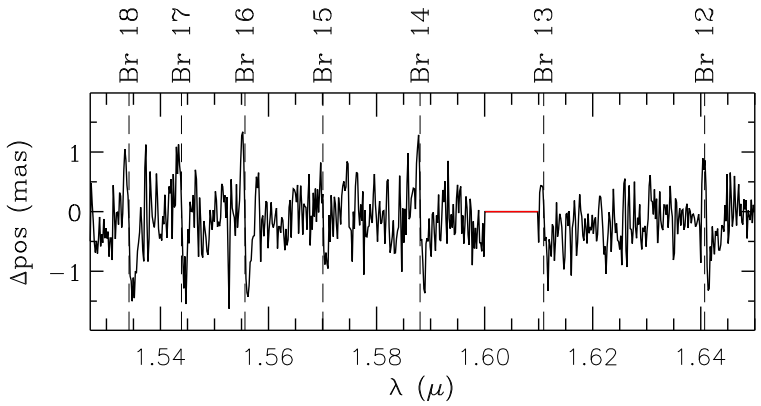

Figure 4.12: *The spectroastrometric signature of PDS 37 in the EW direction.*

on AU scales. Here the results will be placed into context with other work and their implications will be discussed.

Searching the environments of the Herbig Be stars for extended [FeII] emission has revealed that no objects in the sample drive outflows traced by shocked emission. An earlier study of the optical forbidden line emission of HAe/Be stars found that 15 per cent of such stars drive optical outflows (Corcoran & Ray 1997). However, the spectral type of the objects observed ranged from A8 to B0. These data demonstrate that Herbig Be stars as a group do not exhibit optical outflows (excluding isolated detections, e.g. R Mon, Boehm & Catala 1994). Neither collimated outflows or uncollimated outflows traced by Herbig Haro objects were detected (with the possible exception of PDS 37). Therefore, the data do not constrain the location of the proposed 'transition to more poorly-collimated outflows' (McGroarty et al. 2004), if indeed such a transition occurs.

The lack of outflows in the sample could reflect a lack of active accretion, indicating that the Herbig Be stars in the sample are relatively evolved young stellar objects, which is in keeping with the short pre-main-sequence contraction time of massive objects (see e.g. Palla & Stahler 1993). However, several of the objects in the sample exhibit signs of ongoing accretion. Four of the stars in the sample have been observed with the

XSHOOTER instrument on the VLT as part of an extensive spectroscopic survey of HAe/Be stars in the UV, optical and NIR (Oudmaijer, 2010, priv. comm.). Two stars in the sample exhibit HeI emission at 1.083 μm with strong P-Cygni profiles, indicative of accretion driven winds (see e.g. Edwards et al. 2006). Furthermore, two of the objects also exhibit CO 1st overtone bandhead emission at 2.3 μm, indicative of a dense circumstellar disk (see e.g. Bik & Thi 2004; Blum et al. 2004). Therefore, it would appear that at least some of the objects in the sample posses disks and are continuing to accrete. Consequently, it might be expected that some of the objects in the sample should drive outflows, although this is dependent on the rate of accretion, as modest accretion is presumably not sufficient to drive an outflow.

Not much is known about the accretion rates of Herbig Be stars (Garcia Lopez et al. 2006), but they may be of the order of $\sim 10^{-5} M_{\odot} yr^{-1}$ (Kraus et al. 2008b). Such an accretion rate appears sufficient to drive a collimated outflow similar to those associated with T Tauri stars (see e.g. Melnikov et al. 2008). Therefore, the outflows that are thought to be driven by young early type objects (see the evolutionary scenario proposed by Beuther & Shepherd 2005) must be disrupted somehow, perhaps by the dissipation of the outer disks due to the UV radiation of early type HBe stars (see Alonso-Albi et al. 2009, and references therein). Alternatively, outflows from high mass sources may be less efficient than those associated with lower mass objects and require a higher accretion rate than is expected based on an extrapolation of the accretion rate of low mass outflow sources. However, this is assuming all Herbig Be stars accrete at $\sim 10^{-6} - 10^{-5} M_{\odot} yr^{-1}$, when in fact few accretion rates have been directly determined. Further observations to determine the accretion rates of a sample of Herbig Be stars are required to test this hypothesis.

Using spectroastrometry, the source of the HI Br emission lines of the sample was probed with a typical positional accuracy of $\sim$0.5 mas. This translates into probing the origin of these emission lines on AU sized scales. This chapter presents an assessment of the spectroastrometric signatures observed. It is shown that the rectangular pixels of the IFU can result in under-sampling the flux distribution, which in turn can lead to artificial signatures. The technique of IFU spectroastrometry is still in its infancy,

as only two papers have been published utilising this technique (Garcia et al. 1999; Davies et al. 2010). Subsequently, systematics in IFU spectroastrometry are still poorly understood (contrary to conventional spectroastrometry, see e.g. Brannigan et al. 2006). Therefore, this investigation into systematic effects associated with rectangular spatial pixels represents an important limit to the applicability of the technique.

Excluding binary signatures and artifacts caused by insufficient sampling of the spatial profile results in the detection of a spectroastrometric signature for one object (PDS 37). The spectroastrometric signature of PDS 37 over the HI Brackett emission lines suggest that they originate in a bipolar outflow. This is similar to the case of the massive young stellar object W33A which was recently found to drive a bipolar outflow traced by Brγ emission (Davies et al. 2010). This indicates that Herbig Be stars and massive young stellar objects form in a similar fashion, as expected if Herbig Be stars form via disk accretion. It is noted that very few Herbig Be stars are known to drive optical outflows. Therefore, if the detection of an outflow traced in Br line emission emanating from PDS 37 is confirmed, this will represent a significant addition to the sample of early type young stellar objects driving 'optical' outflows.

With the exception of the two binary systems and PDS 37, no spatial signatures are detected. Although the positional accuracy is high ($\sim$0.5 mas), this does not necessarily exclude the presence of disks approximately 1 AU in size. Alternatively, the HI emission could originate in a wind approximately 1 AU in size. The possible detection of a HI emitting outflow associated with PDS 37 is at odds with the scenario of Vink et al. (2002) in which the line emission of Herbig Be objects originates from circumstellar accretion disks. However, PDS 37 is the exception, as most of the stars in the sample do not exhibit spectroastrometric signatures. Therefore, the data do not necessarily rule out that the line emission of the other objects originates in circumstellar disks.

4.5 Conclusions

This chapter presents near infrared integral field unit spectroscopic observations of a sample of nine Herbig Be stars. A search for outflows is conducted by making images of the circumstellar environments of the stars in the shock excited [FeII] line at 1.644 μm.

Here the salient findings of this work are summarised.

None of the Herbig Be stars in the sample are observed to drive collimated optical outflows. Only one of the stars in the sample (PDS 37) is associated with extended shock excited emission. This may trace the jet of a deeply embedded companion star which has yet to become visible in the NIR. Given the lack of outflow activity the data cannot be used to test the hypothesis that there is a transition from well collimated outflows at T Tauri masses to poorly collimated outflows at higher masses. The lack of outflow activity might presumably be linked to the end of accretion activity, as massive objects have short pre-main-sequence contraction timescales. However, several of the objects in the sample exhibit evidence of accretion driven winds and dense circumstellar disks. This suggests that if Herbig Be stars drove outflows in the same fashion as T Tauri, outflows would have been detected. Therefore, the connection between accretion and ejection at high masses may be different than that at solar masses.

In addition, this chapter explores the potential of spectroastrometry to probe the source of the prominent HI emission lines of the Herbig Be stars in the sample with sub-milli-arcsecond accuracy. Two objects are found to be binary systems which display positional excursions of $\sim$10 mas. These signatures are consistent across multiple observations and different emission lines. However, the spectroastrometric observations of other objects contain features which are not internally consistent, suggesting that they are artifacts. It is demonstrated that this is likely to be a consequence of under-sampling the seeing. Therefore, this chapter highlights some of the systematics that must be taken into account when applying spectroastrometry to integral field unit spectroscopy. Only one object, PDS 37, exhibits a positional signature that is not attributable to a systematic effect or a binary system. This signature has an amplitude of $\sim$1 mas and is consistent with the line emission originating in a bipolar outflow. Observations with higher spectral resolution are required to probe the kinematics of the line emission and confirm the detection.

Chapter 5

Constraining the kinematics of Be star disks with spectroastrometry

5.1 Introduction

As shown in Chapter 2, it appears that HAe/Be star binary systems form via disk fragmentation. Since the observational definition of HAe/Be stars includes objects with masses in excess of $8M_{\odot}$, this indirectly confirms the latest simulations of massive star formation via disk accretion, which also feature binary formation through disk fragmentation. Nonetheless, to firmly establish that the most massive stars form via disk accretion requires the direct detection of an accretion disk around a massive young stellar object. Rotating structures have been detected around massive protostars. However, due to the generally large distances to such objects, even with high resolution observations these structures are typically very large (and massive, e.g. 14,000 AU and $40M_{\odot}$, see e.g. Sandell & Wright 2010; Zapata et al. 2009). Consequently, it has been argued that such structures are unstable and may be transient objects, and thus should not be identified as rotationally supported disks (Cesaroni et al. 2007). Therefore, to conclusively establish whether massive stars form via disk accretion requires the detection of small-scale, of the order a few AU, gaseous disks. This in turn requires observations with high spectral resolution and the capability to probe small spatial scales. Spectroastrometry is one of the few techniques which offers this combination.

However, as already seen in this thesis, the environments of young stars are relatively complex and the spectroastrometric observations of such objects may be dominated

by the spatial signatures of unresolved binary systems and other phenomena, rather than circumstellar disks. Therefore, to assess the sensitivity of spectroastrometry to circumstellar disks, observations of objects which possess disks but have less complex circumstellar environments than YSOs are required. Be stars, main sequence B type stars which possess a small-scale, gaseous disk, represent the ideal objects for this test as they are already known to be surrounded by circumstellar disks. Furthermore, as Be stars are relatively bright, a sample of $\sim$10 objects can be observed in only a few hours of observing, unlike YSOs which are several magnitudes dimmer. Therefore, Be stars provide the perfect sample for a pilot study to assess the sensitivity of spectroastrometry to small-scale, circumstellar disks. To this end, this chapter presents spectroastrometric observations of a sample of Be stars over the Hα line with the aim of evaluating spectroastrometry as a means of detecting small-scale circumstellar disks. The technique is then applied to young stellar objects in a subsequent chapter (6).

However, this exercise is not simply a proof of concept test with spectroastrometry before the technique is applied to detect disks around young stellar objects. Spectroastrometry offers one of few opportunities to directly probe the kinematics of Be star disks. Recent work with optical interferometry has determined the kinematics of four Be star disks (Meilland et al. 2007b,a; Carciofi et al. 2009; Pott et al. 2010). However, as these present two different kinematical structures (three appear to rotate in a Keplerian fashion while the rotation law of the remaining disk is substantially shallower) the rotation of Be star disks is still far from understood. In addition, the spectral resolution of AMBER is, in some cases, only just sufficient to resolve the observed velocity structure. Therefore, to better constrain the kinematics of Be star disks, observations of a sample of Be stars with high spectral and angular resolution are required. This chapter addresses these requirements.

Determining the kinematics of Be star disks is important as the rotation of such disks may retain an imprint of their formation mechanism. While the presence of disks around Be stars has been established for some time, their formation mechanism remains unknown. Most Be stars rotate rapidly, of the order of many 100s of km s^{-1} (Porter 1996; Rivinius et al. 2006). This rapid rotation may allow material to be lifted of the

surface off the star and into orbit, thus forming the gaseous circumstellar disk (Struve 1931). However, this requires the star to rotate at close to its critical rate, and it is not known if Be stars rotate this rapidly (Cranmer 2005). Therefore, alternative scenarios such as non-radial pulsations (Rivinius et al. 2003; Cranmer 2009) and Magnetically-Torqued-Disks (e.g. Cassinelli et al. 2002; Brown et al. 2008) have been proposed to lift the material off the star. These models result in Keplerian rotating orbits due to viscosity in the disk and can be described by the viscous deccretion disk family of models (Lee et al. 1991; Porter 1999). It should be noted that magnetically driven winds - contrary to the MTD model - end up as angular momentum conserving disks, just like the Wind Compressed Disk model (Bjorkman & Cassinelli 1993). Therefore, determining the kinematics of Be star disks can directly constrain their formation mechanism. Consequently, the aim of this chapter is not only to demonstrate that spectroastrometry can be used to detect small-scale disks (of the order of 10s of $R_\star$) but also to directly determine the kinematics of a sample of Be star disks for the first time.

This chapter is structured as follows. In Section 5.2 the sample selection, observations and data reduction processes are described. The data are then presented in Section 5.3. A simple model used to fit the observed Hα lines and predict the resultant spectroastrometric signatures is presented in Section 5.4. The spectroastrometric data is then compared to the predicted signatures in Section 5.5. A relatively simple model is used as this allows the line profiles of a large sample to be fit. More sophisticated models take a prohibitively long time to run and therefore cannot be used to fit the data. However, to assess the possible shortcomings of the simple model, the emission line profile of one object is modelled with a state-of-the-art, 3D, Monte Carlo radiative transfer code (described in Section 5.6) in Section 5.6.2. The chapter is concluded in Section 5.9.

5.2 Observations and data reduction

5.2.1 Sample selection

Clearly, Be stars with previously detected disks are the most promising targets for the aims of this chapter. Therefore, the initial sample comprised of objects which have been

shown to be surrounded by disks with long baseline, optical interferometry (see e.g. Quirrenbach et al. 1997; Tycner et al. 2004). However, only a handful of Be star disks have been directly resolved with such observations, and several of these are located in the Northern hemisphere (and the observations in this chapter where obtained at the VLT in the Southern hemisphere). Therefore, this initial sample required supplementing. To the first order, the closest disks will be easier to detect, as the closest disks will subtend the largest angle on the sky. However, disks around bright Be stars are also potentially easier to detect as the increased SNR will lead to a high angular precision. Therefore, the sample was supplemented by selecting Be stars from Yudin (2001) and the Bright Star Catalog (Hoffleit & Jaschek 1982) based on distance and $V-$band magnitude. Table 5.1 presents an overview of the sample of Be stars observed.

Table 5.1: *Properties of the sample and details of the observations. The distance to each object is taken from trigonometric parallax (from Perryman et al. 1997). The predicted disk radii and angular sizes are based on the model of Grundstrom & Gies (2006), the objects' spectral types and the observed Hα equivalent widths.*

Object	HD/HR	Spec type[1]	$v \sin i^2$	T_{eff}[3]	Radius[3]	Mass[3]	i	d	Hα ew	Disk radii	Date
			$km\ s^{-1}$	K	$R_\odot$	$M_\odot$	°	pc	Å	R_*/mas	
η Tau	23630/1165	B7III	173 ± 25	12,794	4.1	4.0	44.6[4]	113	−6.5	5.5/0.9	11/01/09
ζ Tau	37202/1910	B2IV	241 ± 27	23,014	6.3	10.9	85.0[7]	128	−8.1	3.9 / 0.9	13/01/09
α Col	37795/1956	B7IVe	184 ± 5	12,794	3.4	3.7	44.9[4]	82	−10.2	6.2/1.2	14/01/09
β CMi	58715/2845	B8Ve	244 ± 6	11,508	2.6	3.0	54.9[4]	52	−7.2	6.6/1.5	09/12/08
α Eri	10144/472	B3Ve	207 ± 9	19,320	4.1	6.9	24.0[6]	44	+2.7	2.4/1.0	29/10/08
α Eri	also observed on: 30/10/08, 25/11/08 and 09/12/08										
δ Cen	105435/4621	B2IVne	207 ± 46	23,014	6.3	11.0	41.6[4]	121	−18	4.1/0.3	26/02/09
η Cen	127972/5440	B1.5Vne	291 ± 32	24,749	5.3	11.3	57.8[4]	95	−11	4.2/1.1	04/03/09
ω Ori	37490/1934	B3IIIe	171 ± 18	19,320	6.8	8.7	42 ± 7[7]	497	−7.1	4.0/0.25	11/01/09
ν Gem	45542/2343	B6IIIe	193 ± 14	14,191	4.4	4.8	52.5[4]	154	−2.8	4.3/0.6	21-02-09
EW CMa	56014/2745	B3IIIe	144 ± 5	19,320	6.8	8.7	72.6[4]	483	−6.5	3.9/0.3	10-02-09
MV Vel	89890/4074	B3IIIe	70 ± 7	19,320	6.8	8.7	9.1[6]	–	+1.6	2.5/–	10-02-09
V863 Cen	105382/4618	B6IIIe	111 ± 10	14,191	4.4	4.8	15.7[6]	115	+3.2	2.8/0.5	16-03-09

1: SIMBAD, 2: Yudin (2001), 3: Straizys & Kuriliene (1981), 4: Frémat et al. (2005), 5: (Carciofi et al. 2009), 6: Assuming the star is rotating at 90 per cent of its critical velocity and neglecting gravity darkening, 7: Neiner et al. (2003).

5.2.2 Observations

The spectroastrometric data presented in this chapter were obtained with UVES (UV-Visual-Echelle-Spectrograph, see Dekker et al. 2000) on UT2 of the VLT. The observations were conducted in service mode in period 82 during 2008 and 2009. Only the red arm of the instrument was used to concentrate upon the Hα line. UVES uses a mosaic of two CCDs (an MIT-LL and an EEV) to record the echelle spectra. The Hα line was located on the MIT-LL chip. The spatial pixel size was $0.16''$, which is more than capable of resolving the spatial profiles of the data as the average seeing was $0.85''$. A Hα filter was used to isolate the order containing Hα and prevent spatial contamination by other orders. The slit width was set to $0.5''$, which resulted in a spectral resolution of $\sim$80,000, or $\sim 4\,\mathrm{km\,s^{-1}}$.

For each star in the sample, data were obtained at four different slit position angles: 0°, 90°, 180° and 270°. This is to identify, and eliminate, any systematic artifacts in the spectroastrometric signatures. To reach sub milli-arcsecond precision a signal-to-noise-ratio (SNR) of approximately 500 per resolution element, per position angle was required. To achieve this, while avoiding saturation over Hα, many short exposures were taken. Due to the brightness of the sample objects (V $\sim$2–5), the total exposure time per object was typically 5–10 minutes (see Table 5.2). Wavelength calibration was conducted with ThAr arc lamp spectra, which were generally obtained after the observation of each science target, most often at a position angle of 270°.

Table 5.2 contains a summary of the observations.

5.2.3 Data reduction

Data reduction was conducted using the Image Reduction and Analysis Facility (IRAF)[(a)] and routines written in Interactive Data Language (IDL). The data were trimmed in the spectral direction to discard vignetted regions and in the spatial direction to remove the over-scan region. Flat field frames, having been corrected for the average bias level, were combined and the averaged flat field was then normalised. The raw data were then

[(a)] IRAF is written and supported by the IRAF programming group at the National Optical Astronomy Observatories (NOAO) in Tucson Arizona (http://iraf.noao.edu/), see Tody (1993).

Table 5.2: *A summary of the observations. Column 6 contains the SNR of the average intensity spectra, which are re-binned by a factor of 5, the number of pixels per resolution element. The positional uncertainties (Column 7) are defined as the average rms in the continuum regions of the positional spectra, which are also re-binned by a factor of 5.*

Object	V (mag.)	Slit-width ($''$)	Exp time (mins)	Seeing ($''$)	$\mathrm{SNR_{Cont}}$	σ_{pos} (mas)
η Tau	2.87	0.5	2.7	0.9	1090	0.2
ζ Tau	3.03	0.5	2.7	1.2	520	0.3
α Col	2.60	0.5	2.7	0.7	1290	0.1
β CMi	2.89	0.5	2.7	0.7	1530	0.1
α Eri	0.50	0.5	1.8	0.8	1030	0.1
δ Cen	2.56	0.5	2.7	0.8	1080	0.1
η Cen	2.32	0.5	2.7	0.9	50	0.3
ω Ori	4.57	0.5	15.2	1.1	1070	0.2
ν Gem	4.14	0.5	13.0	0.6	1850	0.1
EW CMa	4.65	0.5	15.2	0.9	800	0.3
MV Vel	4.50	0.5	16.2	0.7	1285	0.1
V863 Cen	5.12	0.5	17.7	0.9	510	0.1

corrected using the averaged bias frame and the normalised average flat frame. The few saturated exposures were discarded. Finally, the intensity spectra were extracted from the corrected data in a standard fashion. Wavelength calibration was conducted using ThAr arc spectra, generally taken after the science observations at a position angle of 270°.

Spectroastrometry was performed by fitting Gaussian profiles to the spatial profile of the longslit spectra at each dispersion pixel. This resulted in a positional spectrum – the centroid of the Gaussian as a function of wavelength. The continuum position exhibited a general trend across the CCD chip (of the order of 1 pixel). This was removed by fitting a polynomial function to the continuum regions of the spectrum. This set the continuum position of the centroid to zero. Spot checks were used to ensure line effects were not fit by the function.

All intensity and positional spectra at a given position angle were then combined to

make an average spectrum for each position angle. A correction for slight changes in the dispersion across position angles was determined by cross correlating average intensity spectra at each position angle. This was then applied to both the intensity and positional spectra for each position angle. This was to ensure slight changes in wavelength (e.g. due to flexure of the spectrograph) did not introduce spurious signatures when spectra obtained at differing position angles were combined. The average positional spectra for anti-parallel position angles were combined to form the average North-South (NS) and East-West (EW) positional spectra, i.e.: $(0^{\circ} - 180^{\circ})/2$ and $(90^{\circ} - 270^{\circ})/2$. This procedure eliminates instrumental artifacts as real signatures rotate by 180° when viewed at the anti-parallel position angle, while artifacts remain at a constant orientation. All average position spectra were assessed visually to exclude features only present at a single position angle (e.g. artifacts).

The narrow positional excursions over the Hα emission of α Col (see Figure 5.1) appear to be artifacts as they are only present in the data obtained at a PA of 180°. Artifacts in spectroastrometric data can occur for a variety of reasons, for example, non-uniform illumination, unstable adaptive optics and defective CCDs can all result in artificial signatures (see e.g. Brannigan et al. 2006). For a more detailed discussion on artifacts in spectroastrometric data the reader is referred to Chapter 2. Since these artifacts are only present in data obtained at one PA they cannot be removed by combining data obtained at two anti-parallel position angles. The source of such artifacts is unclear; they could be due to imperfect centering of the object in the slit (Brannigan et al. 2006) or some unstable instrumental component. The crucial point is that these artifacts are identified by obtaining data at sets of anti-parallel position angles and can be neglected from hereon.

5.3 Hα spectroastrometric signatures

The spectroastrometric signatures of the sample are presented in Figure 5.1. The spectroastrometric signatures displayed are normalised to the continuum position and deviations from this are expressed in mas. The positional rms (Root-Mean-Squared) in the spectroastrometric signatures is of the order 0.1 mas, as shown in Table 5.2. Therefore,

the data is of comparable quality to that of Oudmaijer et al. (2008), and in many cases better, making it the among the most accurate spectroastrometric data yet obtained. The data contain a few binary signatures (ν Gem, EW CMa and possibly V863 Cen). In addition, the data also contain a few signatures indicative of rotating disks (e.g. β CMi). Here each point is discussed in turn.

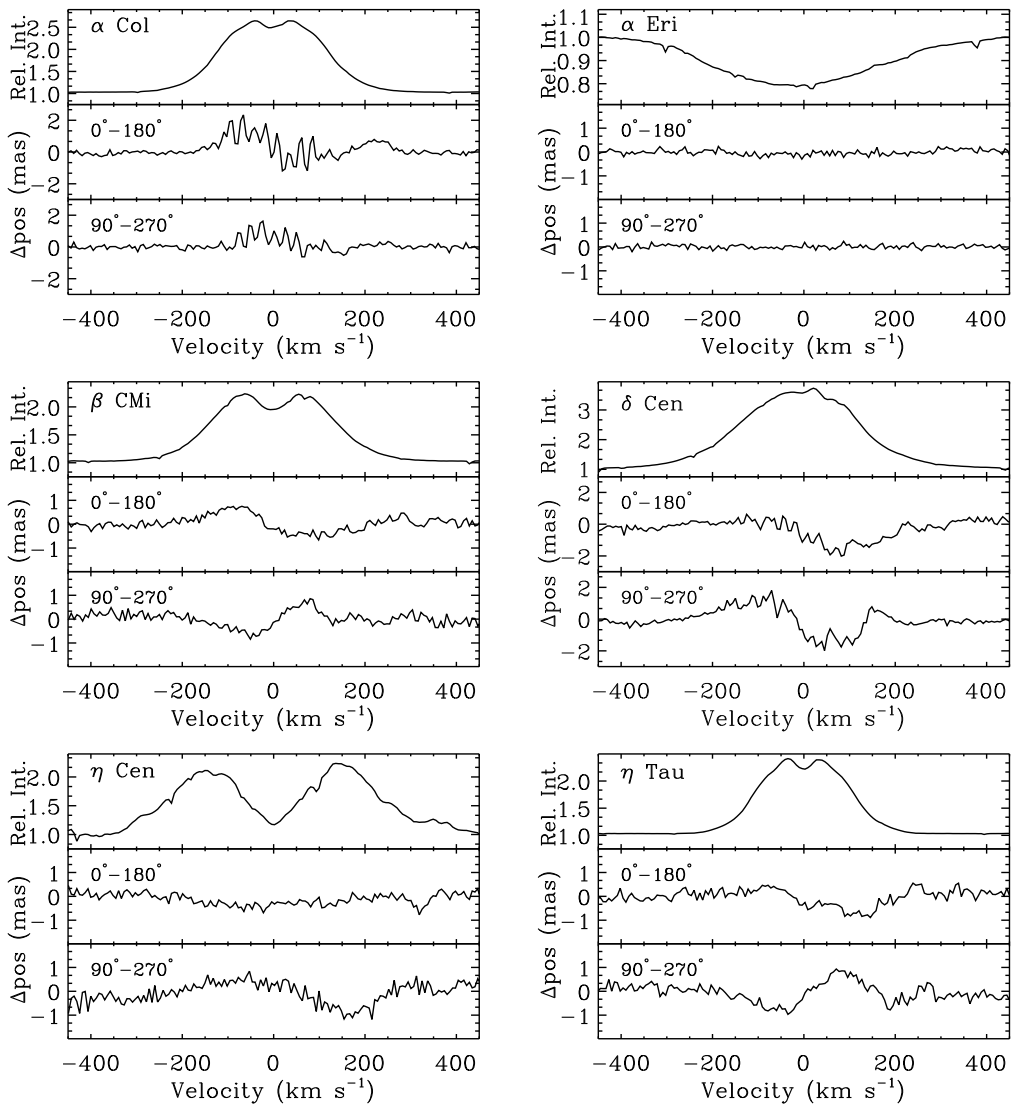

Figure 5.1: *The spectroastrometric signatures over Hα of the sample. The top panels display the total intensity spectra while the lower two panels display the spectroastrometric positional signatures in the* $0° - 180°$ *and* $90° - 270°$ *directions. The data have been re-binned in the dispersion direction by a factor of the number of pixels per resolution element (5).*

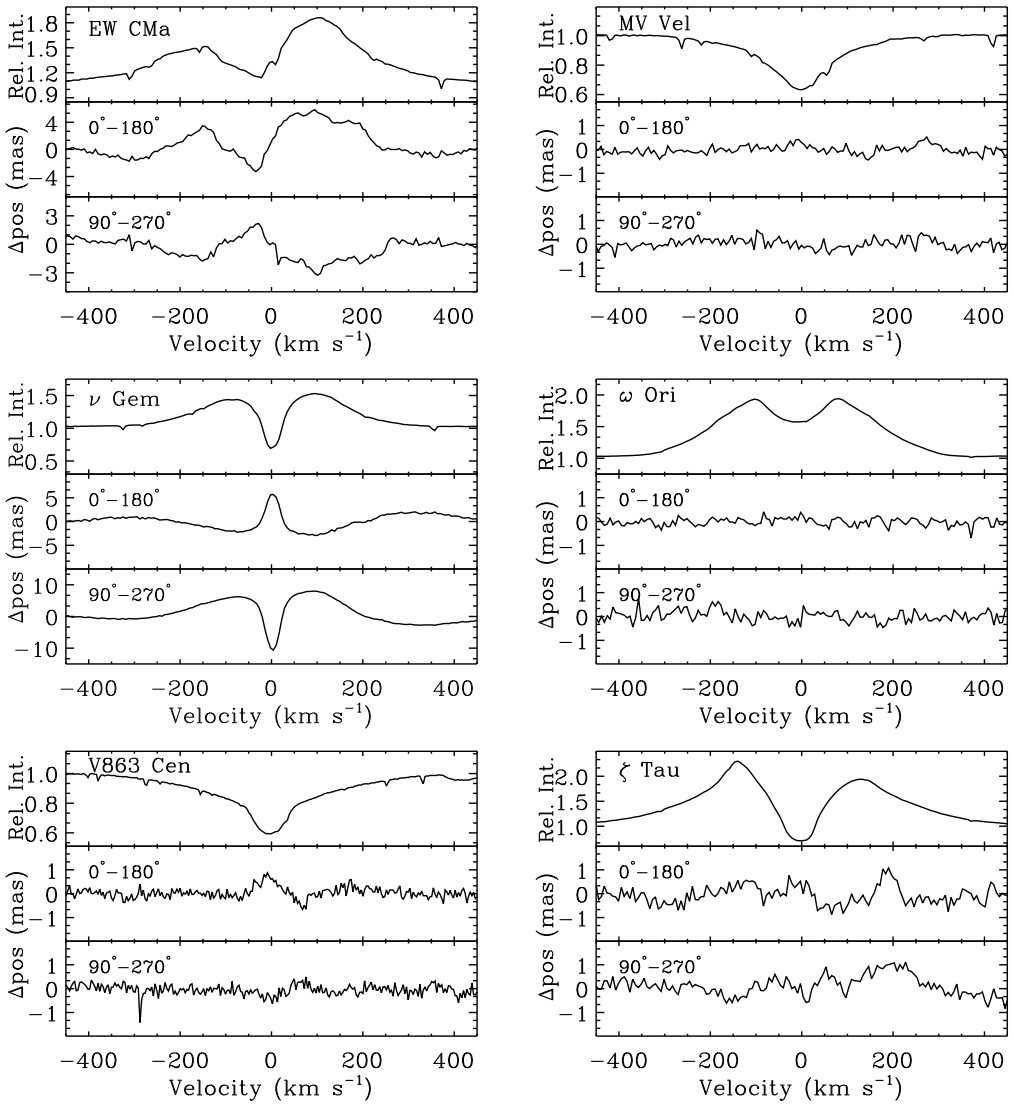

Figure 5.1 continued.

5.3.1 Binary signatures

The positional offsets over the Hα line of ν Gem are clear evidence that this star is part of a binary system (see Chapter 2). Over the emission components of the Hα line the centroid moves to the SE, towards the star associated with the emission. Over the central reversal of the profile, the photo-centre moves to the opposite side of the continuum position, since at this wavelength the non-emitting star will account for a higher fraction of the total flux than it does in the emission line peaks. Both the features in the $0° - 180°$ and the $90° - 270°$ date rotate across anti-parallel position angles, providing a useful

verification of these signatures. This is not a detection of a new binary system as ν Gem has been previously shown to be a binary system with a separation of $0.1826 \pm 0.0040''$ and a mass ratio of 0.719 (Mason 1997). The position angle derived from the positional excursions is approximately consistent with the position angle predicted by the orbit of Cvetković & Ninković (2008, $292.1 \pm 0.6°$ c.f. $293.7°$, see Fig. 5.2). This provides another check on the real nature of the spectroastrometric signatures. In addition, EW CMa also exhibits a clear binary signature. Again, this is not a new detection as EW CMa is already known to be a binary system with a separation of around $0.15''$(Mason et al. 1997), although the orbital parameters are not constrained. Finally, V863 Cen exhibits a small positional offset centered upon its Hα absorption profile, which might be due to a binary companion. If this is the case, this would represent the first detection of a binary companion of this object.

5.3.2 Disk signatures

In a rotating disk the photo-centre of the blue-shifted light will be located on the opposite side of the continuum photo-centre to that of the red-shifted light (see Figures 5.4 and 5.5). As a result, the spectroastrometric signature of a rotating disk is shaped like an 's', with a positional offset to one side of the continuum over negative velocities and an equal offset in the opposite direction over positive velocities (see e.g. Pontoppidan et al. 2008). β CMi, δ Cen, η Cen and η Tau all display spectroastrometric signatures which are quite unlike the binary signatures discussed above and are instead indicative of rotating, disk-like structures. The positional excursions are approximately 1 mas in size, and in general agree with the predicted angular sizes presented in Table 5.1. Non-detections, e.g. ω Ori, have the smallest predicted angular sizes. Therefore, it is concluded that these positional offsets are due to small-scale circumstellar disks surrounding these stars. Subsequently, these data already illustrate the sensitivity of spectroastrometry in that disks of several stellar radii can be detected at distances of up to 100 pc. At 100 pc a disk of 10s of stellar radii will subtend an angle of several mas, which while small, is several times larger than the positional offsets observed. The reason the spectroastrometric signatures do not trace the full extent of the disks (several mas) is that the majority of the disk

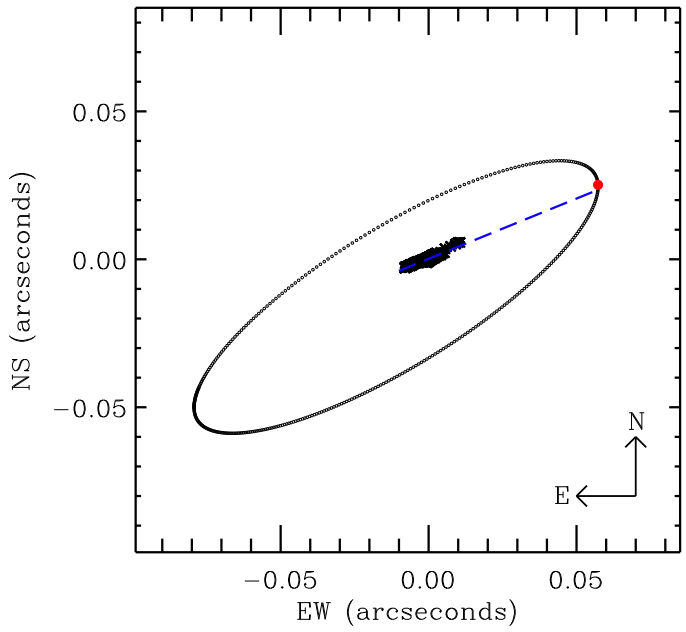

Figure 5.2: *The relative orbit of the secondary component of the ν Gem binary system. The point at 0,0 represents the primary component while the red point represents the position of the secondary at the time of observation (2009.14). The straight line follows the position angle traced by the centroid excursions, as can be seen it almost intersects the predicted position of the secondary.*

flux emanates from the inner regions (due to a decrease of density with radius), which result in a small positional offset (see Figure 5.5). Consequently, the smallest detectable disk has a radius of several mas.

The data have already satisfied one of the goals of this chapter, namely to demonstrate that spectroastrometry can be used to detect only a few mas in size, and is thus an ideal technique to search for accretion disks around MYSOs (which are generally situated several kpc away and thus a disk several AU is size would subtend an angle of a few mas). However, the data also have the potential to constrain the kinematics of Be star disks. In order to achieve this, model calculations of the spectroastrometric signatures of disks surrounding Be stars are required.

5.4 The disk model

The model used here is that presented by Grundstrom & Gies (2006), and is based on early models of accretion disks around cataclysmic variables developed by Horne & Marsh (1986) and Horne (1995). The model assumes that the disk is axisymmetric and located around the equator of the central star. The disk density (ρ) varies in the radial and vertical directions according to:

$$\rho(R,Z) = \rho_0 R^{-n} \exp[-\frac{1}{2}\left(\frac{Z}{H(R)}\right)], \tag{5.1}$$

where R and Z are the radial and vertical distances, ρ_0 is the initial density, $H(R)$ is the disk scale height and n is the exponent of the radial density variation, which is treated as a power law. From fitting the SEDs of Be stars it has been found n ∼2–3.5 (e.g. Waters 1986). The scale height of the disk is set by:

$$H(R) = \frac{C_s}{V_{rot}} R^{\frac{3}{2}} \tag{5.2}$$

where C_S is the sound speed and V_{rot} is the Keplerian velocity of the disk. The neutral hydrogen population in the disk is determined by equating the photo-ionisation and recombination rates (as done by Gies et al. 2007). The gas within the disk is assumed to be isothermal and the temperature is determined by the surface temperature of the central star (e.g. $T_d = 0.6T_{\rm eff}$, as found by Carciofi & Bjorkman 2006). Obscuration by the central star is accounted for via the following:

$$R_o(\phi) = \frac{\sec i}{\sqrt{\cos^2\phi + \sin^2\phi \sec^2\phi}}, \tag{5.3}$$

where R_o is the obscuration radius in stellar radii, i is the inclination of the rotation axis and ϕ is the azimuthal coordinate (see Figure 5.3). This equation is taken from Hummel & Vrancken (2000). Shear velocity (V_{sh}), caused by line photons escaping optically thick regions along rotationally induced shear flows, is described by the following equation:

$$V_{sh} = -\frac{H}{2R} V_{rot} \sin i \tan i \sin\phi \cos\phi, \tag{5.4}$$

which is taken from Horne & Marsh (1986). The final equation describing the optical depth of a line, τ_ν, is:

$$\tau_\nu = \frac{W(R)}{\cos i} \frac{\lambda_0}{\sqrt{2\pi}\Delta V} \exp\left[-\frac{1}{2}\left(\frac{V - V_D(0)}{\Delta V}\right)^2\right], \tag{5.5}$$

where $W(R)$ is the absorption equivalent width, λ_0 is the central wavelength of the line, $V_D(0)$ represents the Keplerian velocity in the plane of the disk, $\Delta V = \sqrt{\Delta V_{ther}^2 + V_{sh}^2}$ and V_{ther} represents the thermal velocity in the disk (see Hummel & Vrancken 2000). The optical depth is then used in the transfer equation, which is given by the following:

$$I_\nu = S_\nu^L(1 - e^{-\tau_\nu}) + I_\nu^S e^{-\tau_\nu}, \tag{5.6}$$

where I_ν is the final intensity in the line, S_ν^L is the source function of the disk and I_ν^S is the specific intensity of the central star (which is the product of a black-body radiating at $T_{\rm eff}$ and a photospheric Hα line taken from the grid of profiles of Martins et al. 2005). This equation is solved along rays through the disk (which is divided into radial and azimuthal cells) to create the final line profile. In addition, the specific intensity of each disk cell is used to make an image of the disk at each velocity bin. These images are then smoothed to represent the effects of atmospheric turbulence and are then used to predict the spectroastrometric signature of the disk. Examples of such images (prior to smoothing) are presented in Figure 5.4.

The parameters of the model are: the spectral type (or rather the mass, radius and temperature) of the central star, the intrinsic line-width, the inclination of the disk, the number density at the inner edge of the disk, the exponent of the radial density power law and the outer disk boundary. Setting as many of these parameters as possible to the values in Table 5.1 results in the model having four free parameters: the initial density, the line-width, the density power law exponent and the outer boundary. These are fit to the observed line profiles simultaneously using the AMOEBA routine (which is based on the downhill simplex algorithm as implemented in Press et al. 1992). Furthermore, the line profiles were fit with two different disk kinematics: Keplerian ($V_{\rm rot} \propto R^{-0.5}$) and angular momentum conserving ($V_{\rm rot} \propto R^{-1}$), to investigate whether the observed signatures could be used to differentiate between these scenarios. The fitting procedure was begun with an initial guess for the parameters. Once the algorithm converged upon a particular set of parameters, the routine was run again with this set of parameters as the initial guess in an attempt to avoid local minimas. It was found that the initial

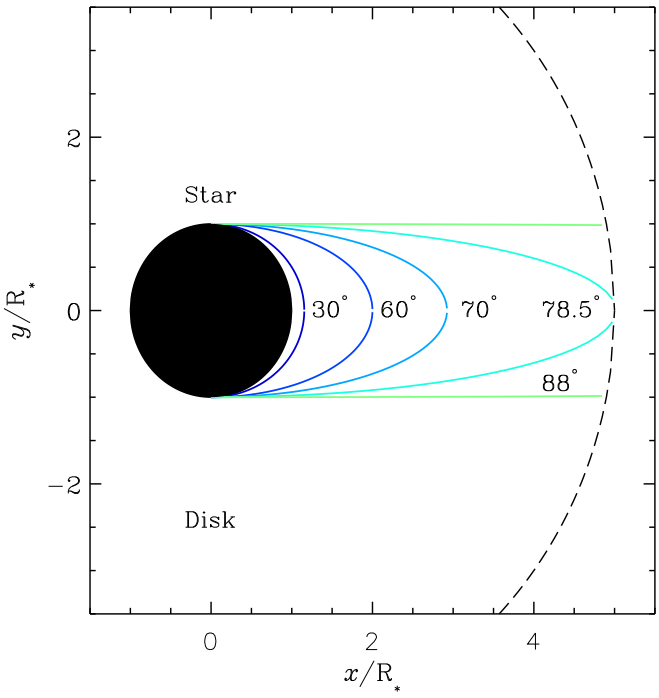

Figure 5.3: *A circumstellar disk with an outer radius of* $5R_\star$ *with several obscuration radii marked. The region projected onto the stellar surface is inclination dependent and increases with increasing inclination. At an inclination of* $\sim 80°$ *the shadowed region extends to the edge of the disk.*

parameters generally had little effect on the resultant best fit model and typically 100 iterations resulted in the model converging.

Objects with no net emission (α Eri, MV Vel and V863 Cen) were not fit with the model. The model does include a photospheric absorption component. However, if the model was applied to objects with no net emission, the fitting process would be dominated by uncertainties in the properties and rotation rate of the central star, and thus any resulting disk properties would be poorly constrained. Objects which exhibit binary signatures in their spectroastrometric data were similarly not fit with the model. While the emission line profiles of these objects could be fit, the predicted spectroastrometric signatures ($\sim$1 mas) would be much less than the observed binary signatures ($\sim$5–10 mas). Therefore, constraining the properties of the disks surrounding these objects via their spectroastrometric signatures is extremely challenging. Consequently,

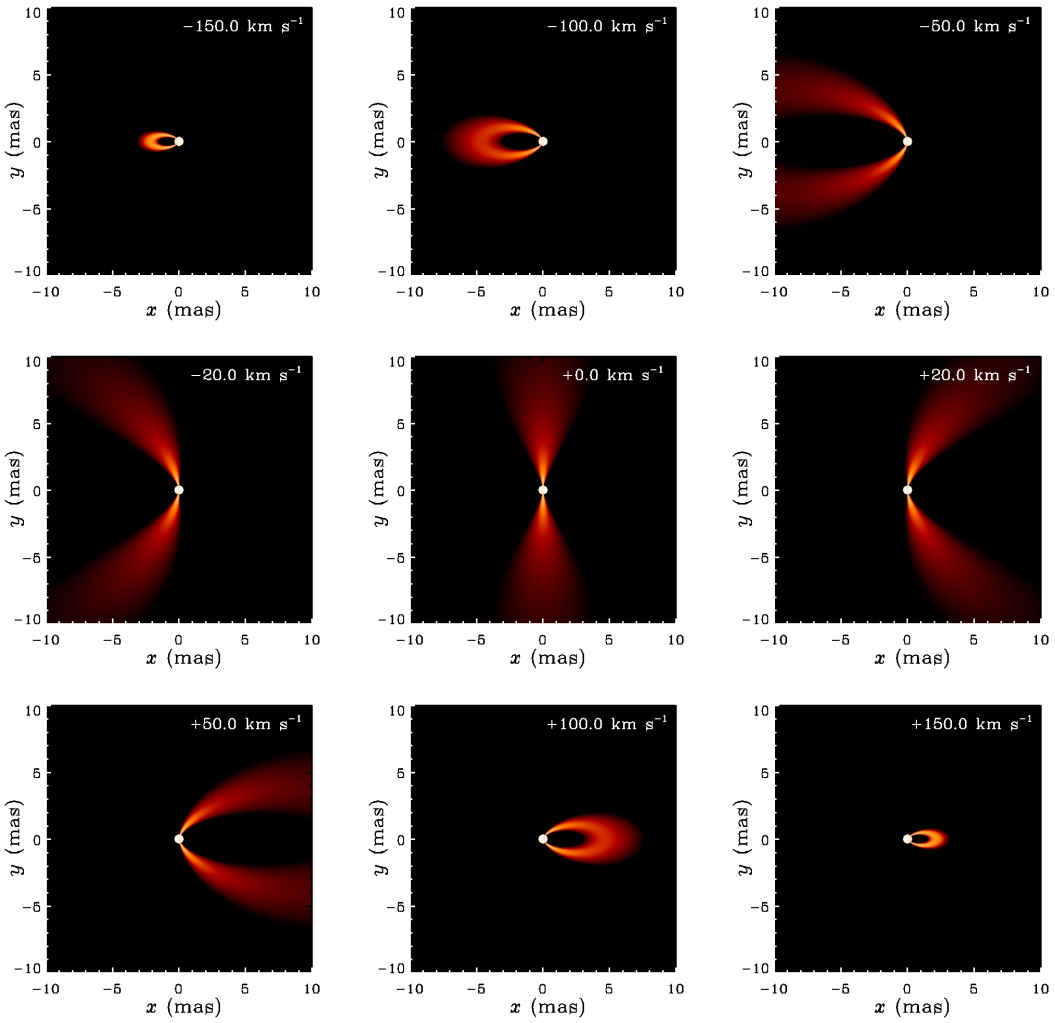

Figure 5.4: *Examples of the images of a model disk in 20* $\mathrm{km\,s^{-1}}$ *bins. The images have been scaled logarithmically to enhance the visibility of the disk. The disk is moderately inclined* i= 54.9° *and has a physical outer radius of 71* $R_\star$ *or 16.6 mas.*

fitting the observed line profiles and modelling the spectroastrometric signatures of the best fitting disk would serve little purpose. Finally, the model was not applied to the line profile of ζ Tau as the axisymmetric model used cannot fit the strongly asymmetric line profile observed (which is due to a one-armed spiral density wave in the disk, see e.g. Carciofi et al. 2009).

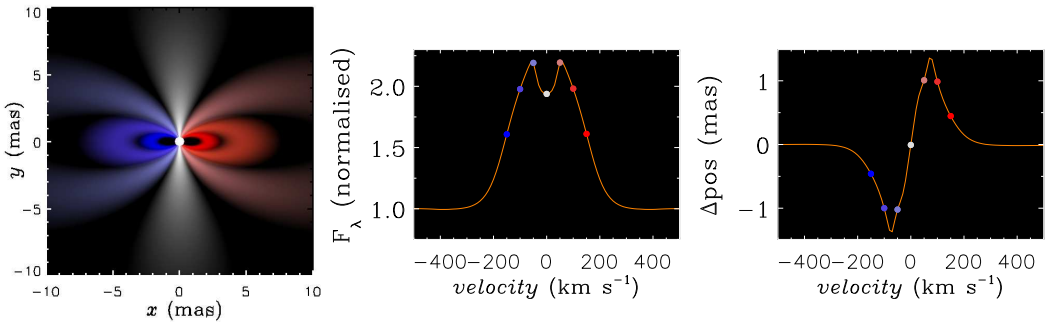

Figure 5.5: *The spectroastrometric signature of a disk. In the left panel various velocity slices of the disk are highlighted in different colours. The flux and spectroastrometric offset at these velocities are presented in the right two panels.*

5.5 Results I

The best fitting model line profiles for both the angular momentum conserving (AMC) and Keplerian disks are presented in Figure 5.6. The associated best fitting parameters are presented in Table 5.3.

5.5.1 Fits to line profiles

In general, both the Keplerian and AMC cases are able to fit the observed line profiles. The quality of the fit provided by each scenario only differed significantly in the case of η Cen, in which case a Keplerian disk initially provided a better fit than an AMC disk. For this object the line profile could not be fit by the AMC model, unless the disk source function was artificially altered (by a factor of $\sim$2). However, the line profile of η Cen was relatively poorly fit by both scenarios, making it difficult to discard the AMC scenario conclusively. The difficulty in fitting the Hα line profile of η Cen with this model has been noted previously by Hummel & Vrancken (2000). These authors also resort to including the disk source function (S_ν^L) as a free parameter. Hummel & Vrancken (2000) find that by suppressing the Hα line emission by a factor of $\sim$20 results in an acceptable fit to the observed line profile for a Keplerian disk, and thus suggest that the disk around η Cen rotates in a Keplerian fashion. However, since the disk source function required substantial modification in order to generate this fit, this

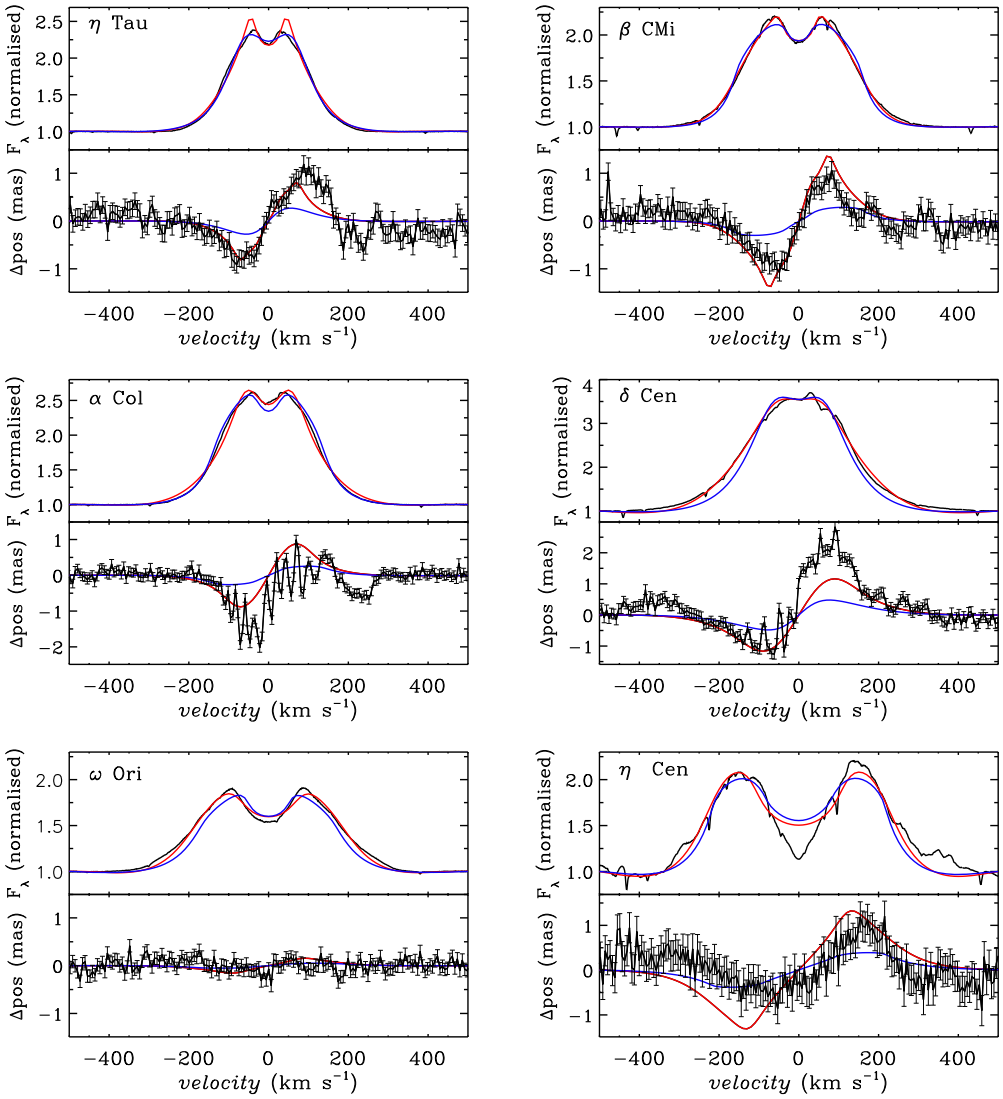

Figure 5.6: *The best fitting line profiles and spectroastrometric signatures of the Keplerian (red) and AMC (blue) disk models. The data are shown re-binned by a factor of 5. The spectroastrometric signatures in the NS and EW directions have been combined to form the total positional offset along the PA of the disk (apart from the case of η Cen – in which case only the EW data is used as a positional offset is not evident in the NS direction).*

conclusion is far from conclusive.

Here, the disk source function is not added as a free parameter in order to improve the fit to line profile of η Cen. This would invalidate comparison of the resulting best fitting parameters with others obtained using the prescribed line source function ($S_\nu^L = \frac{B_\nu(T_{\rm eff})}{B_\nu(T_{\rm d})}$ or the ratio of the stellar and disk Planck functions). Therefore, the best fits to the line emission of η Cen are not sufficiently depressed in the central reversal between the two emission peaks. This may indicate the approximation of an isothermal disk is not valid in this case. Alternatively, the fact that the red peak is stronger than the blue peak may indicate that an asymmetric disk is required to fit the observed profile.

In general, the best fitting Keplerian disks are several 10s of stellar radii in size (which is in rough agreement with the results of Meilland et al. 2009). However, the disks of β CMi and δ Cen are significantly larger, and are larger than typical Be star disk sizes (for example $\sim$20 mas c.f. $\sim$3 mas, see e.g. Quirrenbach et al. 1997). The best fitting Keplerian disks are relatively tenuous (e.g. $\rho_0 \sim 10^{-12}\,{\rm gcm}^{-3}$) and have radial density gradients with an exponent of $\sim$3, which is in agreement with estimates based on fitting the SEDs of Be stars (see e.g. Waters 1986; Dougherty et al. 1994). The best fitting AMC disks are generally smaller (only several stellar radii in size) and denser than their Keplerian counterparts (e.g. $\rho_0 \sim 10^{-11} - 10^{-10}\,{\rm gcm}^{-3}$) and also tend to have steeper radial density power laws. The smaller sizes are a consequence of the rapid reduction in rotational velocity with radius in AMC disks. To fit the observed line profile without increasing the inclination, AMC disks have to be small to ensure the inner, high velocity regions dominate the emission. This is quantified by the following equation:

$$V_{\rm peak} = V_0 \sin i (\frac{R_\star}{R})^j, \tag{5.7}$$

where j is the exponent of the radial rotational velocity law, and is 0.5 for Keplerian rotation and 1.0 for the AMC scenario. For a value of $V_{\rm peak} = 100$ km s^{-1} and $V_0 = 380$ km s^{-1}, Keplerian rotation results in a disk radius of 9 $R_\star$, while the radius for an AMC disk is only 3 $R_\star$ (see Figure 5.7). This reduction in disk radius results in a small emitting area, and as a result the line flux drops. This necessitates an increase in density, explaining the relatively high density of the best fitting AMC disks. The higher

exponents of the radial density distribution in the case of AMC disks are a consequence of their high density. If the high densities were not countered with a rapid drop with radius, the models would over predict the line flux at low velocities. The exception to this is η Cen. However, this may be a result of varying the disk source function in the AMC scenario in an attempt to obtain a reasonable fit (following the example of Hummel & Vrancken 2000).

In general, the parameters of the best fitting AMC models are not inconsistent with typical values for Be star disks. The best fitting radii are generally similar to the values measured by optical interferometry (e.g. Tycner et al. 2005), although as a whole they are slightly less than the typical size of Be star disks (for example $\sim$1 c.f. $\sim$3 mas, see e.g. Quirrenbach et al. 1997). The best fitting density power law exponents are similar to (but in general slightly higher) than the typical observed value (for example 4.25 c.f. 3–4, see Dougherty et al. 1994). As an exception, in the case of ω Ori, the best fitting power law exponent for the AMC disk is substantially higher than the typical value for Be star disks (8 c.f. 3–4). Therefore, in this case Keplerian rotation is favoured and the AMC scenario can be discarded. However, this is the exception, and in general both rotation laws result in best-fitting parameters that are consistent with previous observations.

To summarise, in most cases, neither the Keplerian nor the AMC scenario can be conclusively discarded on the basis of the fits to the line profiles and the best fit properties alone. Additional constraints are required to conclusively differentiate between the two scenarios.

5.5.2 Spectroastrometric constraints

The spectroastrometric data add an additional constraint to the models. Due to the smaller sizes of the best fitting AMC disks, their predicted spectroastrometric signatures are smaller than those of the best fitting Keplerian disks ($\sim$0.3 c.f. $\sim$1.0 mas). As a result, the Keplerian spectroastrometric signatures are generally better able to match the observations (i.e. for η Tau, β CMi and δ Cen the χ^2 value associated with the Keplerian signature is less than that associated with the AMC signature). Furthermore, the spectroastrometric signature of the majority of the best fitting AMC disks would not

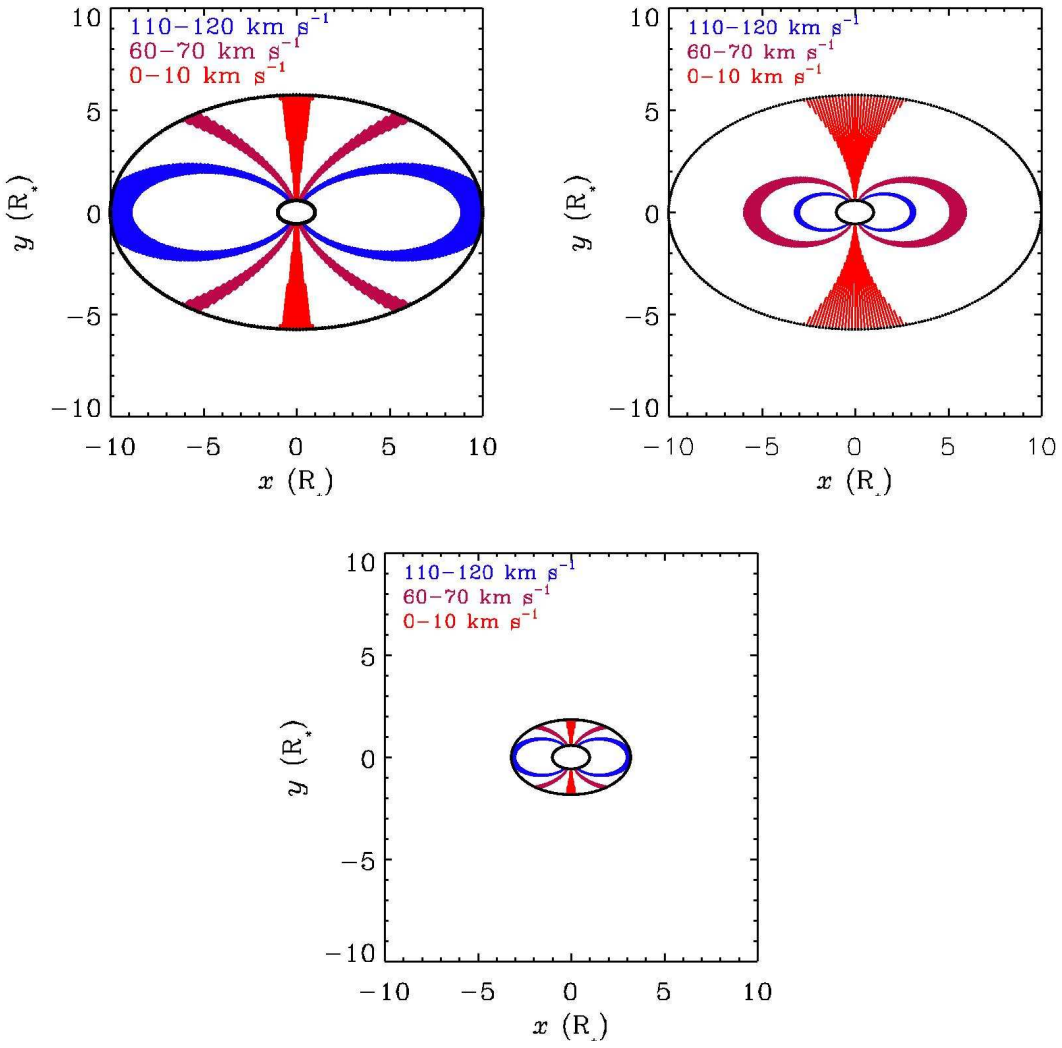

Figure 5.7: *Iso-velocity slices of a Keplerian disk with an outer radius of 10 $R_\star$ (top left), an AMC disk with a radius of 10 $R_\star$ (top right) and an AMC disk with an outer radius of 3.2 $R_\star$ (bottom). The emission peaks of the double peaked profile of a disk correspond to the velocity of the largest iso-velocity area of the disk, which in turn are the largest closed loops. To make the peak velocity of the AMC disk match the Keplerian disk the AMC disk has to be shrunk to 3.2 $R_\star$.*

Table 5.3: *The best fitting parameters of the Keplerian and AMC models.*

	Keplerian				**Angular Momentum Conserving**			
Object	R_D	ρ_0	Δv	m	R_D	ρ_0	Δv	m
	$R_\star$/mas	$\mathrm{g\,cm^{-3}}$	$\mathrm{km\,s^{-1}}$		$R_\star$/mas	$\mathrm{g\,cm^{-3}}$	$\mathrm{km\,s^{-1}}$	
η Tau	57.87/9.77	5.21e-13	1.05	2.94	17.52/2.96	4.28e-12	26.99	4.25
α Col	43.97/8.48	5.69e-13	29.43	2.86	4.06/0.78	9.16e-12	28.27	3.52
β CMi	71.32/16.59	1.09e-12	2.11	3.16	4.17/0.97	6.05e-11	16.90	2.44
δ Cen	78.99/19.13	2.17e-12	48.62	2.96	53.36/12.93	2.33e-11	47.06	4.40
η Cen[a]	22.66/5.88	1.16e-11	19.50	3.51	3.65/0.95	1.49e-10	8.03	1.01
ω Ori	17.39/1.11	1.52e-12	26.59	3.26	3.02/0.19	2.34e-09	25.25	8.22

a: In the AMC case the line source function was used as a quasi-free parameter as per Hummel & Vrancken (2000), as otherwise no good fits were obtained. This best fitting model had a line source function of 1.0, which is within a factor of 2 to that predicted.

be detectable with the current positional precision (∼0.1–0.2 mas, see Figure 5.8). The only clearly detectable best fitting AMC disk out of the four objects which exhibit real spectroastrometric signatures (δ Cen) is excluded by χ^2. Therefore, the AMC scenario can be ruled out for all the objects in the sample which exhibit spectroastrometric signatures consistent with the detection of a circumstellar disk, indicating that these disks rotate in a Keplerian fashion.

The reason the AMC scenario cannot be discarded in the case of ω Ori is that this object is situated at such a distance that neither the best-fitting Keplerian or AMC disks can be detected. This is consistent with the lack of a spectroastrometric signature. The reason the AMC scenario cannot be discarded in the case of α Col is that the positional data of this object is contaminated by artifacts, and thus the predicted positional offsets cannot be meaningfully compared to the observed spectroastrometric data. None the less, since the best fitting AMC disk can be ruled out for four out of six objects whose line profiles are modelled, the data unequivocally indicate that the majority of the disks in the sample rotate in a Keplerian fashion. This chapter constitutes the first time such a statement can be made for a sample of Be stars. The fact that the majority of Be star disks appear to rotate in a Keplerian fashion strongly constrains their formation

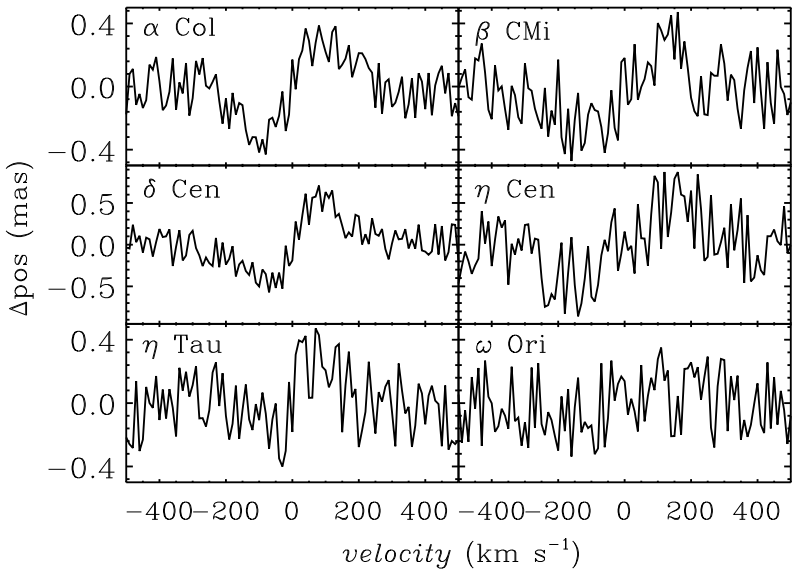

Figure 5.8: *The spectroastrometric signatures of the best fitting AMC disk models with artificial noise added (equivalent to the rms in the spectroastrometric observations).*

mechanism. This is discussed more in Section 5.8.

5.6 3D, NLTE radiative transfer modelling

The advantage of the model presented in Section 5.4 is that it can be run relatively quickly, allowing the observed line profiles to be fit with several free parameters via an iterative process. This is not possible with a more sophisticated model as the running time for the 100s of iterations required to fit the four free parameters would be of the order of several weeks per object, if not more. However, it is important to note the shortcomings of the simple model of Hummel & Vrancken (2000). The primary limitation of this model is that it only considers line profiles and neglects polarisation due to electron scattering in the disk and continuum flux from free-bound and free-free emission in the disk. To check that the previously determined disk properties are consistent with other observations and to derive additional constraints on the disk properties, a more detailed modelling approach is required.

This is done here using the code HDUST, developed by Carciofi & Bjorkman (2006).

HDUST is a fully 3D, non-local thermodynamic equilibrium (NLTE), Monte Carlo code which solves the problems of radiative transfer, radiative equilibrium and statistical equilibrium for pre-defined gas density and velocity distributions. Details of the code and its application can be found in Carciofi & Bjorkman (2006) and Carciofi et al. (2006, 2008, 2009) respectively. Here, the code is used to generate the spectrum of a rapidly rotating star surrounded by a gaseous equatorial disk, in addition to making images of the system. This is done by dividing the central star into numerous latitude bins, each with a specific effective temperature and surface gravity. Each cell is associated with a corresponding Kurucz model atmosphere which is used to determine the emission of photons from the cell. Each photon (or photon packet) is traced through the defined circumstellar environment (here a disk) where it may be scattered and/or absorbed and re-emitted. The scattering leads to polarisation of the photons allowing the code to calculate the polarisation due to the circumstellar material. The absorption events are always followed by re-emission and therefore no photons are destroyed, ensuring radiative equilibrium is enforced. The re-emission of photons is governed by the local emissivity, which in turn includes both continuum and line contributions.

The absorption of photons by the circumstellar material provides a sampling of the radiative rates and the heating of free electrons. Therefore, iterative model runs can be used to solve the rate equations and thus determine level populations and electron temperatures. Once the level populations and electron temperatures have converged the code is run again to determine the emergent spectrum and polarisation. The code is described fully in Carciofi & Bjorkman (2006).

5.6.1 Disk model

The disk model used is the same as that presented by Carciofi & Bjorkman (2006). The disk is assumed to be pressure supported in the vertical direction and centrifugally supported in the radial direction. Determining the self consistent structure of such a disk is a complex problem, and requires solving the equations for vertical hydrostatic equilibrium and radial viscous diffusion in non-isothermal conditions (see Carciofi et al. 2008). This was done by Carciofi et al. (2008), who demonstrated that non-isothermal density structure in Be star disks results in changes in the emergent spectrum with

regard to the isothermal case of the order 10–50 per cent. Here, the disk model is the same as that of Carciofi & Bjorkman (2006) in that the disk is non-isothermal but the disk structure is not determined self-consistently but is assumed to be described by a set function. Therefore, this approach will omit the detailed density structure reported by Carciofi et al. (2008). However, the implementation of the hydrostatic structure and viscous outflow by Carciofi et al. (2008) implicitly assumes Keplerian rotation. As the aim of this chapter is to compare models with different kinematic structure this disk model cannot be used here. This could result in the predicted Hα flux being uncertain by about 50 percent and the polarisation being uncertain by a factor of 2. However, at low densities ($\rho_0 < 5.5 \times 10^{-12}\,\mathrm{g\,cm^{-3}}$) the difference between the outputs of the self-consistent and analytic disk models is almost negligible. As the disk of β CMi is later found to be relatively tenuous (indicated by the modest infrared excess – see Figure 5.9), it is surmised that using an analytic disk model will not significantly affect the results.

It is assumed that the disk is vertically isothermal. Furthermore, it is assumed that the vertical structure is given by the Gaussian result for pressure supported disks with a scale height, H, given by:

$$H(\varpi) = H_0 \left(\frac{\varpi}{R_\star} \right)^\beta, \tag{5.8}$$

where ϖ represents the radial coordinate and H_0 is given by:

$$H_0 = \frac{C_S}{V_{\mathrm{crit}} R_\star}, \tag{5.9}$$

where C_S is the isothermal sound speed and $V_{\mathrm{crit}} = (\mathrm{G}M/R_\star)^{1/2}$. The parameter β describes how the disk flares with radius, and is therefore sensitive to the temperature gradient within the disk. Carciofi & Bjorkman (2006) find that the flaring of Be star disks does not significantly affect the disk heating. Here, β is set to 1.5, representative of a radially isothermal disk. Finally, the density structure of the disk is then given by:

$$\rho(\varpi, Z) = \rho_0 (\frac{R_\star}{\varpi})^n \exp(-\frac{Z^2}{2H^2}), \tag{5.10}$$

where the radial density gradient is treated as a power law with an exponential of n. In the case of steady state, isothermal outflow, n is 3.5 (Lee et al. 1991).

Here, HDUST is used to model the observed properties of one object in particular (β CMi) in order assess whether the earlier conclusion remains valid when additional

data are taken into account and a sophisticated, 3D model is used. This is only done for one object as the running time of HDUST prohibits applying it to the entire sample. HDUST is used to recreate the observed polarisation, optical and infrared SEDs and Hα line profile of β CMi with a Keplerian and AMC disk. As before, the spectroastrometric signatures of the two model disks are compared to check that the earlier conclusion remains valid when using a sophisticated, 3D model. Then, the properties of the best fitting disks are compared to those of the best fitting disks presented in Section 5.5 to assess whether the results of the two models are consistent, and therefore whether the simple model is in agreement with the broadband properties of the objects.

5.6.2 β CMi

5.6.2.1 The data

HDUST is used to simultaneously fit the optical SED and linear polarisation, the infrared SED and the observed Hα profile of β CMi. The linear polarisation used were obtained using the HPOL spectropolarimetry, mounted on the 0.9 m Pine Bluff Observatory telescope. β CMi was observed once on the night of 22/04/1991. These data obtained using a dual Reticon array detector spanning the wavelength range of 3200-7600 with a spectral resolution of 25 Å (e.g. Wolff et al. 1996). In 1995 the Reticon detector was replaced with a CCD detector and two new gratings extended the wavelength coverage to 3400-10500Å and improved the spectral resolution to $\sim$ 10Å (Nordsieck & Harris 1996). Since then β CMi has been observed several times with HPOL (08/02/1995, 25/03/1995, 07/02/2000 & 12/02/2000). The 1991 data were retrieved from the Multimission Archive at the STScI Web site[(b)]. The more recent data were provided by Karen Bjorkman (2010, priv. com.). The infrared data were taken from the 2MASS point source catalogue (Cutri et al. 2003), the IRAS point source catalogue (Beichman et al. 1988) and Ducati (2002). The UV spectrum was obtained from the INES (newly extracted IUE spectra) database[(c)] – see (Wamsteker et al. 2000), and broad-band measurements of the UV flux were taken from Jamar et al. (1995) and Johnson et al. (1966). Optical spectra were taken from the HPOL data-base mentioned above. Further broad-band measurements

[(b)] http://archive.stsci.edu/hpol
[(c)] http://sdc.laeff.inta.es/ines/

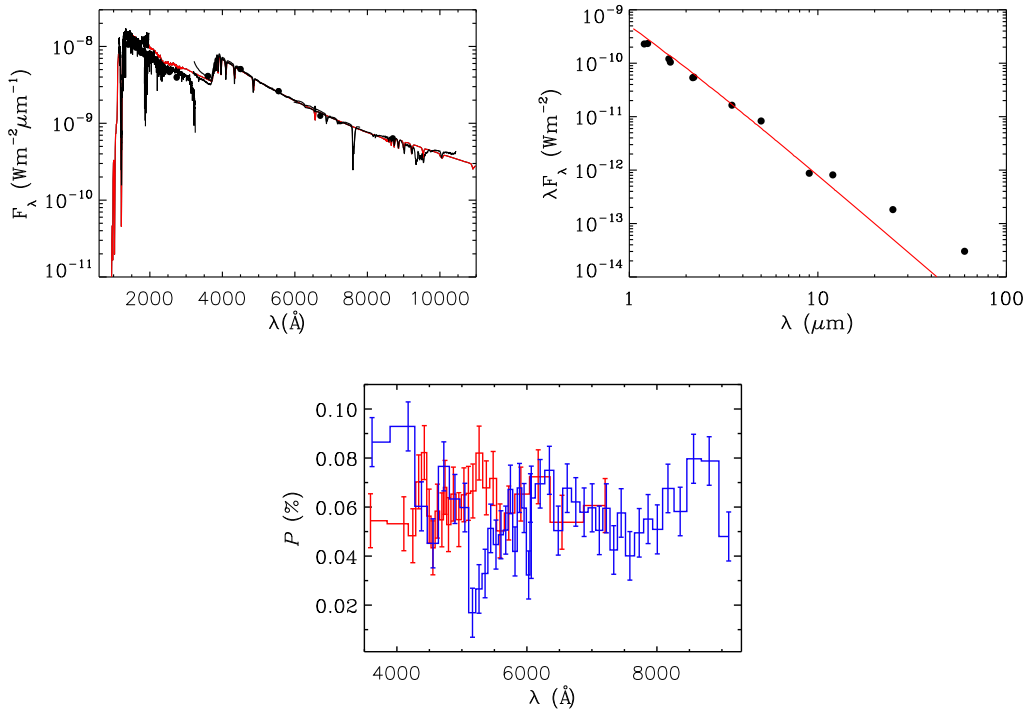

Figure 5.9: *The accumulated observations of β CMi. In the lower panel the Reticon HPOL data are presented in red while the CCD HPOL data are presented in blue. The red line plotted with the infrared data is the SED of a model spectrum with $T_{\rm eff}$=11772 K and log(g)=3.81, suggested parameters for β CMi (Frémat et al. 2005). Similarly, the red line plotted with the UV and optical data is also the SED of a model atmosphere.*

of the optical flux were obtained from Ducati (2002). These data are shown in Figure 5.9.

5.6.2.2 The fitting process

The initial step in finding the best fit model parameters was to determine the properties of the central star. A spherical star with parameters of a B8V star (e.g. $T_{\rm eff}$=12000 and log(g)=4.0) produces too small a Balmer jump (see Figure 5.9). This is resolved by including the effects of gravitational darkening in the code. It is assumed that the star rotates at 80 per cent of its critical velocity (380 km s^{-1}), and that the axis of rotation is inclined at an angle of 55$^{\rm o}$ (Frémat et al. 2005). Rotational effects can significantly

Table 5.4: *Model stellar parameters for β CMi.*

Parameter	Value	Reference
Spectral Type	B8Ve	Slettebak (1954)
distance	52 pc	Perryman et al. (1997)
$R_{\rm e}/R_{\rm p}$	1.3	Frémat et al. (2005)
$V_{\rm crit}$	380 km s^{-1}	Frémat et al. (2005)
$V_{\rm rot}/V_{\rm crit}$	0.80	Assumed
$L_\star$	218 L$_\odot$	Set
$R_{\rm p}$	3.4$R_\odot$	varied to fit UV SED
$T_{\rm p}$	14,000 K	varied to fit UV SED
Mass	3.8 M$_\odot$	Based on R_p and $V_{\rm crit}$

alter the observed SED of a star as rapid rotation results in a redistribution of flux from the stellar surface. Gravity darkening effects were taking into account using the von Zeipel flux distribution (von Zeipel 1924), in which $F(\theta) \propto g_{\rm eff}(\theta) \propto T^4_{\rm eff}(\theta)$, where $g_{\rm eff}(\theta)$ and $T^4_{\rm eff}(\theta)$ are the effective gravity and surface temperature at a given stellar latitude, θ. The degree of oblateness, or the ratio between the equatorial and polar radii was determined from the Roche approximation of the stellar equipotentials (as done by Frémat et al. 2005), and is 1.3. The absolute size scale was set by fitting the amplitude of the resultant UV flux to the observed data, which resulted in a polar radius of 3.3 $R_\odot$. This is a little larger than the typical radius of a main sequence B8 type star. However, as noted by Carciofi et al. (2009), the size of the central star can vary by as much as 10 per cent and not significantly affect the quality of the fit to the stellar SED. Therefore, the polar radius used is essentially consistent with the relationship between polar radius spectral type and rotation rate presented by Frémat et al. (2005). The resultant UV and optical SED is displayed in Figure 5.10. As can be seen the model now provides an acceptable fit to the observed Balmer jump. The final stellar parameters are listed in Table 5.4, and are kept constant though-out.

Once the stellar parameters were established, attention was turned to the properties of the circumstellar disk. Initially, the data presented in Figure 5.9 were fit assuming a Keplerian disk. In its current incarnation the disk model essentially has three free

parameters: the initial density, the outer radius and the intrinsic line width. Starting with an arbitrary disk radius of $\sim$20 $R_\star$, the initial density was varied until the infrared excess was successfully reproduced. The IR excess of β CMi is comparatively modest, and only apparent at wavelengths longer than 3μm (see Figure 5.9). To fit this requires a low initial disk density ($< 5 \times 10^{-12}\,\mathrm{g\,cm^{-3}}$), an order of magnitude lower than for ζ Tau (Carciofi et al. 2009) and two orders of magnitude less than that of δ Scorpii (Carciofi et al. 2006). In turn, this recreates the low polarisation of the star and the modest Hα emission. The outer radius was then varied to recreate the observed double peaked Hα line profile. The central reversal between the emission peaks was fit by varying the turbulent velocity within the disk. This controls the effective emitting area of the disk for a particular velocity. Therefore, increasing this value can smooth out the central reversal and increase the line flux and *vice versa*.

The density that fit the observed infrared excess resulted in a slight over prediction of the optical polarisation (only of the order of 0.05 per cent). Therefore, the density was reduced slightly (the final value was $3.35 \times 10^{-12}\,\mathrm{g\,cm^{-3}}$). However, the predicted polarisation was still in excess of that observed. To further reduce the predicted polarisation with that observed the disk scale height was reduced. The final disk parameters are presented in Table 5.5. The final model output is compared to the observed data in Figure 5.10. As can be seen, the model output agrees with the observations and simultaneously recreates the observed SED, polarisation and line profile. It should be noted that this is not a formal fit in the sense that it does not result from a formal χ^2 minimization procedure, due to the large number of computer hours required. Nonetheless, given the relatively low number of freely varying parameters describing the star plus disk system, the simultaneous match with observations at a range of wavelengths is remarkable.

The procedure is then repeated for a AMC disk. As found in Section 5.5.1, the radius of the disk has to be significantly reduced to recreate the observed double peaked emission line profile, since the velocity falls off much faster with radius in an AMC disk than in a Keplerian disk. Specifically, to reduce the emission at low velocities and create a double peaked profile with peaks at the same velocity as observed requires decreasing

Table 5.5: *Best fitting disk parameters.*

Keplerian		**Angular Momentum Conserving**	
Parameter	Value	Value	Constraint
$R_{\rm out}$ ($R_\star$)	32	3.75	Fit peak separation
m	3.5	3.5	Set by viscous disk model
ρ_0 (g cm^{-3})	3.35×10^{-12}	3.77×10^{-12}	Fit IR excess and polarisation
$V_{\rm Turb}$ (km s^{-1})	10	28	Fit Hα line flux

the disk size by a factor of ∼9. This reduction in size led to a decrease in the Hα emitting area, and thus a decrease in the flux. Consequently, the line width had to be increased to ensure the model line flux matched that observed. This had the consequence of smoothing out the central reversal of the mode profile, resulting in the double peaked structure being smoothed out. As a result, the Hα line is relatively poorly fit by an AMC disk.

As before, the AMC disk over predicted the polarisation, but only by approximately 0.05 per cent. In this case, since the disk is relatively small, changing the scale height not only changed the polarisation but also had a significant effect on the resultant infrared excess and line flux. Therefore, in this case the disk scale height is not varied, resulting in the polarisation being slightly greater than that observed. The model spectrum and SEDs are presented in Figure 5.10, and the associated best-fitting parameters are listed in Table 5.5. While the quality of the fits are not formally assessed via the χ^2 statistic, it is clear that although both scenarios generally resulted in a reasonable fit to the data, the Keplerian disk reproduces the data to a greater extent than the AMC disk.

5.7 Results II

The predicted spectroastrometric signatures of the best fit Keplerian and AMC models are presented in Figure 5.11. As found in Section 5.5.1, the spectroastrometric signature of the best fit AMC disk is significantly smaller than that of the best fitting Keplerian disk. While the quality of the fit to the data is similar for both cases (χ^2 ∼1.5), the AMC disk would be difficult to detect with the current angular precision (see Figure

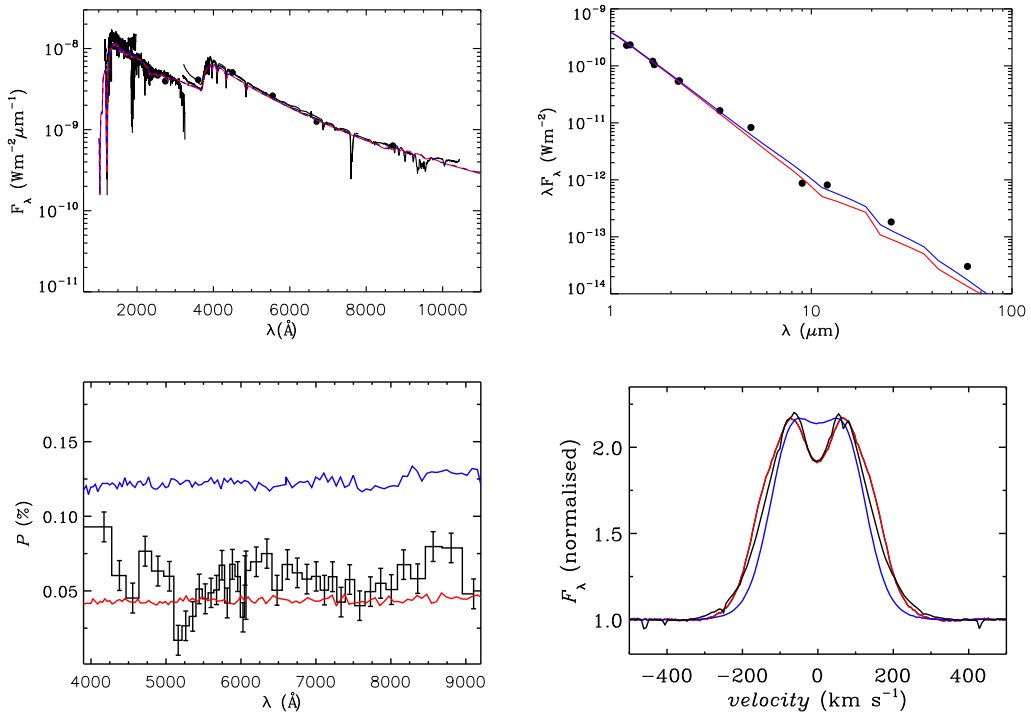

Figure 5.10: *The best fitting HDUST line profiles, SEDs and optical polarisation. The observations are presented in black, the results of the best fitting Keplerian model are presented in red and the output of the best fitting AMC model are plotted in blue. The HPOL CCD fluxes have been scaled to match the broadband measurements (an increase of 15 per cent).*

5.11). Therefore, since a positional signature indicative of a rotating disk is observed across the Hα emission of β CMi, the data indicates that the disk surrounding this Be star rotates in a Keplerian fashion. This is in agreement with the conclusion of Section 5.5.2. The signature of the Keplerian model is larger than that observed. This could be due to an overestimation of the equatorial radius or the critical velocity of β CMi.

In general, the properties of the Keplerian disk here are consistent with the properties of the best fitting Keplerian disk determined with the model of Grundstrom & Gies (2006) presented in Section 5.5.1. The main difference between the two disk models is that the HDUST disk is smaller ($R_D = 32$ c.f. 71 $R_\star$). The HDUST disk is also denser than the previous model ($\rho_0 = 3.35$ c.f. $1.1{\times}10^{-12}$ g cm^{-3}), although the density gradient

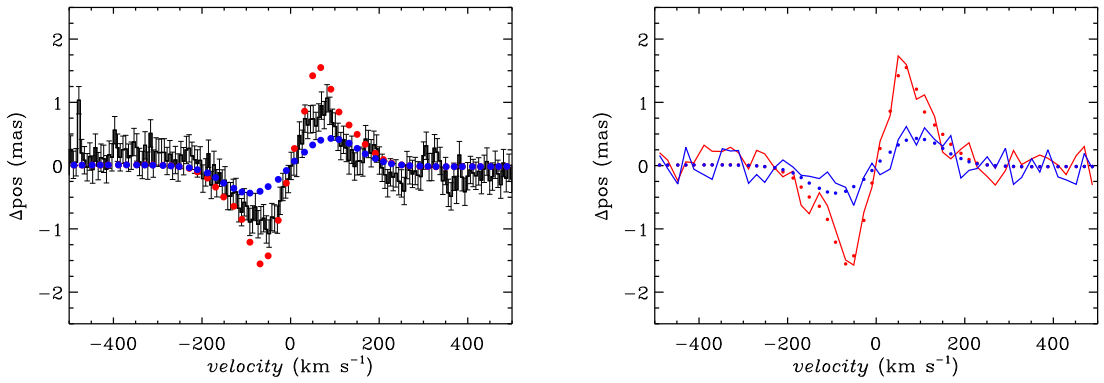

Figure 5.11: *The spectroastrometric signatures of the HDUST models. In the left panel, the spatial signatures of the Keplerian (red) and angular momentum conserving models (blue) are compared to the observed spectroastrometric displacements. In the right panel noise equivalent to the positional accuracy is added to the model signatures to assess whether they would have been detected.*

in the previous model is less steep than in the HDUST model. A comparison between the Hα line predicted by the two models is presented in Figure 5.12. The model of Grundstrom & Gies (2006) is used to predict the Hα line for the best fitting parameters determined using HDUST. The profile generated with the model of Grundstrom & Gies (2006) has a larger peak separation and slightly over-predicts the flux (the line profile presented in Figure 5.12 was generated with a density 25 per cent less than the best fitting HDUST model). This is because the disk in the model in the model of Grundstrom & Gies (2006) is smaller than the HDUST model as the radius of the star in the simpler model is less than that of the HDUST model (and the disk size is expressed in units of stellar radii). Also, the star in the model of Grundstrom & Gies (2006) is not subject to gravity darkening, and thus the star in this model may appear hotter at the equator than the star in the HDUST model, which in turn can lead to increased emission from the disk. However, allowing for these differences, the two model line profiles are reasonably consistent.

The sizes of the two best fitting AMC disk models are similar. However, the density of the previous best fitting model is an order of magnitude higher than in the HDUST

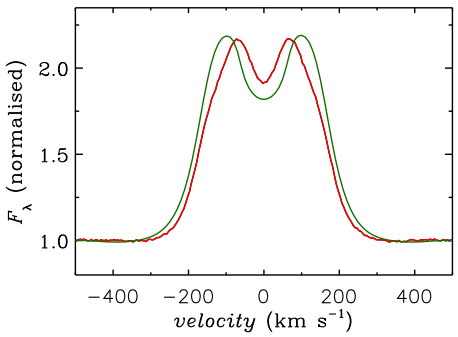

Figure 5.12: *A comparison between the line profiles generated using HDUST (in red) and the model of Grundstrom & Gies (2006) (in green) assuming a Keplerian disk. While the disk parameters are similar, it should be noted the properties of the central star differ between the two models (only HDUST includes the effects of rapid rotation).*

model. This is because the small size of the best fitting AMC disk results in a smaller emitting area than in the Keplerian case. Consequently, if the other disk properties are held constant, the AMC disk models do not match the observed Hα flux. One way to increase the line flux is to increase the disk density (as this increases the optically thick emitting area). In Section 5.5.1 the best fitting AMC disk has a density sixty times greater than the best fitting Keplerian disk, and as a consequence fits the line flux. Such an increase in density is not possible when using HDUST as this would lead to predicted polarisation and infrared flux well in excess of that observed. The only other option to increase the line flux is to increase the turbulent velocity within the disk model. This has the effect of increasing the emitting area at a given velocity and thus increase the line flux without effecting the predicted polarisation or infrared flux. As a result, the best fitting HDUST model has greater turbulent velocity than the previous best fitting AMC model. However, this has the effect of smoothing out the central reversal in the emission line profile, and thus HDUST struggles to recreate the observed line profile with a AMC disk. As a result, the Keplerian scenario is strongly favoured by this exercise. Therefore, the use of HDUST demonstrates (for the first time) that simultaneously fitting the line profile, infrared flux and optical polarisation of a Be star disk can provide insights into its kinematics.

However, the fact that the observed line profile is difficult to recreate using HDUST to model an AMC disk is not sufficient to discard the AMC scenario. Arguably, the inclination of β CMi is poorly constrained. Increasing the inclination of the system by 10° would have the effect of increasing the peak separation by 10 per cent, which would make fitting the line profile substantially easier. However, the predicted spectroastrometric signature of the best fitting HDUST AMC disk unambiguously rules out the AMC scenario as such a disk would be almost impossible to detect with the current spatial precision and this is relatively insensitive to inclination. Therefore, the earlier conclusion that spatial information is crucial in differentiating the various scenarios is shown to remain valid when using a more sophisticated model.

To summarise, the spectroastrometric signatures of the best fitting HDUST and Grundstrom & Gies (2006) models are essentially consistent. Similarly, the properties of the best fitting Keplerian models are also in agreement. Due to the extra constraints of additional data, the best fitting HDUST AMC disk is substantially different to the previous best fitting AMC disk. Consequently, it is difficult to fit the observed line flux for an AMC disk using HDUST. However, this is not in itself sufficient to discard this scenario. However, the spectroastrometric signature observed unambiguously excludes the AMC scenario as the spectroastrometric signatures of the previous best fitting AMC disk and the HDUST AMC disk are substantially smaller than the offsets observed over the Hα emission of β CMi. Therefore, both models indicate that the disk around β CMi rotates in a Keplerian fashion. That both models result in the same conclusion regarding this object suggests that the earlier conclusion regarding the larger sample of Be star disks (based on the simpler model) is robust.

5.8 Discussion

The data presented in this chapter also constitutes the most accurate spectroastrometry of Be stars to date. Therefore, in principle, these data are sensitive to binary systems with separations of less than 0.1 arcsec and differences in brightness of greater than 5 magnitudes (see e.g. Baines et al. 2006). Therefore, these data may also be used to constrain the binarity of Be stars (which is required to assess the suggestion that the

Be phenomenon is a consequence of binary interaction Bjorkman et al. 2002; Kervella et al. 2008). Oudmaijer & Parr (2010) argue that the Be phenomenon is not related to binarity as the binary properties of Be and B type stars are identical at intermediate separations (>0.1 arcsec). These data have the precision to detect systems with even smaller separations. Therefore, in this section the binarity of the sample is discussed.

Given that only two or three stars in the sample show evidence of binarity, it appears very unlikely that the Be phenomenon is related to binarity, given the sensitivity of spectroastrometry to binary systems (Baines et al. 2006). This is in agreement with recent work on the binarity of Be stars (e.g. Oudmaijer & Parr 2010). However, the sample includes a number of known binary systems that were not detected.

α Eri is a binary which has a separation of $\sim$0.15$''$ and a flux difference of $\sim$3.7 magnitudes in the NIR (Kervella et al. 2008). In addition, δ Cen is a binary which has a separation of $\sim$ 0.07$''$ and a flux difference of $\sim$2.8 magnitudes in the NIR (Meilland et al. 2008). The spectroastrometric data clearly have the capability to detect these systems. The only explanation for the non-detection of theses systems is that, due to their short periods ($\sim$ 15yrs), the projected separation of these systems at the time of observing was very small. The data of Kervella et al. (2008) suggest that the companion to HD 10144 is likely to have been around 0.1$''$away from the primary at the time of observing. This should have been detectable in the data, given a precision of <1mas. However, the binary orbit has not yet been determined and the stars could well be closer than 0.1$''$, given the short period. The orbital parameters of the δ Cen binary system are likewise unknown, and therefore the location of the companion at the time of observing cannot be predicted. In addition to these resolved binary systems, ζ Tau is known to be a single-lined, close binary (Jarad 1987). The small separation and large difference in brightness between the two components, 0.005$''$and 5 magnitudes respectively, are presumably the reason a binary signature is not detected in the spectroastrometric observations of this system (as was the case for Tycner et al. 2004).

Finally, the spectroastrometric data of Baines (2004) indicate that δ Cen, η Cen and η Tau are all binary systems with separations in the range $\sim$0.5–1 arcsec. In the data of Baines (2004), each of these objects exhibit positional offsets over the Hα line

of the order of 15–50 mas, substantially greater than the positional offsets observed here. The fact that these systems are not detected here is initially surprising as the data presented here is superior, in terms of spectral resolution and spatial precision, to the data of Baines (2004). The reason that these systems are not detected here is twofold. Firstly, the seeing during the observations if Baines (2004) was considerably worse than the seeing conditions the data presented here were obtained in (1.2–2.6 c.f. 0.6–1.2 arcsec). As a result, it is possible that the binary companions were resolved in the current observations, and thus contributed nothing to the spectroastrometric signatures. Secondly, the slit used during the current observations was narrower than the slit used by Baines (2004, 0.5 c.f. 1.0 arcsec). Since the systems detected by Baines (2004) have separations in excess of 0.5 arcsec, light from the secondary component is likely to have fallen outside the slit during the observations presented here. Consequently, the binary companions were unable to contribute to the spectroastrometric signatures.

To summarise, many known binary systems are not detected. Therefore, these data cannot exclude the hypothesis that the Be phenomenon is related to binarity, despite the high angular precision of the data ($\sim$0.1 mas).

These data constitute the first simultaneous constraints on the kinematics of a sample of Be star disks. Constraining the kinematics of these disks has strong ramifications upon their formation mechanism. Here, the kinematics of the disks observed are compared to various models invoked to explain their formation.

The fact that the majority of Be star disks appear to rotate in a Keplerian manner strongly constrains their formation mechanism. A wide range of mechanisms (ranging from binary interaction, non-radial pulsations and magnetic compression of wind streamlines: Kervella et al. 2008; Cranmer 2009; Brown et al. 2008) have been proposed to be responsible for the creation of the disks around Be stars. However, the various disk models can be separated into two broad categories: viscous deccretion disks and compressed wind disks. Viscous deccretion disks are essentially classical accretion disks working in reverse, in which material is transferred outwards from the star under the influence of some, as yet unknown, source of viscosity. Such disks exhibit Keplerian rotation (Lee et al. 1991; Porter 1999). In general, viscous disk models reproduce many

of the observed properties of Be stars (see e.g. Carciofi et al. 2009), and thus this model is currently favoured as the most accurate representation of Be star disks. However, the alternative model, wind compressed disks, has yet to be conclusively discarded.

The wind compressed disk model was originally proposed by Bjorkman & Cassinelli (1993), who suggested that the rapid rotation of Be stars could lead to the wind stream lines becoming distorted until stream lines from opposing hemispheres meet in the equatorial plane. In the interaction region dense, post-shock material accumulates to form an equatorial disk. In this scenario the disk rotates in an angular momentum conserving fashion ($V_{\rm rot} \propto R^{-1}$), and hence the choice of the two rotation laws in this chapter. Subsequent work on the non-radial component of the line driving force in this scenario revealed that disks cannot be formed in this fashion (Owocki et al. 1996). However, this model has been resurrected by the inclusion of magnetic fields (Cassinelli et al. 2002). Nonetheless, there is some controversy whether such a model is physically viable (Ud-Doula et al. 2006). In general, such wind compressed disk feature angular momentum conserving rotation, unless acted on by viscosity, in which case Keplerian rotation is possible (Brown et al. 2008).

Given that these data unequivocally indicate the disks around Be stars rotate in a Keplerian fashion, the data strongly favour the viscous deccretion disk model. Consequently, the data constrain the formation mechanism of Be star disks in that scenarios which do not result in Keplerian rotation (such as magnetically confined winds with no viscous effects) can be discarded.

5.9 Conclusion

This chapter has presented high spectral resolution, $\sim 4\,{\rm km\,s^{-1}}$, high spatial precision spectroastrometry over the Hα line of Be stars with the aim of detecting the small-scale circumstellar disks around these stars. The data constitute the most accurate spectroastrometric study of Be stars to date, and not only prove capable of detecting Be star disk but also constrain their kinematics. To conclude this chapter the most pertinent results are summarised below.

- The spectroastrometric observations of four objects exhibit position offsets indicative of a rotating disk. Several binary systems are detected and these positional offsets are distinctly different to the disk-like signatures. The non-detections are generally the most distant objects (or binary detections). Therefore, it is concluded that four circumstellar disks are detected.

- As a result, it is shown that spectroastrometry can detect circumstellar disks with angular sizes of only $\sim$5 mas. Therefore, it is shown that spectroastrometry has the potential to detect AU sized accretion disks around MYSOs at distances of up to several kpcs.

- The observed line profiles are fit with a simple model of Hα emission from a circumstellar disk several 10s of stellar radii in size and with two rotation laws: Keplerian rotation and angular momentum conserving. By comparing the predicted spectroastrometric signatures of the best fitting models to the observed signatures it is shown that the majority of Be star disks rotate in a Keplerian fashion. This chapter doubles the current sample of Be star disks with known kinematics and constitutes the first direct test of Be star disk kinematics with a sample of objects.

- Consequently, the data constrain the formation mechanism of Be star disks in that scenarios which do not result in Keplerian rotation (such as magnetically confined winds with no viscous effects) can be discarded.

- Modelling the disk of one object in particular with HDUST, a NLTE Monte Carlo code, it is found that additional data in the form of optical polarisation and the infrared SED can go some way in constraining the kinematics of Be star disks. However, this chapter demonstrates unambiguously differentiation between various rotation laws requires spatially resolved data.

Chapter 6

Probing discs around massive young stellar objects with CO first overtone emission

6.1 Introduction

As noted in Section 1, direct evidence for accretion discs around MYSOs is sparse. Recent simulations indicate that it is indeed possible to form massive stars via disk accretion (e.g. Krumholz et al. 2009). However, as no accretion disk has been directly detected, alternative massive star formation scenarios have not been discounted. The work presented in this thesis (see Chapter 2) indicates that intermediate mass stars form via disk accretion and that this may also be true for massive stars, providing indirect confirmation that massive stars form via disk accretion. Further indirect evidence that massive stars form in this fashion is provided by the discovery of collimated jets and small scale outflows emanating from MYSOs (Davis et al. 2004; Davies et al. 2010). Finally, in a few isolated cases, direct detections of discs and flattened structures around MYSOs have been made (Shepherd et al. 2001; Beltrán et al. 2005; Patel et al. 2005; Okamoto et al. 2009). However, such studies typically probe dust emission at long wavelengths, and thus large distances (of order hundreds to thousands of AU) from the central star. Indeed, the rotating structures detected by Beltrán et al. (2005) are too large to be considered circumstellar discs, as they are unstable and may fragment (see the discussion in Cesaroni et al. 2007). Very recently AMBER at the VLTI was used to

reconstruct an image of a flattened dusty structure (i.e. a disk) approximately 20 AU in size around a MYSO (Kraus et al. 2010). However, direct evidence of small-scale, AU sized, gaseous discs, and thus proof that MYSOs form via disk accretion, is still lacking.

Bik & Thi (2004) and Blum et al. (2004) found that the CO bandhead profiles of intermediate and massive YSOs could be fit with emission from discs with small, $\approx$ 0.1 AU, inner radii. This provides strong support for the formation of massive stars via disc accretion. However, the number of objects observed so far is small, and there are several intermediate mass objects among the observed samples. Furthermore, it has also been suggested that such emission traces shocks, dense winds and large, dense shells rather than small disks (Scoville et al. 1983; Chandler et al. 1995; Grave & Kumar 2007). Consequently, to firmly establish whether the CO emission of MYSOs originates in small-scale disks, and thus whether the most massive stars form via disk accretion, requires the study of a well-selected sample and spatially resolving the source of the CO emission.

This chapter extends the work of Bik & Thi (2004) and Blum et al. (2004) to a sample of MYSOs drawn from the red MSX (Midcourse Space eXperiment) source (RMS) survey catalogue (Urquhart et al. 2008b). The RMS is an unbiased, galaxy wide survey of MYSOs and the most representative sample of this class of object. Previous searches for MYSOs relied on the *IRAS* Point Source Catalogue (e.g. Chan et al. 1996; Molinari et al. 1996; Sridharan et al. 2002). However, due to the large beam of *IRAS* (2–5' at 100 μm), such studies suffered from considerable source confusion, and were biased away from the Galactic Plane, where the majority of MYSOs are expected. The RMS, however, utilises the *MSX* survey of the galactic plane in the mid infrared (Price et al. 2001). The *MSX* survey has a resolution of $20''$ and thus offers a factor of approximately 50 improvement in spatial resolution over *IRAS*, which allows sources to be detected in regions that are otherwise unresolved. Therefore, the use of the *MSX* survey allows a unique and representative sample of MYSOs to be selected. Specifically, the RMS survey used colour selection criteria and the *MSX* and 2MASS catalogues (Egan et al. 2003; Cutri et al. 2003) to select an unbiased sample of approximately 2000 potential MYSOs (see Lumsden et al. 2002). However, this initial sample contains objects such as planetary

nebulae, HII regions and low luminosity YSOs that have a similar appearance to MYSOs in the near and mid infrared. These contaminant objects have been eliminated via an extensive multi-wavelength campaign featuring high resolution (1–2″) observations in the radio continuum (Urquhart et al. 2007a, 2009), the ^{13}CO J=1–0 and J=2–1 lines (Urquhart et al. 2007b, 2008a), the mid infrared (Mottram et al. 2007a) and the near infrared (e.g. Clarke et al. 2006). In total, the RMS database[(a)] provides a large (∼500), well-selected sample of mid infrared bright MYSOs.

Here, the RMS survey is exploited to study the accretion characteristics of a sample of MYSOs. The low resolution, NIR spectroscopy undertaken as a part of the classification stage of the survey (e.g. Clarke et al. 2006) was used to select a sub-sample of objects with CO 1st overtone bandhead emission at 2.3 μm. These objects were then observed at high spectral resolution to investigate whether their CO bandheads are consistent with emission originating in a small-scale circumstellar disc. This is done by comparing the observed bandhead profiles to models of CO emission from small-scale discs.

To fully constrain the models, information on the spatial distribution of the emission is also required. However, the emission region is expected to be small. At a typical distance of 1kpc, a disc of 1 AU in size subtends an angle of only 1 milli-arcsec (mas). Spectroastrometry is one of a few approaches that offers the required, sub-mas, angular precision and high spectral resolution. Indeed, such an approach has already been shown to be able to detect and characterise circumstellar discs with a precision of approximately 0.1 mas (Pontoppidan et al. 2008; van der Plas et al. 2009). Therefore, spectroastrometry is used to probe the spatial behaviour of the bandhead emission with high spectral resolution (which is required to obtain kinematic information).

This chapter is structured as follows. A model of CO overtone emission from a geometrically thin disk is described in Section 6.2. Section 6.3 presents the sample of MYSOs, details of the observations and the data reduction processes used. The resultant data are presented in Section 6.4, alongside the results of fitting the model of CO emission from a circumstellar disc to the data. Section 6.5 presents a discussion of the results. Finally, the chapter concludes in Section 6.6.

[(a)] http://www.ast.leeds.ac.uk/RMS/

6.2 The model

The model of CO 1st overtone bandhead emission is based on that of Kraus et al. (2000). Initially, a simple, geometrically flat disc is constructed, within which the excitation temperature and surface number density decrease with increasing radius. The decrease in temperature and surface number density are treated as power laws. The temperature decreases with $R^{-0.75}$ and the surface number density falls off with $R^{-1.5}$, in line with standard accretion disc theory (Pringle 1981), and following Kraus et al. (2000), who also modelled CO emission from a circumstellar disc. As the disc model is very simple and does not incorporate accretion, the temperature of the disc is determined as follows: $T(R) = T_{\rm eff} \times (\frac{R}{R_\star})^{-0.75}$, where $T_{\rm eff}$ is set based on the luminosity of the star (assuming it to be on the main sequence). The disc is split into radial and azimuthal cells. If the temperature in a cell is greater than 5000 K (the assumed destruction temperature of CO), the flux from the cell is set to zero. If the outer radius of the disc is such that the outer cell temperatures are less than 1000 K, the disc is shrunk until the temperature at the edge is 1000 K. Therefore, while the radii were varied during the fitting process, they are tied to the temperature structure of the disc. The CO emission of each cell is calculated according to the methodology of Kraus et al. (2000), which is briefly described in the following.

CO bandhead emission (or absorption) is due to many individual coupled rotational and vibrational transitions of the CO molecule. The various energy levels can be calculated from:

$$E(\upsilon, J) = \mathrm{hc} \sum_{k,l} Y_{k,l} \left(\upsilon + \frac{1}{2}\right)^k (J^2 + J)^l \tag{6.1}$$

where υ and J are the vibrational and rotational quantum number respectively and $Y_{\rm k,l}$ represents the Dunham coefficients (see Dunham 1932). The Dunham coefficients required to calculate the CO energy levels were taken from Farrenq et al. (1991). The resultant energy levels are presented in Figure 6.1. Each vibrational transition corresponds to a distinct bandhead, within which there are many rotational lines. For example the 1st overtone is due to the 2-0 transition and the R branch of rotational transitions (see Figure 6.2). The population of the CO rotational levels (up to J=100) for the 2-0 vibrational transition in each cell is determined assuming local thermodynamic equilibrium

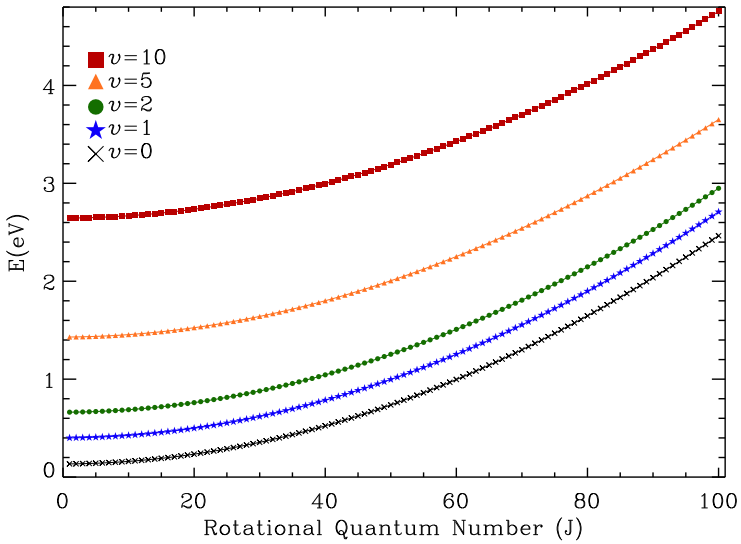

Figure 6.1: *Ro-vibrational energy levels of the CO molecule.*

and using the Boltzmann distribution:

$$n_{\upsilon,J} = \frac{n}{Z}(2J+1)e^{-\frac{E(\upsilon,J)}{\mathrm{kT}}} \tag{6.2}$$

where n denotes the CO number density and Z is the partition function, which was calculated using the following:

$$Z = \sum_{\upsilon} e^{-\frac{E_{\upsilon}}{\mathrm{kT}}} \times \sum_{J}(2J+1)e^{-\frac{E_J}{\mathrm{kT}}} \tag{6.3}$$

(with a maximum υ and J of 15 and 110 respectively, as per Berthoud 2008).

Once the level populations are calculated, they are used in conjunction with the transition probabilities of the respective lines to determine the resulting absorption coefficients according to the following:

$$K_{\nu} = \frac{\mathrm{c}^2 n_{\upsilon J} \mathrm{A}_{\upsilon J,\upsilon' J'}}{8\pi\nu^2}\left(\frac{2J+1}{2J'+1} \times \frac{n_{\upsilon' J'}}{n_{\upsilon} J} - 1\right)\Phi(\nu) \tag{6.4}$$

where the numbers υ and J refer to the upper level of a transition and υ' and J' refer to the lower level, $\Phi(\nu)$ represents the intrinsic line profile and $\mathrm{A}_{\upsilon J,\upsilon' J'}$ denotes the Einstein

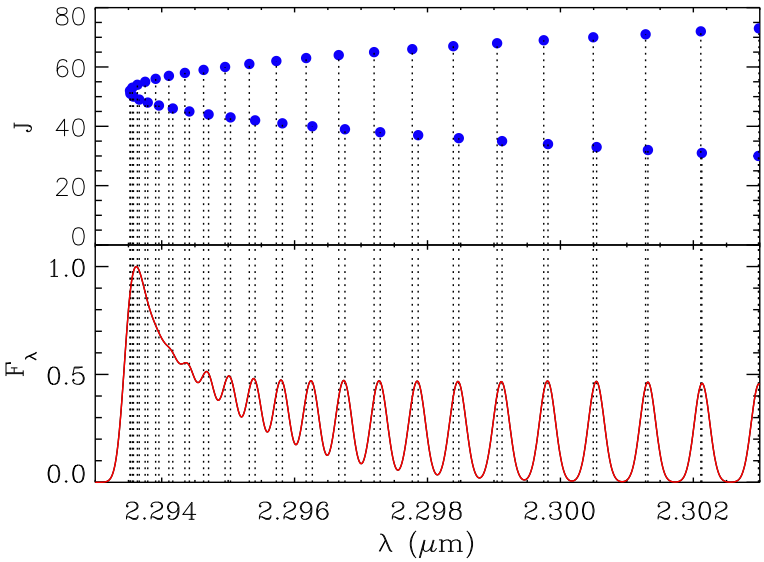

Figure 6.2: *The R branch ($\Delta J{=}-1$) transitions which create the CO 1st overtone bandhead. Note the flux has been normalised.*

coefficient of the transition. The intrinsic line profile is assumed to be Gaussian, with the line-width being a free parameter. The Einstein coefficients of each ro-vibrational transition were taken from Chandra et al. (1996). Assuming the absorption coefficient is constant along the line of sight, the optical depth is given by the product of the absorption coefficient per CO molecule and the CO column density. The column density is given by the surface number density, since a thin disc is used. The intensity of the individual lines at the cell surface are then calculated using equation 6.5.

$$I_\nu = \mathrm{B}_\nu(\mathrm{T})(1 - \mathrm{e}^{-\tau_\nu}) \tag{6.5}$$

Figure 6.3 presents CO 1st overtone emission from CO at various densities and temperatures to illustrate the effect of the changing cell properties on the emerging spectra. Such plots were compared to those presented in Berthoud (2008) to ensure the CO emission was calculated correctly. Once the individual cell spectra are calculated, they are summed to create the total spectrum. This is then convolved with a Gaussian profile to match the spectral resolution of the observations.

To determine the best-fitting model, the downhill simplex algorithm was used. This

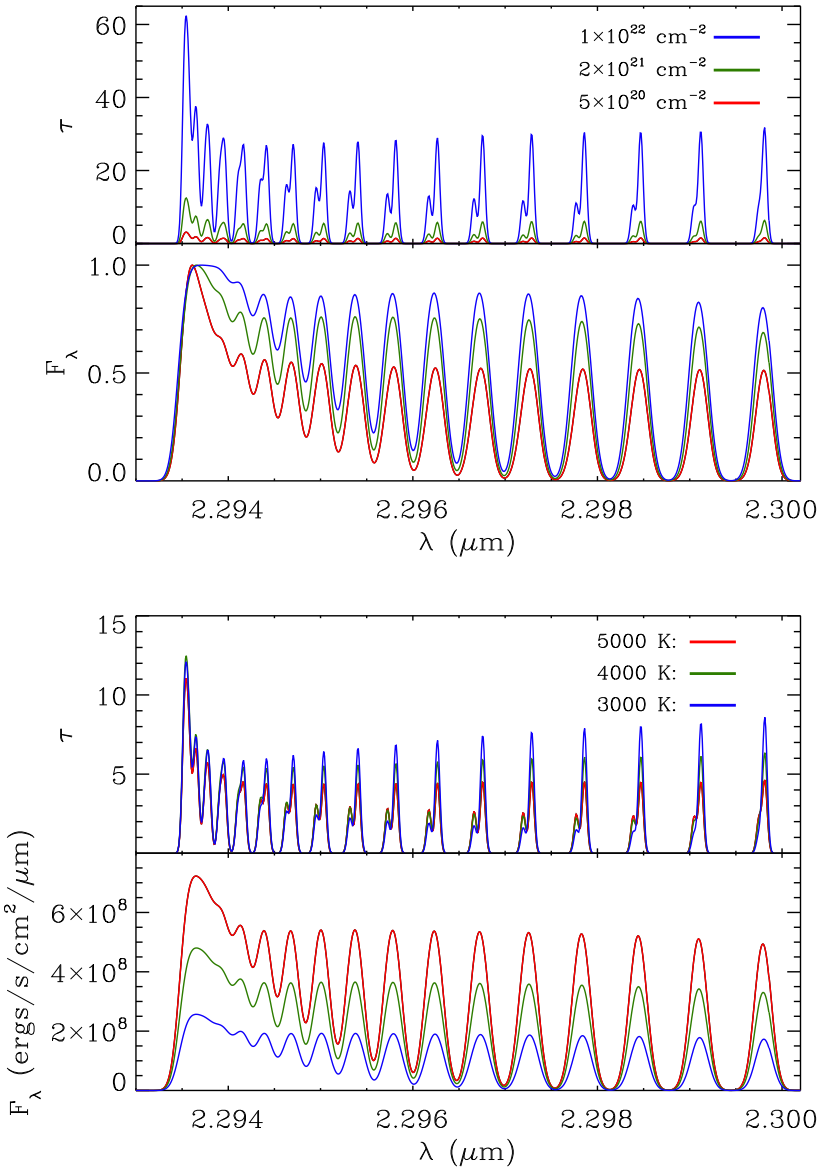

Figure 6.3: *The effect of changes in excitation temperature and number density on the CO* 1st *overtone emission spectrum. The top plot presents the effects of changing the surface number density while holding the excitation temperature constant (at 4000 K). The flux in the upper panel has been normalised. The lower plot presents the reverse scenario in which the column density was kept constant (at* $2 \times 10^{21}\,\mathrm{cm}^{-2}$*) while the excitation temperature was varied.*

algorithm is supplied with the Interactive Data Language distribution (IDL), and is based on the AMOEBA routine. The free parameters are: the inner and outer radius of the disc, the inclination of the disc, the surface number density at the inner edge of the disc and the line width within the disc. The effect of these parameters on the emerging spectrum is presented in Figure 6.4. The value of the inclination affects the extent by which the individual lines are rotational broadened. As a result, at high inclinations the bandhead has a conspicuous blue shoulder due to rotational broadening, while at low inclinations there is a sharp rise from the blue continuum to the bandhead. The surface number density affects the amount of flux emitted by the disk and changes the slope on the red side of the bandhead due to optical depth effects (see also Figure 6.3). The line width also affects the flux in the bandhead as for a given velocity, increasing the line width results in a larger area of the disk emitting flux at the velocity in question (as discussed in Chapter 5).

Once the best-fitting parameters have been determined, the spectroastrometric signature of the best-fitting model is predicted. This is done by mapping the flux from each cell onto an array with orthogonal spatial and dispersion axes that represents a long-slit spectrum. The array is then convolved with a Gaussian profile in the spatial direction, to represent the seeing conditions. The synthetic signature is then generated by fitting a Gaussian profile to the spatial distribution at each dispersion pixel.

The stellar mass is not a free parameter and is set to that listed in Table 6.1, which is generally determined from the luminosity of the source and main sequence relationships (Martins et al. 2005). However, the luminosities of IRAS 08576−4334 and M8E are not known. Therefore, the mass of IRAS 08576−4334 was determined from its position in the K vs $J-K$ diagram of Bik et al. (2006). The distance to IRAS 08576−4334 is revised, and it is found the object is still located in the mid- to early B area of the K vs $J-K$ diagram, and hence assume it has the mass of a B3 type star. The mass of M8E was taken from Linz et al. (2009), and is the mass of the best-fitting model from the grid of models by Robitaille et al. (2007), and is thus subject to considerable uncertainty (see e.g. Follert et al. 2010).

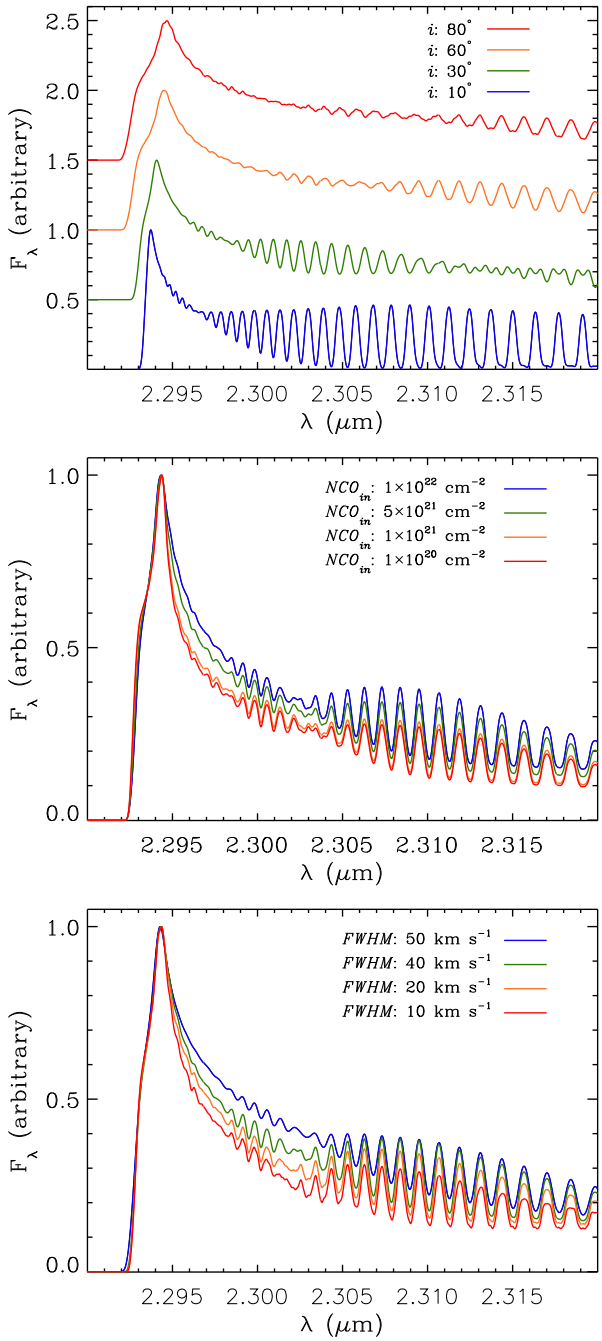

Figure 6.4: *Examples of* 1st *overtone bandhead emission from a disk and the effects of changes in inclination (top), surface number density at the inner rim (middle) and line FWHM (bottom).*

Using the luminosity of a MYSO to determine its mass is subject to some uncertainty as the observed luminosity may be due in part to accretion, resulting in an overestimate of the stellar mass. To evaluate the possible effect this may have, the models of accreting, massive protostars presented by Hosokawa & Omukai (2009) were consulted. During the early adiabatic accretion phase, the accretion luminosity of a massive protostar is greater than its intrinsic luminosity. However, by the time a massive protostar enters its main sequence accretion phase the intrinsic luminosity is greater than the accretion luminosity. While the resultant total luminosity is slightly greater than the zero age main sequence luminosity the two are not different by an order of magnitude. Given the high luminosity of the sample objects, it is likely they are in the Kelvin-Helmholtz contraction or main sequence accretion phases. Therefore, it is unlikely their luminosity is significantly overestimated. Furthermore, given that the objects are most likely in their main sequence accretion phase, the main sequence relationship between mass and luminosity should be applicable. Therefore, it is surmised that using main sequence relationships is sufficient for the purposes of this chapter.

6.3 Observations and data reduction

6.3.1 Observations

The sample was selected using the low resolution K-band spectroscopy undertaken as part of the RMS survey (Cooper et al. in prep.) to identify objects with CO 1^{st} overtone bandhead emission. In addition to the resulting targets, IRAS 08576−4334 and M8E were included in the sample. IRAS 08576−4334 is an intermediate mass YSO known to exhibit CO first overtone emission (Bik & Thi 2004). This object was included in the sample of MYSOs as its CO emission has been reported to be extended on scales of tens of AU (Grave & Kumar 2007), making it an appropriate target to study the spatial distribution of CO emission. M8E is a very bright MYSO that is thought to possess a circumstellar disc (Simon et al. 1985). The final sample is presented in Table 6.1, along with details of the observations.

High resolution spectroscopy of the sample at 2.3μm was obtained using Phoenix at Gemini South (Hinkle et al. 2000) and CRIRES (Kaeufl et al. 2004) on UT1 at the VLT.

When using Phoenix a slit of 0.34 arcsec was used, which resulted in a spectral resolution of approximately 50 000, or 6 $\mathrm{km\,s^{-1}}$. The CRIRES observations were conducted using a slit of 0.4 arcsec, and the same spectral resolution. Observations were conducted using 4 slit position angles (PA): 0°, 90°, 180° and 270°, which is a requirement for accurate spectroastrometry (see Bailey 1998b).

The observations with Phoenix were conducted with the K4396 filter, which has a central wavelength of 2.295 μm, to isolate the region surrounding the CO 1$^{\mathrm{st}}$ overtone bandhead. When using CRIRES, the $\mathrm{K_s}$ filter was used with the spectral configuration identified by the reference wavelength 2.2932 μm. This resulted in the CO 1$^{\mathrm{st}}$ overtone bandhead being located on the third chip, with a few ro-vibrational lines evident on the fourth (e.g. between $\sim 2.30 - 2.31\mu$m). All observations were conducted using a standard nodding sequence along the slit to remove the sky background. Where a natural guide star was available (G332.8256−00.5498 and G347.0775−00.3927) the adaptive optic capabilities of the VLT, the Multi-Application Curvature Adaptive Optics facility, was utilised. All the observations with Phoenix at Gemini South were conducted with natural seeing. The resulting Full Width at Half Maximum (FWHM) of the spectral spatial profiles ranged from 0.27 to 0.75 arcsec, and was typically 0.5 arcsec.

Telluric standard stars, late B type or early A type dwarfs, were observed with the identical instrumental setup as the science observations, and at similar air-masses. These spectra were subsequently used to correct the science spectra for telluric lines, and to provide a rough photometric calibration.

Table 6.1: *A summary of the sample and observations. The luminosities (Col. 5) are taken from the* RMS database†, *and are based on the work of Mottram et al. (2010) and Mottram et al. (2010: in prep.). The distances (Col. 7) are taken from the literature as indicated. The masses (Col. 4) are estimated from the bolometric luminosities and main sequence relationships (Martins et al. 2005), unless otherwise stated. Finally, the K-band magnitudes (Col. 6) are from the* 2MASS Catalog‡ *and the literature.*

Name	RA	Dec	M	L_{Bol}	K	d_{kin}	Time	Δpos	Date
	J2000	J2000	$M_\odot$	$L_\odot$	mag	kpc	hours	mas	
IRAS 08576−4334* (GS)	08 59 25.2	−43 45 46.0	6.1$^\diamond$		9.4*	2.2*	4.27	0.76	2008: 01/-02,-10,-23
G287.3716+00.6444 (GS)	10:48:04.6	−58:27:01.0	15.4	2.9×10^4	7.5	5.6	3.20	0.25	2008: 01/-10,-21
M 8E* (GS)	18 04 53.3	−24 26 42.3	13.5$^\triangle$		4.4	1.9$^\bullet$	0.27	0.47	2007: 10/04
G308.9176+00.1231 (VLT)	13:43:01.6	−62:08:51.3	42.6	3.9×10^5	6.4	5.3	0.60	0.13	2009: 04/-08,-11
G332.8256−00.5498 (VLT)	16:20:11.1	−50:53:16.2	24.5	1.3×10^5	8.9	3.8$^\square$	2.40	0.32	2009: 05/08, 08/19
									09/-01,-08
G347.0775−00.3927 (VLT)	17:12:25.8	−39:55:19.9	17.7	4.3×10^4	8.5	14.9	2.80	0.15	2009: 07/-17,-19
									08/-03,-15
G033.3891+00.1989 (VLT)	18:51:33.8	+00:29:51.0	11.8	1.3×10^4	7.2	5.5	1.22	0.63	2009: 05/14, 07/05
									08/-02,-15,-19

†: http://www.ast.leeds.ac.uk/RMS/, ○: the distances in the RMS database are from Bronfman et al. (1996); Urquhart et al. (2007b, 2008a), ‡: Cutri et al. (2003), ⋆: Kinematic distance from the rotation curve of Brand & Blitz (1993) and a V_{LSR} of 7.5km s^{-1} (Bronfman et al. 1996), •: Chini & Neckel (1981), ∗: Bik et al. (2006), △: Linz et al. (2009), ⋄: based on the photometry and K vs $J-K$ diagram of Bik et al. (2006), a distance of 2.17 kpc and the data of Harmanec (1988), □: Near/Far ambiguity, here, the smallest possible distance is used.

6.3.2 Data reduction

The data were reduced in a standard fashion. An average flat frame was constructed, corrected for dark current and bias levels and normalised. The individual exposures were then corrected by the normalised, average flat frame (the IRAS 08576−4334 and G287.3716+00.6444 data were corrected with a median smoothed flat frame due to a discrepancy between the flat response and the behaviour of the A and B spectra). Pairs of spectra defined by the A and B nodding positions were subtracted from one-another, and the individual intensity spectra were extracted from the resultant data. Spectroastrometry was conducted by fitting a Gaussian profile to the spatial profile of the spectrum at each dispersion pixel. This resulted in a position spectrum; the photo-centre of the spectrum as a function of wavelength, associated with each conventional spectrum. The centroid may be determined with high precision, allowing the centre of the emission to be traced to within a fraction of a pixel (for example see Oudmaijer et al. 2008; van der Plas et al. 2009, Chapter 2). Visual inspections were used to ensure the Gaussian profile was a valid representation of the Point Spread Function. As noted by Takami et al. (2003), the precision of spectroastrometry scales linearly with the width and signal to noise ratio (SNR) of the spatial profile. As a consequence of the high SNR data (typically 200-300), and narrow spatial profiles, an angular precision down to approximately 0.2 mas was achieved.

The individual flux spectra at a given PA were combined, as were the positional spectra, to form an average spectrum for the PA in question. The intensity spectra were divided by the spectrum of a telluric standard to correct for telluric absorption lines. Finally, the intensity spectra at each PA were combined to form the average for the object in question. Dispersion correction was performed using the telluric lines in the telluric standard spectra and the high resolution NIR spectrum of Arcturus presented by Hinkle et al. (1995). The dispersion correction typically had an rms of 0.5 $\mathrm{km\,s^{-1}}$, i.e. less than $\frac{1}{10}$ the resolution. The positional spectra at anti-parallel position angles were combined to form the average North-South and East-West position spectra as follows: (0-180)/2 and (90-270)/2. This eliminates artificial signatures which do not follow the slit rotation (see Bailey 1998b).

Finally, the object spectra were flux calibrated using the telluric standards. Dividing the science data by a telluric standard spectrum allowed the continuum brightness ratio to be determined. The K-band magnitude of the science object was then estimated from the flux ratio and the telluric's K-band magnitude from 2MASS. The result was generally within 10 per cent of the published K-band magnitude. Therefore, the objects' K-band magnitudes were used to estimate the continuum flux density. The flux over the bandhead was then determined based on the observed strength of the CO emission.

6.3.3 Extinction determination

In Section 6.4.2 the flux densities of the best-fitting models are compared with the observed values, a consistency check that is often not performed in similar studies. In order to assess the intrinsic bandhead flux, the extinction towards each object must be determined.

To achieve this, the methodology of Porter et al. (1998) is used, along with the NIR extinction law of Stead & Hoare (2009) and the low resolution, H-band spectroscopy undertaken as part of the RMS survey. It is important to note that the general extinction law for the interstellar medium may not be applicable to regions of high extinction (e.g. see Moore et al. 2005). However, the flattening of the NIR extinction law reported by Moore et al. (2005) only becomes apparent at an extinction of approximately 4 magnitudes in K, and in general the extinction towards MYSOs is less than this (e.g. Porter et al. 1998). Therefore, the general interstellar extinction law should be applicable to the sample presented here.

It is assumed that the science targets are relatively hot, early type stars. The NIR continuum of a hot star is well approximated by the Rayleigh-Jeans (RJ) tail (Porter et al. 1998). By reddening the RJ slope, $F_\lambda \propto \lambda^{-4}$, until it fits the observed H-band continuum, the extinction can be determined. This is shown in Fig. 6.5 for the RMS sources for which low resolution NIR spectra have been obtained. Only the H-band spectral continuum is used, as it is less likely to be contaminated with emission from hot dust than the K-band. Extinction estimates for MYSOs derived from the continuum in the H-band are generally consistent with the results of other methods (Porter et al. 1998). However, extinction values based on the continuum from the H-band and into the

K-band tend to be overestimates, due to infrared excess emission from hot circumstellar dust (Porter et al. 1998). Therefore, the wavelength range $\sim 1.5 - 1.6$ μm is used to estimate the extinction towards the science targets. The determined values of A_V and A_K are presented in Table 6.2.

The uncertainty in determining the extinction towards an object using the slope of its NIR continuum is typically 10–15 per cent (Porter et al. 1998, based on visually assessing the quality of the fit). The uncertainty based on the χ^2 statistic associated with fitting the continuum is also generally 10 percent, or approximately 0.1–0.3 magnitudes. While this uncertainty is in agreement with previous work there is an important caveat to consider. This approach assumes the continuum observed is purely photospheric in origin. If the stellar continuum is contaminated by hot dust emission, the blue to red slope will become steeper, and the extinction will be overestimated. Conversely, if continuum is contaminated by scattered light the extinction will be underestimated due to a shallower slope.

In general the values of A_V are similar, with most values close to 20–30. However, the derived extinction of A_V=70 to G332.8256−00.5498 is significantly higher than the other values. Contamination of the continuum by dust emission may have resulted in the extinction being over estimated as the wavelength range used to determine the extinction was extended to 1.6–1.7 μm (as no flux was observed at 1.5–1.6 μm). Assessing the presence of dust-excess emission by SED modelling is beyond the scope of this chapter. However, the ratio of the HI lines in the low resolution spectrum can be used to assess the extinction independently of the continuum using the following equations (see e.g. Landini et al. 1984; Lumsden & Puxley 1996; Moore et al. 2005):

$$\Delta\tau_{12} = -\ln \frac{[I(\lambda_2)/I(\lambda_1)]_{\rm obs}}{[I(\lambda_2)/I(\lambda_1)]_{\rm theory}}, \tag{6.6}$$

$$\Delta\tau_{12} = \tau_{\lambda_1}[(\lambda_2/\lambda_1)^{-\alpha} - 1], \tag{6.7}$$

where α represents the slope of the NIR extinction law and the ratio of two lines, $I(\lambda_2)/I(\lambda_2)$, can be predicted from models like those of Storey & Hummer (1995), assuming a certain temperature and density. Using the ratio of the Bγ and Br10 lines (~ 3 between 10^{4-6} cm^{-3} and 500–30000 K) and a value of 2.1 for the slope of the NIR

extinction law results in a value of A_K=2.4±0.3. This value is consistent with the mean value of the sample, and since it is not affected by emission from hot dust is likely to be closer to the correct value than the previous value of 7.9. Therefore, this value of A_K for this object is used. It is noted that determining the extinction towards an object via the ratio of HI recombination lines is only valid if the intrinsic line ratios can be estimated via hydrogen recombination models (e.g. Storey & Hummer 1995). This requires that case B of Baker & Menzel (1938) applies, which in principle limits this method to HII regions. As G332.8256−00.5498 is the only HII region in the sample, this is the only object this method can be applied to.

These extinction estimates are subject to some uncertainty (of the order 10 per cent), which translates to a substantial uncertainty in the de-reddened continuum fluxes (up to approximately 50 per cent). Nonetheless, the derived fluxes will provide a useful check on the modelling results.

6.4 Results

6.4.1 The spectra

Continuum normalised spectra of the MYSO sample at 2.3μm are presented in Fig. 6.6. The objects exhibit a range of CO bandhead profiles. Some display a clear blue 'shoulder' at the bandhead (e.g. G332.8256−00.5498), while others exhibit a relatively sharp rise from the blue continuum to the bandhead (e.g. IRAS 08576−4334). The peak fluxes for the RMS objects are of order 10 per cent the continuum, much less than that of IRAS 08576−4334 (~ 80 percent). Bandhead profiles with a prominent blue shoulder are indicative of emission from a rotating disc (e.g. Najita et al. 1996). Nonetheless, the profiles with sharper edges to the bandhead can also be fit with disc models (see Bik & Thi 2004), provided the disc is large or the inclination is low, thereby minimising the rotational broadening of the bandhead.

A simple model is used to first fit the bandhead profiles. The predicted spectroastrometric signatures of the best-fitting models are then compared with the data.

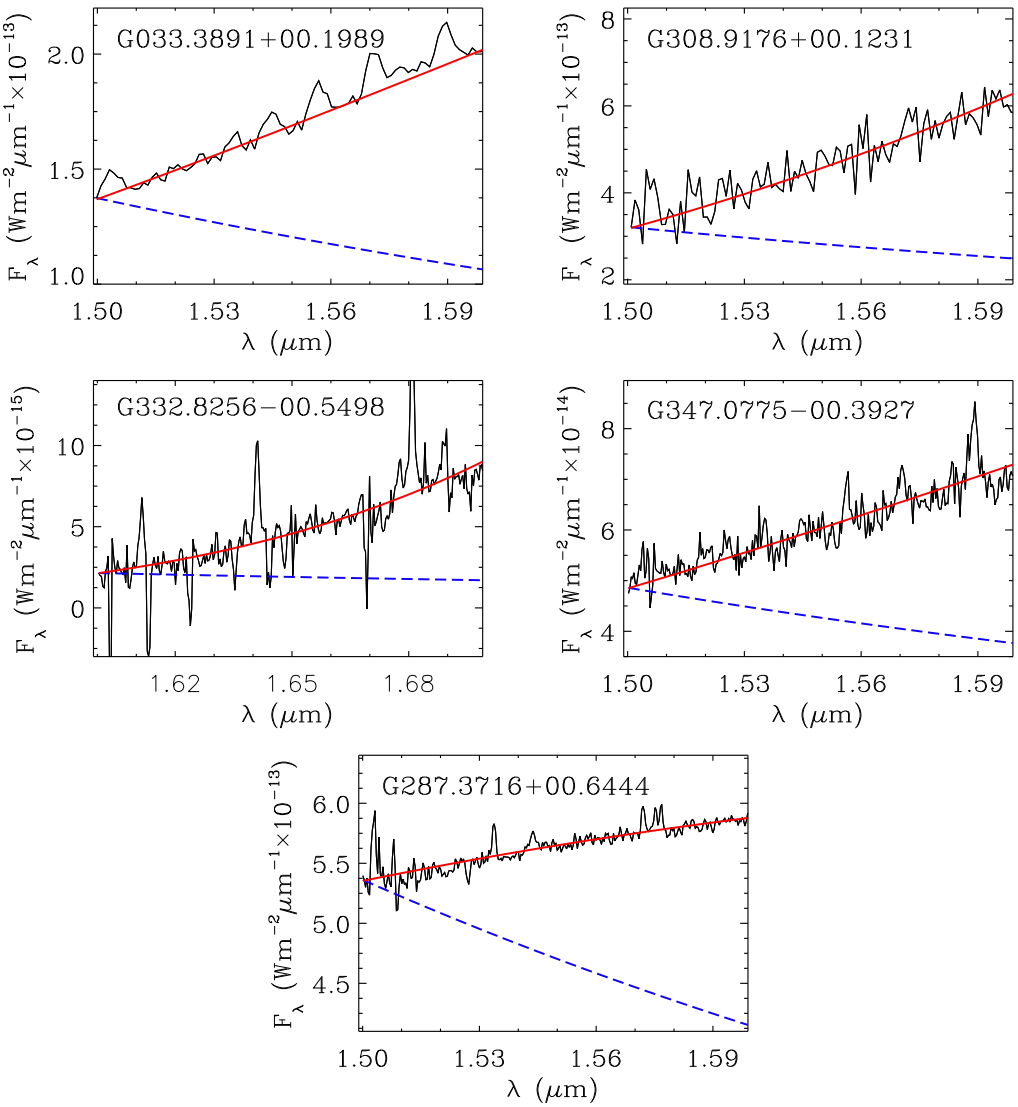

Figure 6.5: *The RMS sources for which low resolution NIR spectra have been obtained as part of the follow-up program of observations for the RMS survey. The dashed line represents the Rayleigh-Jeans tail of a hot star ($F_\lambda \propto \lambda^{-4}$). The solid line is this tail reddened to fit the slope of the H-band spectra.*

Table 6.2: *The extinction (Cols 2 & 3) towards each object (Col. 1). The A_V values are determined from the best-fitting A_K values and the relationship between optical and NIR extinction from Cardelli et al. (1989). In addition, the table also presents the K-band continuum flux density of each object, based on its K-band magnitude (Col. 4), and the estimated flux density at the peak of the CO 1st overtone bandhead (Col. 5). Finally, we de-redden the CO bandhead flux (Col. 6) and compare it to the flux of the best-fitting model (Col. 7, see Section 6.4.2). The uncertainty in the extinction values are estimated from assessing the fit to the continuum with χ^2 (where the fitting range was specified to avoid lines and artefacts in the spectra). The uncertainty in the extinction is then used to determine the error in the flux.*

Object	A_V	A_K	F_{cont} $Wm^{-2}\mu m^{-1}$	F_{CO}(observed) $Wm^{-2}\mu m^{-1}$	F_{CO}(de-reddened) $Wm^{-2}\mu m^{-1}$	F_{CO}(model) $Wm^{-2}\mu m^{-1}$
IRAS 08576−4334	12†	1.4	5.8×10^{-14}	4.4×10^{-14}	1.6×10^{-13}	2.8×10^{-13}
G287.3716+00.6444	12	1.3±0.1	3.3×10^{-13}	2.6×10^{-14}	$8.6\pm0.8\times10^{-14}$	see §6.5.3
M8 E	25‡	2.8	5.8×10^{-12}	8.1×10^{-13}	1.1×10^{-11}	6.2×10^{-12}
G308.9176+00.1231	32	$3.6^{+0.4}_{-0.5}$	9.1×10^{-13}	7.3×10^{-14}	$2.0^{+0.9}_{-0.7}\times10^{-12}$	3.0×10^{-12}
G033.3891+00.1989	22	2.5±0.3	4.4×10^{-13}	5.2×10^{-14}	$5.2^{+1.6}_{-1.3}\times10^{-13}$	3.7×10^{-13}
G332.8256−00.5498	70	2.4±0.3	9.1×10^{-14}	1.9×10^{-14}	$1.7^{+0.6}_{-0.4}\times10^{-13}$	3.6×10^{-13}
G347.0775−00.3927	23	2.6±0.3	1.3×10^{-13}	1.3×10^{-14}	$1.4^{+0.5}_{-0.3}\times10^{-13}$	5.0×10^{-14}

†: Bik et al. (2006), ‡: Porter et al. (1998)

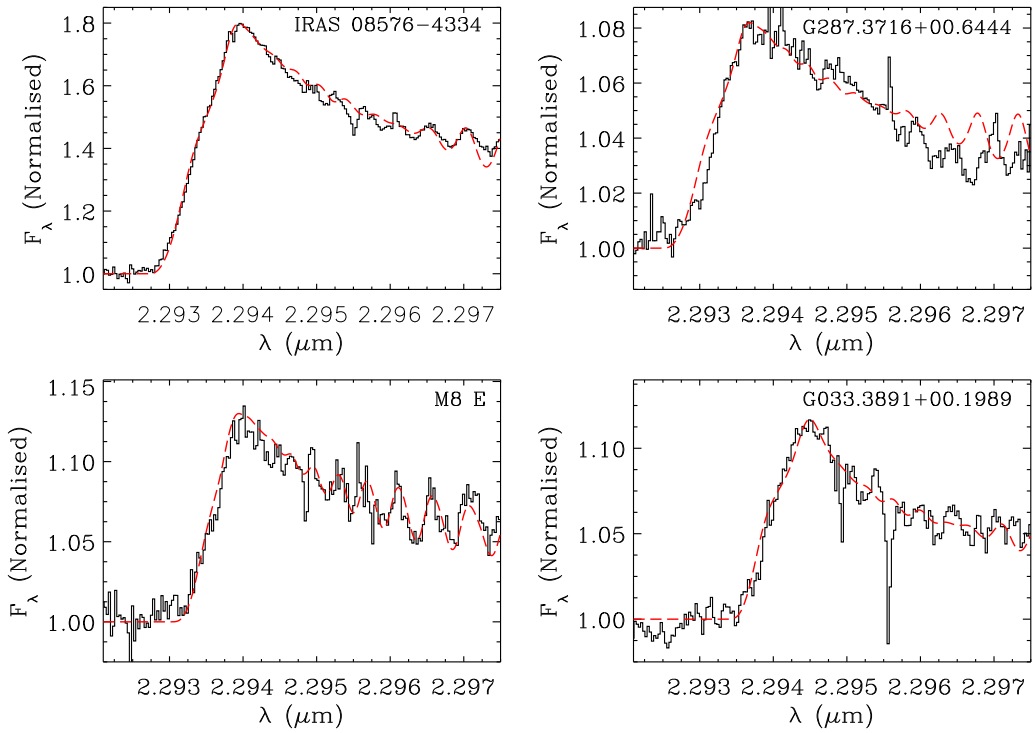

Figure 6.6: *The spectra of the sample around the CO* 1st *overtone bandhead. The spectra have been divided by standard spectra, normalised, and re-binned by a factor of 3. The dashed line represents the best-fitting model, which is described in Section 6.2. The absorption features present in the spectra of G033.3891+00.1989 are telluric effects.*

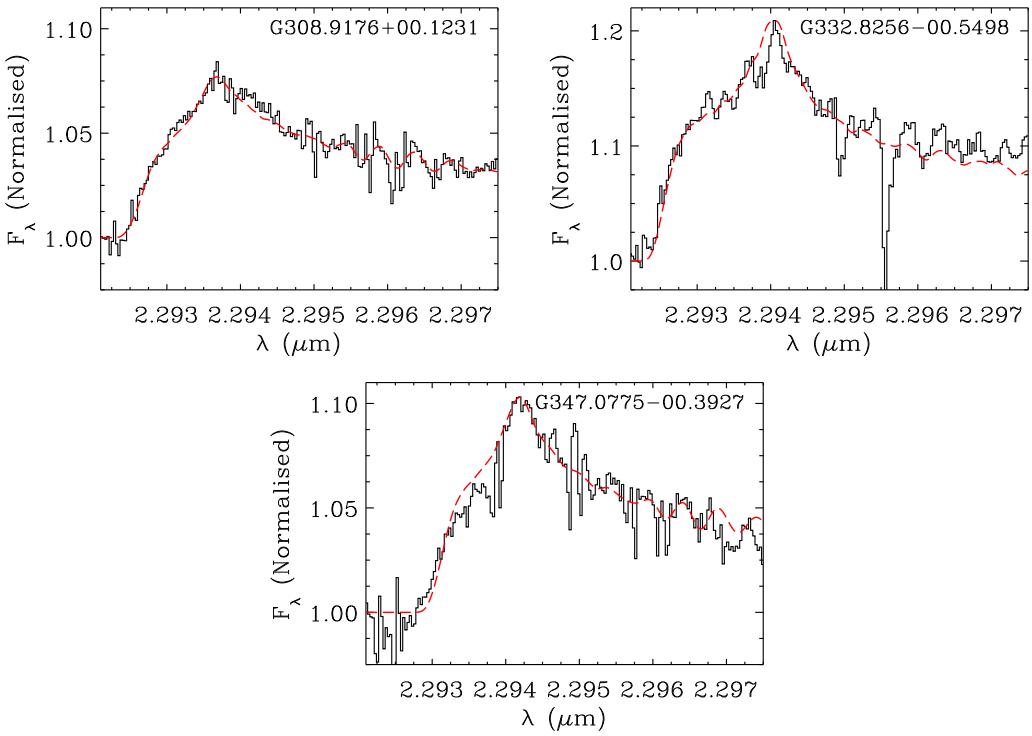

Figure 6.6 continued. The absorption features present in the spectra G332.8256-00.5498 are residual telluric effects.

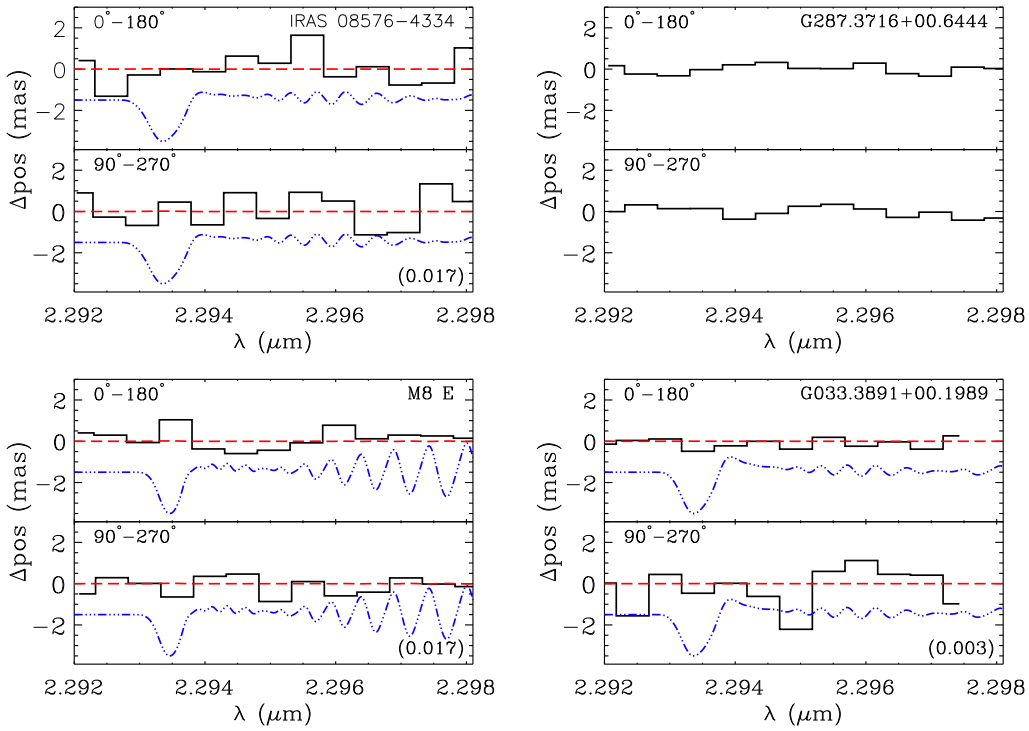

Figure 6.7: *The spectroastrometric signatures of the sample over the CO* 1st *overtone bandhead emission, shown normalised to the continuum position. The data, the solid line, have been re-binned with a bin size of 65* km s^{-1} *(approximately 11 times the resolution element). In addition, the predicted signatures of the best-fitting model (see Section 6.4.2) for each object are presented, bar G287.3716+00.6444 (see Section 6.5.3), to illustrate the signature of a rotating disc. The model signature is shown twice (at the un-binned spectral resolution): 1. with its predicted amplitude (dashed line), and 2. amplified to a fixed amplitude of 2 mas in the negative direction to enhance its visibility (offset dot-dashed line). The maximum predicted signature is presented in the lower right corner of each plot (in mas).*

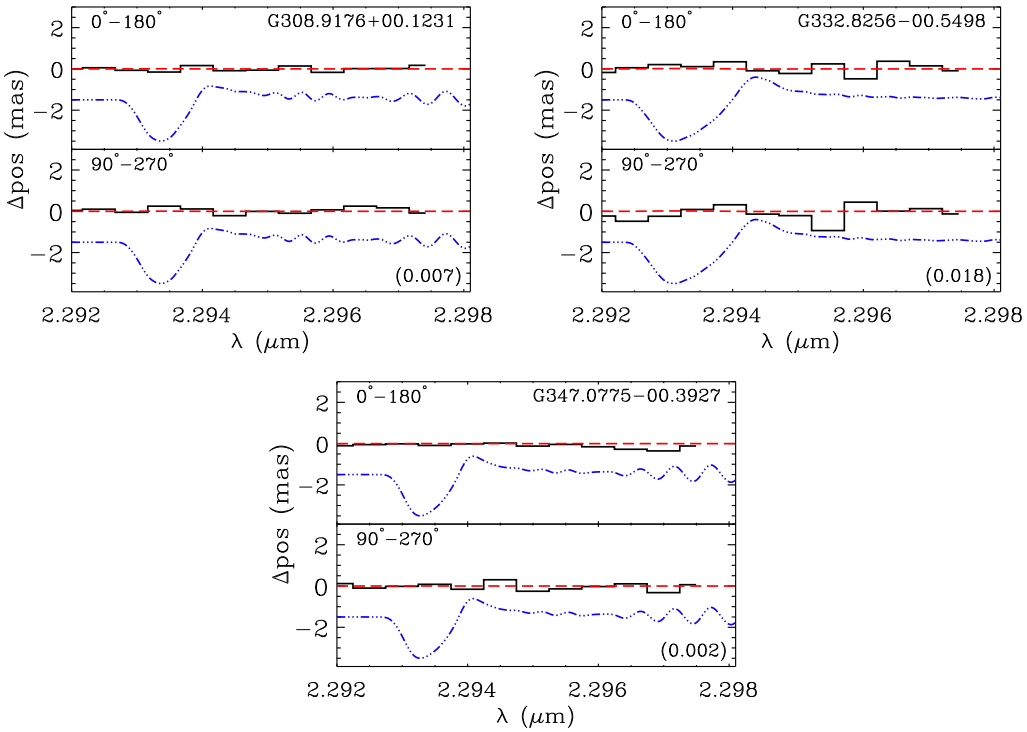

Figure 6.7 *continued.*

6.4.2 Model fits and results

Over the wavelength range available, few individual ro-vibrational lines are visible. The fitting process is therefore dominated by the shape of the CO bandhead peak and shoulder. The appearance of the shoulder is set by the rotational profile of the individual lines, and is thus dependent on the inclination and the inner and outer disc radii (as the stellar mass is not varied). However, the temperature of the disc is also a function of distance from the central star. In general few individual lines are evident, indicative of relatively high temperatures – and/or high rotational broadening. As a result, the inner disc radii are generally small, of the order 0.1 AU. Changing the outer radii has little effect on the quality of the fit as the surface number density, and thus flux, falls off steeply. As a consequence, it is the inclination that dominates the fit to the bandhead profile. The object with the most prominent blue shoulder is fit with the largest inclination (G332.8256−00.5498: $\sim 42°$), while the objects with the steepest slopes from the blue continuum to the bandhead peak (IRAS 08576−4334 and M8E) are fit with the lowest inclinations ($\sim 18°$ & $16°$).

The best fit parameters are presented in Table 6.3, and the resultant bandhead profiles are plotted with the data in Fig. 6.6. As can be seen from the reduced χ^2 values (the mean is 1.68) the model of CO emission originating from a circumstellar disc generally provides a good fit to the data. The sole exception to this is G287.3716+00.6444, which is discussed in more detail in Section 6.5.3.

The predicted bandhead fluxes are compared to the un-reddened observed fluxes as a consistency check. As mentioned in Section 6.3.3, these un-reddened fluxes are inevitably subject to considerable uncertainties, yet still serve as an important validity test. Both the model and source fluxes are presented in Table 6.2. These are similar to within a factor of 2–3, and generally consistent within the uncertainty from the extinction estimate (neglecting the additional error due to uncertainties in the kinematic distances). Therefore, the observed and model fluxes are essentially consistent. This provides a further confirmation that disc models provide a good fit to the data.

6.4.3 Spectroastrometric signatures

The spectroastrometric signatures associated with the spectra presented in Fig. 6.6 are displayed in Fig. 6.7. The spectroastrometric data have been re-binned by a factor of $\sim$11 times the resolution element. This rebinning factor was chosen as it was the maximum bin size that could still resolve the expected spectroastrometric signatures across the bandhead. The resulting average positional precision is approximately 0.4 mas. In principle, this means the data probe AU size scales at the kpc distances of the sample. Here, we compare the spectroastrometric data to the best-fitting models to determine whether these data can be used to further probe the circumstellar environments of the sample.

The spectroastrometric signatures associated with the best-fitting models are also presented in Fig. 6.7. The predicted signatures are generally small, and to illustrate their appearance, an enhanced spectrum is shown offset in each panel. The largest excursion occurs on the blue side of the bandhead, which is due to the asymmetry of the bandhead profile. Over the blue shoulder of the bandhead all the emission is blue-shifted. Therefore, at these wavelengths the side of the disc coming towards the observer

Table 6.3: *The parameters of the best-fitting models. The mass is determined from the luminosity presented in Table 6.1. The uncertainties in i, $NCO_{\rm in}$ and Δv are determined by holding all other parameters constant and determining the change required to increase the reduced χ^2 by 1.0.*

Name	Mass ($M_\odot$)	Inclination (°)	$R_{\rm in}^{\ddagger}$ (AU)	$R_{\rm out}^{*}$ (AU)	$NCO_{\rm in}$ ($\rm cm^{-2}$)	Δv ($\rm km\,s^{-1}$)	χ^2
IRAS 08576−4334	6.1	$17.8^{+0.8}_{-0.4}$	0.09	0.78	$7.9^{+1.3}_{-1.7}\times10^{21}$	$20.0^{+3.1}_{-3.1}$	2.18
G287.3716+00.6444	See §6.5.3						
M8 E	13.5	$15.8^{+2.0}_{-2.8}$	0.31	2.61	$1.1^{+7.9}_{-1.1}\times10^{23}$	$7.6^{+2.0}_{-2.8}$	1.38
G033.3891+00.1989	11.8	$18.0^{+2.8}_{-3.7}$	0.24	2.05	$9.4^{+7.6}_{-6.6}\times10^{21}$	$19.9^{+36.4}_{-16.1}$	1.95
G308.9176+00.1231	42.6	$29.0^{+5.4}_{-3.9}$	0.94	8.00	$4.9^{+12.9}_{-3.3}\times10^{22}$	$13.6^{+15.0}_{-8.6}$	1.14
G332.8256−00.5498	24.5	$42.3^{+4.4}_{-11.7}$	0.59	5.08	$2.2^{+5.7}_{-\dagger}\times10^{21}$	$18.6^{+35.4}_{-17.6}$	2.79
G347.0775−00.3927	17.7	$30.6^{+15.0}_{-14.3}$	0.45	3.81	$1.7^{+7.4}_{-\dagger}\times10^{22}$	$19.9^{+86.2}_{-18.9}$	0.62

‡: No uncertainties are presented as these inner radii are the inner radii of the region where CO emission is possible, i.e. $T<5000$K. Therefore, decreasing the inner radii did not affect the quality of the fits.
∗: No uncertainties are presented as these outer radii are the outer radii of the region where CO emission is possible, i.e. $T>1000$K. Therefore, increasing the outer radii did not affect the quality of the fits.
†: χ^2 flat down to $10^{18}\rm cm^{-2}$, the minimum surface number density considered. Therefore, no error is presented here.

is significantly brighter than the other side, which results in the prominent spectroastrometric signature at these wavelengths. Conversely, red-wards of the bandhead peak the receding side of the disc is brightest, resulting in a positional excursion in the opposite direction. However, at these wavelengths red-shifted emission from the peak of the bandhead is mixed with blue-shifted emission of ro-vibration lines at longer wavelengths. As a consequence, the spectroastrometric signature is smaller to the red of the bandhead peak than on the blue side. Over individual, resolved ro-vibrational lines, the two sides of the disc are almost equally bright, and thus the excursions at positive and negative velocities are nearly symmetrical, resulting in the classic 'S' shaped signature of a disc (Pontoppidan et al. 2008; van der Plas et al. 2009, Chapter 5). As the individual ro-vibrational lines are located close together, the adjacent positional signatures result in an oscillating signature.

The largest predicted excursions are of the order 0.01 mas, which is much smaller than the precision of the spectroastrometric data. The small-scale of the spectroastrometric signatures is largely due to the large distances to the objects, coupled with relatively weak CO emission, which is typically 10 per cent of the continuum flux. The largest predicted signatures are those of IRAS 08576−4334 and M8E (both 0.017 mas), due to their proximity. Even with a positional precision of 0.15 mas, the best in the sample, such excursions would not be detected.

While the spectroastrometric data do not provide constraints to the model fitting process per se, they are entirely consistent with the best-fitting models of emission originating in circumstellar discs. Moreover, the data do provide additional constraints on the source of the emission. It is noted that the spectroastrometric signature of IRAS 08576−4334 exhibits no detectable excursion with a precision of approximately 0.7 mas. This is contrary to the finding of Grave & Kumar (2007), who report an excursion of approximately 18 mas, corresponding to a minimum size of 40 AU at 2.17 kpc, and likely several times this. Here, it is suggested that the feature in their data is an instrumental artefact, which is not present in the data as our practice of subtracting anti-parallel position spectra eliminates artefacts (the data of Grave & Kumar (2007) were obtained using a single PA.)

6.5 Discussion

6.5.1 A discussion on the best-fitting parameters

The best-fitting inner disc radii are typically of the order 0.1 AU, and the best-fitting outer disc radii are generally 1–5 AU. These values are consistent with those of Bik & Thi (2004), and indicate that the CO emission arises from small-scale circumstellar discs. At such small distances from the central star, CO molecules should be disassociated by ultraviolet photons. However, the best-fitting number surface densities are sufficient for the CO molecules to self-shield, as found by Bik & Thi (2004). It is noted that the simplistic treatment of the temperature gradient within the disc allows CO to be excited within 1 AU of the central star. However, a full treatment of viscous heating in such a disc keeps the mid-plane temperature above ∼5000 K out to approximately 1 AU (Vaidya

et al. 2009). This would have the effect of moving the inner radius of the CO emitting region further from the central star. The difference between the best-fitting inner radii and the radius at which the mid-plane temperature of a massive accretion disc drops below 5000K is of the order a few, and thus is unlikely to significantly affect the best-fitting properties. In addition, the viscous heating is dependent upon the accretion rate, which is uncertain and thus incorporating viscous heating in the model would introduce an additional unknown. Therefore, the simplistic temperature gradient is deemed to be sufficient for the purposes of this chapter.

In the model, the excitation temperature in the disc varies as a function of radius. If the disc is sufficiently large, the outer temperature falls below 1000 K and the outer cells contribute no flux to the total spectrum. In this situation, increasing the outer radius will not affect the resultant χ^2, as the output spectrum will not be changed. However, the physical disc may well be much larger than the CO emitting region, which constitutes the warmer and denser part of the disc. In this respect the outer regions of the CO emitting region are consistent with the models of Vaidya et al. (2009), who show that accretion discs around massive protostars may well be stable out to approximately 80 AU. The dust sublimation radii associated with MYSOs are typically greater than 10 AU (de Wit et al. 2007; Vaidya et al. 2009). Therefore, the CO emission of the best-fitting models originates from within the dust sublimation radius, and thus offers a unique tracer of gas prior to its accretion onto the central star.

The inner radii set the initial excitation temperature, which is a function of the distance from the central star. As a result, changing the inner radius affects both the temperature in the disc and the rotational broadening of the bandhead. To consistently determine the temperature structure of the disc, and thus more stringent constraints, a detailed radiative transfer model of the disc is required. However, even if the gas disc were modelled in detail, the properties of the central star are essentially unknown. For example the star may swell to several times its main sequence size as a consequence of high accretion rates (Hosokawa & Omukai 2009), which will reduce its effective temperature. Therefore, even a sophisticated disc model wold be subject to several unknowns.

The best-fitting line-widths are generally greater than the value of $\sim 4\,\mathrm{km\,s^{-1}}$ deter-

mined by Berthoud et al. (2007), who fit the CO 1st overtone emission of the Be star 51 Oph with a circumstellar disc model. The line widths are also approximately ten times the thermal broadening due to motion of the CO molecules. Therefore, the dominant contribution must be due to turbulence. However, shear broadening is not considered in the model. If this were taken into account, the turbulent velocity may well be less than the best-fitting values presented in Table 6.3. The properties of accretion discs around MYSOs has only recently begun to be examined in detail (Vaidya et al. 2009), and incorporating vertical disc structure to the disc model (which is required to assess shear broadening Horne & Marsh 1986; Hummel & Vrancken 2000) is beyond the scope of this chapter. Therefore, shear velocity is neglected. However, it is important to note that neglecting vertical structure may artificially limit the extent of the CO emitting region. In a disc with a vertical extent, the upper regions of the disc may be hot enough to excite CO emission at radii where the mid-plane temperature has dropped below the required ~ 2000 K. Therefore, incorporating vertical structure in the model may allow CO emission from a wider range of radii than the thin disc model. This would have the affect of increasing the resulting spectroastrometric signatures, and thus the predictions presented here may be lower limits.

6.5.2 Comparisons with previous work

Little is known about the circumstellar environments of the RMS objects. In particular, there are no previous high resolution studies with which to compare the best-fitting model parameters. However, the two non-RMS objects in the sample, M8 E and IRAS 08576−4334 have been both been studied previously. Here, the best-fitting models for these objects are compared with other observations.

Bik & Thi (2004) determine the inclination of IRAS 08576−4334 to be $27^{\circ}{}^{+2}_{-14}$ based on fitting the CO 1st overtone bandhead. The best-fitting value of $\sim 18^{\circ}$ determined here is thus consistent with the previous value. This might be expected as the same methodology is used, nonetheless, this provides an important check that the method and results are consistent with previous work. Turning to M8E, Simon et al. (1985) postulate that this object possesses an edge on disc; contrary to the best-fitting inclination of $\sim 16^{\circ}$. However, Linz et al. (2009) find an inclination $< 30^{\circ}$ is required to fit the SED

of M8E. These authors suggest that the interpretation of the lunar occultation data of Simon et al. (1985) is complicated by the presence of scattered light and outflow cavities. Given that the conclusion of Linz et al. (2009) is based on the SED of M8 E from the visible to mid infrared, in addition to the grid of models of Robitaille et al. (2007), it is suggested the inclination determined by Linz et al. (2009) is currently the best estimate, which is in agreement with the best-fitting value. Therefore, the best-fitting models are consistent with results in the literature, although only a few are available, indicating that the best-fitting model parameters are representative of the circumstellar environments of the sample.

6.5.3 G287.3716+00.6444

In all but one case, the disc model not only provided a good fit to the data (as measured with χ^2), but was also consistent with the observed flux densities, and where they existed, previous observations. Therefore, it would appear that small-scale discs are present around the majority of the sample. However, it was not possible to fit the CO 1$^{\rm st}$ overtone bandhead of G287.3716+00.6444 with the circumstellar disc model used to fit the other profiles. As shown in Fig. 6.6, the disc model could not fit the observed the bandhead shoulder, nor the slope red-wards of the peak. Furthermore, the bandhead could not be fit with emission from an isothermal, non-rotating body of CO. Therefore, alternative scenarios may be required to explain the emission and its profile.

Besides hot, dense discs there are other viable sources of CO 1$^{\rm st}$ overtone bandhead emission. One such scenario is a dense, neutral wind. Chandler et al. (1995) were able to fit the CO 1$^{\rm st}$ overtone bandheads of several YSOs with models of neutral winds, but note that the mass loss rates required were relatively high, up to $10^{-6}\,{\rm M}_{\odot}{\rm yr}^{-1}$. Chandler et al. (1995) consider it unlikely CO 1$^{\rm st}$ overtone emission originates in a wind as such mass loss rates are much higher than observed for solar mass YSOs. However, the winds of MYSOs may well lead to mass loss rates of $10^{-6}\,{\rm M}_{\odot}{\rm yr}^{-1}$ (Drew et al. 1993). Consequently, CO 1$^{\rm st}$ overtone emission from a dense wind should perhaps be re-considered in this case. Alternatively, Scoville et al. (1983) propose that the CO 1$^{\rm st}$ overtone bandhead emission of the Becklin-Neugebauer object is created in shocks (as the observed velocity dispersion and estimated emitting area are both small).

It is noted that Blum et al. (2004) also report that the CO 1st overtone bandhead of one of their sample (of four YSOs) was difficult to fit with a model of CO emission from a circumstellar disc. Following the example of Kraus et al. (2000), they suggest that this may be due to the circumstellar disc exhibiting an outer bulge, which shields the inner regions of the disc. The effect of this would be to limit the visible CO emitting region to low velocity regions, resulting in a narrow profile. In this case, however, it is not the width of the profile that cannot be fit, but rather the slope of the profile red-wards of the bandhead peak. Most formation scenarios, such as winds and discs, result in excess blue-shifted emission, therefore this bandhead profile is difficult to explain.

It is conceivable that the emission from several, discrete regions in a shock, will have different excitation temperatures, and when superimposed, will result in a different slope to the bandhead than the disc model. If such shocks exist, the shocked region must be located close to the central star, within a few AU, as no positional excursion are observed in the spectroastrometric data. However, it is difficult to envisage a scenario in which the shock emission is predominately red-shifted. As an alternative, it may be that the emission does originate in a disc, but the receding part of the disc is significantly brighter than the approaching side, similar to the V/R variations exhibited by Be stars (e.g. Hanuschik et al. 1995). Regardless, it is apparent that while the majority of MYSO CO bandheads are well fit by models of circumstellar discs, the circumstellar environments of MYSOs are not yet completely understood.

6.6 Conclusions

This chapter presents high resolution near infrared spectroastrometry around 2.3μm of a sample of young stellar objects, most of which are drawn from the RMS survey. The RMS constitutes the largest catalogue of massive young stellar objects to date, and thus provides a unique sample to study massive star formation. The CO 1st overtone bandhead emission detected is compared to a simple model of a circumstellar disc in Keplerian rotation. In addition, the sub milli-arcsecond precision spectroastrometric data are compared to the spatial signatures of the best-fitting models.

The observed bandhead profiles are, on the whole, well fit by models of the emis-

sion originating in circumstellar discs. This concurs with the generally accepted view that this emission arises in small-scale accretion discs. The observed bandhead of one object cannot be fit with a circumstellar disc model. This could be due to the emission emanating from an asymmetric disc or shock. This highlights that the circumstellar environments of massive young stellar objects are still not completely understood.

No spatial signatures of discs are revealed in the spectroastrometric data, which have a precision of approximately 0.4 mas. This is entirely consistent with the sizes of the best-fitting models. Due to the small sizes of the discs, the large distances to them and the decrease in brightness with radius the predicted signatures are of the order of 0.01 mas. This is well below the current detection limit. However, the predicted signatures could, in principle, be revealed by differential phase observations with spectro-interferometers instruments such as the VLTI with AMBER and the Keck Interferometer.

To summarise, in general the model of emission from a circumstellar disc provides a good fit to the observed bandheads, and is consistent with the observed flux densities. This indicates that the majority of MYSOs with CO 1^{st} overtone emission possess small-scale, circumstellar discs. In turn, this provides further evidence that massive stars form via disc accretion, as suggested by the simulations of Krumholz et al. (2009).

Chapter 7

Conclusions

This thesis presents a study of young stellar objects of intermediate, $2 - 10\mathrm{M}_{\odot}$, and high mass, $\mathrm{M}_{\star} > 10\mathrm{M}_{\odot}$, on small angular scales. The goal is to determine how such objects form and to elucidate the differences and similarities between intermediate and high mass star formation. Spectroastrometry is used over optical and near infrared wavelengths to probe the circumstellar environments of intermediate mass, pre-main-sequence, stars; main sequence stars with circumstellar disks and massive young stellar objects on milli-arcsecond scales. In addition, other techniques, such as linear spectropolarimetry and near infrared integral field unit spectroscopy, are used to probe the source of the characteristic emission lines in the spectra of Herbig Ae/Be stars. The results are used to constrain how intermediate and massive stars form, and thus to infer how the star formation mechanism depends on mass. Finally, the results provide an important insight into how the enigmatic Be stars lose mass to form equatorial disks.

This chapter presents an overview of the main findings of the previous chapters and reviews possible future studies.

7.1 An overview of this thesis

The majority of HAe/Be stars reside in binary systems (Baines et al. 2006). Given that HAe/Be stars have yet to reach the main sequence, the properties of these systems are likely to retain an imprint of their formation mechanism. In Chapter 2, spectroastrometric observations of Herbig Ae/Be stars in the $B-$ and $R-$ band are used to detect otherwise unresolved binary systems. A dedicated spectroastrometric routine is used to separate the composite binary spectra into their constituent spectra, doing so for the

first time for a sample of young stars. The individual component spectra are then used to determine the spectral types of the binary components, and hence the mass ratio of the binary systems. The distribution of mass ratios is strongly biased towards high values. This mass ratio distribution, in addition to the separation distribution of the systems detected, is broadly consistent with binary formation via disk fragmentation. Therefore, alternative scenarios invoked to explain the formation of binary systems, such as stellar capture (Moeckel & Bally 2007), can most likely be discarded. Furthermore, given that the sample of HAe/Be stars encompasses several massive objects, the evidence of binary formation via disk fragmentation indirectly confirms the latest simulations of massive star formation, which also feature binary formation through disk fragmentation (Krumholz et al. 2009). Therefore, the results of Chapter 2 suggest that intermediate and massive stars form in the same fashion – in contradiction to previous models such as competitive accretion (see e.g. Bonnell et al. 2004). This is substantiated by recent detections of dusty disks surrounding both intermediate and massive young stellar objects (Okamoto et al. 2009; Kraus et al. 2010).

A key prediction of binary formation via rotationally dominated fragmentation is that the binary orbit and circumstellar disks will be co-planar. This has been investigated in the case of the lower mass T Tauri stars (with mixed results, see e.g. Wolf et al. 2001; Jensen et al. 2004; Monin et al. 2006). Little is known about the relative orientations of HAe/Be binary systems. Based on a variety of indirect constraints, Maheswar et al. (2002) argue that it is likely the orbital planes and circumstellar disks of HAe/Be binary systems are coplanar. However, these authors only consider binary position angles, which do not trace the orbital plane, unless the system is seen edge on. In a similar fashion, Baines et al. (2006) used binary position angles and circumstellar disk position angles, determined from spectropolarimetry, in an attempt to exclude random orientation, but only do so at a 2σ level. Therefore, it has yet to be shown that the orbits and circumstellar disks of HAe/Be binaries are co-planar or otherwise. In Chapter 3, the orientation of HAe/Be binary systems is compared to the orientation of circumstellar disks in the system (determined via linear spectropolarimetry). A simple model is used to predict the difference between binary and disk position angle expected

if the orbit and circumstellar disks are co-planar. This study highlights the fact that previous conclusions were based on small samples, and that a conclusive test requires a large sample of ∼50, which is larger than that currently available. Nonetheless, it is shown that the scenario in which HAe/Be binary orbital planes and circumstellar disks are co-planar is consistent with the available data. In turn, this is consistent with the findings of the previous chapter and puts the scenario of disk fragmentation on a firmer footing.

Chapter 4 presents a study of the emission lines in the spectra of Herbig Ae/Be stars in order to investigate the transition from magnetospheric accretion to direct disk accretion thought to occur over the HAe/Be mass range. This chapter describes the search for collimated outflows emanating from Herbig Be stars and probing the origin of HI emission lines via near infrared integral field unit spectroscopic observations. No collimated optical outflows are observed. However, no wide angle outflows are observed either, and therefore the data cannot be used to constrain the proposed transition from collimated to uncollimated outflows, which has been suggested to occur over the Herbig Be mass range.

Spectroastrometry was used to probe the origin of the HI emission of the sample with an angular precision of 0.5 mas, which corresponds to approximately 0.25 AU at the typical distance of the sample. The presence of artifacts in the data is assessed and it is found under-sampling of the seeing may well result in artificial signatures. One object, PDS 37, is found to exhibit a spectroastrometric signature that is not directly attributable to a binary system or this problem associated with under-sampling. The spectroastrometric signature is approximately 1 mas in amplitude and suggests that the HI line emission originates in a bipolar outflow. Further observations with higher spectral resolution are required to confirm this. If the presence of an outflow is confirmed, the sample of Herbig Be stars with bipolar outflows will be significantly enlarged.

Chapter 5 presents high spectral resolution, spectroastrometric observations of a sample of classical Be stars over the Hα line. The observations demonstrate this technique can achieve a precision of ∼0.1 mas. As a result, it is shown that spectroastrometry can detect circumstellar disks only several mas in size. This demonstrates that it is a

viable technique to search for AU sized accretion disks around massive young stellar objects. Furthermore, it is shown that the combination of high spectral resolution and angular precision allows the kinematics of the disks around Be stars to be constrained. By comparing the spectroastrometric signatures observed to models of circumstellar disks, it is shown for the first time that the majority, if not all, of the disks around Be stars rotate in a Keplerian fashion. This constrains the formation mechanism of Be star disks in that scenarios which do not result in Keplerian rotation (such as magnetically confined winds with no viscous effects) can be discarded.

Finally, Chapter 6 presents a search for AU sized, accretion disks around MYSOs. This search is conducted with sub-mas precision spectroastrometry over the CO first overtone bandhead emission of such objects. This emission is thought to trace hot, dense gas in the inner few AU of circumstellar disks (see e.g. Bik & Thi 2004). Therefore, spectroastrometry over this emission offers the potential to unambiguously detect a gaseous accretion disk around a massive young stellar object for the first time. A sample of massive young stellar objects are observed with a typical angular precision <0.5 mas. No spatial signatures of disks are detected. The observed profiles of the CO 1^{st} overtone bandhead emission are modelled using a simple model of a geometrically thin disk. In general, the observed bandheads are well fitted with the disk model, which is consistent with the belief that this emission originates in circumstellar disks. Incorporating a temperature gradient within the disk demonstrates that the emission originates in the hottest, inner regions of the disks, which are generally less than an AU in size. As a result, the predicted spectroastrometric signatures of the models could not be detected with the current precision.

7.2 Discussion and future work

Chapter 3 investigated the relative orientation of HAe/Be circumstellar disks and binary orbital planes. In this chapter it is demonstrated that, although a firm conclusion could not be reached due to the small sample, the observations are consistent with the scenario of co-planar disks and binary orbits. In turn, this is consistent with binary formation via disk fragmentation, which is suggested by the results of Chapter 2.

Since the sample presented in Chapter 3 was not sufficiently large to allow an unambiguous conclusion to be drawn, future work will focus on enlarging the sample of HAe/Be stars with constrained circumstellar geometry. Additional spectropolarimetric observations will be conducted. However, spectropolarimetry alone is unlikely to provide the numbers required since it requires very high signal-to-noise data, and is therefore most applicable to the brightest objects (most of which have already been observed). Conversely, near infrared spectro-interferometry is severely under exploited in determining the geometry of circumstellar disks around HAe/Be stars. Recent studies of HAe/Be disks with the VLTI have focused on constraining the physical properties of individual disks via multi-wavelength, multi-baseline observations. A mini-survey of a sample of HAe/Be stars over the Brγ line using a few well-selected baselines has the potential to deliver the basic geometry of a sample of disks. Combined spectro-interferometric and spectropolarimetric observations should allow the alignment of HAe/Be binary orbits and circumstellar disks to be conclusively tested.

Spectropolarimetry has been used in a similar fashion to observe T Tauri stars and probe the relative orientations of disks and binary systems. In particular, Jensen et al. (2004) report that the circumstellar disks of the 14 T Tauri binary systems they observed are definitely not coplanar. In addition, high resolution studies of low mass, proto-stellar binary systems have uncovered further evidence of mis-aligned systems (Scholz et al. 2010; Kang et al. 2008). Consequently, it would seem there may be a dichotomy in binary properties between young low and high mass stars. It is postulated that this is due to the differing importance of turbulence and radiative heating across the stellar mass spectrum. In the high mass regime, radiation feedback effectively prevents fragmentation (Krumholz 2006; Krumholz et al. 2007). Consequently, binary formation, a crucial way to remove excess angular momentum from an accreting protostar (Larson 2003), has to occur via disk fragmentation. Conversely, at low masses, the radiative feedback is not sufficient to prevent the fragmentation of a collapsing core, and thus fragmentation is initiated by turbulence causing regions of enhanced density which collapse independently, resulting in mis-aligned binary systems. Therefore, the work presented in this thesis may provide a tentative confirmation of the importance of

radiative feedback in massive star formation.

However, mis-aligned binary orbital planes and circumstellar disk could also be the result of dynamical interactions that occur during the early evolution of a young binary system. Most of the current population of HAe/Be stars are located in nearby, relatively low density regions of star formation (e.g. Orion and Auriga), where interactions are unlikely. Nonetheless, to confirm the above trend of binary properties with mass, the importance of dynamical interactions in the evolution of young binary systems must be assessed. Therefore, a logical extension of the work presented in Chapter 2 would be to investigate the dependence of the HAe/Be binary fraction and binary properties on environment. Determining whether the binary properties of this class of objects is different in regions of higher stellar density would establish important constraints on the effect of dynamical interactions on the properties of young binary systems. To achieve this, the sample of HAe/Be stars would have to be expanded substantially. This could be achieved by utilising *IPHAS* (the INT Photometric Hα Survey of the Northern Galactic Plane), which may allows the identification of a unique sample of young emission line objects in a range of environments (see e.g. Vink et al. 2008).

If intermediate and massive stars form in a similar fashion, the high binary fraction of Herbig Ae/Be stars ($\gtrsim$ 70 per cent) indicates that the majority of massive young stellar objects also reside in binary systems. Observations of massive young stellar objects have yet to reveal evidence of a high binary fraction. Indeed, even the diffraction limited imaging of de Wit et al. (2009) lacked the resolution to resolve the characteristic fragmentation radius of accretion disks around massive young stellar objects ($\sim$1000 AU, see Chapter 2). Therefore, the binary fraction of massive young stellar objects is relatively unconstrained by observations.

By way of contrast, the binary properties of the resultant main sequence OB stars are well studied. Many main sequence O type stars (40–70 per cent) reside in spectroscopic binary systems, and these systems exhibit a preponderance of high mass ratios (e.g. Sana et al. 2009, 2008). This high binary fraction is in accordance with the prediction made by extrapolating the binary fraction of intermediate mass stars to higher masses. However, the short periods of the O + OB binaries correspond to separations significantly smaller

than predicted by the scenario of disk fragmentation. Krumholz & Thompson (2007) note that the high mass ratios of massive binary systems may be due to mass transfer between the components during their formation. Rapidly accreting protostars may swell to many times their main sequence size (see Hosokawa & Omukai 2009) and thus overflow their Roche lobe, resulting in mass transfer. While this scenario explains the high mass ratios of massive binary systems, it requires a small binary separation (<1 AU). In turn, this requires that the secondary component forms in a circumstellar disk and migrates inward (Krumholz & Thompson 2007), i.e. it is not captured (as proposed by Bonnell & Bate 2005). Therefore, the binary properties of massive stars are essentially consistent with the scenario above in which massive stars form via disk accretion. Intermediate mass stars are not known to exhibit an excess of spectroscopic binary systems with a high mass ratio (see e.g. Corporon & Lagrange 1999). This could indicate that the migration mechanism required to explain the small separations of O type binary systems is only active at high masses. Therefore, the migration mechanism may require the high accretion rates exhibited by the most massive young stellar objects. Alternatively, such migration may require hardening via dynamical interaction which only occurs in the dense clusters in which massive stars generally form.

Chapter 4 presents a search for optical outflows emanating from Herbig Be stars. No extended outflows traced in shocked emission were observed. The lack of outflows from Herbig Be stars initially suggests that the Herbig Be stars are generally seen at a later evolutionary stage than Herbig Ae and T Tauri objects, and as a result, accretion and outflow activity of Herbig Be objects has subsided. This calls into question the change in accretion mechanisms across the Herbig Ae/Be mass range proposed by Vink et al. (2002, 2005a), as the change in spectropolarimetric signatures could, in principle, be explained by an evolutionary effect. However, Herbig Be stars do exhibit spectroscopic signs of ongoing accretion, and indeed have a higher occurrence of CO bandhead emission (thought to be a tracer of accretion disks) than Herbig Ae stars (Oudmaijer, 2010, priv. comm.). This is consistent with interferometric observations of HAe/Be stars in the $K-$band which have revealed that while the observations of most HAe/Be disks are well fit by a disk model with an optically thin dust free central region, the disks around

luminous Herbig Be stars are smaller than expected (Monnier 2005). These authors suggest that this signifies luminous Be stars possess optically thick, inner gaseous disks (i.e. an accretion disks).

Since Herbig Be stars exhibit signs of accretion it might be expected that they drive outflows. Since no outflows are observed, the outflows that are thought to be driven by young early type objects (see the evolutionary scenario proposed by Beuther & Shepherd 2005) must be disrupted somehow, perhaps by the dissipation of the outer disks due to the UV radiation of early type HBe stars (see Alonso-Albi et al. 2009, and references therein). Alternatively, outflows from high mass sources may be less efficient than those associated with lower mass objects and require a higher accretion rate than is expected based on an extrapolation of the accretion rate of low mass outflow sources. This may provide constraints on the driving engine of the mechanism of such outflows. However, observations of a sample of 'proto' Herbig Be stars are still required to disentangle intrinsic differences between Herbig Ae and Be stars and differences due to varying evolutionary states. The RMS survey could be used to create a sample of such objects by selecting objects with infrared colours similar to massive young stellar objects and luminosities of approximately 1000 $L_{\odot}$.

If the scenario of Vink et al. (2002) is correct and the HI line emission of the majority of Herbig Be objects originates in circumstellar disks several AU in size, this emission will offer a unique probe of the accretion geometry of intermediate mass stars. Furthermore, since it appears that intermediate and massive stars form in the same fashion, the accretion geometry of Herbig Be stars may be extrapolated to high masses. Therefore, the line emission of Herbig Be stars may allow the process by which massive stars gain mass to be studied. However, only spectrally and spatially resolved observations of the emission lines can determine the properties of such disks. Since Chapter 4 demonstrates that spectroastrometric data which approaches the required precision is subject to systematic artifacts, spectro-interferometry may be the only way to study such disks.

Spectro-interferometry also provides an important extension of the work on Be star disks presented in Section 5. This thesis demonstrates that spectroastrometry can be used to differentiate between various rotation laws. However, its precision is limited to

0.1 mas, and thus the inner few stellar radii of Be star disks remain inaccessible. Differential phase observations with AMBER offer the potential to probe such disks with a precision of micro-arcseconds, allowing the inner regions to be studied. Several mechanisms have been proposed to create equatorial disks rotating in a Keplerian fashion (for example non-radial pulsations and magnetic torques). The only difference between the various scenarios is how material is injected into the equatorial plane, which presumably occurs within a few stellar radii of the central star. Therefore, spectro-interferometry may provide unique insights on the formation mechanism of Be star disks.

Modelling the CO emission of massive young stellar objects with emission from a disk with a radial temperature gradient has revealed that the size of the emitting region is very small, of the order of 1 AU. The predicted spectroastrometric signatures of the models demonstrate that these small sizes, in conjunction with the typically large distances to MYSOs, make detecting such disks using spectroastrometry unlikely. Even in good seeing conditions and with perfect instruments, spectroastrometric data would require a SNR of > 6000 to achieve the precision necessary to detect the largest positional signature. Such high quality data are unrealistic – and it is likely systematics would prevent the accuracy reaching the required μas precision. Therefore, while spectroastrometry is able to probe disks located within ~ 100 pc which have an outer radii greater than 10 AU (as demonstrated in this thesis), it is unlikely to detect small disks around MYSOs. The only alternative to obtain the required simultaneous spatial and kinematic information is to use spectro-interferometry. The only instrument that offers the spectral resolution required to study the CO $1^{\rm st}$ overtone bandhead is the AMBER instrument at the VLTI.

Tatulli et al. (2008) demonstrate that AMBER can be used to probe the spatial structure of CO emission (in this case from a B[e] star) on sub-AU scales. However, the object in question is 130 pc away, as opposed to the typical MYSO distance of several kpc. The resolution of AMBER can be approximated by $1.22\lambda/\mathrm{B}$, which, for the maximum UT baseline, is approximately 3 mas at 2.3μm. This is approximately 15 AU at the typical MYSO distance of 5 kpc. Therefore, as this work indicates the CO emitting regions are typically less than a few AU in size, spectro-interferometry will

also struggle to detect disks around MYSOs

The disk model used in Chapter 6 neglected viscous heating and vertical structure. In a disc with a vertical extent the upper regions of the disc may be hot enough to excite CO emission at radii where the mid-plane temperature has dropped below the minimum required to excite such emission. Therefore, incorporating vertical structure in the model may result in CO emission from a wider range of radii than the thin disc model, which would increase the resulting spectroastrometric signatures. Furthermore, the temperature structure of the disk will be substantially changed by incorporating viscous heating into the disk model (i.e. by using an α disk model). This may allow CO emission at larger radii than in the simple model used, due to an increase in temperature due to the viscous heating. Consequently, disk models which incorporate viscous heating may well result in larger spectroastrometric signatures. As no signatures were detected in Chapter 6 neither model is preferred. However, if the source of the CO emission was resolved (which may be possible with AMBER observations of HAe/Be stars), the different models could be compared via simultaneous fits to the spectral and spatial data. This would enable a detailed study of the accretion geometry of the stars in question and would for the first time unambiguously prove (or refute) that such emission originates in circumstellar disks and provide a direct estimate of the accretion rate of luminous young stellar objects.

However, this will be challenging due to the predicted small sizes of the emitting area and the fact that such objects are typically dim in the near infrared. Therefore, attention will be focused on the disks around luminous Herbig Be stars, which are thought to form in a similar fashion to massive stars. As mentioned previously, even interferometers like the VLTI will struggle to resolve the small CO emitting region of circumstellar disks.

Nonetheless, spectro-interferometry also allows the spatial distribution of unresolved emission to be probed on μas scales. By measuring variations in phase across spectrally dispersed data, AMBER can be used to search for changes in position of the incoming radiation as a function of wavelength. This differential phase information can be used to probe the difference between the spatial distribution of an emission line and the adjacent continuum on very small angular scales (in a manner directly analogous to

spectroastrometry). Currently, AMBER offers a differential phase precision of 1°, which translates to an accuracy of 8 μas (although an even higher accuracy is possible, see e.g. Le Bouquin et al. 2009), which is almost sufficient to detect the disk corresponding to the largest predicted spectroastrometric signature. However, MYSOs are generally too faint to obtain fringes with AMBER. In the high resolution K band mode, AMBER requires a K band magnitude < 5 for accurate differential phase information. Given that the SED of MYSOs peaks at around 100μm, MYSOs are simply too faint to be observed with AMBER (e.g. K $\sim$10). Indeed, currently it is impossible to observe any RMS objects with the desired precision. Several Herbig Be stars exhibit CO 1st overtone bandhead emission and are sufficiently bright to be observed with AMBER. Such stars offer a valuable opportunity to study the morphology and kinematics of the CO emitting material with AMBER to gain unique insights into the inner gaseous disks of luminous young stellar objects. Given that it is now thought that intermediate and massive stars form in the same fashion, the results should be also applicable to massive young stellar objects with CO bandhead emission.

It was noted in Chapter 6 that the mass loss of massive young stellar objects via winds is relatively poorly constrained. This could be rectified by exploiting the unique sample of massive young stellar objects provided by the RMS and the extensive wavelength coverage of the XSHOOTER instrument on the VLT. In the near infrared XSHOOTER covers the wavelength range $1 - 2.5\,\mu$m with a spectral resolution of $\sim$30 km s^{-1}. Observations of a sizable sample would allow the mass loss characteristics of near infrared bright massive young stellar objects to be studied on an unprecedented scale (see e.g. Bunn et al. 1995).

7.2.1 Future facilities

The most immediate future facilities which will provide new insights into star formation at intermediate and high masses are new VLTI instruments.

Of these, the closest to being operational is PRIMA, which is currently in the verification stage. The goal of PRIMA is to conduct μas astrometry of stars in order to search for the astrometric signatures of planets. To achieve this, the system is designed to perform simultaneous interferometric observations of two objects. The brightest object is

used as a reference for stabilizing the fringes and for the correction of the atmospheric disturbances, which enables a longer integration for the fainter object. In turn, this results in an improved sensitivity, with the result that the limiting magnitude for the UTs in the $K-$ band is anticipated to change from 10 to 13 magnitudes. Therefore, PRIMA may allow MYSOs to be studied with spectro-interferometry in the near future, which in turn will offer the potential to study their circumstellar environments on the mas scale.

Several years in the future the second generation of VLTI instruments will come online. An example of which is MATISSE. This instrument is a near to mid infrared spectro-interferometer combining the beams of up to four of the VLTI telescopes. This will allow the instrument to measure closure phase relations and meet its primary aim of providing images in the $N-$, $L-$, $M-$, and $Q-$ bands. Furthermore, it is thought that MATISSE will also provide several spectroscopic modes with a range of spectral resolutions. In this regard, MATISSE is the successor of both MIDI and AMBER by providing imaging capabilities in the mid-infrared while observing in the NIR (2.7 μm) and providing a spectral resolution of up to 2000. MATISSE will provide key insights into the formation of massive stars as the instrument will enable high resolution images of circumstellar disks, which is currently challenging in the near infrared (see e.g. Renard et al. 2010) and impossible in the mid infrared. Such images will not suffer the ambiguities of current MIDI observations with only several baselines, and will thus allow a detailed study of the environments of massive young stars.

However, such instruments are not yet under construction and it will be several years before they see first light.

Other new facilities that are expected to provide significant advances in our understanding of intermediate and massive star formation are new interferometers such as the Atacama Large Millimeter Array (ALMA), e-MERLIN and the Square Kilometer Array (SKA).

ALMA is a millimeter interferometer currently under construction and is anticipated to be completed by 2013. The interferometer will be comprised of an array of at least 66 12 m antennas and will have baselines as large as 16 km. An additional, compact array

of 7 m and 12 m antennas will also be incorporated to enhance ALMA's ability to image extended sources. ALMA will operate in the millimeter regime between wavelengths of 0.3 to 3.6 millimeters. The array is expected to provide a resolution as high as 5 mas. This resolution will allow the kinematics, morphology and chemical evolution of circumstellar disks around massive young stellar objects to be determined, which will provide key constraints to models of massive star formation. The upgrade of the MERLIN radio interferometer to e-Merlin will provide an interferometer consisting of seven radio telescopes with a maximum baseline of 217km, resulting in a resolution of 10–150 mas. The instrument is currently being commissioned. The resolution of e-Merlin will enable outflows from young stars to be observed at higher resolution than before which will allow the dependence on the outflow properties on stellar mass and magnetic fields to be studied in more detail than is currently possible. Finally, the SKA is a planned radio interferometer that will have a collecting area of a square kilometer and will consequently be 50 times more sensitive than existing radio instruments. With baselines of up to 3000 km, the SKA will provide a resolution as high as 1 mas. This will allow thermal emission from dust in disks to be imaged with unprecedented detail and the high sensitivity will aid in detecting magnetic fields in jets (see e.g. Ray 2009). Therefore, the SKA promises many advances in our understanding of star formation as a whole. However, the SKA is not scheduled to be fully operational until 2022.

Finally, future telescopes such as the James Webb Space Telescope and the European-Extremely Large Telescope will provide a significant improvement in sensitivity over the current generation of telescopes.

The James Webb Space Telescope, which is currently scheduled to be launched in 2014, is a near to mid infrared telescope with a primary mirror 6.5 m in diameter. The telescope will enable studies of massive stellar objects at a much greater sensitivity than is currently available on the ground due to thermal emission from the atmosphere. Much further in the future, the E-ELT is envisaged as an optical and near infrared telescope with a diameter of 42 m. Due to its collecting area, the E-ELT will be able to gather approximately 15 times more light than the current generation of optical telescopes. The telescope is planned to have fully integrated adaptive optics enabling it to resolve

circumstellar disks in the infra red, allowing the processes by which stars form and gain mass to be studied in unprecedented detail. However, building is not expected to start until 2018.

To summarise, there are several facilities either being constructed or planned that will offer substantial improvements in spatial resolution and sensitivity. The increased spatial resolution in particular will provide key insights into the process of forming stars, both at low and high masses.

7.3 Concluding remarks

This thesis has explored the potential of spectroastrometry to probe the environments of early type emission line stars on milli-arcsecond scales. In particular, the binary and disk properties of intermediate and massive young stellar objects are studied to constrain their formation mechanism. The results are consistent with the scenario of star formation via monolithic disk accretion at all masses. Therefore, the results suggest that alternative scenarios invoked to overcome perceived difficulties in forming massive stars in this manner are unnecessary.

While it is shown disks play an important role in massive star formation, exactly how the star formation changes with mass is still not fully understood. More specifically, how the accretion and ejection mechanisms change with mass is unknown. To make progress, the circumstellar environment of intermediate and massive young stellar objects must be probed on sub milli-arcsecond scales. The spectroastrometric work presented in this thesis represents the first step in achieving this. Furthermore, the work presented here establishes a foundation for future work with spectro-interferometry, which has the potential to address this remaining uncertainty regarding star formation at high masses.

Bibliography

Agra-Amboage, V., Dougados, C., Cabrit, S., Garcia, P. J. V., & Ferruit, P. 2009, A&A, 493, 1029

Alecian, E., Catala, C., Wade, G. A., et al. 2008, MNRAS, 385, 391

Alecian, E., Wade, G. A., Catala, C., et al. 2009, MNRAS, 400, 354

Alonso-Albi, T., Fuente, A., Bachiller, R., et al. 2009, A&A, 497, 117

Alvarez, M. A., Bromm, V., & Shapiro, P. R. 2006, ApJ, 639, 621

Alves, F. O., Franco, G. A. P., & Girart, J. M. 2008, A&A, 486, L13

Ascenso, J., Alves, J., Vicente, S., & Lago, M. T. V. T. 2007, A&A, 476, 199

Azevedo, R., Folha, D. F. M., Gameiro, J. F., & Calvet, N. 2007, ApJ, 670, 1234

Bacciotti, F., Ray, T. P., Mundt, R., Eislöffel, J., & Solf, J. 2002, ApJ, 576, 222

Bachiller, R. 1996, ARA&A, 34, 111

Bachiller, R. & Cernicharo, J. 1986, A&A, 166, 283

Bachiller, R., Guilloteau, S., Dutrey, A., Planesas, P., & Martin-Pintado, J. 1995, A&A, 299, 857

Bachiller, R., Martin-Pintado, J., & Planesas, P. 1991, A&A, 251, 639

Bachiller, R., Martin-Pintado, J., Tafalla, M., Cernicharo, J., & Lazareff, B. 1990, A&A, 231, 174

Bailey, J. 1998a, MNRAS, 301, 161

Bailey, J. A. 1998b, Proc. SPIE, 3555, 932

Baines, D. 2004, PhD thesis, University of Leeds UK

Baines, D., Oudmaijer, R. D., Porter, J. M., & Pozzo, M. 2006, MNRAS, 367, 737

Baker, J. G. & Menzel, D. H. 1938, ApJ, 88, 52

Balbus, S. A. & Hawley, J. F. 1991, ApJ, 376, 214

Ballesteros-Paredes, J., Hartmann, L., & Vázquez-Semadeni, E. 1999, ApJ, 527, 285

Bally, J. & Devine, D. 1994, ApJL, 428, L65

Bally, J. & Zinnecker, H. 2005, AJ, 129, 2281

Balog, Z., Muzerolle, J., Rieke, G. H., et al. 2007, ApJ, 660, 1532

Balona, L. A., Koen, C., & van Wyk, F. 2002, MNRAS, 333, 923

Banerjee, R. & Pudritz, R. E. 2007, ApJ, 660, 479

Barnes, P. J., Yonekura, Y., Ryder, S. D., et al. 2010, MNRAS, 402, 73

Bate, M. R. & Bonnell, I. A. 1997, MNRAS, 285, 33

Beichman, C. A., Myers, P. C., Emerson, J. P., et al. 1986, ApJ, 307, 337

Beichman, C. A., Neugebauer, G., Habing, H. J., Clegg, P. E., & Chester, T. J., eds. 1988, Infrared astronomical satellite (IRAS) catalogs and atlases. Volume 1: Explanatory supplement, Vol. 1

Beltrán, M. T., Cesaroni, R., Neri, R., et al. 2005, A&A, 435, 901

Bence, S. J., Richer, J. S., & Padman, R. 1996, MNRAS, 279, 866

Benedettini, M., Nisini, B., Giannini, T., et al. 1998, A&A, 339, 159

Benisty, M., Tatulli, E., Ménard, F., & Swain, M. R. 2010, A&A, 511, A75+

Benson, P. J. & Myers, P. C. 1989, ApJS, 71, 89

Bergin, E. A., Plume, R., Williams, J. P., & Myers, P. C. 1999, ApJ, 512, 724

Berio, P., Stee, P., Vakili, F., et al. 1999, A&A, 345, 203

Bernasconi, P. A. & Maeder, A. 1996, A&A, 307, 829

Berthoud, M. G. 2008, PhD thesis, Cornell University

Berthoud, M. G., Keller, L. D., Herter, T. L., Richter, M. J., & Whelan, D. G. 2007, ApJ, 660, 461

Bertout, C., Robichon, N., & Arenou, F. 1999, A&A, 352, 574

Beuther, H., Churchwell, E. B., McKee, C. F., & Tan, J. C. 2007, Protostars and Planets V, 165

Beuther, H. & Shepherd, D. 2005, in Cores to Clusters: Star Formation with Next

Generation Telescopes, ed. M. S. N. Kumar, M. Tafalla, & P. Caselli, 105–119

Bidelman, W. P. 1954, ApJS, 1, 175

Bik, A., Kaper, L., & Waters, L. B. F. M. 2006, A&A, 455, 561

Bik, A., Lenorzer, A., Thi, W. F., et al. 2008, in Astronomical Society of the Pacific Conference Series, Vol. 387, Massive Star Formation: Observations Confront Theory, ed. H. Beuther, H. Linz, & T. Henning, 78

Bik, A. & Thi, W. F. 2004, A&A, 427, L13

Bjerkeli, P., Liseau, R., Olberg, M., et al. 2009, A&A, 507, 1455

Bjorkman, J. E. & Cassinelli, J. P. 1993, ApJ, 409, 429

Bjorkman, K. S., Miroshnichenko, A. S., McDavid, D., & Pogrosheva, T. M. 2002, ApJ, 573, 812

Blitz, L. & Stark, A. A. 1986, ApJL, 300, L89

Blum, R. D., Barbosa, C. L., Damineli, A., Conti, P. S., & Ridgway, S. 2004, ApJ, 617, 1167

Boehm, T. & Catala, C. 1994, A&A, 290, 167

Bok, B. J. & Reilly, E. F. 1947, ApJ, 105, 255

Bondi, H. 1952, MNRAS, 112, 195

Bondi, H. & Hoyle, F. 1944, MNRAS, 104, 273

Bonnell, I. A. & Bate, M. R. 2002, MNRAS, 336, 659

Bonnell, I. A. & Bate, M. R. 2005, MNRAS, 362, 915

Bonnell, I. A. & Bate, M. R. 2006, MNRAS, 370, 488

Bonnell, I. A., Bate, M. R., Clarke, C. J., & Pringle, J. E. 1997, MNRAS, 285, 201

Bonnell, I. A., Bate, M. R., & Vine, S. G. 2003, MNRAS, 343, 413

Bonnell, I. A., Bate, M. R., & Zinnecker, H. 1998, MNRAS, 298, 93

Bonnell, I. A., Clarke, C. J., Bate, M. R., & Pringle, J. E. 2001, MNRAS, 324, 573

Bonnell, I. A., Vine, S. G., & Bate, M. R. 2004, MNRAS, 349, 735

Bonnet, H., Abuter, R., Baker, A., et al. 2004, The Messenger, 117, 17

Bontemps, S., Motte, F., Csengeri, T., & Schneider, N. 2010, A&A, 524, A18+

Bourke, T. L., Garay, G., Lehtinen, K. K., et al. 1997, ApJ, 476, 781

Bourke, T. L., Myers, P. C., Robinson, G., & Hyland, A. R. 2001, ApJ, 554, 916

Bouvier, J., Alencar, S. H. P., Harries, T. J., Johns-Krull, C. M., & Romanova, M. M. 2007, in Protostars and Planets V, ed. B. Reipurth, D. Jewitt, & K. Keil, 479–494

Bouvier, J. & Corporon, P. 2001, in IAU Symp., Vol. 200, The Formation of Binary Stars, ed. H. Zinnecker & R. Mathieu, 155–164

Brand, J. & Blitz, L. 1993, A&A, 275, 67

Brannigan, E., Takami, M., Chrysostomou, A., & Bailey, J. 2006, MNRAS, 367, 315

Bronfman, L., Nyman, L., & May, J. 1996, A&AS, 115, 81

Brown, J. C., Cassinelli, J. P., & Maheswaran, M. 2008, ApJ, 688, 1320

Brown, J. C., Telfer, D., Li, Q., et al. 2004, MNRAS, 352, 1061

Brunt, C. M. 2003, ApJ, 583, 280

Buehrke, T., Mundt, R., & Ray, T. P. 1988, A&A, 200, 99

Bunn, J. C., Hoare, M. G., & Drew, J. E. 1995, MNRAS, 272, 346

Burkert, A. & Hartmann, L. 2004, ApJ, 616, 288

Cameron, C., Saio, H., Kuschnig, R., et al. 2008, ApJ, 685, 489

Carciofi, A. C. & Bjorkman, J. E. 2006, ApJ, 639, 1081

Carciofi, A. C., Domiciano de Souza, A., Magalhães, A. M., Bjorkman, J. E., & Vakili, F. 2008, ApJL, 676, L41

Carciofi, A. C., Miroshnichenko, A. S., Kusakin, A. V., et al. 2006, ApJ, 652, 1617

Carciofi, A. C., Okazaki, A. T., Le Bouquin, J., et al. 2009, A&A, 504, 915

Cardelli, J. A., Clayton, G. C., & Mathis, J. S. 1989, ApJ, 345, 245

Carmona, A., van den Ancker, M. E., & Henning, T. 2007, A&A, 464, 687

Carr, J. S. 1989, ApJ, 345, 522

Caselli, P., Benson, P. J., Myers, P. C., & Tafalla, M. 2002a, ApJ, 572, 238

Caselli, P., Walmsley, C. M., Zucconi, A., et al. 2002b, ApJ, 565, 344

Cassen, P. & Moosman, A. 1981, Icarus, 48, 353

Cassinelli, J. P., Brown, J. C., Maheswaran, M., Miller, N. A., & Telfer, D. C. 2002, ApJ, 578, 951

Catala, C. & Kunasz, P. B. 1987, A&A, 174, 158

Cesaroni, R., Galli, D., Lodato, G., Walmsley, C. M., & Zhang, Q. 2007, in PPV, ed. B. Reipurth, D. Jewitt, & K. Keil, 197–212

Chan, S. J., Henning, T., & Schreyer, K. 1996, A&AS, 115, 285

Chandler, C. J., Carlstrom, J. E., & Scoville, N. Z. 1995, ApJ, 446, 793

Chandra, S., Maheshwari, V. U., & Sharma, A. K. 1996, A&AS, 117, 557

Chini, R., Hoffmeister, V., Kimeswenger, S., et al. 2004, Nat, 429, 155

Chini, R. & Neckel, T. 1981, A&A, 102, 171

Chrysostomou, A., Bacciotti, F., Nisini, B., et al. 2008, A&A, 482, 575

Cidale, L., Zorec, J., & Tringaniello, L. 2001, A&A, 368, 160

Clarke, A. J. 2008, PhD thesis, University of Leeds UK

Clarke, A. J., Lumsden, S. L., Oudmaijer, R. D., et al. 2006, A&A, 457, 183

Clarke, D. & McLean, I. S. 1974, MNRAS, 167, 27P

Coffey, D., Bacciotti, F., Ray, T. P., Eislöffel, J., & Woitas, J. 2007, ApJ, 663, 350

Coffey, D., Bacciotti, F., Woitas, J., Ray, T. P., & Eislöffel, J. 2004, ApJ, 604, 758

Collins, II, G. W. 1987, in IAU Colloq. 92: Physics of Be Stars, ed. A. Slettebak & T. P. Snow, 3–19

Corcoran, D. & Ray, T. P. 1995, A&A, 301, 729

Corcoran, M. & Ray, T. P. 1997, A&A, 321, 189

Corcoran, M. & Ray, T. P. 1998, A&A, 336, 535

Corporon, P. & Lagrange, A.-M. 1999, Astronomy and Astrophysics Supplement, 136, 429

Cote, J. & Waters, L. B. F. M. 1987, A&A, 176, 93

Coyne, G. V. & Kruszewski, A. 1969, AJ, 74, 528

Cranmer, S. R. 2005, ApJ, 634, 585

Cranmer, S. R. 2009, ArXiv e-prints

Crapsi, A., Caselli, P., Walmsley, M. C., & Tafalla, M. 2007, A&A, 470, 221

Crutcher, R. M. 1999, ApJ, 520, 706

Cutri, R. M., Skrutskie, M. F., van Dyk, S., et al. 2003, 2MASS All Sky Catalog of point sources.

Cvetković, Z. & Ninković, S. 2008, New Astronomy, 13, 587

Dachs, J., Hanuschik, R., Kaiser, D., & Rohe, D. 1986, A&A, 159, 276

Dame, T. M., Elmegreen, B. G., Cohen, R. S., & Thaddeus, P. 1986, ApJ, 305, 892

Davies, B., Lumsden, S. L., Hoare, M. G., Oudmaijer, R. D., & de Wit, W.-J. 2010, MNRAS, 402, 1504

Davies, M. B., Bate, M. R., Bonnell, I. A., Bailey, V. C., & Tout, C. A. 2006, MNRAS, 370, 2038

Davis, C. J., Varricatt, W. P., Todd, S. P., & Ramsay Howat, S. K. 2004, A&A, 425, 981

Davis, O., Clarke, C., & Freitag, M. 2010, ArXiv e-prints

de Wit, W. J., Hoare, M. G., Oudmaijer, R. D., & Lumsden, S. L. 2009, ArXiv e-prints

de Wit, W. J., Hoare, M. G., Oudmaijer, R. D., & Lumsden, S. L. 2010, A&A, 515, A45

de Wit, W. J., Hoare, M. G., Oudmaijer, R. D., & Mottram, J. C. 2007, ApJL, 671, L169

de Wit, W. J., Testi, L., Palla, F., & Zinnecker, H. 2005, A&A, 437, 247

Dekker, H., D'Odorico, S., Kaufer, A., Delabre, B., & Kotzlowski, H. 2000, in SPIE Conf. Ser., Vol. 4008, SPIE Conf. Ser., ed. M. Iye & A. F. Moorwood, 534–545

Deleuil, M., Bouret, J., Catala, C., et al. 2005, A&A, 429, 247

Devine, D., Grady, C. A., Kimble, R. A., et al. 2000, ApJL, 542, L115

di Francesco, J., Evans, II, N. J., Harvey, P. M., Mundy, L. G., & Butner, H. M. 1994, ApJ, 432, 710

Domiciano de Souza, A., Kervella, P., Jankov, S., et al. 2003, A&A, 407, L47

Donati, J., Babel, J., Harries, T. J., et al. 2002, MNRAS, 333, 55

Donati, J., Howarth, I. D., Bouret, J., et al. 2006a, MNRAS, 365, L6

Donati, J., Howarth, I. D., Jardine, M. M., et al. 2006b, MNRAS, 370, 629

Doucet, C., Pantin, E., Lagage, P. O., & Dullemond, C. P. 2006, A&A, 460, 117

Dougados, C., Cabrit, S., Lavalley, C., & Ménard, F. 2000, A&A, 357, L61

Dougherty, S. M. & Taylor, A. R. 1992, Nature, 359, 808

Dougherty, S. M., Waters, L. B. F. M., Burki, G., et al. 1994, A&A, 290, 609

Drew, J. E., Bunn, J. C., & Hoare, M. G. 1993, MNRAS, 265, 12

Drew, J. E., Proga, D., & Stone, J. M. 1998, MNRAS, 296, L6

Drissen, L., Moffat, A. F. J., Walborn, N. R., & Shara, M. M. 1995, AJ, 110, 2235

Ducati, J. R. 2002, VizieR Online Data Catalog, 2237, 0

Duchêne, G., Delgado-Donate, E., Haisch, Jr., K. E., Loinard, L., & Rodríguez, L. F. 2007, in Protostars and Planets V, ed. B. Reipurth, D. Jewitt, & K. Keil, 379–394

Dunham, J. L. 1932, Phys. Rev., 41, 721

Duquennoy, A. & Mayor, M. 1991, A&A, 248, 485

Edgar, R. & Clarke, C. 2004, MNRAS, 349, 678

Edwards, S., Fischer, W., Hillenbrand, L., & Kwan, J. 2006, ApJ, 646, 319

Egan, M. P., Price, S. D., & Kraemer, K. E. 2003, in Bulletin of the American Astronomical Society, Vol. 35, Bulletin of the American Astronomical Society, 1301–

Eisenhauer, F., Abuter, R., Bickert, K., et al. 2003, in Presented at the Society of Photo-Optical Instrumentation Engineers (SPIE) Conference, Vol. 4841, Society of Photo-Optical Instrumentation Engineers (SPIE) Conference Series, ed. M. Iye & A. F. M. Moorwood, 1548–1561

Eisner, J. A., Lane, B. F., Akeson, R. L., Hillenbrand, L. A., & Sargent, A. I. 2003, ApJ, 588, 360

Eisner, J. A., Lane, B. F., Hillenbrand, L. A., Akeson, R. L., & Sargent, A. I. 2004, ApJ, 613, 1049

Eisner, J. A., Monnier, J. D., Woillez, J., et al. 2010, ApJ, 718, 774

Ekström, S., Meynet, G., Maeder, A., & Barblan, F. 2008, A&A, 478, 467

Enoch, M. L., Evans, II, N. J., Sargent, A. I., et al. 2008, ApJ, 684, 1240

Evans, II, N. J. 1999, ARA&A, 37, 311

Fabricius, C. & Makarov, V. V. 2000, A&A, 356, 141

Farrenq, R., Guelachvili, G., Sauval, A. J., Grevesse, N., & Farmer, C. B. 1991, JMoSp, 149, 375

Fedele, D., van den Ancker, M. E., Acke, B., et al. 2008, A&A, 491, 809

Ferreira, J., Dougados, C., & Cabrit, S. 2006, A&A, 453, 785

Ferreira, J., Pelletier, G., & Appl, S. 2000, MNRAS, 312, 387

Finkenzeller, U. & Mundt, R. 1984, A&AS, 55, 109

Follert, R., Linz, H., Stecklum, B., et al. 2010, ArXiv e-prints

Frémat, Y., Zorec, J., Hubert, A., & Floquet, M. 2005, A&A, 440, 305

Friesen, R. K., Di Francesco, J., Shirley, Y. L., & Myers, P. C. 2009, ApJ, 697, 1457

Fruchter, A. S. & Hook, R. N. 2002, PASP, 114, 144

Fu, H.-H., Hartkopf, W. I., Mason, B. D., et al. 1997, AJ, 114, 1623

Fuente, A., Alonso-Albi, T., Bachiller, R., et al. 2006, ApJ, 649, L119

Fukagawa, M., Tamura, M., Itoh, Y., et al. 2006, ApJL, 636, L153

Fuller, G. A. & Myers, P. C. 1992, ApJ, 384, 523

Galli, D. & Shu, F. H. 1993a, ApJ, 417, 220

Galli, D. & Shu, F. H. 1993b, ApJ, 417, 243

Garay, G., Brooks, K. J., Mardones, D., & Norris, R. P. 2003, ApJ, 587, 739

Garay, G., Mardones, D., Bronfman, L., et al. 2007, A&A, 463, 217

Garcia, P. J. V., Thiébaut, E., & Bacon, R. 1999, A&A, 346, 892

Garcia Lopez, R., Natta, A., Testi, L., & Habart, E. 2006, A&A, 459, 837

Genzel, R. & Stutzki, J. 1989, ARA&A, 27, 41

Gies, D. R., Bagnuolo, Jr., W. G., Baines, E. K., et al. 2007, ApJ, 654, 527

Girart, J. M., Beltrán, M. T., Zhang, Q., Rao, R., & Estalella, R. 2009, Science, 324,

1408

Girart, J. M., Rao, R., & Marrone, D. P. 2006, Science, 313, 812

Goodman, A. A., Benson, P. J., Fuller, G. A., & Myers, P. C. 1993, ApJ, 406, 528

Goodwin, S. P., Kroupa, P., Goodman, A., & Burkert, A. 2007, in Protostars and Planets V, ed. B. Reipurth, D. Jewitt, & K. Keil, 133–147

Grady, C. A., Perez, M. R., Talavera, A., et al. 1996, A&AS, 120, 157

Grady, C. A., Sitko, M. L., Bjorkman, K. S., et al. 1997, ApJ, 483, 449

Grady, C. A., Woodgate, B., Torres, C. A. O., et al. 2004, ApJ, 608, 809

Grave, J. M. C. & Kumar, M. S. N. 2007, A&A, 462, L37

Gray, R. O. & Corbally, C. J. 1994, AJ, 107, 742

Grundstrom, E. D. & Gies, D. R. 2006, ApJL, 651, L53

Grunhut, J. H., Wade, G. A., Marcolino, W. L. F., et al. 2009, MNRAS, 400, L94

Gueth, F. & Guilloteau, S. 1999, A&A, 343, 571

Guetter, H. H. 1968, PASP, 80, 197

Hamann, F., Depoy, D. L., Johansson, S., & Elias, J. 1994, ApJ, 422, 626

Hamann, F. & Persson, S. E. 1992, ApJS, 82, 285

Hanson, M. M., Luhman, K. L., & Rieke, G. H. 2002, ApJS, 138, 35

Hanuschik, R. W. 1996, A&A, 308, 170

Hanuschik, R. W., Hummel, W., Dietle, O., & Sutorius, E. 1995, A&A, 300, 163

Harju, J., Walmsley, C. M., & Wouterloot, J. G. A. 1991, A&A, 245, 643

Harmanec, P. 1988, Bull. Astron. Inst. Czechoslovakia, 39, 329

Harrington, D. M. & Kuhn, J. R. 2007, ApJL, 667, L89

Harrington, D. M. & Kuhn, J. R. 2009a, ApJS, 180, 138

Harrington, D. M. & Kuhn, J. R. 2009b, ApJ, 695, 238

Hartigan, P., Edwards, S., & Ghandour, L. 1995, ApJ, 452, 736

Hartkopf, W. I., Mason, B. D., McAlister, H. A., et al. 1996, AJ, 111, 936

Hartmann, L., Ballesteros-Paredes, J., & Bergin, E. A. 2001, ApJ, 562, 852

Hartmann, L., Hewett, R., Stahler, S., & Mathieu, R. D. 1986, ApJ, 309, 275

Hartmann, L., Kenyon, S. J., & Calvet, N. 1993, ApJ, 407, 219

Hatchell, J., Fuller, G. A., Richer, J. S., Harries, T. J., & Ladd, E. F. 2007, A&A, 468, 1009

Hawley, J. F. & Balbus, S. A. 1991, ApJ, 376, 223

Hawley, J. F., Gammie, C. F., & Balbus, S. A. 1995, ApJ, 440, 742

Hawley, J. F., Gammie, C. F., & Balbus, S. A. 1996, ApJ, 464, 690

Hayashi, C. 1966, ARA&A, 4, 171

Heger, A., Kolbe, E., Haxton, W. C., et al. 2005, PhysLB, 606, 258

Hennebelle, P. & Ciardi, A. 2009, A&A, 506, L29

Hennebelle, P. & Fromang, S. 2008, A&A, 477, 9

Herbig, G. H. 1960, ApJ Supplement, 4, 337

Herbig, G. H. & Bell, K. R. 1988, Catalog of emission line stars of the orion population : 3 : 1988 (Lick Obse. Bull.)

Hernández, J., Calvet, N., Briceño, C., Hartmann, L., & Berlind, P. 2004, AJ, 127, 1682

Herrero, A., Kudritzki, R. P., Vilchez, J. M., et al. 1992, A&A, 261, 209

Hillenbrand, L. A. 1997, AJ, 113, 1733

Hillenbrand, L. A., Strom, S. E., Vrba, F. J., & Keene, J. 1992, Astrophysical Journal, 397, 613

Hiltner, W. A. 1956, ApJS, 2, 389

Hinkle, K., Wallace, L., & Livingston, W. 1995, PASP, 107, 1042

Hinkle, K. H., Joyce, R. R., Sharp, N., & Valenti, J. A. 2000, in , 720

Hirth, G. A., Mundt, R., & Solf, J. 1994, A&A, 285, 929

Hoare, M. G. 2006, ApJ, 649, 856

Hoare, M. G., Drew, J. E., Muxlow, T. B., & Davis, R. J. 1994, ApJL, 421, L51

Hoare, M. G. & Franco, J. 2007, ArXiv e-prints

Hobson, M. P. 1992, MNRAS, 256, 457

Hoffleit, D. & Jaschek, C. 1982, The Bright Star Catalogue

Horne, K. 1995, A&A, 297, 273

Horne, K. & Marsh, T. R. 1986, MNRAS, 218, 761

Hosokawa, T. & Omukai, K. 2009, ApJ, 691, 823

Hosokawa, T., Yorke, H. W., & Omukai, K. 2010, ApJ, 721, 478

Hubrig, S., Pogodin, M. A., Yudin, R. V., Schöller, M., & Schnerr, R. S. 2007, A&A, 463, 1039

Hubrig, S., Stelzer, B., Schoeller, M., et al. 2009, ArXiv e-prints

Hummel, W. & Vrancken, M. 2000, A&A, 359, 1075

Iben, I. J. 1965, ApJ, 141, 993

Isella, A., Tatulli, E., Natta, A., & Testi, L. 2008, A&A, 483, L13

Jamar, C., Macau-Hercot, D., Monfils, A., et al. 1995, VizieR Online Data Catalog, 3039, 0

Jarad, M. M. 1987, Ap&SS, 139, 83

Jensen, E. L. N., Mathieu, R. D., Donar, A. X., & Dullighan, A. 2004, ApJ, 600, 789

Jiang, Z., Tamura, M., Hoare, M. G., et al. 2008, ApJL, 673, L175

Jijina, J. & Adams, F. C. 1996, ApJ, 462, 874

Johnson, H. L., Iriarte, B., Mitchell, R. I., & Wisniewski, W. Z. 1966, Communications of the Lunar and Planetary Laboratory, 4, 99

Jones, C. E., Sigut, T. A. A., & Porter, J. M. 2008, MNRAS, 386, 1922

Kaeufl, H., Ballester, P., Biereichel, P., et al. 2004, in , 1218

Kahn, F. D. 1974, A&A, 37, 149

Kang, M., Choi, M., Ho, P. T. P., & Lee, Y. 2008, ApJ, 683, 267

Kervella, P., Domiciano de Souza, A., & Bendjoya, P. 2008, A&A, 484, L13

Keto, E. 2003, ApJ, 599, 1196

Klessen, R. S. 2001, ApJ, 556, 837

Klessen, R. S., Heitsch, F., & Mac Low, M. 2000, ApJ, 535, 887

Kouwenhoven, M. B. N., Brown, A. G. A., Goodwin, S. P., Portegies Zwart, S. F., & Kaper, L. 2009, A&A, 493, 979

Kouwenhoven, M. B. N., Brown, A. G. A., Zinnecker, H., Kaper, L., & Portegies Zwart, S. F. 2005, A&A, 430, 137

Krasnopolsky, R. & Königl, A. 2002, ApJ, 580, 987

Kratter, K. M., Matzner, C. D., Krumholz, M. R., & Klein, R. I. 2010, ApJ, 708, 1585

Kraus, M., Krügel, E., Thum, C., & Geballe, T. R. 2000, A&A, 362, 158

Kraus, S., Hofmann, K., Malbet, F., et al. 2009, A&A, 508, 787

Kraus, S., Hofmann, K., Menten, K. M., et al. 2010, Nat, 466, 339

Kraus, S., Hofmann, K.-H., Benisty, M., et al. 2008a, A&A, 489, 1157

Kraus, S., Preibisch, T., & Ohnaka, K. 2008b, ApJ, 676, 490

Kroupa, P. 1995, MNRAS, 277, 1507

Kroupa, P. 2001, MNRAS, 322, 231

Kroupa, P. & Burkert, A. 2001, ApJ, 555, 945

Krumholz, M. R. 2006, ApJL, 641, L45

Krumholz, M. R., Klein, R. I., & McKee, C. F. 2007, ApJ, 656, 959

Krumholz, M. R., Klein, R. I., McKee, C. F., Offner, S. S. R., & Cunningham, A. J. 2009, Sci, 323, 754

Krumholz, M. R. & McKee, C. F. 2005, ApJ, 630, 250

Krumholz, M. R., McKee, C. F., & Klein, R. I. 2005a, ApJL, 618, L33

Krumholz, M. R., McKee, C. F., & Klein, R. I. 2005b, Nat, 438, 332

Krumholz, M. R. & Tan, J. C. 2007, ApJ, 654, 304

Krumholz, M. R. & Thompson, T. A. 2007, ApJ, 661, 1034

Kuhn, J. R., Berdyugina, S. V., Fluri, D. M., Harrington, D. M., & Stenflo, J. O. 2007, ApJL, 668, L63

Kuiper, R., Klahr, H., Beuther, H., & Henning, T. 2010, ArXiv e-prints

Lada, C. J. & Lada, E. A. 2003, ARA&A, 41, 57

Lada, C. J., Muench, A. A., Rathborne, J., Alves, J. F., & Lombardi, M. 2008, ApJ, 672, 410

Lada, C. J. & Shu, F. H. 1990, Sci, 248, 564

Ladd, E. F., Lada, E. A., & Myers, P. C. 1993, ApJ, 410, 168

Landini, M., Natta, A., Salinari, P., Oliva, E., & Moorwood, A. F. M. 1984, A&A, 134, 284

Larson, R. B. 1969, MNRAS, 145, 271

Larson, R. B. 1981, MNRAS, 194, 809

Larson, R. B. 2003, Reports on Progress in Physics, 66, 1651

Larson, R. B. & Starrfield, S. 1971, A&A, 13, 190

Launhardt, R., Evans, II, N. J., Wang, Y., et al. 1998, ApJS, 119, 59

Le Bouquin, J., Absil, O., Benisty, M., et al. 2009, A&A, 498, L41

Lee, C., Mundy, L. G., Reipurth, B., Ostriker, E. C., & Stone, J. M. 2000, ApJ, 542, 925

Lee, C., Mundy, L. G., Stone, J. M., & Ostriker, E. C. 2002, ApJ, 576, 294

Lee, U., Osaki, Y., & Saio, H. 1991, MNRAS, 250, 432

Leinert, C., Haas, M., Ábrahám, P., & Richichi, A. 2001, A&A, 375, 927

Leinert, C., Richichi, A., & Haas, M. 1997, A&A, 318, 472

Linz, H., Henning, T., Feldt, M., et al. 2009, A&A, 505, 655

Lizano, S. & Shu, F. H. 1989, ApJ, 342, 834

Lumsden, S. L., Hoare, M. G., Oudmaijer, R. D., & Richards, D. 2002, MNRAS, 336, 621

Lumsden, S. L. & Puxley, P. J. 1996, MNRAS, 281, 493

Lynden-Bell, D. 2003, MNRAS, 341, 1360

Lynden-Bell, D. & Kalnajs, A. J. 1972, MNRAS, 157, 1

Mac Low, M. & Klessen, R. S. 2004, Reviews of Modern Physics, 76, 125

Mac Low, M. & McCray, R. 1988, ApJ, 324, 776

Machida, M. N., Inutsuka, S., & Matsumoto, T. 2007, ApJ, 670, 1198

Maheswar, G., Manoj, P., & Bhatt, H. C. 2002, A&A, 387, 1003

Maíz-Apellániz, J., Walborn, N. R., Galué, H. Á., & Wei, L. H. 2004, ApJS, 151, 103

Malbet, F., Benisty, M., de Wit, W., et al. 2007, A&A, 464, 43

Malfait, K., Bogaert, E., & Waelkens, C. 1998, A&A, 331, 211

Mannings, V. & Sargent, A. I. 1997, ApJ, 490, 792

Manoj, P., Ho, P. T. P., Ohashi, N., et al. 2007, ApJL, 667, L187

Maret, S. & Bergin, E. A. 2007, ApJ, 664, 956

Marti, J., Rodriguez, L. F., & Reipurth, B. 1993, ApJ, 416, 208

Marti, J., Rodriguez, L. F., & Reipurth, B. 1995, ApJ, 449, 184

Martins, F., Schaerer, D., & Hillier, D. J. 2005, A&A, 436, 1049

Mason, B. D. 1997, AJ, 114, 808

Mason, B. D., Ten Brummelaar, T., Gies, D. R., Hartkopf, W. I., & Thaller, M. L. 1997, AJ, 114, 2112

Masson, C. R. & Chernin, L. M. 1993, ApJ, 414, 230

Masunaga, H. & Inutsuka, S. 2000, ApJ, 531, 350

Masunaga, H., Miyama, S. M., & Inutsuka, S. 1998, ApJ, 495, 346

Matt, S. & Pudritz, R. E. 2004, ApJL, 607, L43

Matt, S. & Pudritz, R. E. 2005, ApJL, 632, L135

Matt, S. & Pudritz, R. E. 2008, ApJ, 678, 1109

Matthews, B. C., Lai, S., Crutcher, R. M., & Wilson, C. D. 2005, ApJ, 626, 959

Matzner, C. D. 2002, ApJ, 566, 302

Mazzitelli, I. & Moretti, M. 1980, ApJ, 235, 955

McCray, R. & Kafatos, M. 1987, ApJ, 317, 190

McGroarty, F., Ray, T. P., & Bally, J. 2004, A&A, 415, 189

McKee, C. F. & Ostriker, E. C. 2007, ARA&A, 45, 565

McKee, C. F. & Tan, J. C. 2003, ApJ, 585, 850

McKee, C. F., van Buren, D., & Lazareff, B. 1984, ApJL, 278, L115

McLean, I. S. & Clarke, D. 1979, MNRAS, 186, 245

McSwain, M. V., Huang, W., Gies, D. R., Grundstrom, E. D., & Townsend, R. H. D. 2008, ApJ, 672, 590

Megeath, S. T., Herter, T., Beichman, C., et al. 1996, A&A, 307, 775

Meilland, A., Millour, F., Stee, P., et al. 2007a, A&A, 464, 73

Meilland, A., Millour, F., Stee, P., et al. 2008, A&A, 488, L67

Meilland, A., Stee, P., Chesneau, O., & Jones, C. 2009, A&A, 505, 687

Meilland, A., Stee, P., Vannier, M., et al. 2007b, A&A, 464, 59

Mellon, R. R. & Li, Z. 2009, ApJ, 698, 922

Melnikov, S., Woitas, J., Eislöffel, J., et al. 2008, A&A, 483, 199

Mestel, L. & Paris, R. B. 1979, MNRAS, 187, 337

Mestel, L. & Spitzer, Jr., L. 1956, MNRAS, 116, 503

Meynet, G. & Maeder, A. 2005, A&A, 429, 581

Miettinen, O., Harju, J., Haikala, L. K., Kainulainen, J., & Johansson, L. E. B. 2009, A&A, 500, 845

Millan-Gabet, R., Schloerb, F. P., & Traub, W. A. 2001, ApJ, 546, 358

Miroshnichenko, A., Ivezic, Z., & Elitzur, M. 1997, ApJ, 475, L41

Moeckel, N. & Bally, J. 2007, ApJ, 656, 275

Molinari, S., Brand, J., Cesaroni, R., & Palla, F. 1996, A&A, 308, 573

Monin, J.-L., Ménard, F., & Peretto, N. 2006, A&A, 446, 201

Monnier, J. D., Berger, J.-P., Millan-Gabet, R., et al. 2006, ApJ, 647, 444

Monnier, J. D., Tannirkulam, A., Tuthill, P. G., et al. 2008, ApJL, 681, L97

Monnier, J. D. e. a. 2005, ApJ, 624, 832

Montesinos, B., Eiroa, C., Mora, A., & Merín, B. 2009, A&A, 495, 901

Moore, T. J. T., Lumsden, S. L., Ridge, N. A., & Puxley, P. J. 2005, MNRAS, 359, 589

Mora, A., Eiroa, C., Natta, A., et al. 2004, A&A, 419, 225

Mora, A., Merín, B., Solano, E., et al. 2001, A&A, 378, 116

Mottram, J. C., Hoare, M. G., Lumsden, S. L., et al. 2010, A&A, 510, A89

Mottram, J. C., Hoare, M. G., Lumsden, S. L., et al. 2007a, A&A, 476, 1019

Mottram, J. C., Vink, J. S., Oudmaijer, R. D., & Patel, M. 2007b, MNRAS, 377, 1363

Mouschovias, T. C. 1987, in NATO ASIC Proc. 210: Physical Processes in Interstellar Clouds, ed. G. E. Morfill & M. Scholer, 453–489

Mouschovias, T. C. 1991, in NATO ASIC Proc. 342: The Physics of Star Formation and Early Stellar Evolution, ed. C. J. Lada & N. D. Kylafis, 449

Mouschovias, T. C. & Paleologou, E. V. 1979, ApJ, 230, 204

Movsessian, T. A., Magakian, T. Y., & Afanasiev, V. L. 2002, A&A, 390, L5

Muench, A. A., Lada, C. J., Rathborne, J. M., Alves, J. F., & Lombardi, M. 2007, ApJ, 671, 1820

Mundt, R., Buehrke, T., Solf, J., Ray, T. P., & Raga, A. C. 1990, A&A, 232, 37

Mundt, R. & Fried, J. W. 1983, ApJL, 274, L83

Mundt, R. & Ray, T. P. 1994, in A.S.P. Conf. Ser., Vol. 62, The Nature and Evolutionary Status of Herbig Ae/Be Stars, ed. P. S. The, M. R. Perez, & E. P. J. van den Heuvel, 237

Muzerolle, J., D'Alessio, P., Calvet, N., & Hartmann, L. 2004, ApJ, 617, 406

Myers, P. C. & Benson, P. J. 1983, ApJ, 266, 309

Najita, J., Carr, J. S., Glassgold, A. E., Shu, F. H., & Tokunaga, A. T. 1996, ApJ, 462, 919

Nakano, T. 1989, ApJ, 345, 464

Natta, A., Grinin, V. P., & Tambovtseva, L. V. 2000, ApJ, 542, 421

Natta, A., Prusti, T., Neri, R., et al. 2001, A&A, 371, 186

Neiner, C., Hubert, A.-M., Frémat, Y., et al. 2003, A&A, 409, 275

Nielbock, M., Chini, R., Hoffmeister, V. H., et al. 2008, MNRAS, 388, 1031

Nisini, B., Bacciotti, F., Giannini, T., et al. 2005, A&A, 441, 159

Nisini, B., Caratti o Garatti, A., Giannini, T., & Lorenzetti, D. 2002, A&A, 393, 1035

Nordsieck, K. H. & Harris, W. 1996, in Astronomical Society of the Pacific Conference Series, Vol. 97, Polarimetry of the Interstellar Medium, ed. W. G. Roberge & D. C. B. Whittet, 100

Novak, G., Dotson, J. L., & Li, H. 2009, ApJ, 695, 1362

Okamoto, Y. K., Kataza, H., Honda, M., et al. 2009, ApJ, 706, 665

Okazaki, A. T. 1991, PASJ, 43, 75

Okazaki, A. T. 2001, PASJ, 53, 119

Oudmaijer, R. D. & Drew, J. E. 1999, MNRAS, 305, 166

Oudmaijer, R. D., Parr, A., Baines, D., & Porter, J. 2008, A&A, 489, 627

Oudmaijer, R. D. & Parr, A. M. 2010, MNRAS, 405, 2439

Oudmaijer, R. D., van der Veen, W. E. C. J., Waters, L. B. F. M., et al. 1992, A&AS, 96, 625

Owocki, S. 2006, in A.S.P Conf. Ser, Vol. 355, Stars with the B[e] Phenomenon, ed. M. Kraus & A. S. Miroshnichenko, 219–+

Owocki, S. & Ud-Doula, A. 2003, in Astronomical Society of the Pacific Conference Series, Vol. 305, Astronomical Society of the Pacific Conference Series, ed. L. A. Balona, H. F. Henrichs, & R. Medupe, 350–+

Owocki, S. P., Cranmer, S. R., & Gayley, K. G. 1996, ApJL, 472, L115+

Padoan, P. & Nordlund, Å. 2002, ApJ, 576, 870

Palla, F. & Stahler, S. W. 1993, ApJ, 418, 414

Parker, R. J. & Goodwin, S. P. 2007, MNRAS, 380, 1271

Parker, R. J., Goodwin, S. P., Kroupa, P., & Kouwenhoven, M. B. N. 2009, MNRAS, 397, 1577

Parsons, H., Thompson, M. A., & Chrysostomou, A. 2009, MNRAS, 399, 1506

Patel, M., Oudmaijer, R. D., Vink, J. S., Mottram, J. C., & Davies, B. 2006, MNRAS, 373, 1641

Patel, N. A., Curiel, S., Sridharan, T. K., et al. 2005, Nat, 437, 109

Perrin, M. D., Duchêne, G., Kalas, P., & Graham, J. R. 2006, ApJ, 645, 1272

Perrin, M. D. & Graham, J. R. 2007, ApJ, 670, 499

Perryman, M. A. C., Lindegren, L., Kovalevsky, J., et al. 1997, A&A, 323, L49

Petit, V., Wade, G. A., Drissen, L., Montmerle, T., & Alecian, E. 2008, MNRAS, 387, L23

Petrov, R. G. & Lagarde, S. 1992, in A.S.P Conf. Ser., Vol. 32, IAU Colloq. 135: Complementary Approaches to Double and Multiple Star Research, ed. H. A. McAlister & W. I. Hartkopf, 477

Pietrinferni, A., Cassisi, S., Salaris, M., & Castelli, F. 2004, ApJ, 612, 168

Pirzkal, N., Spillar, E. J., & Dyck, H. M. 1997, ApJ, 481, 392

Podio, L., Bacciotti, F., Nisini, B., et al. 2006, A&A, 456, 189

Poeckert, R. 1975, ApJ, 196, 777

Poeckert, R. & Marlborough, J. M. 1976, ApJ, 206, 182

Poetzel, R., Mundt, R., & Ray, T. P. 1992, A&A, 262, 229

Pontoppidan, K. M., Blake, G. A., van Dishoeck, E. F., et al. 2008, ApJ, 684, 1323

Porter, J. M. 1996, MNRAS, 280, L31

Porter, J. M. 1999, A&A, 348, 512

Porter, J. M., Drew, J. E., & Lumsden, S. L. 1998, A&A, 332, 999

Porter, J. M., Oudmaijer, R. D., & Baines, D. 2004, A&A, 428, 327

Porter, J. M. & Rivinius, T. 2003, PASP, 115, 1153

Pott, J., Woillez, J., Ragland, S., et al. 2010, ArXiv e-prints

Preibisch, T., Kraus, S., Driebe, T., van Boekel, R., & Weigelt, G. 2006, A&A, 458, 235

Prentice, A. J. R. & Ter Haar, D. 1971, MNRAS, 151, 177

Press, W. H., Teukolsky, S. A., Vetterling, W. T., & Flannery, B. P. 1992, Numerical recipes in C. The art of scientific computing, ed. Press, W. H., Teukolsky, S. A., Vetterling, W. T., & Flannery, B. P.

Price, S. D., Egan, M. P., Carey, S. J., Mizuno, D. R., & Kuchar, T. A. 2001, AJ, 121, 2819

Pringle, J. E. 1981, ARA&A, 19, 137

Pudritz, R. E. & Norman, C. A. 1986, ApJ, 301, 571

Pudritz, R. E., Ouyed, R., Fendt, C., & Brandenburg, A. 2007, Protostars and Planets V, 277

Qiu, K. & Zhang, Q. 2009, ApJL, 702, L66

Quirrenbach, A., Bjorkman, K. S., Bjorkman, J. E., et al. 1997, ApJ, 479, 477

Quirrenbach, A., Buscher, D. F., Mozurkewich, D., Hummel, C. A., & Armstrong, J. T. 1994, A&A, 283, L13

Raga, A. C. & Kofman, L. 1992, ApJ, 386, 222

Rathborne, J. M., Jackson, J. M., & Simon, R. 2006, ApJ, 641, 389

Ray, T., Dougados, C., Bacciotti, F., Eislöffel, J., & Chrysostomou, A. 2007, Protostars and Planets V, 231

Ray, T. P. 1987, A&A, 171, 145

Ray, T. P. 2009, in Revista Mexicana de Astronomia y Astrofisica Conference Series, Vol. 36, Revista Mexicana de Astronomia y Astrofisica Conference Series, 179–185

Ray, T. P., Mundt, R., Dyson, J. E., Falle, S. A. E. G., & Raga, A. C. 1996, ApJL, 468, L103+

Ray, T. P., Poetzel, R., Solf, J., & Mundt, R. 1990, ApJL, 357, L45

Reed, B. C. 2003, AJ, 125, 2531

Reipurth, B. 1989, NAT, 340, 42

Reipurth, B. & Bally, J. 2001, ARA&A, 39, 403

Reipurth, B., Heathcote, S., Morse, J., Hartigan, P., & Bally, J. 2002, AJ, 123, 362

Reipurth, B., Pedrosa, A., & Lago, M. T. V. T. 1996, A&AS, 120, 229

Renard, S., Malbet, F., Benisty, M., Thiébaut, E., & Berger, J. 2010, ArXiv e-prints

Rivinius, T., Baade, D., & Štefl, S. 2003, A&A, 411, 229

Rivinius, T., Štefl, S., & Baade, D. 2006, A&A, 459, 137

Robitaille, T. P., Whitney, B. A., Indebetouw, R., & Wood, K. 2007, ApJS, 169, 328

Rodgers, B., Wooden, D. H., Grinin, V., Shakhovsky, D., & Natta, A. 2002, ApJ, 564, 405

Rodríguez, L. F., Garay, G., Brooks, K. J., & Mardones, D. 2005, ApJ, 626, 953

Rodríguez, L. F., Moran, J. M., Franco-Hernández, R., et al. 2008, AJ, 135, 2370

Rosolowsky, E. W., Pineda, J. E., Foster, J. B., et al. 2008, ApJS, 175, 509

Rousselet-Perraut, K., Benisty, M., Mourard, D., et al. 2010, A&A, 516, L1+

Sana, H., Gosset, E., & Evans, C. J. 2009, MNRAS, 400, 1479

Sana, H., Gosset, E., Nazé, Y., Rauw, G., & Linder, N. 2008, MNRAS2008, 386, 447

Sandell, G. & Wright, M. 2010, ApJ, 715, 919

Santiago-García, J., Tafalla, M., Johnstone, D., & Bachiller, R. 2009, A&A, 495, 169

Sargent, A. I. 1977, ApJ, 218, 736

Sbordone, L., Bonifacio, P., Castelli, F., & Kurucz, R. L. 2004, Memorie della Societa Astronomica Italiana Supplement, 5, 93

Schaller, G., Schaerer, D., Meynet, G., & Maeder, A. 1992, A&ASS, 96, 269

Schnerr, R. S., Henrichs, H. F., Neiner, C., et al. 2008, A&A, 483, 857

Scholz, A., Wood, K., Wilner, D., et al. 2010, ArXiv e-prints

Scoville, N., Kleinmann, S. G., Hall, D. N. B., & Ridgway, S. T. 1983, ApJ, 275, 201

Shang, H., Li, Z.-Y., & Hirano, N. 2007, in Protostars and Planets V, ed. B. Reipurth, D. Jewitt, & K. Keil, 261–276

Shatsky, N. & Tokovinin, A. 2002, A&A, 382, 92

Shepherd, D. S., Claussen, M. J., & Kurtz, S. E. 2001, Sci, 292, 1513

Shepherd, D. S. & Kurtz, S. E. 1999, ApJ, 523, 690

Shevchenko, V. S. & Vitrichenko, E. A. 1994, in A. S. P. Conf. Ser., Vol. 62, The Nature and Evolutionary Status of Herbig Ae/Be Stars, ed. P. S. The, M. R. Perez, & E. P. J. van den Heuvel, 55–56

Shu, F., Najita, J., Ostriker, E., et al. 1994, ApJ, 429, 781

Shu, F. H. 1977, ApJ, 214, 488

Shu, F. H., Adams, F. C., & Lizano, S. 1987, ARA&A, 25, 23

Shull, J. M. & Beckwith, S. 1982, ARA&A, 20, 163

Siess, L., Dufour, E., & Forestini, M. 2000, A&A, 358, 593

Silvester, J., Neiner, C., Henrichs, H. F., et al. 2009, ArXiv e-prints

Sim, S. A., Drew, J. E., & Long, K. S. 2005, MNRAS, 363, 615

Simon, M., Peterson, D. M., Longmore, A. J., Storey, J. W. V., & Tokunaga, A. T. 1985, ApJ, 298, 328

Simon, R., Jackson, J. M., Rathborne, J. M., & Chambers, E. T. 2006a, ApJ, 639, 227

Simon, R., Rathborne, J. M., Shah, R. Y., Jackson, J. M., & Chambers, E. T. 2006b, ApJ, 653, 1325

Sitko, M. L., Carpenter, W. J., Kimes, R. L., et al. 2008, ApJ, 678, 1070

Slettebak, A. 1954, ApJ, 119, 146

Slettebak, A. 1982, ApJS, 50, 55

Smith, K. W., Balega, Y. Y., Duschl, W. J., et al. 2005, A&A, 431, 307

Smith, M. A. 1972, ApJ, 175, 765

Snell, R. L., Bally, J., Strom, S. E., & Strom, K. M. 1985, ApJ, 290, 587

Snell, R. L., Loren, R. B., & Plambeck, R. L. 1980, ApJL, 239, L17

Soderhjelm, S. 1980, A&A, 89, 100

Söderhjelm, S. 2007, A&A, 463, 683

Solomon, P. M., Sanders, D. B., & Rivolo, A. R. 1985, ApJL, 292, L19

Spitoni, E., Matteucci, F., Recchi, S., Cescutti, G., & Pipino, A. 2009, A&A, 504, 87

Spitzer, L. 1978, Physical processes in the interstellar medium, ed. Spitzer, L.

Sridharan, T. K., Beuther, H., Schilke, P., Menten, K. M., & Wyrowski, F. 2002, ApJ, 566, 931

Stahler, S. W. 1988, ApJ, 332, 804

Stahler, S. W. & Palla, F. 2005, The Formation of Stars, ed. Stahler, S. W. & Palla, F.

Stead, J. J. & Hoare, M. G. 2009, MNRAS, 400, 731

Stecklum, B., Eckart, A., Henning, T., & Loewe, M. 1995, A&A, 296, 463

Storey, P. J. & Hummer, D. G. 1995, MNRAS, 272, 41

Straizys, V. & Kuriliene, G. 1981, ApSS, 80, 353

Strickland, D. K. & Stevens, I. R. 1999, MNRAS, 306, 43

Strom, S. E., Strom, K. M., Yost, J., Carrasco, L., & Grasdalen, G. 1972, ApJ, 173, 353

Struve, O. 1931, ApJ, 73, 94

Tafalla, M., Myers, P. C., Caselli, P., & Walmsley, C. M. 2004a, A&A, 416, 191

Tafalla, M., Santiago, J., Johnstone, D., & Bachiller, R. 2004b, A&A, 423, L21

Takami, M., Bailey, J., & Chrysostomou, A. 2003, A&A, 397, 675

Takami, M., Bailey, J., Gledhill, T. M., Chrysostomou, A., & Hough, J. H. 2001, MNRAS, 323, 177

Tassis, K. & Mouschovias, T. C. 2004, ApJ, 616, 283

Tatulli, E., Malbet, F., Ménard, F., et al. 2008, A&A, 489, 1151

Terebey, S., Shu, F. H., & Cassen, P. 1984, ApJ, 286, 529

Testi, L., Palla, F., & Natta, A. 1999, A&A, 342, 515

Thé, P. S., de Winter, D., & Perez, M. R. 1994, A&AS, 104, 315

Thomas, S. J., van der Bliek, N. S., Rodgers, B., Doppmann, G., & Bouvier, J. 2007, in IAU Symp, Vol. 240, IAU Symp., ed. W. I. Hartkopf, E. F. Guinan, & P. Harmanec, 250–253

Tjin A Djie, H. R. E., The, P. S., Andersen, J., et al. 1989, A&AS, 78, 1

Tody, D. 1993, in A.S.P. Conf.Ser., Vol. 52, Astronomical Data Analysis Software and Systems II, ed. R. J. Hanisch, R. J. V. Brissenden, & J. Barnes, 173–183

Townsend, R. H. D., Owocki, S. P., & Howarth, I. D. 2004, MNRAS, 350, 189

Troland, T. H. & Crutcher, R. M. 2008, ApJ, 680, 457

Turner, N. J., Quataert, E., & Yorke, H. W. 2007, ApJ, 662, 1052

Tycner, C., Hajian, A. R., Armstrong, J. T., et al. 2004, AJ, 127, 1194

Tycner, C., Lester, J. B., Hajian, A. R., et al. 2005, ApJ, 624, 359

Ud-Doula, A. & Owocki, S. P. 2002, ApJ, 576, 413

Ud-Doula, A., Owocki, S. P., & Townsend, R. H. D. 2008, MNRAS, 385, 97

Ud-Doula, A., Townsend, R. H. D., & Owocki, S. P. 2006, ApJ, 640, L191

Ungerechts, H. & Thaddeus, P. 1987, ApJS, 63, 645

Urquhart, J. S., Busfield, A. L., Hoare, M. G., et al. 2007a, A&A, 461, 11

Urquhart, J. S., Busfield, A. L., Hoare, M. G., et al. 2007b, A&A, 474, 891

Urquhart, J. S., Busfield, A. L., Hoare, M. G., et al. 2008a, A&A, 487, 253

Urquhart, J. S., Hoare, M. G., Lumsden, S. L., Oudmaijer, R. D., & Moore, T. J. T. 2008b, in , 381

Urquhart, J. S., Hoare, M. G., Purcell, C. R., et al. 2009, A&A, 501, 539

Vaidya, B., Fendt, C., & Beuther, H. 2009, ApJ, 702, 567

Vakili, F., Mourard, D., Stee, P., et al. 1998, A&A, 335, 261

van den Ancker, M. E., de Winter, D., & Tjin A Djie, H. R. E. 1998, A&A, 330, 145

van der Plas, G., van den Ancker, M. E., Acke, B., et al. 2009, A&A, 500, 1137

Vieira, S. L. A., Corradi, W. J. B., Alencar, S. H. P., et al. 2003, AJ, 126, 2971

Vink, J. S. 2008, New Astronomy Review, 52, 419

Vink, J. S., Drew, J. E., Harries, T. J., & Oudmaijer, R. D. 2002, MNRAS, 337, 356

Vink, J. S., Drew, J. E., Harries, T. J., Oudmaijer, R. D., & Unruh, Y. 2005a, MNRAS, 359, 1049

Vink, J. S., Drew, J. E., Steeghs, D., et al. 2008, MNRAS, 387, 308

Vink, J. S., O'Neill, P. M., Els, S. G., & Drew, J. E. 2005b, A&A, 438, L21

Vinković, D. & Jurkić, T. 2007, ApJ, 658, 462

Vlemmings, W. H. T., Surcis, G., Torstensson, K. J. E., & van Langevelde, H. J. 2010, MNRAS, 404, 134

von Zeipel, H. 1924, MNRAS, 84, 665

Wade, G. A., Bagnulo, S., Drouin, D., Landstreet, J. D., & Monin, D. 2007, MNRAS, 376, 1145

Walmsley, M. 1995, in Revista Mexicana de Astronomia y Astrofisica Conference Series, Vol. 1, Revista Mexicana de Astronomia y Astrofisica Conference Series, ed. S. Lizano & J. M. Torrelles, 137

Wamsteker, W., Skillen, I., Ponz, J. D., et al. 2000, ApSS, 273, 155

Ward-Thompson, D., Sen, A. K., Kirk, J. M., & Nutter, D. 2009, MNRAS, 398, 394

Waters, L. B. F., Marlborough, J. M., van der Veen, W. E. C., Taylor, A. R., & Dougherty, S. M. 1991, A&A, 244, 120

Waters, L. B. F. M. 1986, A&A, 162, 121

Weigelt, G., Balega, Y. Y., Hofmann, K.-H., & Preibisch, T. 2002, A&A, 392, 937

Wheelwright, H. E., Oudmaijer, R. D., & Schnerr, R. S. 2009, A&A, 497, 487

Whelan, E. T., Ray, T. P., & Davis, C. J. 2004, A&A, 417, 247

Whitworth, A. P., Chapman, S. J., Bhattal, A. S., et al. 1995, MNRAS, 277, 727

Whitworth, A. P. & Stamatellos, D. 2006, A&A, 458, 817

Williams, J. P., Blitz, L., & McKee, C. F. 2000, Protostars and Planets IV, 97

Williams, J. P., de Geus, E. J., & Blitz, L. 1994, ApJ, 428, 693

Woitas, J., Bacciotti, F., Ray, T. P., et al. 2005, A&A, 432, 149

Wolf, S., Stecklum, B., & Henning, T. 2001, in IAU Symp., Vol. 200, The Formation of Binary Stars, ed. H. Zinnecker & R. Mathieu, 295–304

Wolff, M. J., Nordsieck, K. H., & Nook, M. A. 1996, AJ, 111, 856

Wolfire, M. G. & Cassinelli, J. P. 1987, ApJ, 319, 850

Woosley, S. E., Langer, N., & Weaver, T. A. 1993, ApJ, 411, 823

Wyithe, J. S. B. & Loeb, A. 2003, ApJL, 588, L69

Yorke, H. W., Bodenheimer, P., & Laughlin, G. 1993, ApJ, 411, 274

Yorke, H. W. & Sonnhalter, C. 2002, ApJ, 569, 846

Yudin, R. V. 2001, A&A, 368, 912

Zapata, L. A., Ho, P. T. P., Schilke, P., et al. 2009, ApJ, 698, 1422

Zapata, L. A., Palau, A., Ho, P. T. P., et al. 2008, A&A, 479, L25

Zapata, L. A., Schmid-Burgk, J., Muders, D., et al. 2010, A&A, 510, A2

Zhang, Q., Wang, Y., Pillai, T., & Rathborne, J. 2009, ApJ, 696, 268

Zinnecker, H., McCaughrean, M. J., & Rayner, J. T. 1998, Nat, 394, 862

Zinnecker, H. & Yorke, H. 2007, ARA&A, 45, 481

Zorec, J. & Briot, D. 1997, A&A, 318, 443

Zorec, J., Frémat, Y., & Cidale, L. 2005, A&A, 441, 235